DESIGN AND USE OF A LARGE–FORMAT CCD INSTRUMENT FOR THE IDENTIFICATION AND STUDY OF DISTANT GALAXY CLUSTERS

by

GERARD ANTHONY LUPPINO

B.S. Astronomy and Physics
The Pennsylvania State University
(1983)

SUBMITTED IN PARTIAL FULFILLMENT
OF THE REQUIREMENTS FOR THE
DEGREE OF

DOCTOR OF PHILOSOPHY IN PHYSICS

at the

MASSACHUSETTS INSTITUTE OF TECHNOLOGY

August, 1989

Signature of Author _____
Department of Physics
August, 1989

Certified by _____
George R. Ricker
Thesis Supervisor

Accepted by _____
George Koster
Chairman, Department Committee

DESIGN AND USE OF A LARGE-FORMAT CCD INSTRUMENT FOR THE IDENTIFICATION AND STUDY OF DISTANT GALAXY CLUSTERS

by

GERARD A. LUPPINO

SUBMITTED TO THE DEPARTMENT OF PHYSICS OF THE MASSACHUSETTS INSTITUTE OF TECHNOLOGY ON AUGUST 1989, IN PARTIAL FULFILLMENT OF THE REQUIREMENTS FOR THE DEGREE OF DOCTOR OF PHILOSOPHY IN PHYSICS

ABSTRACT

This dissertation describes a search for distant clusters of galaxies (z>0.3). Cluster candidates were selected from a sample of radio sources with steep, low-frequency spectra since such radio sources are often found in rich nearby galaxy clusters. The steep-spectrum radio source (SSRS) is thought to be produced by the confinement of the radio plasma by the thermal pressure of a hot intracluster gas; therefore, we expect clusters discovered by this selection criterion to be bright x-ray sources and excellent targets for future x-ray satellites such as *ROSAT*, *ASTRO-D* and *AXAF*. These objects are also more likely to be true physical associations rather than the chance superpositions of galaxies that may plague some optically selected samples, particularly those at faint magnitudes. In order to identify the optical counterpart of the SSRS and see if the radio source was part of a distant cluster of galaxies, optical images to faint limiting magnitudes were required. Therefore, an imaging instrument incorporating mosaics of CCDs was designed and built . With this instrument, it is possible to observe faint, distant clusters of galaxies with spatial resolution limited by atmospheric seeing, while at the same time covering a relatively large field of view.

The major task in the creation of this instrument was the design and construction of two separate CCD camera systems; each based on different CCD mosaics. The first camera system incorporates four prototype, TI 850 × 750 virtual-phase CCDs (22.3 μm square pixels) arranged in a square pattern with the device packages abutted. The second camera system is designed to operate a four-chip CCD imager made by MIT Lincoln Laboratory. The imaging area of this CCD mosaic is 840 × 840 pixels (27 μm square pixels) formed by abutting four 840 × 420 framestore devices with seam losses less than 6 pixels. Details of the CCD camera electronics design as well as details of the mechanical design of the CCD cameras and LN_2 dewars are described.

A total of 30 SSRS fields were observed with this CCD instrument mounted on the 1.3m and 2.4m telescopes of the Michigan-Dartmouth-MIT (MDM) Observatory on Kitt Peak. Additional CCD images of 5 of these radio sources were obtained with the Kitt Peak 4m telescope equipped with the KPNO prime focus CCD. Of these 30 SSRSs, 26 have been optically identified. In all, 15 of the observed fields contain visible clusters of galaxies, some of which are quite rich. Of the remaining 15 SSRSs, 6 are identified with faint galaxies , 2 are identified with poor groups, 3 are probably quasars, and 4 of the fields have uncertain or no optical counterpart. The median value for the estimated redshift of the 15 clusters is z=0.43 and the median richness is Abell Class 2. Nearly all of the radio sources have classical double-lobed morphology, and in half of the sources associated with clusters, the radio source is identified with a fainter cluster member rather than with the brightest cluster galaxy. In all cases where the cluster is BM Type I, however, the radio source is identified with the optically dominant galaxy.

Observations are also presented of three distant clusters that were not part of the radio selected sample: 0414+009, an x-ray bright BL Lac object coincident with the optically dominant galaxy in a Richness Class 1 cluster; 1217+1006, a compact group containing an extremely blue $(B-R) \approx 0.0$ object that may be either a QSO or a BL Lac; and 1358+6245, a new, x-ray luminous (L_X (0.5–4.5 keV) = 8.4×10^{44} erg s^{-1}), extremely rich (Richness Class 3 or 4), distant cluster of galaxies (z=0.323) which exhibits the Butcher-Oemler effect with a blue galaxy fraction $f_b = 0.18$ or $f_b = 0.10$ depending on the background galaxy correction.

ACKNOWLEDGMENTS

This instrument and scientific program would not have been possible without the help of a large number of people. First of all, I would like to thank my thesis advisor, George Ricker, who gave me access to a large number of CCDs and allowed me to use some of the best of them in this instrument. He also provided guidance and encouragement, and allowed me the freedom to be creative in the instrument design. I am also indebted to Ian McHardy and Brin Cooke, who developed this method for searching for distant galaxy clusters, and graciously accepted me as a collaborator. I appreciate the constructive comments and advice I received from my thesis committee members, Claude Canizares, and John Tonry. I am especially grateful to John, who taught me how to think as a scientist, and changed my perspective on instrumentation, urging me to "put the science first and let the science requirements drive instrument designs." John was always there to answer questions and help me wring the most out of my data. In addition, as the reader will later discover, nearly all of the software tools I use for data reduction in this thesis were developed and kindly provided by John. Also, thanks to Paul Schechter for helpful advice and criticism during the final stages of this project.

During my first three years as a graduate student, I worked closely with John Vallerga, who taught me almost everything I know about CCDs. The time I spent working with John was the most "productive fun" I ever had in the laboratory. And, I can never thank Roland Vanderspek enough. During my entire time at MIT Roland has been my best friend, companion, and advisor. He has helped me with virtually everything and I will be eternally grateful. I also appreciated the "baked goods" that often appeared when I was working on some particularly tedious or difficult problem.

The designs for much of the CCD electronics used in the instrument described later are based on original designs by John Doty. I first met John when I visited MIT 6 1/2 years ago, and he greatly influenced my decision to come to MIT to work in the CCD Lab (then the Balloon Lab). I have never regretted that decision. The Center for Space Research (CSR) CCD Lab has been a great place to work: partly because of the facilities, but mostly because of the people. I thank Mark Bautz and Pat Mock for relieving me of my responsibilities for the laboratory x-ray CCD system so that I could spend my time working on optical instrumentation and the scientific program for this thesis. Mark has also been an endless source of scientific advice and information about clusters of galaxies, and I appreciate the time he spent answering many of my questions. Pat not only helped me finish some unfinished electronic designs, he designed and built the hardware to interface the laboratory CCD cameras to our SUN and MicroVAX computers. Pat also went observing for me when I was too busy. Lawrence Shing and Ed Boughan deserve the credit for debugging the electronic design for the Lincoln Laboratory CCD system and actually constructing the circuits and making them work while I was busy writing this thesis. I have also enjoyed working with (as well as sharing a house with) George Mitsuoka (thanks for all the *stargate*) and Steve Rosenthal. A few years ago, I got my feet wet working at MDM Observatory when George and I upgraded the MASCOT with new CCDs and electronics. George also wrote MIDAS to interface the MASCOT to one of our old generic computers. Recently, Steve wrote the CCD_tool program and ultimately interfaced the MASCOT and (later) the BRICC to the MDM Observatory SUN computers. I must also thank Mike Decker, who helped me sift through many TI-4849 CCDs while I was searching for the one to use in the BRICC, and Suzan DeFreitas who helped with much of the galaxy cluster data reduction and with the

construction of some of the instrument hardware. I thank Rosemary Hanlon for her help with some of the figures (and for dealing with Graphic Arts), and for her useful tips concerning WORD and the Macintosh. And thanks, Shep, for always making me laugh.

CSR machinists David Breslau and Leo Rogers were responsible for actually bringing the instrument design to life. During the course of construction, their excellent suggestions often improved the instrument design and their craftsmanship and attention to detail is evident in the final product. In addition, I am especially grateful to our CSR purchaser, Dan Calileo, who was always able to obtain the parts and services I required.

I would like to thank Barry Burke and his co-workers in Group 87 at MIT Lincoln Laboratory for their marvelous CCDs. I have enjoyed working with Barry and I am grateful for the education he has given me concerning some of the details of CCD design and manufacture. Barry was also kind enough to provide the photographs of the Lincoln Laboratory CCDs shown in Chapter 4. I am grateful to Stephanie Gajar for years of friendship and companionship. In addition, as part of the Lincoln Laboratory Group, she has been a source of useful information about these CCDs and she has served as a "CCD courier" between our group and Lincoln Laboratory. I would also like to thank the (former and present-day) CCD designers at Texas Instruments responsible for the TI-4849 and the TI 850 × 750 CCDs: Mark Wadsworth, Dan McGrath, Harold Hossack, and Jack Freeman.

The astronomers from University of Michigan, Dartmouth College, and MIT are fortunate to have an observatory (the MDM Observatory) staffed by outstanding people: Matt Johns (now at NOAO), Bob Barr and Larry Breuer. Special thanks to Matt for his excellent auxiliary instrumentation (the MIS instrument adaptor and intensified TV finder and guider) which were necessary for the proper operation of my CCD camera. Matt and Bob helped me debug the electronics at the telescope, and Bob is now responsible for the day-to-day maintenance of the instrument. He also fixes it when it breaks, and has mechanically adapted the CCD camera to the Observatory spectrographs. And thanks to Larry and Bob for cleaning the telescope mirrors before some of my observing runs. I'd like to thank the other astronomers with whom I've spent many productive (as well as cloudy) nights at the telescope: John Vallerga, Roland Vanderspek, George Ricker, Ian McHardy, Brin Cooke, Ed Ajhar, Pat Mock, Claude Canizares, Peter Vedder, John Tonry, and Mark Bautz. I must confess I've learned to love optical observing.

I would like to acknowledge the excellent astronomical education I received (both in and out of the classroom) as an undergraduate at Penn State. My good friend Jim McCarthy showed me how easy (and fun) it was to build a telescope and play in a machine shop. Larry Ramsey gave me my first opportunity to work with real optical instrumentation, and Gordon Garmire introduced me to high-energy astrophysics and gave me my first CCD to play with.

Finally, special thanks to Kristine for her love, support, patience, and good cheer. Well, it's finally finished. Here's what I've been doing for the last two years.

Table of Contents

List of Figures

List of Tables

To my Family:

Mary, Anthony, and Mark Luppino

Chapter 1

Introduction

Rich clusters of galaxies provide astronomers with some of the most powerful tools for measuring the global features of our universe. Numerous cosmological tests (such as the magnitude-redshift test, angular-size-redshift test, and Sunyaev-Zel'dovich effect) can be applied to distant clusters to try to ascertain the correct universe world model. Unfortunately, the luminosity and dynamical evolution of the galaxies in these clusters presents observational cosmologists with a formidable problem: cosmology and evolution appear to be inextricably tied together, and evolution must be understood before useful cosmological information can be extracted from measurements of distant clusters. Study of these problems requires a large sample of rich clusters of galaxies at moderate to high redshifts (z>0.2) where cosmological effects start to become important, and where cluster galaxy populations can be observed at different look-back times.

Until recently, only a handful of distant clusters have been studied in great detail, since normal galaxies at high redshift are extremely faint, and distant clusters of galaxies are not easy to find. The best known and well-studied sample of clusters is the *Catalog of Rich Clusters of Galaxies* by Abell (1958), which includes 2712 clusters, of which only 8 are at redshifts greater than z=0.3 (from the ~600 with known redshifts). Many of the currently known distant clusters were serendipitous discoveries found by searching deep optical photographic plates (Kron, Spinrad and King 1977; Koo 1981), or by searching the fields of bright radio galaxies and QSOs (Spinrad and Djorgovski 1986). One would ideally prefer a distant cluster population which was systematically selected and not associated with some exotic object. Such a sample has been optically selected by Gunn, Hoessel, and Oke (1986), and contains 418 distant clusters, with redshifts ranging from 0.15<z<0.92 (for the number that have measured redshifts).

McHardy and Cooke (1989) have suggested that one might also find distant, rich clusters of galaxies in fields containing low-frequency (38–178 MHz), steep-spectrum[1] radio sources, since there is a well established correlation between such sources and nearby rich clusters (Slingo 1974; Roland *et al.* 1976; Burns 1989). This method should not be particularly sensitive to selection effects since the physical mechanism producing the steep-spectrum radio emission is not associated with some exotic object, but originates from the confinement of the radio source by the thermal pressure of hot intracluster gas (Slingo 1974; Guthrie 1977). The clusters in this sample are also likely to be bright x-ray sources, and excellent targets for the *ROSAT*, *ASTRO-D*, and

---

[1] The non-thermal radio spectra of extragalactic radio sources is well-characterized by a "power law," where the flux density per unit frequency interval is proportional to the frequency to some power *i.e.* $S_\nu \propto \nu^{-\alpha}$. Steep-spectrum radio sources have α>1.5, whereas "normal" radio sources have α~0.8.

AXAF, since the same intracluster gas responsible for confining the radio source is expected to be a copious emitter of thermal bremmstrahlung.

A large number of suitable steep-spectrum radio sources (SSRS) from the 4C and Culgoora catalogs were mapped by McHardy using the *VLA* to provide precise source positions for deep optical imaging (McHardy and Cooke 1989). In order to confirm the presence of a cluster at the radio position, and to study the properties of such clusters, deep optical images of the *VLA* fields were required. The imaging detector used for these observations must have enough resolution to allow optimal spatial sampling of the stellar seeing disk; only then will it be possible to reliably classify faint objects as stars or galaxies. The detector must also have a relatively large field of view since even very distant clusters often have large angular sizes[1].

The high quantum-efficiency, linearity, and large dynamic range of charge-coupled devices (CCDs) make them the detector of choice for observing faint objects such as high redshift cluster galaxies. Currently available (single) CCDs, however, do not meet both of the requirements mentioned above. If the pixel size is optimally matched to the seeing, the field of view is too small. If too large a field of view is mapped onto a single CCD, it becomes impossible to adequately separate stars from faint galaxies. This thesis describes the design and construction of a sensitive, large-format, CCD imaging instrument which incorporates *mosaics* of CCDs. With this instrument, it is possible to observe faint, distant clusters of galaxies with spatial resolution limited by the atmospheric seeing, while at the same time covering a relatively large field of view.

The major task in the creation of this instrument was the design and construction of two separate CCD camera systems, each based on different CCD mosaics. The first of these camera systems incorporates four TI 850 × 750 virtual-phase CCDs (22.3 μm square pixels) arranged such that the device *packages* are abutted. These CCDs suffer from low-level charge transfer problems and have readout noise levels of 18-20 electrons rms. The second camera system is designed to operate a high-performance 840 × 840 CCD mosaic designed and built at MIT Lincoln Laboratory[2]. This hybrid imager is formed by abutting four 840 × 420 framestore CCDs (27 μm square pixels) with seam losses less than 6 pixels. These CCDs are three-phase devices with excellent charge-transfer properties and a readout noise levels of 2 electrons rms. The camera system has been designed to operate both the thick, frontside-illuminated and the thinned, backside-illuminated versions of these sensors.

---

[1] The characteristic size of a cluster of galaxies is the Abell radius, R_A, which equals 3 megaparsecs (Mpc). At z=0.5, this radius subtends an angle θ_A, of 422 arcseconds, and at z=1.25, θ_A=350 arcseconds. In fact, for a Friedmann cosmology with q_0>0, the angle subtended by fixed metric length goes through a minimum at z=1.25 (see Chapter 2, §2.3b), thus the Abell radius for distant clusters will always have an angular size θ_A>6 arcminutes. The above calculation assumes a standard Friedmann cosmology with values of H_0 = 50 km s^{-1} Mpc^{-1} and q_0=1/2 for the Hubble constant and the deceleration parameter, respectively.

[2] Note that this second system is still under construction and was not used to acquire data for this thesis.

We observed the distant galaxy cluster fields with this CCD instrument mounted on the 1.3m and 2.4m telescopes of the Michigan-Dartmouth-MIT (MDM) Observatory on Kitt Peak. The bulk of the observations for this dissertation were carried out while the instrument was still under construction.

In the following chapters, we describe the design of the large-format CCD instrument, and discuss the results of observations carried out with this instrument. We will start by reviewing, in detail, the properties of clusters of galaxies, and we will describe some cosmological tests that can be applied to high-redshift clusters, and briefly discuss the problem of cluster galaxy evolution. In Chapter 3 , we will discuss methods for finding high redshift clusters, and explain why a low-frequency, steep-spectrum radio sources is often a good indicator of the presence of a rich cluster of galaxies. In Chapter 4, we describe the CCD instrument design including the specifics of the mechanical design of the camera heads and dewars, and the details of the electronic controllers. The selection and characterization of the CCDs, and the photometric calibration of the instrument is presented in Chapter 5.

The observations of the distant galaxy cluster fields are summarized in Chapter 6. In addition, we also describe the new distant clusters and their optical and radio properties. In Chapter 7, we present the results of detailed *BVRI* photometry of Cl 1358+6245, the most spectacular cluster of galaxies in this investigation. This cluster is not part of the steep-spectrum radio sample, but was discovered with the *Einstein* observatory. Finally, in Chapter 8 we outline future plans for cluster observations, instrument modifications, and CCD improvements.

REFERENCES:

Abell, G.O. 1958, "The Distribution of Rich Clusters of Galaxies," *Ap.J. Supp.*, **3**, 211.

Abell, G.O., Corwin, H.G., and Olowin, R.P. 1989, "A Catalog of Rich Clusters of Galaxies," *Ap.J.Supp.*, **70**, 1. ACO

Baldwin, J.E., and Scott, P.F. 1973, "Extragalactic Radio Sources with Steep, Low Frequency Spectra," *M.N.R.A.S.*, **165**, 259.

Burns, J. 1989, "The Radio Properties of cD galaxies in Abell Clusters I. An X-ray Selected Sample," *Preprint*

Gunn, J.E., Hoessel, J.G., and Oke, J.B. 1986, "A Systematic Survey for Distant Galaxy Clusters," *Ap.J.*, **306**, 37.

Guthrie, B.N.G. 1976, "A Search for Steep Low-Frequency Radio Spectra Among Quasars and Clusters of Galaxies," *Astrophys. and Space Science*, **46**, 429.

Kron, R., Spinrad, H., and King, I. 1977, "Observations of a distant cluster of galaxies," *Ap.J.*, **217**, 951.

McHardy, I. and Cooke, B. 1989, in preparation.

Roland, J., Veron, P., Pauliny-Toth, I., Preuss, E., and Witzel, A. 1976, "Radio Sources and Clusters of Galaxies," *Astron.Ap.*, **50**, 165.

Slingo, A. 1974, "Observations of Ten Extragalactic Radio Sources with Very Steep Spectra," *M.N.R.A.S.*, **166**, 101.

Slingo, A. 1974, "The Structure and Origin of Radio Sources with Very Steep Spectra," *M.N.R.A.S.*, **168**, 307.

Spinrad, H. 1986, "Faint Galaxies and Cosmology," *P.A.S.P.*, **98**, 269.

Spinrad, H., and Djorgovski, S. 1987, "The Status of the Hubble Diagram in 1986," in *IAU Symposium 124, Observational Cosmology*, ed. Hewitt, Burbidge, and Fang (Dordrecht: Reidel), p. 129.

Chapter 2

Clusters of Galaxies

Clusters of galaxies are among the largest known objects in the universe. They often occupy a region of space in excess of three megaparsecs in diameter and contain hundreds to thousands of visible galaxies. Other than quasars, bright active galaxies, and the cosmic microwave background, large clusters are among the few objects that can be seen at great distances (at redshifts greater than one); they therefore provide observational astronomers with tools for studying the large scale distribution of matter and the properties of galaxies at earlier epochs. A study of the properties of clusters of galaxies may help answer questions concerning the origin and evolution of the universe. Clusters of galaxies are also very interesting objects in their own right: they are dynamical laboratories where one observes evidence for dark matter, they are known to act as gravitational lenses (Soucail *et al.* 1988; Lynds and Petrosian 1989), and they may trace out the density fluctuations in the early universe that led to their collapse.

Rich clusters of galaxies were first discovered as pronounced enhancements of the surface number density of galaxies on optical photographic plates. Although clusters are also often bright x-ray sources (thermal bremsstrahlung from hot, low density intracluster gas) and radio sources (nonthermal synchrotron emission from discrete sources associated with a member galaxy of the cluster), a cluster of galaxies is still classified and defined primarily by its optical properties. This chapter will review these optical properties of clusters of galaxies, as well as briefly discuss their x-ray and radio characteristics, and explain how distant clusters can be used to measure the global features of the universe.

Section 2.1 describes the classification of clusters of galaxies, and briefly reviews their optical, x-ray and radio properties. Particular attention is given to some of the characteristics that will actually be measured for a number of clusters in this thesis. Since high-redshift, rich clusters are used as probes to measure various properties of the universe world model, the relevant equations of the standard Friedmann cosmological model used throughout this thesis are presented in Section 2.2. Although various forms of these equations can be found in most textbooks (Weinberg 1972; Peebles 1971), they are presented here, using a standard system of notation, for completeness, and with emphasis on the observables. Section 2.3 describes, in detail, some cosmological tests that rely on measurements of properties of rich clusters of galaxies, and Section 2.4 briefly addresses the subject of galaxy evolution in distant clusters, and the current problems evolution presents for cosmological interpretation.

2.1 Properties of Clusters of Galaxies

a) Catalogs

Most of what is known about clusters of galaxies has been derived from the study of the relatively nearby objects included in the two largest and best known catalogs: the catalog of Rich Clusters of Galaxies by Abell (1958) which contains 2712 very rich members, and the far more extensive *Catalogue of Galaxies and of Clusters of Galaxies* by Zwicky *et al.* (1961-1968). These researchers have developed methods to measure and classify clusters based on their sizes, shapes, galactic content, distance, surface number density profile (contrast), and luminosity function: properties that often provide one with clues about the physical environment of the cluster.

Since galaxy clustering ranges from small, irregular groups of a few galaxies, to large, dense aggregates containing thousands of members, it is difficult to define unambiguously what is meant by a cluster (and particularly a rich cluster) of galaxies. The inclusion of a cluster in a catalog is dependent on the selection criteria used to define the catalog. Abell specifically searched for rich clusters: to be included in the catalog, a cluster had to have: 1) at least 30 galaxies in the magnitude range defined by m_3 and m_3+2 where m_3 is the magnitude of the third brightest cluster galaxy; 2) these 30 galaxies (or more) had to be contained within a $3.0h_{50}^{-1}$ Mpc radius[1] circle; and, 3) the estimated redshift of the cluster (based on the magnitude of the tenth brightest galaxy, m_{10}, had to be between $0.02<z<0.20$. Abell only selected clusters from declinations north of $\delta=-27^{o}$ and in regions not known to be obscured by our galaxy. Zwicky's criteria were less restrictive and that catalog therefore contains many more entries: a total of 9134 clusters. For a cluster to be included in Zwicky's catalog, it had to have: 1) at least 50 galaxies within the magnitude range defined by m_1 and m_1+3; and, 2) these 50 galaxies had to be contained within the contour where the galaxy surface number density fell to twice the background density. No distance limits were placed on Zwicky's clusters. The clusters in both of these catalogs were discovered on photographic plates from the 1.2m Schmidt telescope of the Palomar Observatory. The plates were taken while compiling the original Palomar Observatory Sky Survey (POSS).

The southern hemisphere extension of the *Catalog of Rich Clusters of Galaxies* has recently been completed by Abell, Corwin and Olowin (1989; ACO), using the UK 1.2m Schmidt telescope with IIIaJ plates. Galaxy clusters were selected using essentially the same criteria as Abell (1958). The ACO catalog contains 1635 clusters at declinations less than $\delta=-17^{o}$, and includes clusters in the $\delta=-17^{o}$ and $\delta=-27^{o}$ overlap region with Abell clusters. The all-sky catalog of rich clusters of galaxies now contains 4073 members. ACO have also revised the northern catalog; they have updated the coordinates to E1950.0 and E2000.0, and they have included Bautz-Morgan types (see below) and redshifts where known.

---

[1] The parameterization of the Hubble constant, $h_{50} \equiv H_0 / 50$ km s^{-1} Mpc^{-1} is used throughout this thesis.

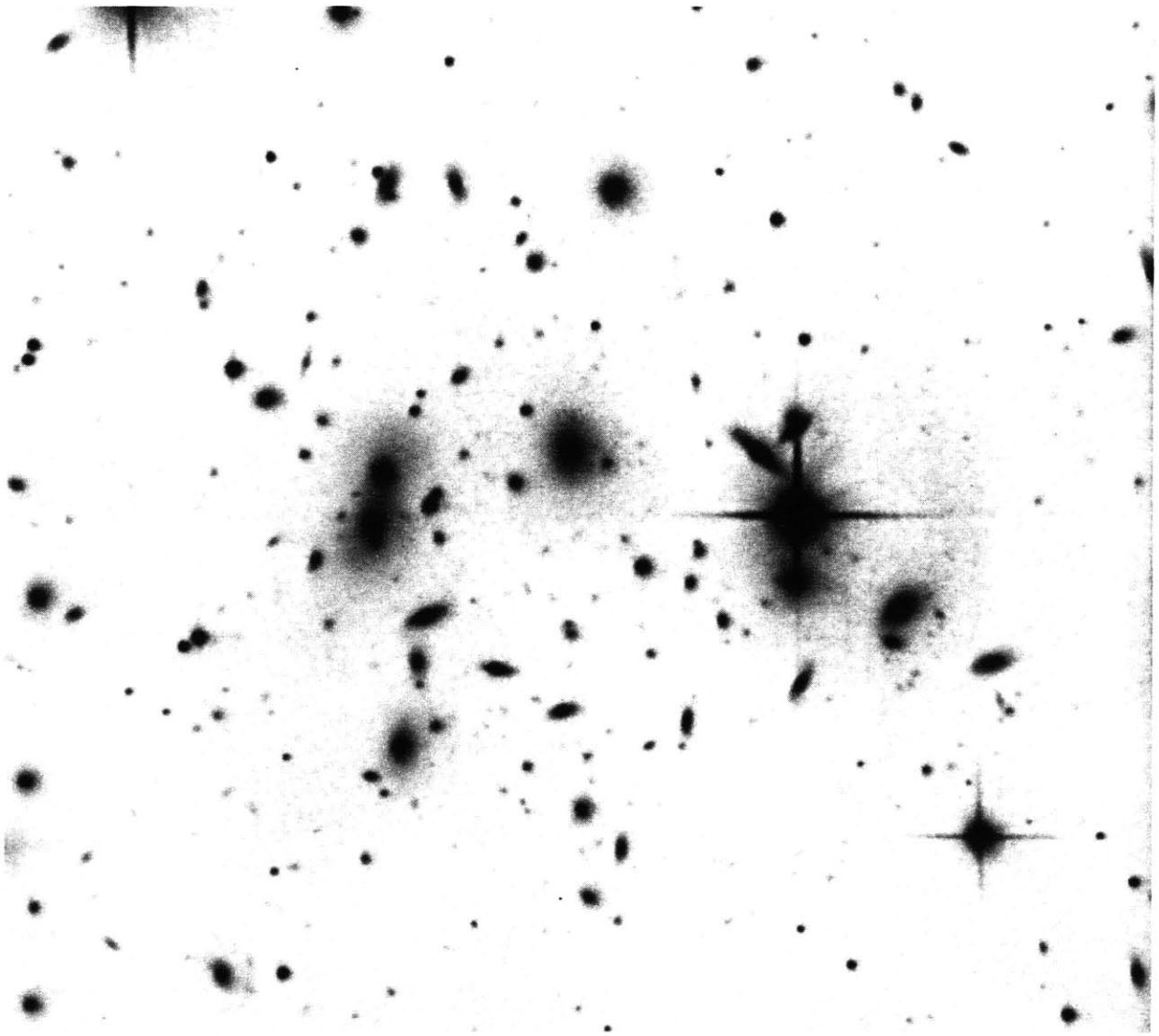

FIGURE 2.1 A CCD image of the core of the Corona Borealis cluster of galaxies (Abell 2065) illustrating some of the morphological characteristics of galaxy clusters discussed in this chapter. This regular cluster is at a distance of ~ 430 Mpc (z = 0.072) and is Bautz-Morgan type II. Only the central 700 kpc of the cluster is shown on the CCD frame. Abell counted 109 galaxies in the magnitude range defined by m3 and m3 + 2 within one Abell radius (~ 3Mpc), placing this cluster in richness class 2. This image is a 600 second exposure in R-band obtained on a 1.3m telescope with a single TI 850 × 750 CCD in the instrument described later in this thesis. The plate scale is 0.47 arcseconds/pixel (North is up and East is to the left).

Abell (and ACO) attempted to exclude clusters at distances greater than z=0.2 (since these faint clusters would be very sensitive to selection effects and would be difficult to identify in any case from photographic plates). Nevertheless, the Abell catalog does contain a number of clusters at redshifts greater than this limit (see §3.1). A catalog of very distant clusters of galaxies has been published by Gunn, Hoessel and Oke (1986; GHO). During the course of the preparation of this distant cluster catalog, GHO used hypersensitized photographic plates, image intensifiers coupled to photographic plates, and ultimately, CCDs to detect 418 faint clusters at redshifts out to at least z=0.92. There is only slight overlap with Abell and Zwicky clusters. More will be said about these distant clusters in the following chapter.

b) Morphological Classification

The Bautz-Morgan (1970) classification system for clusters of galaxies is based on the apparent contrast of the brightest cluster galaxy relative to the fainter cluster members. BM Type I clusters are dominated by a single, luminous, central galaxy which is often a cD galaxy[1]. BM Type II cluster have more than one giant elliptical of comparable brightness, and BM Type III clusters have no dominant galaxy. BM Types I-II and II-III are intermediates between the above cases. The Bautz-Morgan type of a cluster can be determined quantitatively using the method of Dressler (1978). The magnitudes of the first, second and third brightest cluster galaxies are used to form the quantity $\Delta \equiv (m_2 - m_1) + (m_3 - m_1)$. The cluster is then classified according to the value of Δ: BM type I clusters have $\Delta > 2.25$ mag; BM type II clusters have $2.25 > \Delta > 1.03$ mag; and, BM Type III clusters have $\Delta < 1.03$ mag. See Dressler (1978) for details.

An alternative, popular morphological classification scheme is the revised Rood-Sastry (RS) system (Struble and Rood 1982) based on the arrangement of the ten brightest cluster galaxies. There are six RS classifications arranged in a forked sequence: RS type cD - cluster has a supergiant, dominant galaxy with extended enveleope (very similar to BM type I); RS type B - cluster has two close, supergiant galaxies; RS type C - core-halo arrangement of the ten brightest, centrally located galaxies; RS type L - elongated, line arrangement of brightest galaxies; RS type I - irregular, or clumpy distribution with no well-defined center; and RS type F - flattened configuration often with numerous subclumps.

Various authors have correlated cluster features (*e.g.* x-ray luminosity, richness, and average separation of central galaxies - to name just a few) with both the BM and RS types. The BM system still appears to be the most popular and widespread, especially since clusters in the BM system are ordered in a monotonic, rather than a forked, sequence.

---

[1] cD galaxies, as defined by Mathews, Morgan and Schmidt (1964), are very luminous giant elliptical galaxies embedded in a gigantic, low-surface brightness halo that may extend as far as 1 Mpc from the galaxy center. Other than galaxies with active nuclei (*e.g.* QSOs and Seyferts), cD galaxies are the most luminous galaxies known. They are found at the centers of compact clusters, and they often have double or multiple nuclei. It is believed that cD galaxies may be produced by mergers of galaxies within the cores of rich clusters.

c) Richness and Galaxy Content

The richness of a cluster is a measure of the number of galaxies within a cluster. In his catalog, Abell (1958) classified cluster richness based on the number of galaxies, N_A, counted within one Abell radius, R_A, in the magnitude range defined by m_3 and m_3+2 where, again, $m3$ is the magnitude of the third brightest cluster galaxy. There were 6 Abell richness classifications: richness class 0 — $30 \leq N_A \leq 49$; richness class 1 — $50 \leq N_A \leq 79$; richness class 2 — $80 \leq N_A \leq 129$; richness class 3 — $130 \leq N_A \leq 199$; richness class 4 — $200 \leq N_A \leq 299$; and richness class 5 — $N_A > 300$. The Abell richness is largely independent of distance, but richness estimates for the z>0.2 clusters are often wrong, since the clusters were just too faint for Abell to get accurate count information. For example, cluster A851 was listed as a Richness Class 1 object (albeit very distant) but subsequent spectroscopic observations by GHO show this object to be extremely rich at z=0.4 (although Gunn argues that Abell may have identified a foreground group in the field, and not the z=0.4 cluster; see Figure 3.1). Another example is A370 which is listed as Richness Class 0; this cluster is actually Richness Class 3 (Kristian, Sandage and Westphal 1978; KSW), but it is quite distant at z=0.37.

Bahcall (1981) described an alternative method for determining the cluster richness, as well as the central galaxy density which is defined as the number of galaxies, $N_{0.5}$, in the magnitude range defined by m_3 and m_3+2 projected within a $0.5h_{50}^{-1}$ Mpc radius of the cluster center. It turns out that this number, corrected for background and cluster richness, is strongly correlated with the velocity dispersion in the cluster (Bahcall 1981). This correlation will be used in later chapters to estimate the velocity dispersion of clusters for which there is no spectroscopic data.

d) Optical Luminosity Function

The luminosity function for a cluster of galaxies describes the distribution of luminosities of the galaxies in the cluster. As stated by Schechter (1976), luminosity functions can be obtained for any subclass of objects which can be identified by criteria other than luminosity. Two different luminosity functions are often mentioned: the integrated luminosity function $N(L)$ which is just the number (or number density) of galaxies with luminosity greater than L, and the differential luminosity function $n(L)dL$ which is the number (or, again, the number density) of galaxies with luminosities in the range L to $L + dL$. Clearly, $n(L) = -dN(L)/dL$.

The following analytic expression for the differential luminosity function was proposed by Schechter (1976)

$$n(L)\,dL = N^* \,(L/L^*)^{\alpha} \exp(-L/L^*)\,d(L/L^*) \quad . \qquad (2.1.1)$$

It can be interpreted as a power law, $(L/L^*)^{\alpha}$, for the faint galaxies ($L<<L^*$), and an exponential which dominates for the bright galaxies ($L>L^*$). The region where $n(L)$ changes rapidly is called the break in the

luminosity function, and is characterized by the parameter L^*. Schechter (1976), and more recently, Lugger (1986) showed that the value of L^* is nearly the same for rich clusters of galaxies with an equivalent value, $M_V^* \simeq -21.5 + 5\log h_{50}$ and a power-law slope of $\alpha = -1.25$. Since M^* appears to be constant, it has been suggested that it could be used as a standard candle; by measuring m^*, one could directly measure the distance to a cluster (Schechter and Press 1976). This will be discussed further in §2.3.

e) x-ray emission

Clusters of galaxies have been known to be sources of x-rays since the late 1960's when x-ray emission was seen coming from M87 and the Virgo cluster. This cluster was the first extragalactic object seen in x-rays. In the next decade, the x-ray satellites *Uhuru, OSO-7, Ariel V, SAS-3, OSO-8* and *HEAO-A* confirmed that many nearby, rich clusters were bright x-ray sources with luminosities in the range of 10^{43} to 10^{45} ergs/s: . In fact, clusters of galaxies are among the most luminous x-ray sources in the universe. The emision mechanism for these spatially-extended sources was eventually determined to be thermal bremmstrahlung from hot (10^8 K), low density (10^{-3} cm^{-3}) gas which filled the volume between the galaxies and had a mass approximately equal to the mass of all the stars in the galaxies that make up the cluster. The thermal interpretation was supported by observations of x-ray line emission from iron, which also indicates the intracluster gas originated in stars and was somehow ejected from the galaxies in the cluster. A recent review of the physics and observations of x-ray emission from clusters of galaxies is given in by Sarazin (1986).

f) radio emission

Radio emission from clusters of galaxies is non-thermal synchrotron radiation due to the interaction of relativistic electrons with an intergalactic (or intragalactic) magnetic field. The source is usually associated with an individual galaxy, often one of the brightest optical galaxies, near the center of the cluster (McHardy 1979). A large fraction (~20%) of all extragalactic radio sources are in clusters of galaxies, but this may be simply explained by the fact that giant ellipticals, which occur preferentially in rich clusters rather than in the field, are the major class of strong radio galaxies (McHardy 1979). McHardy (1978) also found that strong radio sources were more likely to be found in x-ray luminous clusters. The intracluster gas that is known to be present from x-ray observations has an effect on the morphology and spectrum of the radio emission. Cluster radio sources have trail or distorted morphology indicating the interaction of a convential double-lobed radio source with the intracluster gas (Miley 1980). Radio sources in clusters also have steeper spectra: $\alpha > 1.2$ (where $S_\nu \propto \nu^{-\alpha}$) for sources in clusters, whereas $\alpha \sim 0.8$ for sources in the field. It is this property of clusters that serves as the selection criterion for the distant clusters in this thesis. The details of this selection method and the physical models for the radio emission are discussed fully in the next chapter.

2.2 Standard Friedmann Cosmology

a) preliminaries

The standard world model used throughout the following discussions assumes a globally homogeneous, isotropic universe correctly described by the equations of general relativity. In this universe, the most general possible line element is given by the Robertson-Walker metric (Sandage 1989 and references therein),

$$ds^2 = c^2\,dt^2 - R^2(t)\left[\frac{dr^2}{\sqrt{1-kr^2}} + r^2\,d\theta^2 + r^2\sin^2\theta\,d\varphi^2\right] \qquad (2.2.1)$$

where the coordinates are comoving, $R(t)$ is the universe scale factor ($R(t) = 0$ at $t = 0$), and k is a constant (+1, 0, or -1) that determines the spatial curvature of the universe. When the above metric is inserted into the Einstein field equations, along with the assumptions mentioned above, one obtains the two fundamental differential equations of cosmology (Weinberg 1972; Sandage 1961)

$$\frac{\dot{R}^2}{R^2} + \frac{2\ddot{R}}{R} + \frac{8\pi G}{c^2}p = \frac{-kc^2}{R^2} + \Lambda c^2$$

$$\frac{\dot{R}^2}{R^2} - \frac{8\pi G}{3}\rho = \frac{-kc^2}{R^2} + \frac{\Lambda c^2}{3} \qquad (2.2.2)$$

that describe the time evolution of the geometry of the universe. In these equations, p is the pressure of matter and radiation, ρ is the density of matter and energy, and Λ is the cosmological constant originally introduced by Einstein in an attempt to obtain a static universe that would have been impossible otherwise. Models with zero pressure and $\Lambda=0$ are currently the most popular since they seem to describe the universe *now*. Only these models will be considered below. In this case, the Einstein equations reduce to

$$\dot{R}^2 + 2\ddot{R}R = -kc^2 \qquad (2.2.3)$$

$$\dot{R}^2 - \frac{8\pi G\rho}{3}R^2 = -kc^2 \qquad (2.2.4)$$

Solutions to these equations will be discussed later in part *d)* where the time evolution of R(t) is discussed.

Equations relating the expansion factor $R(t)$ to the redshift and other observables are presented below (note that all terms subscripted with 0 should be evaluated at the present epoch, *i.e.*, now). These observables are the Hubble constant, H_0, the deceleration parameter, q_0, or density parameter, Ω_0,

$$H_0 = \dot{R}_0(t)\, R_0^{-1}(t) = \dot{R}_0 R_0^{-1} \tag{2.2.5}$$

$$q_0 = -R_0\, \ddot{R}_0\, \dot{R}_0^{-2} \tag{2.2.6}$$

$$\Omega_0 = \frac{\rho_0}{\rho_c} = \frac{8\pi G \rho_0}{3H_0^2} = 2\, q_0 \tag{2.2.7}$$

Another important observable is the redshift, z, which is defined as $z \equiv \Delta\lambda/\lambda$, or

$$1 + z = \frac{\lambda_o}{\lambda_e} = \frac{\nu_e}{\nu_o} = \frac{R_0}{R(t)} \tag{2.2.8}$$

where the subscript o refers to the observed wavelength (or frequency), while the subscript e refers to the emitted wavelength (or frequency).

b) luminosity distance and angular size

Since all astronomical observations of distant objects rely on the detection of photons, it is necessary to consider the aspects of the propagation of light through the universe. The *proper distance* along a null geodesic ($ds = 0$) is obtained by integrating the Roberston-Walker metric (details of this integration are given in Weinberg 1972),

$$\int_0^r \frac{dr}{\sqrt{1 - k r^2}} = \int_e^o \frac{c\, dt}{R(t)} \tag{2.2.9}$$

yielding, for the comoving radial coordinate r, the expression (Mattig 1958)

$$r = \frac{c}{q_0^2 H_0 (1+z)} \left[q_0 z + (q_0 - 1)\left((1 + 2 q_0 z)^{1/2} - 1 \right) \right] . \tag{2.2.10}$$

The more useful term, however, is the *luminosity distance*, d_L, which is defined so that it forces the bolometric flux f (in units of ergs cm^{-2} s^{-1}) received from an object of bolometric luminosity L (in units of ergs s^{-1}) to obey the inverse square law of flat Euclidean spacetime, *i.e.*,

$$f = \frac{L}{4\pi\, d_L^2} . \tag{2.2.11}$$

The luminosity distance can be related to the proper distance, which is only a function of the observables H_0, q_0, and z, by considering the true relation between observed flux and emitted luminosity. For small distances, spacetime can be considered to be locally flat, therefore $f_o = L_e / 4\pi r^2$ for small redshifts. As the redshift increases, the time interval, dt_o, as measured in the observer's frame is larger than the time interval, dt_e, measured in the emitter's frame by a factor of (1+z). Also, each arriving photon is redshifted in frequency by a factor of (1+z). When these two factors of (1+z) are included, the correct expression for the observed bolometric flux becomes

$$f_o = \frac{L_e}{4\pi r^2 (1+z)^2} \quad . \tag{2.2.12}$$

It is obvious from this equation that the luminosity distance, as defined by equation 2.2.11, can be written as (Weinberg 1972)

$$d_L = r(1+z) = \frac{c}{q_0^2 H_0}\left[q_0 z + (q_0 - 1)\left((1 + 2q_0 z)^{1/2} - 1 \right) \right] \tag{2.2.13}$$

The above equation, which is exact for all z and q_0, reduces to

$$d_L \approx \frac{c}{H_0}\left[z + \frac{1}{2}(1 - q_0) z^2 \right] \tag{2.2.14}$$

for small z. Note that this equation is exact for the two cases q_0=0 and 1 (Weinberg 1972).

Further cosmological effects must be considered when observing distant extended objects, such as galaxies at high redshift. Here, surface brightness becomes the limiting factor in the detection and study of these objects (Weedman and Williams 1987). Consider a galaxy of proper metric (comoving) diameter D. The observed angular diameter is then

$$\theta(q_0, z) = \frac{(1+z)D}{r} = \frac{H_0}{c}\left(\frac{D}{1\ Mpc} \right) \frac{q_0^2 (1+z)^2}{q_0 z + (q_0 - 1)\left((1 + 2q_0 z)^{1/2} - 1 \right)} \tag{2.2.15}$$

where D is in units of Mpc if H_0 is in units of km s^{-1} Mpc^{-1}. It is obvious from this equation that θ can also be written as $\theta=(1+z)^2 D/d_L$. Therefore, one can also define an *angular distance* , d_A, such that (Weinberg 1972)

$$d_A = \frac{D}{\theta} = \frac{d_L}{(1+z)^2} \quad . \tag{2.2.16}$$

Observed surface brightness, Σ, which is defined as observed flux per (observed) solid angle, can now be written as

$$\Sigma = \frac{f}{\theta^2} = \frac{L}{4\pi D^2 (1+z)^4} \cdot \quad \text{ergs cm}^{-2}\,\text{s}^{-1}\,\text{str}^{-1} \qquad (2.2.17)$$

where D is in units of Mpc as in equation 2.2.14. Notice that the surface brightness decreases as $(1+z)^4$, which places severe limits on the detectability of normal galaxies with redshifts greater than unity (assuming distant galaxies are similar to nearby galaxies). This will be discussed in greater detail below and in the following chapter.

The expressions relating observed flux and emitted luminosity presented so far are only applicable to bolometric quantities (energy at all frequencies or wavelengths). In practice, observations are made in a finite bandpass, and the appropriate equations for monochromatic flux and luminosity must be used. In this presentation, I will use notation similar to Gunn and Oke (1975) or Schneider, Gunn and Hoessel (1983 [SGH]), where any ν or λ subscript refers to an observed quantity, while an emitted quantity, which arises at a different frequency or wavelength in the emitters frame, has a subscript written in terms of the observed ν or λ (using equation 2.5). The monochromatic energy flux is given by

$$f_\nu = \frac{L_{\nu(1+z)}(1+z)}{4\pi d_L^2} \qquad \text{ergs cm}^{-2}\,\text{s}^{-1}\,\text{Hz}^{-1} \qquad (2.2.18)$$

and

$$f_\lambda = \frac{L_{\lambda/(1+z)}}{4\pi d_L^2 (1+z)} \qquad \text{ergs cm}^{-2}\,\text{s}^{-1}\,\text{Å}^{-1}\,. \qquad (2.2.19)$$

The monochromatic surface brightness then becomes

$$\Sigma_\lambda = \frac{L_{\lambda/(1+z)}}{4\pi D^2 (1+z)^5} \text{ ergs cm}^{-2}\,\text{s}^{-1}\,\text{Å}^{-1}\,\text{str}^{-1}\,. \qquad (2.2.20)$$

and the cosmological surface brightness dimming becomes even more severe.

c) magnitudes

The apparent magnitude in filter i, of an object detected by a system with sensitivity $S_i(\nu)$ is defined as

$$m_i = -2.5 \log \int_0^\infty f_\nu S_i(\nu)\, d\nu + C \tag{2.2.21}$$

and the absolute magnitude at the position of the galaxy (well, 10 pc away) is given by

$$M_i = -2.5 \log \int_0^\infty \frac{L_\nu S_i(\nu)}{4\pi\, d_0^{\,2}}\, d\nu + C \qquad d_0 = 10 \text{ parsecs.} \tag{2.2.22}$$

Using equation 2.2.18 to replace the flux in equation 2.2.21 with the luminosity, one obtains the following expression for the apparent magnitude

$$m_i = -2.5 \log \int_0^\infty \frac{L_{\nu(1+z)}(1+z)}{4\pi\, d_L^{\,2}} S_i(\nu)\, d\nu + C \tag{2.2.23}$$

Therefore, one can write,

$$m_i - M_i = -2.5 \log \int_0^\infty \frac{L_{\nu(1+z)}(1+z)}{4\pi\, d_L^{\,2}} S_i(\nu)\, d\nu + C + 2.5 \log \int_0^\infty \frac{L_\nu S_i(\nu)}{4\pi\, d_0^{\,2}}\, d\nu - C$$

$$= 2.5 \log \frac{4\pi\, d_L^{\,2}}{4\pi\, d_0^{\,2}} + 2.5 \log \frac{\int_0^\infty L_\nu S_i(\nu)\, d\nu}{(1+z)\int_0^\infty L_{\nu(1+z)} S_i(\nu)\, d\nu} \tag{2.2.24}$$

$$m_i - M_i = 5 \log d_L + 25 - 2.5 \log(1+z) + 2.5 \log \frac{\int_0^\infty L_\nu S_i(\nu)\, d\nu}{\int_0^\infty L_{\nu(1+z)} S_i(\nu)\, d\nu}$$

$$= 5 \log d_L + 25 + K_\nu(z) \tag{2.2.25}$$

where d_L is given in Mpc, and $K_\nu(z)$ is the K-correction as defined in Oke and Sandage (1968) that accounts for the redshifting of the continuous energy distribution, L_ν, through the fixed spectral response, $S_i(\nu)$ of the detector. The K-correction, as written above, is composed of two parts: the 2.5 log(1+z) term that accounts for

the change in bandwidth, and the wavelength dependent portion that is important if $L[\nu]$ is not equal to $L[\nu(1+z)]$. For the case where the flux per unit wavelength, rather than unit frequency, is specified , the difference between apparent and absolute magnitude is given by

$$m_i - M_i = 5\log d_L + 25 + 2.5\log(1+z) + 2.5\log \frac{\int_0^\infty L_\lambda S_i(\lambda)\, d\lambda}{\int_0^\infty L_{\lambda(1+z)} S_i(\lambda)\, d\lambda} \qquad (2.2.26)$$

$$= 5\log d_L + 25 + K_\lambda(z)$$

Instruments today, however, typically employ photon counting detectors, not energy sensitive devices (this includes CCDs where each absorbed optical photon creates one electron-hole pair). Therefore, the following two equations relate the observed monochromatic photon flux, n_ν or n_λ, to the emitted photon luminosity $N_{\nu(1+z)}$ or $N_{\lambda/(1+z)}$. Equation 2.2.19 can be obtained by dividing both sides of equation 2.2.10 by hν and converting $L_{\nu(1+z)}/h\nu$ to $N_{\nu(1+z)}$ by dividing by a factor of (1+z) [note, $N_{\nu(1+z)} \equiv L_{\nu(1+z)}/h\nu(1+z)$]. Equation 2.2.20 is obtained in a similar fashion.

$$n_\nu = \frac{N_{\nu(1+z)}\,(1+z)^2}{4\pi\, d_L^2} \quad \text{photons cm}^{-2}\,\text{s}^{-1}\,\text{Hz}^{-1} \qquad (2.2.27)$$

$$n_\lambda = \frac{N_{\lambda/(1+z)}}{4\pi\, d_L^2} \quad \text{photons cm}^{-2}\,\text{s}^{-1}\,\text{Å}^{-1} \qquad (2.2.28)$$

Again, these expressions use the same notation as in SGH. Equations relating the apparent and absolute magnitude can therefore be written

$$m_i - M_i = 5\log d_L + 25 - 2.5\log(1+z)^2 + 2.5\log \frac{\int_0^\infty N_\nu S_i(\nu)\, d\nu}{\int_0^\infty N_{\nu(1+z)} S_i(\nu)\, d\nu} \qquad (2.2.29)$$

$$m_i - M_i = 5\log d_L + 25 + 2.5\log \frac{\int_0^\infty N_\lambda S_i(\lambda)\, d\lambda}{\int_0^\infty N_{\lambda/(1+z)} S_i(\lambda)\, d\lambda} \qquad (2.2.30)$$

In this case, the *K*-correction is defined in terms of the photon luminosity, the implications of which are discussed by SGH.

d) look-back time

When we observe distant objects, we are also looking at them as they existed at an earlier time in the universe. In order to understand the relationship between the redshift and time, we return to the differential equations 2.2.3 and 2.2.4 that describe the time evolution of the universe scale factor $R(t)$. These equations can be combined (for the simple case where $q_0=1/2$, *i.e.* the spatial curvature $k=0$ - this is usually called an Einstein-deSitter universe), and integrated

$$\int_0^R \sqrt{R}\; dR = \int_0^t \sqrt{\tfrac{8}{3}\pi G\, \rho_0}\; dt \tag{2.2.31}$$

to yield the following expression for $R(t)$

$$R = [6\pi G\, \rho_0]^{1/3}\; t^{2/3} \tag{2.2.32}$$

Knowing R and dR/dt, and $H_0 \equiv R_0^{-1} dR_0/dt$, one can express the age of the universe in terms of the Hubble time ($1/H_0$)

$$t = \frac{2}{3}\,\frac{1}{H_0} \tag{2.2.33}$$

In a $q_0=1/2$, $\Lambda=0$ universe, the Hubble time is $20h_{50}^{-1}$ Gyr, so the present age of the universe is $13.3h_{50}^{-1}$ Gyr.

The look-back time, τ, is defined as the difference between the age of the universe at the time of light reception (now) and the age of the universe at the time of light emission

$$\tau = t_o - t_e = t_o\left(1 - \frac{t_e}{t_o}\right) = \frac{2}{3H_0}\left[1 - \left(\frac{R(t_e)}{R(t_o)}\right)^{3/2}\right]$$

$$= \frac{2}{3H_0}\left[1 - \frac{1}{(1+z)^{3/2}}\right] \tag{2.2.34}$$

This illustrates the fact that when we look at galaxies at $z=1$, we are looking at light that left those galaxies over 8 billion years ago when the universe was less than half its present age.

2.3 Cosmological tests that rely on measurements of properties of rich clusters of galaxies

a) apparent magnitude - redshift (m,z) relation (Hubble diagram)

The apparent magnitude - redshift (m,z) test as applied to the brightest galaxies in clusters (BCG's) is one of the classic methods for measuring the geometry of the universe. The test has been refined over the past thirty years by a number of investigators (Humason, Mayall and Sandage 1956; Sandage 1972; Gunn and Oke 1975; Kristian, Sandage and Westphal 1978; Hoessel, Gunn and Thuan 1980; Schneider, Gunn and Hoessel 1983; Postman, Huchra, Geller, and Henry 1985; and Spinrad and Djorgovski 1987), using, for the most part, clusters of galaxies from the Abell catalog. The principle of the test is simple: the brightest cluster galaxy (or possibly the break in the luminosity function, M^*) is assumed to be a standard candle. The relation between apparent magnitude m_λ, the known absolute magnitude M_λ, and the luminosity distance $d_L(z,q_0)$ is given by

$$m_\lambda = M_\lambda + 5\log d_L + 25 + K_\lambda(z) + A_G(\lambda) + E_\lambda(z) \qquad (2.3.1)$$

where $K_\lambda(z)$ is the K-corrrection, $A_G(\lambda)$ is the correction for galactic absorption, and $E_\lambda(z)$ is the evolution term (see §2.4). The measured magnitude must also be corrected so that the photometry is done through a standard metric aperture (the aperture effect), the size of which is a function of q_0. However, the q_0 dependence of this correction is negligibly weak (Sandage 1989). Sandage (1976) and Kristian, Sandage and Westphal (1978) have shown that the absolute magnitude of brightest E and S0 galaxies in rich clusters exhibit a remarkably small dispersion of ±0.35 mag about a mean of $M_V(1) = -23.3 + 5\log h_{50}$ after small corrections for Bautz-Morgan type and richness. The Schechter (1976) luminosity function predicts a stronger correlation of brightest cluster galaxy absolute magnitude with cluster richness; however, Schechter and Peebles (1976) later argued that the apparent absence of such a correlation is caused by a combination of statistics and selection effects. It is still not clear whether the small dispersion in $M(1)$ is just a statistical sampling effect or is due to some special physical condition the affected the formation of the brightest cluster galaxies.

Armed with the brightest cluster galaxy standard candles (whatever their nature), and ignoring evolutionary considerations, which at the time were not known to be important, Gunn and Oke (1975; GO) and Kristian, Sandage and Westphal (1978; KSW) attempted to measure q_0 using the Hubble diagram at optical wavelengths. GO, using a fixed metric aperture of $27h_{50}^{-1}$ kpc (GO actually used a 32 kpc aperture assuming H_0=60 km s^{-1} Mpc^{-1} and q_0=1/2) found values for q_0 ranging from 0.33 to −1.27±0.7 depending on whether or not they included the high-redshift cluster 3C 295 at z=0.46. KSW, using clusters extending to z=0.4, found q_0=1.6±0.4. They made their photometric measurements through an 86 kpc diameter aperture (assuming H_0=55 km s^{-1} Mpc^{-1} and q_0=1). Hoessel, Gunn and Thuan (1980) anchored the bright end of the Hubble diagram by

measuring the brightest cluster galaxies in 116 nearby Abell clusters. This data, when combined with the high-redshift clusters of GO yield a formal value for q_0 of -0.55 ± 0.45. It is now believed that these inconclusive and somewhat contradictory results are caused, at least in part, by uncertainties in galaxy evolution (the $E\lambda(z)$ term discussed in §2.4).

Spinrad and Djorgovski (1987) have extended the Hubble diagram to z=1.8 using bright 3CR radio galaxies and "1 Jy" class radio sources. Concerns regarding the use of radio galaxies are countered by the observation that $m(z)$ does not seem to depend strongly on the radio power of the galaxy, *i.e.* bright 3CR galaxies and relatively faint "1 Jy" sources seem to have the same optical properties. They present strong evidence for evolution, concluding that the data for z>0.8 cannot be fit by <u>any</u> value of q_0 in the no-evolution [$E\lambda(z)$=0] case.

Shanks, Couch, McHardy, Cooke and Pence (1988) presented CCD observations of 5 clusters with redshifts ranging from z=0.37 to z=0.57. With this very small sample, they conclude the R magnitudes of the brightest cluster galaxies are consistently brighter than expected in q_0~0 universe. They find that Friedmann models with q_0=0.5 are consistent with the Hubble diagram of KSW including these 5 clusters if one assumes field galaxies and cluster galaxies have undergone the same evolution.

b) angular size - redshift (θ,z) relation

The principal behind the (θ,z) test is simple, and is similar to the (m,z) test: instead of using brightest cluster galaxies as standard candles, one uses some property (yet to be defined) of the cluster as a "standard yardstick" and measures the the variation of the angular diameter of this "yardstick" as a function of redshift to determine q_0 as given by equation 2.2.14.

For a universe with q_0>0, the angular diameter - redshift relation has a minimum at some finite redshift This can be seen by looking at the z-derivative of $\theta(q_0,z)$ for a q_0=1/2 universe. In this case, equation 2.2.14 reduces to

$$\theta(q_0=\tfrac{1}{2},z)=\frac{H_0}{2c}\left(\frac{D}{1\ Mpc}\right)\frac{(1+z)^{3/2}}{\sqrt{1+z}-1} \qquad (2.3.2)$$

and if $d\theta/dz$ is set equal to zero, one finds the well known result that $\theta(1/2,z)$ has a minimum at z=5/4. Observers have searched for this effect, but it has not, as yet, been observed. Sandage (1989) states that the lack of observational evidence for a minimum in the (θ,z) relation "raises the most serious doubt to date about the standard model," and "to save the phenomenon, we must again invoke evolution of the size of the standard rod in look-back-time."

Part of the problem arises from the exact definition of a standard metric rod. Hickson (1977), and Bruzual and Spinrad (1978) measured the harmonic mean angular separation of the brightest cluster galaxies within some fixed radius in the cluster (which, of course, depends on q_0). After measuring 95 clusters out to z=0.46, and correcting for the systematic effect of q_0 on cluster radius (an effect similar to the aperture effect of the (m,z) relation), and known evolutionary effects, Hickson (1977) measured a formal value of $q_0 = -0.8 \pm 0.4$. The Bruzual and Spinrad (1978) sample of 54 clusters included 44 of those from Hickson (1977) as well as nine more clusters up to z=0.95, and find that $q_0 = 0.25 \pm 0.5$.

This (θ,z) test was also applied to double-lobed radio sources by Miley (1971) and others who showed θ values dropped monotonically with z as $\theta \propto z^{-1}$ out to z~2 with a large dispersion caused by projection effects and a variety of sizes associated with the linear radio structures. In a recent review, Kapahi (1987) concludes 'the physics of the evolution of individual sources and the various factors responsible for the inferred evolution with epoch are, however far from being understood," and "there is little hope at this stage of using the relation as a test of the geometry of the universe." Sandage (1989) points out that even though the $\theta \propto z^{-1}$ dependence is seen at low redshifts for both the optical and radio data, actually extracting the deceleration parameter may be impossible since high redshift clusters are still in the process of formation, and he states "measurement of the second order curvature effect (*i.e.* q_0) using such an evolving metric rod must be questioned."

c) Sunyaev - Zel'dovich effect

Sunyaev and Zel'dovich (1972) recognized that the thermal spectrum of the 3K primordial background radiation could be perturbed at wavelengths in the Rayleigh-Jeans part of the spectrum along lines of sight passing through the optically thin, high temperature gas present in rich clusters of galaxies. Inverse Compton scattering of the 3K photons with the 10^8K electrons of the intracluster gas effectively heats the cosmological background radiation resulting in a shift of the thermal spectrum to shorter wavelengths, and a reduction of the intensity at millimeter wavelengths (a microwave decrement). Sarazin (1986) describes this effect as "shadows in the microwave background..." and he mentions that "it is somewhat paradoxical that heating the background radiation lowers its brightness temperature at low frequencies." In fact, this effect actually distorts the thermal spectrum of the background radiation which loses photons on the Rayleigh-Jeans side but gains them on the Wien side. Microwave observations of the Sunyaev-Zel'dovich effect can be combined with x-ray observations to directly determine the luminosity distance to both nearby and distant clusters of galaxies (Gunn 1978; Silk and White 1978). The essential features of this distance measuring technique are summarized as follows. In the Raleigh-Jeans limit, the change in brightness temperature, T_b, of the cosmic background radiation after passage through the hot, intracluster gas is given by

$$\frac{\Delta T_b}{T_b} = -\int \frac{2kT_e}{m_e c^2}\,\sigma_T\, n_e\, dl \qquad h\nu << kT \qquad (2.3.3)$$

where T_e is the electron temperature of the gas and σ_T is the Thompson cross-section (Sarazin 1986). Clearly, the microwave decrement, $\Delta T_b/T_b$ is just proportional to the electron number density, the electron temperature, and the characteristic size of the cluster scattering region, obtained by integrating the above equation along the line of sight, *dl*, through the cluster, *i.e.*

$$\frac{\Delta T_b}{T_b} \approx n_e T_e r_c \tag{2.3.4}$$

The x-ray emissivity produced by thermal bremsstrahlung from the hot intracluster gas can be written as

$$j(\nu) \propto Z^2 n_e n_i T_e^{-\frac{1}{2}} e^{-\frac{h\nu}{kT_e}} \tag{2.3.5}$$

where the ions responsible for accelerating the free electrons have atomic number Z and number density n_i. If one integrates equation 2.3.5 over the volume of the emitting region, and over the bandpass of the x-ray detector,

$$\begin{aligned} L_x &\propto \int_{vol} dV \int_{\nu} j(\nu)\, d\nu \\ &\propto \frac{4}{3}\pi r_c^3 n_e^2 T_e^{-\frac{1}{2}} \int_{\nu_1}^{\nu_2} e^{-\frac{h\nu}{kT_e}}\, d\nu \end{aligned} \tag{2.3.6}$$

assuming that the gas is primarily hydrogen so that $n_i = n_e$ and $Z = 1$, one obtains the following expression for the x-ray luminosity,

$$L_x \propto n_e^2 T_e^{-\frac{1}{2}} r_c^2 \tag{2.3.7}$$

The x-ray luminosity can also be re-written as

$$L_x \propto \left(\frac{\Delta T_b}{T_b}\right)^2 T_e^{-\frac{5}{2}} r_c \tag{2.3.8}$$

by combining equation 2.3.7 with equation 2.3.4, eliminating the electron density, n_e. The x-ray luminosity and the x-ray flux are related by $4\pi d_L^2 f_x = L_x$, allowing one to write

$$d_L^2 \propto f_x^{-1} \left(\frac{\Delta T_b}{T_b}\right)^2 T_e^{-\frac{5}{2}} r_c \tag{2.3.9}$$

Replacing r_c, the characteristic size of the hot gas in the cluster, with the observed angular size, $\theta_c = r_c/d_A$, where the angular diameter distance is related to the luminosity distance by equation 2.2.15 , $d_A = d_L/(1+z)^2$, one obtains an expression for the luminosity distance

$$d_L \propto f_x^{-1} \left(\frac{\Delta T_b}{T_b} \right)^2 T_e^{-\frac{5}{2}} \theta_c \, (1+z)^{-2} \qquad (2.3.10)$$

which is a function of five observable quantities: the microwave decrement, $\Delta T_b/T_b$, the electron temperature, T_e, the x-ray flux, f_x, the angular size of the x-ray scattering region, θ_c, and the cluster redshift, z.

The x-ray flux (or, equivalently, the x-ray surface brightness), and the angular size of the hot gas are obtained from x-ray observations of the cluster with an imaging x-ray telescope such as *Einstein* or *AXAF*. The temperature is estimated from the x-ray spectrum. Note that the validity of the above relations depends on the assumption that the intracluster gas is isothermal - an important assumption that may not be true and should somehow be tested independently before believable values of H_0 and q_0 can be determined. Perhaps the most difficult observable to measure, however, is the microwave decrement term, $\Delta T_b/T_b$, since it is such a small effect and is easily masked by many different sources of background and noise (see Uson 1986 for a review). The magnitude of the microwave decrement is $\Delta T_b/T_b \approx 5\times10^{-4}$ so that the central brightness temperature effect is just $\Delta T_b\,(0) \approx -1.3$ mK. Problems with beam switching to properly measure the "background" in the nearby "blank" sky, and atmospheric emission at frequencies above 35 GHz and intrinsic cluster radio emission at frequencies below 15 GHz further complicate the measurement.

In spite of these problems, two recent independent detections of the Sunyaev-Zel'dovich effect are reported by Uson (1986) and Birkinshaw (1986). Uson has detected the effect in the clusters CL 0016+16, A401, and A665. There is some evidence that the effect may also have been seen in A2218, A1763, and CL 1558+41. Birkinshaw has claimed detections of the effect in the clusters CL 0016+16, A665 and A2218. Based on his own and Birkinshaw's combined measurements of Cl 0016+16, Uson (1986) calculates the Hubble constant lies in the range 30 km s^{-1} $Mpc^{-1} < H_0 < 200$ km s^{-1} Mpc^{-1}. The large uncertainty in H_0 is caused by the large errors in the x-ray temperature measurements and the (possibly incorrect) assumption that the ICM is isothermal.

d) x-ray observations of resonance absorption lines from quasars behind clusters of galaxies

An exciting and potentially powerful technique for determining H_0 and q_0 from measurements of the angular diameter distances to distant galaxy clusters has recently been proposed by Krolik and Raymond (1988). This method is similar, in principle to that described in the last section; however, instead of measuring the microwave decrement of the cosmic background radiation (Sunyaev-Zel'dovich effect), one measures the equivalent widths of x-ray absorption lines from x-ray bright quasars lying in or behind the cluster of galaxies. This information is combined with x-ray measurements of the size and temperature of the hot intracluster gas to give a value for the distance to the cluster that is a function of observables. Of course, this method depends on the existence of x-ray-bright quasars in or behind rich, x-ray-bright galaxy clusters.

The equivalent width may, in principle, be easier to measure than the microwave decrement (see Krolik and Raymond 1988 for details). There are also a number of lines that may be used in the same cluster in order to over-constrain the problem. As Krolik and Raymond point out, however, this measurement depends on the successful construction and launch of a high-resolution x-ray spectrometer such as the microcalorimeter planned for *AXAF* (Holt 1987). The x-ray surface brightness can be easily mapped with *ACIS*, the *AXAF CCD Imaging Spectrometer* (Nousek 1987), which will be available on the same satellite.

2.4 Galaxy Evolution in Distant Clusters

a) statement of the problem

It is clear from the problems associated with two of the classical cosmological tests outlined above (both the (m,z) and (θ,z) tests) that galaxy evolution must be understood before meaningful conclusions can be drawn from the data. There are two evolutionary processes that must be considered: 1) *spectral evolution* which considers the time evolution of the light from a stellar population as stars age and new stars are born, and 2) *dynamical evolution* which considers the formation, interaction, and environment of galaxies and the contribution of these factors to the morphology, mass, and light distribution of the resulting galaxy or cluster of galaxies. Study of the spectral evolution of galaxies has become a very popular area of research in the past few years, as indicated by the number of reviews and conference proceedings on the subject. Evolutionary synthesis models (Bruzual 1983) have been developed assuming an analytical form for the star formation rate (SFR) and the initial mass function (IMF). Although one might expect the IMF and the SFR to depend on the details of the environment (*i.e.* on the dynamics), to first order, it is usually assumed that spectral and dynamical evolution occur independently.

The current situation concerning dynamical evolution is discussed in a review by Dressler (1984). One aim of this research is to understand the formation of brightest cluster galaxies, in particular the giant cD galaxies

found in many rich clusters: are these galaxies merely the tail-end of the luminosity function, or were they formed through special processes such as mergers (Ostriker and Tremaine 1975) or massive cooling flows (Fabian *et al.* 1986; Vedder 1988). Astronomers are also struggling to understand the clumpiness and substructure seen in clusters (Fitchett 1988) and the constraints these observations place on models of cluster formation.

It is beyond the scope of this thesis to comment in detail on galaxy evolution. What follows is merely a brief discussion of some of the results of the last ten years. This section will present at least the form of the evolution correction mentioned in the previous description of the Hubble diagram work. Following the notation of Yoshii and Takahara (1988), the luminosity evolution term $E_\lambda(z)$ is given by

$$E_\lambda(z) = -2.5 \log \frac{\int_0^\infty f_{\lambda/(1+z)}(z)\, S_\lambda(\lambda)\, d\lambda}{\int_0^\infty f_{\lambda/(1+z)}(0)\, S_\lambda(\lambda)\, d\lambda} \qquad (2.4.1)$$

where $f_{\lambda/(1+z)}(z)$ is the flux at the rest frame wavelength at a look-back time corresponding to redshift z, and $f_{\lambda/(1+z)}(0)$ is the flux, also at the rest frame wavelength, of a nearby galaxy now.

Tinsley (1977) has shown that elliptical and S0 galaxies should appear significantly bluer at $z \geq 0.5$ when evolutionary effects are considered. The amount of color evolution strongly depends on the exact redshift of galaxy formation, z_F. Incorporating their own spectral evolution models, Yoshii and Takahara (1988) show that all existing data for a number of cosmological tests, including the Hubble diagram, are consistent with $q_0 \sim 1/2$ provided that galaxies formed at a redshift $z_F \sim 3$-5.

b) observational evidence for evolution

At this point, one should ask are these models for evolution necessary merely to explain why our cosmological models don't seem to fit the observational data, or is there independent, direct evidence of spectral and dynamical evolution in distant galaxies? Of course, we expect some evolution if the big bang actually occurred and galaxies formed as the universe cooled. But as Sandage (1989) warns, we cannot "use standard model predictions to prove that evolution has occurred without having a priori proof that the standard model is correct." We must therefore find evidence of evolution that is independent of the predictions of the standard model.

Independent evidence for galaxy evolution was discovered over a decade ago by Butcher and Oemler (1978a; BOI), who found an excess of blue galaxies in the cores of two rich, compact, distant clusters of galaxies (3C 295 at z=0.46 and Cl 0024+16 at z=0.39. This excess of blue galaxies (the Butcher-Oemler [BO] effect) is not

seen in nearby clusters (Butcher and Oemler 1978b; BOII). Following the initial BO observations, Butcher, Oemler and Wells (1983; BOW), Couch and Newell (1984), and Butcher and Oemler (1984; BOV) confirmed the existence of the BO effect in a larger sample (a total of ~30) of distant clusters (z>0.2). BOV found that for z>0.1, the fraction of blue galaxies, f_b, increases systematically with redshift reaching f_b~0.25 at z~0.5; nearby clusters have f_b<0.03. However, BO's conclusions are based on photometric rather than spectroscopic data, and a number of authors have raised serious doubts about the reality of the effect (Koo 1981; Koo 1988; Koo *et al.* 1988; Dressler and Gunn 1983). The primary criticism concerns the separation of cluster galaxies from the "background" field, which has been shown to have a higher blue galaxy fraction than the clusters (BOV).

In order to resolve the controversy, a number of spectroscopic observations of BO clusters were started. The first results were reported by Dressler and Gunn (1982) who examined the original BO clusters 3C 295 and Cl 0024+16. They found a large number of emission-line galaxies and elliptical galaxies that appear to have undergone a recent burst of star formation (~1 to 2 Gyr ago). This Dressler-Gunn effect has now been confirmed in a larger sample of clusters (Dressler and Gunn 1983; Dressler, Gunn and Schneider 1985; Sharples *et al.* 1985; Couch and Sharples 1987; Lavery and Henry 1986; Henry and Lavery 1987). In addition, Newberry, Kirshner, and Boroson (1988) have verified spectroscopically the colors of BO galaxies in seven BO clusters and find the slope of the BO effect of df_b/dz=0.60 is consistent with the photometric value of df_b/dz=0.52 presented by BOV, and certainly is not zero.

Why are the blue galaxies blue? The look-back time to a cluster at z=0.3 is ~$4.5h_{50}^{-1}$ Gyr; thus, some mechanism must have depleted the cluster population of star-forming galaxies within the last ~3–5 Gyr. A variety of scenarios, including ram-pressure stripping through interaction with a dense intracluster medium (Gunn and Gott 1982), and galaxy-galaxy interactions (Lavery and Henry 1987), have been proposed to explain this depletion.

Dressler (1987) concludes that we <u>are</u> witnessing galaxy evolution in clusters, at least in clusters at z>0.4. The environments of rich clusters of galaxies were different 5 billion years ago than they are today, and it appears that galaxy evolution is real and has not been invoked just to "save the standard model." The hope remains that someday, when we finally understand evolution, we can go back and apply the appropriately corrected cosmological tests described above, and ultimately measure q_0.

REFERENCES:

Abell, G.O. 1958, "The Distribution of Rich Clusters of Galaxies," *Ap.J. Supp.*, **3**, 211.

Abell, G.O., Corwin, H.G., and Olowin, R.P. 1989, "A Catalog of Rich Clusters of Galaxies," *Ap.J.Supp.*, **70**, 1. ACO

Bahcall, N. 1977, "Clusters of Galaxies," *Ann. Rev. Astron. Astrophys.*, **15**, 505.

Bahcall, N. 1981,"The relation between velocity dispersion and central density in clusters of galaxies," *Ap.J.*, **247**, 787.

Bautz, L., and Morgan, W. 1970, "On the Classification of the Forms of Clusters of Galaxies," *Ap.J.*, **162**, L149.

Birkinshaw, M., Gull, S.F., and Moffet, A.T. 1981, "Observations of a decrement in the Microwave Background Radiation Toward the Distant Cluster of Galaxies 0016+16," *Ap.J.*, **251**, L69.

Birkinshaw, M. 1979, "Limits to the Value of the Hubble Constant Deduced from Observations of Clusters of Galaxies," *M.N.R.A.S.*, **187**, 847.

Birkinshaw, M. 1986, "New Results on the Sunyaev-Zel'dovich Effect in 0016+16, A665, and A2218," n *Radio Continuum Processes in Clusters of Galaxies - NRAO Workshop #16*, Green Bank: NRAO. p. 261.

Bruzual, G. 1983, "Spectral Evolution of Galaxies. I. Early-Type Systems," *Ap.J.*, **273**, 105.

Bruzual, G. 1981, *Spectral Evolution of Galaxies*, Ph.D. Thesis, University of California, Berkeley.

Bruzual, G., Spinrad, H. 1978, "The Characteristic Size of Clusters of Galaxies: A Metric Rod Used for a Determination of q_0," **220**, 1.

Butcher, H., and Oemler, A. 1978a, "The Evolution of Galaxies in Clusters. I. ISIT Photometry of Cl 0024+1654 and 3C 295," *Ap.J.*, **219**, 18 (BOI).

Butcher, H. and Oemler, A. 1978b, "The Evolution of Galaxies in Clusters II. The Galaxy Content of Nearby Clusters," *Ap.J.*, **226**, 559 (BOII).

Butcher, H. Oemler, A. and Wells, D. 1983, "The Evolution of Galaxies in Clusters. III. Photometry of 17 Intermediate Redshift Clusters," *Ap.J.Supp.*, **52**, 183 (BOW).

Butcher, H. and Oemler, A. 1985, "The Evolution of Galaxies in Clusters. IV. Photometry of 10 Low-Redshift Clusters" *Ap.J.Supp.*, **57**, 665 (BOIV).

Butcher, H. and Oemler, A. 1984,"The Evolution of Galaxies in Clusters. V. A Study of Populations since z~0.5," *Ap.J.*, **285**, 426 (BOV).

Cavaliere, A., Danese, L., and DeZotti, G. 1979, "Cosmic Distances from X-ray and Microwave Observations of Clusters of Galaxies," *Astron.Ap.*, **75**, 322.

Couch, W.J. and Newell, E.B. 1984, "Distant Clusters of Galaxies. I. Uniform Photometry of 14 Rich Clusters," *Ap.J.*, **56**, 143.

Couch, W., Ellis, R., Godwin, J., and Carter, D. 1983, "Spectral Energy Distributions for Galaxies in High Redshift Clusters - I. Methods and Application to Three Clusters with $0.22 < z < 0.31$," *M.N.R.A.S.*, **205**, 1287.

Couch, W., and Sharples, R. 1988, "A Spectroscopic Study of Three Rich Galaxy Clusters at z=0.31," *M.N.R.A.S.*, **229**, 423.

Djorgovski, S. 1987, "Galaxies at Very High Redshifts (z>1)," in *Nearly Normal Galaxies: From the Planck Time to the Present*, ed. Faber (Berlin: Springer-Verlag).

Dressler, A. 1978, "Bautz-Morgan Classes and the Luminosity Function for Clusters of Galaxies," *Ap.J.*, 222, 23.

Dressler, A. 1978, "A Comprehensive Study of 12 Very Rich Clusters of Galaxies. I. Photometric Technique and Analysis of the Luminosity Function," *Ap.J.*, **223**, 765.

Dressler, A. 1984, "The Evolution of Galaxies in Clusters," in *Ann. Rev. Astron. Astrophys.*, **22**, 185.

Dressler, A., and Gunn, J.E. 1982, "Spectroscopy of Galaxies in Distant Clusters. I. First Results for 3C295 and 0024+1654," *Ap.J.*, **263**, 533.

Dressler, A., and Gunn, J.E. 1983, "Spectroscopy of Galaxies in Distant Clusters. II. The Population of the 3C295 Cluster," *Ap.J.*, **270**, 7.

Dressler, A., Gunn, J.E., and Schneider, D.P. 1985, "Spectroscopy of Galaxies in Distant Clusters. III. The Population of Cl 0024+1654," *Ap.J.*, **294**, 70.

Ellis, R., Couch, W., MacLaren, I., and Koo, D., 1985, "Spectral Energy Distributions for Galaxies in High Redshift Clusters - II. 0016+16 at z=0.54," *M.N.R.A.S.*, **217**, 239.

Fabian, A.C., Arnaud, K.A., Nulsen, P. and Mushotzky, R. 1986, "The Detection of Distant Cooling Flows and the Formation of Dark Matter," *Ap.J.*, **305**, 9.

Forman , W. and Jones, C. 1982, "X-ray Imaging Observations of Clusters of Galaxies," *Ann.Rev.Astron.Ap.*, **20**, 547.

Gunn, J.E., 1978, "The Friedmann Models and Optical Observations in Cosmology," in *Observational Cosmology, 8th Advanced Course of the Swiss Society of Astronomy and Astrophysics* (Sauverny, Switzerland: Geneva Observatory).

Gunn, J.E., Hoessel, J.G., and Oke, J.B. 1986, "A Systematic Survey for Distant Galaxy Clusters," *Ap.J.*, **306**, 37.

Gunn, J.E., and Oke, J.B. 1975, "Spectrophotometry of Faint Cluster Galaxies and the Hubble Diagram: An Approach to Cosmology," *Ap.J.*, **195**, 255.

Gunn, J.E. and Gott, J.R. 1982, *Ap.J.*, **176**, 1.

Hamilton, D. 1985, "The Spectral Evolution of Galaxies. I. An Observational Approach," *Ap.J.*, **297**, 371.

Henry, J.P., Soltan, A., Briel, U., and Gunn, J.E. 1982, "Evolution of the Cluster X-ray Luminosity Function Slope," *Ap.J.*, **262**, 1.

Hickson, P. 1977a, "The Angular Size-Redshift Relation. I. Sizes and Shapes of Nearby Clusters of Galaxies," *Ap.J.*, **217**, 16.

Hickson, P. 1977b, "The Angular Size-Redshift Relation. II. A Test for the Deceleration Parameter," *Ap.J.*, **217**, 964.

Hoessel, J.G., Gunn, J.E., and Thuan, T.X. 1980, "The Photometric Properties of Brightest Cluster Galaxies. I. Absolute Magnitudes in 116 Nearby Abell Clusters," *Ap.J.*, **241**, 486.

Hoessel, J.G. 1980, "The Photometric Properties of Brightest Cluster Galaxies. II. SIT and CCD Surface Photometry," *Ap.J.*, **241**, 493.

Hoessel, J.G., and Schneider, D. 1985, "CCD Observations of Abell Clusters. IV. Surface Photometry of 175 Brightest Cluster Galaxies," *Astron. J.*, **90**, 1648.

Kapahi, V.K. 1987, "The angular size - redshift relation as a cosmological tool," in *Observational Cosmology. IAU Symposium 124*, ed. A. Hewitt, G. Burbidge, L.Z. Fang, (Dordrecht: Reidel).

Koo, D. 1981, "Multicolor Photometry of the Red Cluster 0016+16 at z=0.54," *Ap.J.*, **251**, L75.

Koo, D. 1988, "Comments on the Reality of the Butcher-Oemler Effect," in *Towards Understanding Galaxies at Large Redshifts*, ed. R.G. Kron and A. Renzini (Dordrecht: Reidel).

Koo, D., Kron, R., Nanni, D., Trevese, D., and Vignato, A. 1988, "II Zw 1305.4+2941 at z=0.24: Another Rich, Red, Compact Cluster," *Ap.J.*, **333**, 586.

Kristian, J., Sandage, A., and Westphal, J. 1978, "The Extension of the Hubble Diagram. II. New Redshifts and Photometry of Very Distant Galaxy Clusters: First Indication of a Deviation of the Hubble Diagram from a Straight Line," *Ap.J.*, **221**, 383.

Krolik, J.H., and Raymond, J.C. 1988, "Measuring H_0 and q_0 with X-ray Lines from Galaxy Clusters," *Ap.J.*, **335**, L39.

Lavery, R.J., and Henry, J.P. 1988, "Evidence for Galaxy-Galaxy Interactions as an Active Agent of the Butcher-Oemler Effect at a Redshift of 0.2," *Ap.J.*, **330**, 596.

Lynds, R., and Petrosian, V. 1988, "Luminous Arcs in Clusters of Galaxies," *Ap.J.*, **336**, 1.

MacLaren, I., Ellis, R., and Couch, W. 1988, "Spectral Energy Distributions of Galaxies in High Redshift Clusters - III. Abell 370 at z = 0.37," *M.N.R.A.S.*, **230**, 249.

Mathews, T.A., Morgan, W.W., and Schmidt, M. 1964, *Ap.J.*, **140**, 35.

McHardy, I. 1974, "The Bautz-Morgan Classification of Clusters Containing Radio Galaxies," *M.N.R.A.S.*, **169**, 527.

McHardy, I. 1979, "4C Radio Sources in Clusters of Galaxies - III," *M.N.R.A.S.*, **188**, 495.

McHardy, I. 1978, "X-Ray Sources in Clusters of Galaxies," *M.N.R.A.S.*, **184**, 783.

Miley, G. 1971, *M.N.R.A.S.*, **152**, 477.

Miley, G. 1980, "The structure of Extended Extragalactic Radio Sources," *Ann.Rev.Astron.Ap.*, **18**, 165.

Newbarry, M.V., Kirshner, R.P., and Boroson, T.A. 1988, "Spectra of Galaxies in Clusters. I. The Butcher-Oemler Effect," *Ap.J.*, **335**, 629.

Oke, J.B. 1987, "Spectroscopic Surveys of High-z Galaxies," in *High Redshift and Primeval Galaxies* (Paris: Editions Frontieres), p.19.

Oke, J.B., and Sandage, A. 1968, "Energy Distributions, K Corrections, and the Stebbins-Whitford Effect for Giant Elliptical Galaxies," *Ap.J.*, **154**, 21.

Peebles, P.J.E. 1971, *Physical Cosmology*, (Princeton: Princeton Univ. Press).

Postman, M., Huchra, J., Geller, M., and Henry, J.P. 1985, "The Magnitude-Redshift Relation for 561 Abell Clusters," *Astron.J.*, **90**, 1400.

Sandage, A. and Hardy, E. 1973, "The Redshift Distance Relation. VII. Absolute Magnitudes of the First Three Ranked Cluster Galaxies as Functions of Cluster Richness and Bautz-Morgan Cluster Type: The Effect on q_0," *Ap.J.*, **183**, 743.

Sandage, A. 1961, "The Ability of the 200-Inch Telescope to Discriminate Between Selected World Models," *Ap.J.*, **133**, 355.

Sandage, A. 1972, "The Redshift-Distance Relation. II. The Hubble Diagram and Its Scatter for First-Ranked Cluster Galaxies: A Formal Value for q_0," *Ap.J.*, **178**, 1.

Sandage, A. 1976, "The Absolute Magnitude of First-Ranked Cluster Galaxies as a Function of Cluster Richness," *Ap.J.*, **205**, 6.

Sandage, A. 1989, "Observational Tests of World Models," *Ann.Rev.Astron.Ap.*,

Sarazin, C.L. 1986, "X-ray Emission from Clusters of Galaxies," *Rev. Modern Physics*, **58**,1.

Schechter, P. 1976, "An Analytic Expression for the Luminosity Function for Galaxies," *Ap.J.*, **203**, 297.

Schechter, P. and Press, W. 1976, "Method for Determining Maximum-Likelihood Distance Moduli for Groups of Galaxies," *Ap.J.*, **203**, 557.

Schechter, P, and Peebles, P.J.E. 1976, "On the Significance of the Luminosities of First-Ranked Members of Sparse Groups of Galaxies," *Ap.J.*, **209**, 670.

Schneider, D.P., Gunn, J.E., and Hoessel, J.G. 1983a, "CCD Photometry of Abell Clusters. I. Magnitudes and Redshifts for 84 Brightest Cluster Galaxies," *Ap.J.*, **264**, 337.

Schneider, D.P., Gunn, J.E., and Hoessel, J.G. 1983b (SGH), "CCD Photometry of Abell Clusters. II. Surface Photometry of 249 Cluster Galaxies," *Ap.J.*, **268**, 476.

Shanks, T., Couch, W., McHardy, I., Cooke, B., and Pence, W. 1987, "Observations of High Redshift Galaxy Clusters: Implications for Cosmology," in *High Redshift and Primeval Galaxies* (Paris: Editions Frontieres), 1987.

Silk, J., and White, S.D.M. 1978, "The Determination of q_0 using X-ray and MicrowaveObservations of Galaxy Clusters," *Ap.J.*, **226**, L103.

Soucail, G., Fort, B., Mellier, Y., and Picat, J.P. 1987, "A Blue Ring-Like Structure in the Center of the A370 Cluster of Galaxies," *Astron. Ap.*, **172**, L14.

Soucail, G., Mellier, Y., Fort, B., Mathez, G., and Cailloux, M. 1988, "The Giant Arc in A370: Spectroscopic Evidence for Gravitational Lensing from a Source at z=0.724," *Astron. Ap.* , **191**, L19.

Spinrad, H. 1986, "Faint Galaxies and Cosmology," *P.A.S.P.*, **98**, 269.

Spinrad, H., and Djorgovski, S. 1984, "3C324 - An Extremely Distant Cluster Radio Galaxy," *Ap.J.*, **280**, L9.

Spinrad, H., and Djorgovski, S. 1987, "The Status of the Hubble Diagram in 1986," in *IAU Symposium 124, Observational Cosmology*, ed. Hewitt, Burbidge, and Fang (Dordrecht: Reidel), p. 129.

Struble, M.F., and Rood H.J. 1982,"Morphological Classification of Abell Clusters in D<4 and an Analysis of Observed Correlations," *AstronJ.*, **87**, 7.

Sunyaev, R. and Zel'Dovich Ya. 1972, *Comm. Astrophys. Sp.Sci.*, **4**, 173.

Thompson, L. 1986, "High-Resolution Imaging fron Mauna Kea: Surface Photometry of Galaxies in Cl 0024+16," *Ap.J.*, **300**, 639.

Thompson, L. 1986, "Galaxy Distribution in Butcher-Oemler Clusters," *Ap.J.*, **306**, 384.

Thompson, L. 1988, "High-Resolution Imaging from Mauna Kea: Morphology of Butcher-Oemler Galaxies," *Ap.J.*, **324**, 112.

Tinsley, B. 1976, "Surface Brightness Parameters as Tests of Galactic Evolution," *Ap.J.*, **210**, L49.

Uson, J. 1986, "The Sunyaev-Zel'Dovich Effect: Measurements and Implications," in *Radio Continuum Processes in Clusters of Galaxies - NRAO Workshop #16*, Green Bank: NRAO. p. 255.

Weedman, D.W., and Williams, K.L. 1987, "Isophotal Diameters of Galaxies at High Redshifts," *Ap.J.*, **318**, 585.

Weedman, D.W. 1986, *Quasar Astronomy*, (Cambridge: Cambridge University Press).

Weinberg, S. 1972, *Gravitation and Cosmology*, (New York: Wiley).

White, S.D.M., Silk, J., and Henry, J.P. 1981, "The X-ray Structure of a Galaxy Cluster at z=0.54: Implications for Cluster Evolution and Cosmology," *Ap.J.*, **251**, L65.

Yoshii, Y, and Takahara, F. 1988, "Galactic Evolution and Cosmology," *Ap.J.*, **326**, 1.

Zwicky, F., Herzog, E., Wild, P. Karpowics, M, and Kowal, C.T. 1961-1968, *Catalogue of Galaxies and of Clusters of Galaxies*, (Pasadena: California Institute of Technology), Vols. I - VI.

Chapter 3

Searching for High-Redshift Galaxy Clusters

The need for a large, unbiased sample of clusters of galaxies with redshifts $z \geq 0.5$ is evident from the work described in the last chapter. But how does one go about finding such objects? At $z>0.5$, the optical light from most of the galaxies in clusters will be extremely faint, and by $z \geq 1.5$, these galaxies will be nearly undetectable from the ground with currently available instrumentation and telescopes. Nevertheless, ongoing optical surveys complete to faint limiting magnitudes are currently underway (Gunn, Hoessel and Oke 1986; Gunn 1989). It is possible, however, to find distant clusters based on properties other than the optical light from the member galaxies. We discuss one of these alternative methods in this chapter. First, in Section 3.1, we review the current state of optical observations of high-redshift clusters, and outline some of the difficulties with optical observations of normal galaxies at $z>0.5$. Then, in Section 3.2, we describe an alternative method for identifying distant clusters by looking in fields containing radio sources with steep low-frequency spectra.

3.1 Optical Searches for Distant Clusters

The number of well-studied clusters of galaxies with $z>0.3$ is presently so small they can be listed in a table that fits on one page (see Table 3.1) [The entries in this table were gathered from the *published* literature, and do not include the considerable number of distant clusters currently under investigation by Gunn and collaborators (Gunn 1989; 1987)]. As of 1987, 578 of the 2712 Abell clusters have measured redshifts (Struble and Rood 1987): 9 of these have $z>0.3$ and are listed in Table 3.1. While it may be possible that a number of clusters with $0.2<z<0.5$ may be hiding in the remainder of the Abell catalog, it is unlikely that the catalog contains any clusters with $z>0.5$. The only existing catalog of distant clusters of galaxies is that of Gunn, Hoessel and Oke (1986;GHO), which was briefly mentioned in the beginning of the last chapter. This catalog contains 418 optically selected members found using a variety of instrumentation. Initially, GHO used hypersensitized photographic plates on the Palomar Schmidt telescope, followed by hypersensitized photographic plates on the Hale 5m and Kitt Peak 4m telescopes. They eventually obtained deep CCD pictures for all of their clusters using the PFUEI and 4-Shooter on the Hale 5m telescope. They have not measured redshifts yet for all of the clusters in the sample, but those with redshifts have $0.15<z<0.92$ (GHO). As an example of what some exceptionally rich, high-redshift clusters of galaxies look like, a CCD image of the richest cluster in their sample, Cl 0939+47, is shown in Figure 3.1 (the CCD image was taken with the instrument to be described later in this thesis). This cluster has a redshift of $z=0.402$ and should be compared to the Corona Borealis cluster (at $z=0.07$) shown in Figure 2.1 in the last chapter. In addition to the catalog of GHO, Gunn and collaborators (Postman, Oke, Hoessel, and Schneider) have begun an ambitious project to scan a 6^{o} area of the

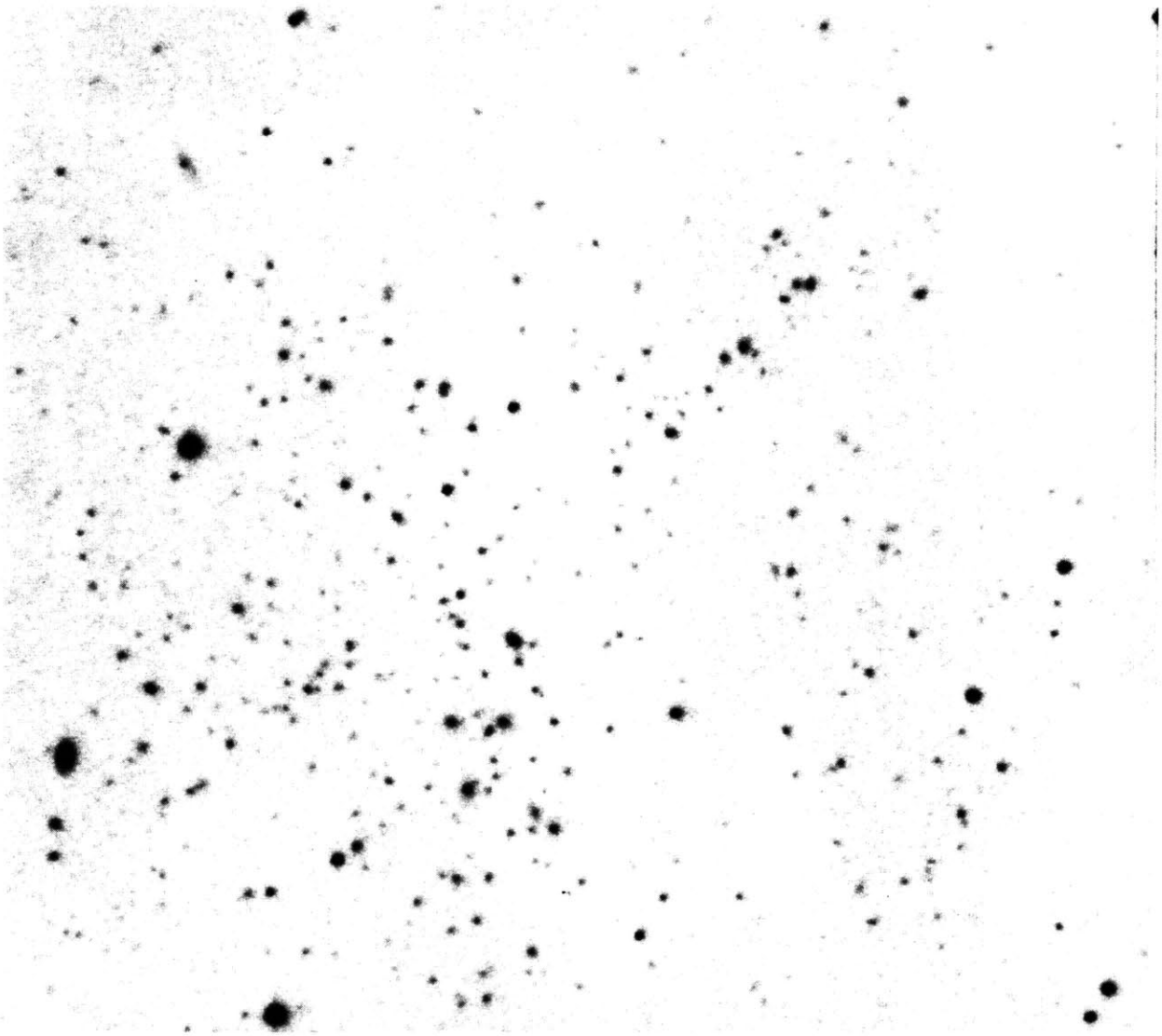

FIGURE 3.1 A CCD image of the extremely rich cluster *Gunn 0939+47* at a redshift of 0.402. This 1800 second R-band image was taken on the MDM Observatory 1.3m telescope with a single TI 850 × 750 CCD in the instrument described later in this thesis. The image scale is 0.47 arcseconds per pixel (North is up and east is to the left).

Table 3.1 Distant Abell Clusters and Other Optically-Well-Studied Clusters of Galaxies with $z > 0.3$

CLUSTER	REDSHIFT	REFERENCES	NOTES
AC 118	0.31	3	=? in ACO - shows BO effect
0016+16	0.541	8,12	extremely rich, red cluster, and one of the most luminous x-ray clusters known with $L_x \sim 3 \times 10^{45}$ erg s^{-1}
0024+1654	0.391	1,7,5	Butcher-Oemler cluster. Koo recently found a possible luminous arc in this cluster.
0055−279	0.57	3	some evidence of BO effect
A370	0.373	1,14,15	contains famous luminous arc
A851	0.402	10	Abell cluster with largest known redshift (although Abell may have actually identified a foreground group at z~0.2). Richest cluster in sample of distant clusters of Gunn, Hoessel and Oke (1986). Gunn claims this is the richest cluster known (see Figure 3.1).
A895	0.360	1,2,16	
A908	0.390	1,2,16	
A913	0.366	1,2,16	
A1576	0.302	1,2,16	
A1722	0.328	1,2,16	
A2084	0.342	1,2,16	
A2444	0.324	1,2,16	
3C 295	0.465	9,5,6	bizarre object. bright radio source, but cluster is not very rich (only Richness Class 0). blue galaxies identified by BO turned out to be foreground objects, but DG found a large active fraction of E+A galaxies.
2244−02	0.328	11,14	another luminous arc
1305+2952	0.947	13	cluster with highest published redshift?
1446+2619	0.369	1	Butcher-Oemler cluster
AC 114	0.31	4	= S1077 in ACO - shows BO effect
AC 103	0.31	4	= S0910 in ACO - shows BO effect

1 Butcher, H. and Oemler, A. 1984, *Ap.J.*, **285**, 426. (BOV)

2 Butcher, H., Oemler, A., and Wells, D. 1983, *Ap.J.Supp.*, **52**, 183.

3 Couch, W., Shanks, T., and Pence, W. 1985, *M.N.R.A.S.*, **213**, 215.

4 Couch, W. and Sharples, R. 1987, *M.N.R.A.S.*, **229**, 423.

5 Dressler, A. and Gunn, J.E. 1982, *Ap.J.* , **263**, 533.

6 Dressler, A., and Gunn, J.E. 1983, *Ap.J.*, **270**, 7.

7 Dressler, A., Gunn, J., and Schneider, D. 1985, *Ap.J.*, **294**, 70.

8 Ellis, R., Couch, W., MacLaren, I., and Koo, D., 1985, *M.N.R.A.S.*, **217**, 239.

9 Gunn, J.E., and Oke, J.B. 1975, *Ap.J.*, **195**, 255.

10 Gunn, J., Hoessel, J., and Oke, J.B. 1986, *Ap.J.*, **306**, 30. (GHO)

11 Kristian, J., Sandage, A., and Westphal, J. 1978, *Ap.J.*, **221**, 383.

12 Koo, D. 1981, *Ap.J.*, **251**, L75.

13 Kron, R., Spinrad, H., and King, I. 1977, *Ap.J.*, **217**, 951.

14 Lynds, R. and Petrosian, V. 1989, *Ap.J.*, **336**, 1.

15 MacLaren, I., Ellis, R., and Couch, W. 1988, *M.N.R.A.S.*, **230**, 249.

16 Struble, M. and Rood, H. 1987, *Ap.J.Supp.*, **63**, 543.

sky with CCDs (Gunn 1987; 1989). They have developed computer software to find distant clusters using well-defined selection criteria, and expect to detect a complete sample of Abell Richness Class 2 clusters out to z=1.

b) optical observations of galaxies at high redshift

Since the angular diameter of a galaxy of fixed metric size decreases little beyond z=1[1] , the limitation on the detection of such a galaxy is determined by surface brightness, not total flux. The surface brightness of an object at redshift z (in mag arcsec^{-2}) compared to the surface brightness of an object at z=0 is given in the following equation (also see §2.2)

$$s_\lambda(z) = s_\lambda(0) + 10\log(1+z) + 2.5\log(1+z) + 2.5\log\frac{\int_0^\infty L_\lambda S_\lambda(\lambda)\,d\lambda}{\int_0^\infty L_{\lambda/(1+z)} S_\lambda(\lambda)\,d\lambda} \quad (3.1.1)$$

We can see from this equation that the surface brightness will decrease by 5 factors of (1+z): the $(1+z)^4$ dimming term and one factor from the K-correction. This is an enormous effect. At z=1, and ignoring the wavelength-dependent portion of the K-correction, the surface brightness is reduced by a factor of 32 or 3.8 magnitudes arcsec^{-2}. At z=1.5, the surface brightness is reduced by a factor of 100!

The reason high-redshift clusters of galaxies are so hard to find is simple. They fade away (and are certainly not detectable as galaxies *i.e.*, extended objects) when the angular diameter of the isophote corresponding to the the limiting detectable isophote (surface brightness) becomes smaller than the resolution of the detector used for the observations. This problem was addressed by Weedman and Huenemoerder (1985) and later Weedman and Williams (1987; WW) who calculated isophotal diameters for galaxies as a function of redshift assuming the limiting detection isophote was 26 mag arcsec^{-2} at 6500Å. They computed the correction for the change in spectral energy distribution (the last term in equation 3.1.1) using observed (including IUE UV observations) spectral energy distributions (SEDs) for a number of galaxies, including some starburt galaxies (N1068, N4736) with disks of unusually high surface brightness. Table 3 of WW lists these isophotal diameters. At z>1.0, all galaxies except those with exceptionally bright disks will be indistinguishable from stars, and beyond z>1.5 they become essentially undetectable.

Another limitation for finding distant clusters arises from the observed redward shift of their spectral energy distributions (SED). The flux per unit wavelength from a normal elliptical galaxy decreases dramatically for λ<4000Å (see SED plots in Chapter 7, Figure 7.7). For z=0.5, rest frame 4000Å is observed at 6000Å, in the R band, and the center of rest frame V is observed at 8250Å, in the middle of the I band. At z=1, rest frame 4000Å is observed at 8000 Å and rest frame V has been shifted out of the sensitivity region of CCDs and into

[1] In fact it increases with distance beyond z=1.25 for a Friedmann cosmologies with q_0>0 (see §2.3).

the infrared. This problem was dramatically illustrated by Gunn (1989) who showed CCD images of a cluster of galaxies at z=0.75 taken through V, R, and I filters. The exceedingly rich cluster was essentially undetectable in V, visible in R, and striking in I. It is therefore important to look in the near infrared to find clusters with z>0.5.

3.2 Steep-Spectrum Radio Sources and Clusters of Galaxies

Clusters of galaxies are often sources of radio emission: the radio source being associated with a member galaxy. A large fraction of all extragalactic radio sources are found in clusters of galaxies, but this is probably because giant ellipticals occur preferentially in rich clusters, and giant ellipticals are a major class of extragalactic radio source. Pilkington (1964) showed that the probability of an Abell cluster having an associated radio source is proportional to the cluster richness (*i.e.*, the number of galaxies in the cluster), suggesting cluster membership has nothing to do with the probability of a galaxy being a radio galaxy. This was modified by McHardy (1979), who found that 4C radio sources do not occur significantly more often in rich clusters, but do occur more often in BM Type I clusters, with the source ususlly associated with the giant cD galaxy. This suggests that the probability that a radio source will be produced may depend on the optical luminosity of the giant elliptical core.

The radio emission from extragalactic radio sources is non-thermal synchrotron radiation which is well characterized by a power law spectrum, $S_\nu \propto \nu^{-\alpha}$, where α is defined as the spectral index. In the early days of extragalactic radio astronomy, many attempts were made to correlate the spectral index of radio sources with their other properties. Baldwin and Scott (1973; BS) pioneered the systematic investigation of radio sources with steep spectra (α>1.2) at low frequencies (ν~178 MHz) by selecting 29 sources from the 4C (178 MHz) and WKB (Williams Kenderdine and Baldwin) (38 MHz) catalogs which have a number of well defined sources with α (178 MHz) > 1.2. Sources from the well-known 3C catalog were not selected since only ~2% of the 3C sources will have α>1.2 at 178 MHz (BS). The 4C and WKB catalogs, however, reach lower limiting flux densities of 2 Jy[1] and 14 Jy respectively, and were expected to contain a larger number of sources with α>1.2. BS found that 11 of the 29 radio sources they studied were associated with rich Abell clusters of galaxies, 1 with a Zwicky cluster, and 4 with apparently isolated galaxies. The remaining 13 radio sources remain unidentified. In the area where the Abell catalog is complete, only 2 percent of 4C radio sources are associated with Abell clusters. The fraction of steep-spectrum radio sources, 38 percent, associated with Abell clusters is significantly higher than that for the 4C catalog as a whole. In addition, BS compiled a list of 31 steep-spectrum sources that were outside the area where the Abell catalog is considered to be complete. In spite of the increased galactic obscuration, 4 of these sources were associated with Abell clusters and 1 with a Zwicky cluster.

---

[1] Jy = Jansky $\equiv 10^{-26}$ Watts m^{-2} Hz^{-1} = 10^{-23} ergs s^{-1} cm^{-2} Hz^{-1} = 10^{3} mJy

This work was continued by Slingo (1974a) and Slingo (1974b) who obtained radio maps of the BS sources at 408 and 1407 MHz using the Cambridge One-Mile telescope. SOme of the unidentified sources of BS were found to be associated with Zwicky clusters and some isolated galaxies. Two of the sources appeared to be in very distant clusters. Ultimately, Slingo (1974b) concluded "steep spectrum sources occur exclusively in rich clusters of galaxies and that many of those previously unidentified are in clusters having $z>0.2$." He also argues that these sources evolved from powerful double radio galaxies which are 10^9 to 10^{10} years old and have been confined by a hot intracluster medium.

a) physics of the radio emission

Radio source models require some mechanism for producing the relativistic particles responsible for the resulting synchrotron radiation. The most common scenarios involve massive black holes fueled by gas in the cores of the powerful radio galaxies. It is beyond the scope of this thesis to comment on the source of the relativistic particles; we will merely assume that such a source exists. Considering only synchrotron radiation, it is instructive to consider the time evolution of the relativistic electron population. If we assume the population has an initial power-law energy spectrum

$$N(E, t=0) \propto E^{-\gamma} \tag{3.2.1}$$

and we know the losses due to synchrotron radiation are

$$\frac{dE}{dt} \propto -B^2 E^2 \tag{3.2.2}$$

where B is the magnetic field, then the resulting electron spectrum will be

$$N(E, t) \propto E^{-\gamma} (1 - k B^2 t)^{\gamma-2} \qquad \text{for } E<E_c \tag{3.2.3}$$

and $N(E,t)=0$ for $E>E_c$, where $E_c \propto B^{-2}t^{-1}$. The frequency spectrum of synchrotron radiation will show a power law dependence, $S_\nu \propto \nu^{-\alpha}$, if $\gamma>2$ where $\alpha=(\gamma-1)/2$ (van der Laan and Perola 1969). We see that the higher energy electrons are depleted from the population first with none remaining above some critical energy E_c. This corresponds to a critical frequency given by $\nu_c \sim 1000\, B^{-3}t^{-2}$ MHz where B is measured in Gauss and t in years (Slingo 1974a). Typical magnetic fields in clusters are thought to range from 1 to 20 μGauss[1]. Such a radio source outside a cluster of galaxies would disperse from adiabatic expansion, and the radio luminosity would decrease and eventually be undetectable (the expansion will weaken the radio emission but will not affect the spectrum). We know, however, from x-ray observations that rich clusters contain large amounts of hot gas, and

[1] Simple equipartition arguments can be used to estimate the cluster magnetic field strength. If the magnetic field energy density is in "equipartition" with the gas thermal pressure, then $B^2/8\pi \approx n_{icm}kT_g$. If we assume kT_g is of order 6 keV and n_{icm} is approximately 10^{-3} cm^{-3}, we find $B \approx 10$ μG.

the thermal pressure of this gas would equal the magnetic pressure of a field of ~10 μGauss and could act to slow or even halt the adiabatic expansion of the radio source thus allowing the source "to age" so that synchrotron losses (and also inverse Compton in some cases) steepen the spectrum. McHardy (1974) and Slingo (1974b) claim that such steep-spectrum sources in some rich clusters are 10^9 to 10^{10} years old.

b) implications of steep-spectrum radio emission from clusters of galaxies

Rich clusters of galaxies often show evidence for large cooling flows. Burns (1989) investigated the radio and x-ray properties of 27 cD galaxies in rich Abell clusters. Using *Einstein* IPC data and *VLA* radio maps, he explored the relationship between x-ray cooling cores and the power and morphology of the radio emission, and found that 73 percent of cDs in clusters with x-ray cooling cores were radio loud (with $S_{5GHz} > 0.2$ mJy) whereas only 23 percent of cDs without cooling cores have detectable radio emission at this flux level[1]. Burns also points out that radio sources in these cooling flow clusters tend to have steeper-spectra, and he suggests that the cooling core plays a role in steepening the spectrum. This is consistent with the source confinement model discussed above: since cooling core clusters have higher central pressure than non-cooling cores, we expect the radio source to be better confined and thus longer lived so that synchrotron losses steepen the spectrum with age. In addition, Burns noted a fundamental difference in radio morphology between sources in clusters with and without cooling flows. He mentions that one class of radio galaxy often associated with optically dominant cluster galaxies, wide-angle tailed (WAT) sources, are found exclusively in clusters without cooling cores. Of course, if the cooling flow plays some role in fueling the radio source located in the cD galaxy, and the cD galaxy is essentially at rest in the center of the cluster potential well, then we would not expect to see the distorted morphology (radio-trail or WAT sources for example) indicative of the radio galaxy moving through the intracluster medium.

We expect the radio emission and the x-ray emission from steep-spectrum radio source clusters to be correlated, especially since the hot and dense ICM is confining the radio source. We might therefore expect that clusters of galaxies selected because of the presence of an SSRS will also be bright x-ray sources. In addition, this sample of clusters may preferentially select clusters with cooling flows. Also, steep-spectrum radio sources in clusters at high redshifts may help put limits on the epoch of galaxy formation. These radio sources may be as old as 10^{10} years, and the corresponding redshift for a look-back-time of 10^{10} years is $\Delta z = 1.7$ (H_0=50; q_0=0.5). Therefore a galaxy observed at $z = 1$ that contains a steep-spectrum radio source believed to be 10^{10} years old must have formed earlier than $z = 2.7$ in support of an epoch of galaxy formation earlier than $z_F > 3$.

---

[1] There are, however, some notable exceptions. A classic cooling flow cluster A1795 is associated with the radio source 4C 26.42 but only has a spectral index $\alpha \approx 1$.

c) the sample

In order to look for distant clusters based on their expected steep-spectra, McHardy and Cooke (1989) selected a sample of radio sources from the Culgoora 3 low-frequency catalog (Slee 1977), and from the the 4C catalog in an area where the Abell (1958) catalog is not complete. The 4C sources were taken from BS. The Culgoora 3 catalog lists flux densities at 80 and 160 MHz for ~2000 radio sources in the declination range $-48^{o}<\delta<35^{o}$. They computed the two point spectral index for these sources and selected those with $\alpha>1.5$. This index is steeper than the value of 1.2 used by BS, and it is large enough to avoid contamination of the sample by sources whose apparently steep spectra are due to uncertainties in α. Sources known to be associated with objects other than clusters of galaxies, and sources at low galactic latitude were rejected. The remaining sample of ~125 sources were mapped with the *VLA*. The remainder of this dissertation will describe, for the most part, an instrument built to acquire deep optical images of a portion of these fields, and will present the preliminary results from these observations.

REFERENCES:

Abell, G.O. 1958, "The Distribution of Rich Clusters of Galaxies," *Ap.J. Supp.*, **3**, 211.

Abell, G.O., Corwin, H.G., and Olowin, R.P. 1989, "A Catalog of Rich Clusters of Galaxies," *Ap.J.Supp.*, **70**, 1. ACO

Baum, S., and Heckman, T. 1986, "The relationship of optical emission line gas and extended radio emission in the centers of cooling flow clusters," in *Radio Continuum Processes in Clusters of Galaxies*, ed. C. O'Dea and J. Uson (Green Bank: NRAO), p. 119.

Baldwin, J.E., and Scott, P.F. 1973, "Extragalactic Radio Sources with Steep, Low Frequency Spectra," *M.N.R.A.S.*, **165**, 259. BS

Burns, J. 1989, "The Radio Properties of cD galaxies in Abell Ckusters I. An X-ray Selected Sample," *Preprint*

Dressler, A. 1987, "Evolution of Cluster Galaxies Since z=1," in *Nearly Normal Galaxies: From the Planck Time to the Present*, ed. Faber (New York: Springer).

Eales, S.A. 1985, "CCD observations of a rich, distant cluster of galaxies (1046+35) containing a classical double radio source," *M.N.R.A.S.*, **214**, 27.

Gunn, J.E., Hoessel, J.G., and Oke, J.B. 1986, "A Systematic Survey for Distant Galaxy Clusters," *Ap.J.*, **306**, 37. GHO

Gunn, J.E. 1989, in *Clusters of Galaxies: STScI Workshop on Clusters of Galaxies.*

Gunn, J.E. 1987, "Current Instrumentation on Ground-Based Telescopes, in *Instrumentation for Cosmology*, ed. R.L. Davies (Tucson: NOAO), p.5.

Guthrie, B.N.G. 1977, "Dynamical Evolution in Clusters of Galaxies with Low-Frequency Radio Emission," *Astrophys. and Space Science*, **52**, 177.

Guthrie, B.N.G. 1976, "A Search for Steep Low-Frequency Radio Spectra Among Quasars and Clusters of Galaxies," *Astrophys. and Space Science*, **46**, 429.

Hintzen, P. and Scott, J. 1980, "Distorted Radio Sources in Abell 2255: Evidence of Intergalactic Gas 2.5 to 5 Mpc from the Cluster Center," *Ap.J.*, **239**, 765.

Kardashev, N.S. 1962, "Nonstationariness of Spectra of Young Sources of Nonthermal Radio Emission," *Soviet Astronomy*, **6**, 317.

Kron, R., Spinrad, H., and King, I. 1977, "Observations of a distant cluster of galaxies," *Ap.J.*, **217**, 951.

McHardy, I. 1974, "The Bautz-Morgan Classification of Clusters Containing Radio Galaxies," *M.N.R.A.S.*, **169**, 527.

McHardy, I. 1979, "4C Radio Sources in Clusters of Galaxies - III," *M.N.R.A.S.*, **188**, 495.

McHardy, I. 1978, "The Structure and Properties of 4C Radio Sources in Abell Clusters - II. The Declination Ranges 10 - 20^{o} and $>50^{o}$," *M.N.R.A.S.*, **185**, 185.

McHardy, I. 1978, "X-Ray Sources in Clusters of Galaxies," *M.N.R.A.S.*, **184**, 783.

Miley, G. 1971, *M.N.R.A.S.*, **152**, 477.

Miley, G. 1980, "The structure of Extended Extragalactic Radio Sources," *Ann.Rev.Astron.Ap.*, **18**, 165.

Oke, J.B. 1987, "Spectroscopic Surveys of High-z Galaxies," in *High Redshift and Primeval Galaxies* (Paris: Editions Frontieres), 19.

Pacholczyk, A.G. 1970, *Radio Astrophysics*, (San Francisco: W.H. Freeman).

Roland, J., Veron, P., Pauliny-Toth, I., Preuss, E., and Witzel, A. 1976, "Radio Sources and Clusters of Galaxies," *Astron.Ap.*, **50**, 165.

Sarazin, C.L. 1986, "X-ray Emission from Clusters of Galaxies," *Rev. Modern Physics*, **58**,1.

Slee, O.B. 1977, *Aust.J.Phys.Astrophys.Supp.*, **43**.

Slingo, A. 1974a, "Observations of Ten Extragalactic Radio Sources with Very Steep Spectra," *M.N.R.A.S.*, **166**, 101.

Slingo, A. 1974b, "The Structure and Origin of Radio Sources with Very Steep Spectra," *M.N.R.A.S.*, **168**, 307.

van der Laan, H. and Perola, G. 1969, "Aspects of Radio Galaxy Evolution," *Astron.Ap.*, **3**, 468.

Weedman, D.W., and Huenemoerder, D. 1985, "IUE Observations of a Starburst Disk and the Detectability of High Redshift Galaxies," *Ap.J.*, **291**, 72.

Weedman, D.W., and Williams, K.L. 1987, "Isophotal Diameters of Galaxies at High Redshifts," *Ap.J.*, **318**, 585.

Williams, Kenderdine, and Baldwin 1966, *M.N.R.A.S.*, **70**, 53.

Chapter 4

Large-Format CCD Instrument Design

CCDs are almost perfect optical detectors (see Mackay 1986 or Janesick 1987 for a review). The best of these devices have peak quantum efficiencies greater than 80 percent, linear response over a dynamic range of five orders of magnitude, and readout noise approaching the level at which it will be possible to detect single photons. CCDs are geometrically and photometrically stable, allowing precise and repeatable astrometric and photometric measurements. A major limitation of these devices so far is their small size; the largest CCD in regular use today is the TI 800 × 800 3PCCD developed for Space Telescope, which is less than 0.5 inches (12 mm) on a side (15 μm pixels). The need for a larger device is obvious. In 1985, Tektronix announced plans to build a scientific quality CCD that is 2048 × 2048 pixels; this image sensor is a single, wafer-scale device which is two inches (50 mm) on a side (27 μm pixels) (Blouke *et al.* 1987); however, this device has yet to be routinely used for astronomical research.

As an alternative to a single, wafer-scale device, it is possible to image an astronomical scene onto a number of smaller CCDs. The CCDs can be *optically abutted* using a scheme such as Gunn's *4-Shooter* (Gunn *et al.* 1987) – a mirrored pyramid quadrisects the cassegrain beam of the Hale 5m telescope, and each of the four portions of the beam is reimaged onto one of four separate TI 800 × 800 CCDs – or the CCDs can be *physically abutted* and the resulting mosaic can be used like a single large-format device. The second scheme is potentially simpler than the first, but it requires that the CCDs be manufactured so that they are edge abuttable; *i.e.*, that they have minimal gate and surface structure on at least two of the four sides of the device, so that appreciable gaps do not appear when the devices are mounted next to each other. Two abuttable CCD designs were available from two different suppliers (Texas Instruments and MIT Lincoln Laboratory) at the time the design of the instrument for this thesis research was begun. The remainder of this chapter is devoted to a detailed description of an instrument which operate mosaics of either the TI or Lincoln Laboratory abuttable sensors.

The properties of the CCD types used in this instrument are described in Section 4.1. Section 4.2 presents the mechanical and electronic details of the CCD system designed and constructed to operate four TI 850 × 750 virtual-phase chips. This section also describes the large-format CCD coaxial dewar built to hold either of the two focal-plane arrangements used in this instrument. The camera system designed to operate an 840 × 840 mosaic of four 420 × 420 Lincoln Laboratory chips is described in Section 4.3.

4.1 Instrument CCDs

The CCDs used in this instrument are prototypes primarily developed as x-ray imaging spectrometers for instruments on two x-ray satellite missions: the *AXAF CCD Imaging Spectrometer* (*ACIS*) (Nousek *et al.* 1987) for the NASA *Advanced X-ray Astrophysics Facility* (*AXAF*), and the Dual CCD Imaging Spectrometer (*DUCIS*) for the Japanese ASTRO-D satellite. Because of the requirement that x-ray CCDs have extremely good charge transfer properties and low readout noise, these devices are also well suited to optical applications.

Figure 4.1 shows three of the CCD types available in our lab for use in this instrument. The small device at the left is a Texas Instruments (TI) 4849 virtual-phase sensor which has 548 × 390 pixels; each pixel is 22.3 μm square. This device is described in detail in Luppino *et al.* (1987). The best TI-4849 CCDs have readout noise less than 10 electrons and excellent charge-transfer efficiency (> 0.99999). Before construction of the large-format CCD instrument began, a prototype CCD camera was built that incorporated one of the best of our TI-4849 CCDs. This instrument is now in regular use at the MDM Observatory, and is described in detail by Luppino (1989).

The device in the center of Figure 4.1 is a TI 850 × 750 virtual-phase CCD. This sensor was designed as a scaled-up version of the TI-4849 CCD, and was developed primarily for the ACIS experiment. The TI 850 × 750 chip has 22.3 μm square pixels, and is designed to be edge abuttable on three sides with a gap between active areas of less than 18 pixels. At the present time, however, the prototype devices being used for this instrument are not edge abuttable since they have been permanently mounted in packages. The best of these devices have readout noise of ~18 electrons rms and poor to moderate low-level charge-transfer efficiency (~0.9999)[1]. The performance of these devices proved to be unsatisfactory for x-ray imaging-spectroscopy. Nevertheless, for astronomical, broad-band, optical imaging, where neither readout noise nor low-level charge-transfer efficiency is particularly important[2], these CCDs can provide useful data. Their main advantage is a large full-well capacity in excess of 250,000 electrons, linearity over most of this large dynamic range, and, of course, their large format.

---

[1] Charge-transfer-efficiency (*CTE*) is a measure of the percentage of charge that is successfully clocked from one pixel to the next when the device is being read out. A *CTE* of 0.9999 means 99.99% of the charge is transferred, or, conversely, 0.01% gets left behind each time the a charge packet is transferred through a pixel. For example, if you start with a 10,000 electron packet at the far corner of a 1000x1000 CCD, this packet will go through 2000 transfers and will lose ~1800 electrons before being reaching the on-chip amplifier. *CTE* is discussed further in §5.1.

[2] For broad-band, imaging observations on 1m class or larger telescopes, one becomes "sky dominated" in a relatively short period of time (a few minutes). This means the shot noise in the signal produced by the bright night sky exceeds the readout noise. The night sky background also provides an effective bias or "fat zero" charge level which helps to remedy any low-level charge transfer problems.

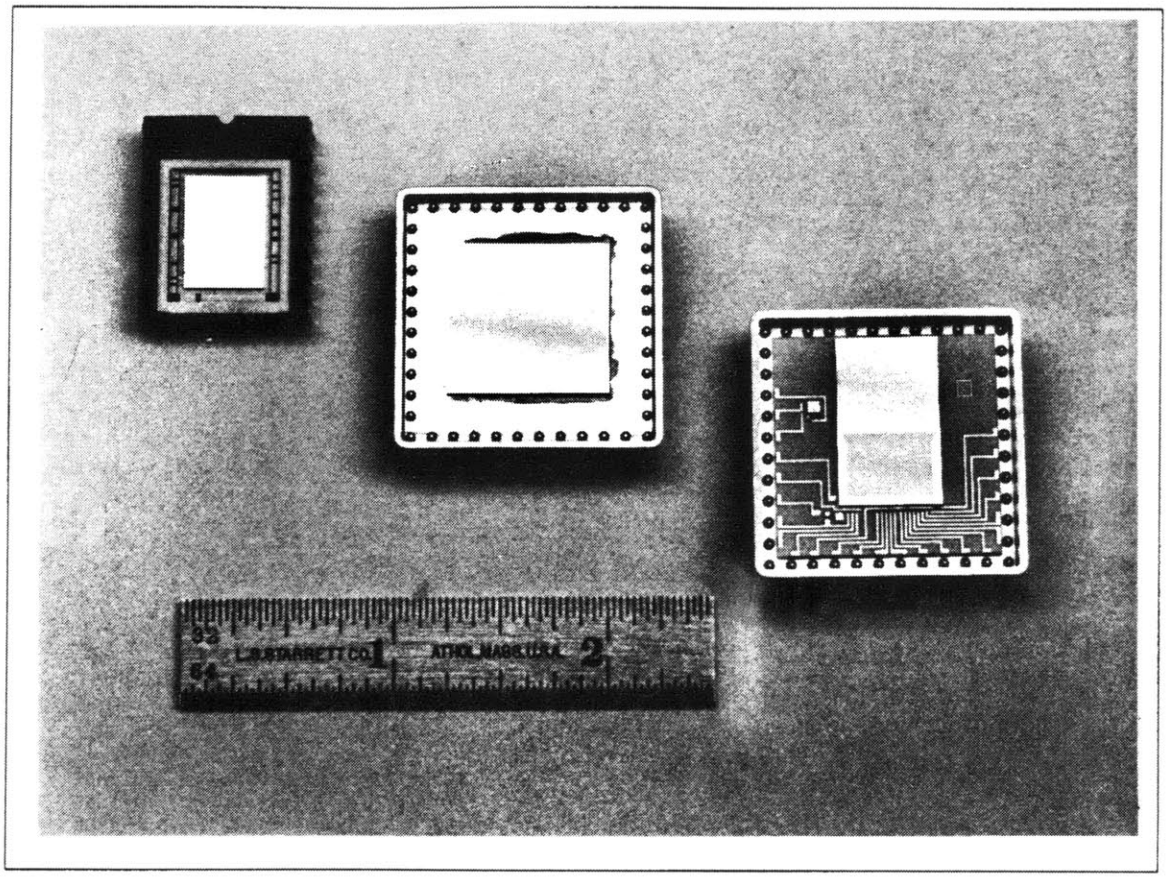

FIGURE 4.1 Instrument CCDs - TI 4849 (584 × 390), TI 850 × 750, and LL-CCID7 (420 × 840 framestore).

The device shown at the far right of Figure 4.1 is an MIT-Lincoln Laboratory CCID-7. This sensor is a framestore CCD[1] with an imaging area of 420 × 420 (27 μm square) pixels and a storage area of 420 × 420 smaller, rectangular pixels. Note on the photograph how the two regions are adjoined (also see Figure 4.13 for a close-up view). The device was fabricated in this manner to allow the multiphase clock busses to be run up the side of the device to the imaging area, and still enable the device to be three-side abuttable with very small gaps of only 100 to 200 μm (~4-6 pixels). The sensor shown forms one-fourth of the LL 840 × 840 CCD mosaic described in Section 4.3. A similar mosaic using non-framestore devices is described in Burke *et al.* (1987). The CCID-7 CCD is fabricated with 3-phase polysilicon gates and the imager shown in the photo is frontside-illuminated (thinned backside-iluminated versions of these devices are also being developed by the Lincoln Laboratory group; see Chapter 8). The CCID-7 is actually mounted on a ceramic substrate which contains gold traces that bring out the CCD pads to the kovar package pins. This ceramic also holds a small U309 JFET preamplifier visible at the lower left corner of the device, and a MAT-02 transistor used as a temperature sensor mounted at the upper left center of the package. These devices made by Lincoln Laboratory define the state-of-the-art for low-noise CCDs. These sensors have been operated in our lab and elsewhere (Janesick *et al.* 1988) at noise levels less than 2 electrons rms and with low-level charge-transfer efficiency in excess of 0.999999.

4.2 CCD Camera System Design for Four TI 850 × 750 CCDs

a) CCD Focal Plane

The ideal focal plane configuration would be obtained if the devices could be abutted with minimal gaps between active areas. Unfortunately, the prototype devices cannot be non-destructively removed from their packages. A focal plane arrangement was therefore designed that abutted the packages rather than the devices. The layout of the four CCDs is shown in Figure 4.2. The active area of each CCD is 0.75 in × 0.66 in (19 mm × 17 mm), while the package dimensions are 1.25 in × 1.25 in (31.8 mm × 31.8 mm). The device centers are separated by 1.25 inches. As can be seen in Figure 4.2, the vertical gap between the device active areas is 0.59 inches (15.0 mm) and the horizontal gap is 0.50 inches (12.7 mm): in both cases these gaps are smaller than the width or length of the CCDs. Consequently, one can obtain a contiguous image of an area of the sky

[1] All of the above CCDs have "frame transfer" architecture where charge is clocked down vertical "columns" one "row" at a time into a serial shift register. For each row, the charge in the serial register is clocked pixel-by-pixel onto the output amplifer. A "framestore" CCD is a type of frame transfer CCD which is divided into two independently controlled vertical halves, one of which is blocked by an optically opaque cover: the portion not covered is called the imaging area and the covered portion is called the storage area. This type of device can be used without a shutter (it was originally invented for TV applications) since the accumulated charge in the imaging area can be transferred quickly (~ 1 msec) to the storage area. Then, while the charge is being read out of the storage area row-by-row and pixel-by-pixel (the total readout time often exceeds a few seconds) a new image can be acquired in the imaging area. If shutterless operation is not required and larger detector format is important, the storage area can also be used for imaging if the cover is eliminated and the storage area pixels are the sime size as the imaging area pixels.

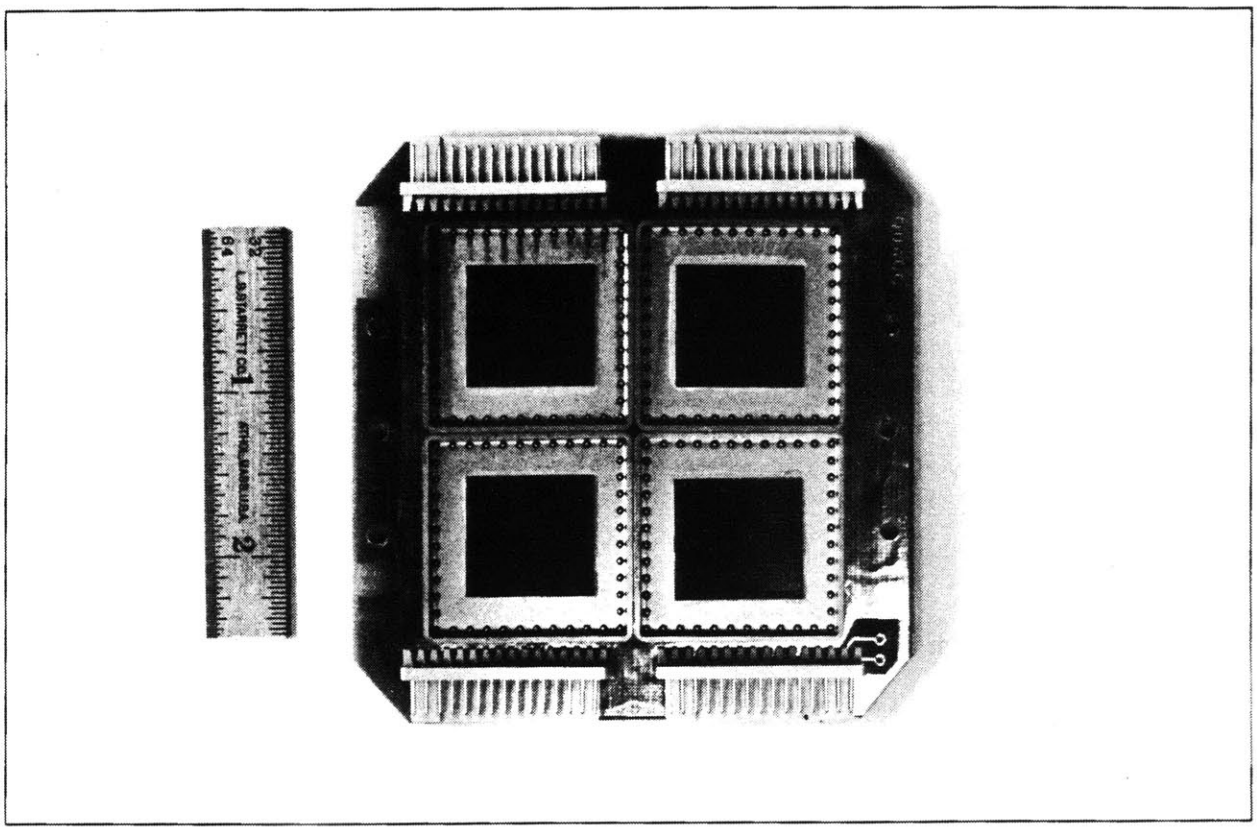

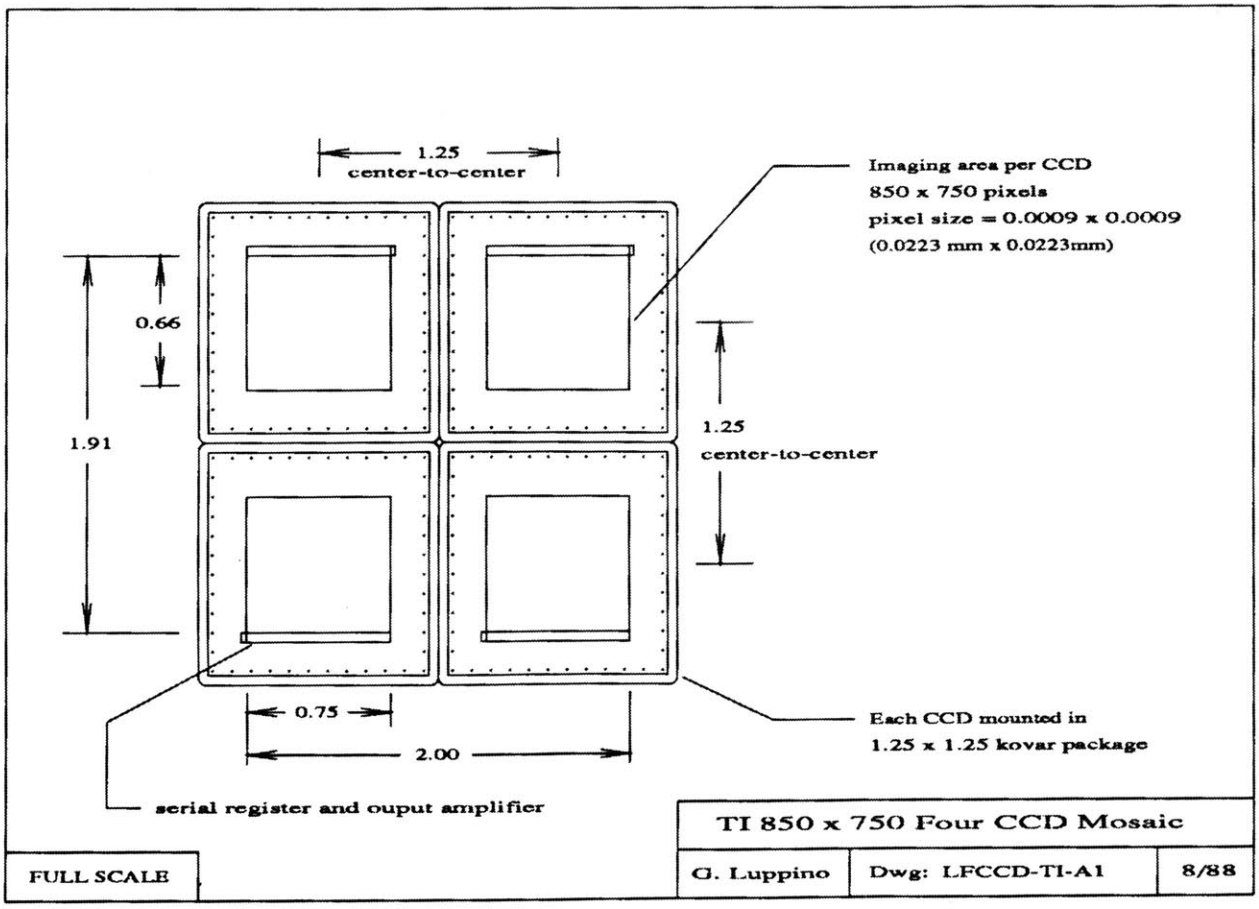

FIGURE 4.2 Drawing and photograph showing the focal-plane layout of the TI 850 x 750 four CCD mosaic

by combining four separate exposures with the telescope moved between the exposures to fill the gaps between the CCDs. The four detectors are mounted on a custom printed circuit board that brings in the electrical signals through four connectors shown in Figure 4.2 (the actual cable harnesses connected to the PC board are shown in the interior dewar photograph in Figure 4.4). Holes are cut into the PC board behind the CCD packages to allow an aluminum cold finger to make contact with the CCDs. Good thermal contact is ensured by the use of a thin indium gasket. One drawback of this design is the difficulty one has in inserting and removing CCDs from the sockets on the PC board. A zero-insertion-force (ZIF) socket could not be obtained for this application since the CCD mosaic pins were not on 0.100" standard centers. When the CCDs are installed in the board, a black-anodized, aluminum clamping cover is mounted onto the focal-plane assembly to ensure that the CCDs are properly aligned and in good thermal contact with the cold finger. This cover also reduces stray reflections off of the silver-colored, kovar CCD packages.

b) CCD Dewar Design

CCDs must be cooled to temperatures ranging from -70^{o}C to -125^{o}C to reduce (or eliminate) the amount of thermally generated charge (dark current) that accumulates in the pixel potential wells during the integration of an astronomical image. There are essentially four currently available technologies for cooling solid-state detectors to these temperatures: closed cycle refrigeration, Joule-Thomsen refrigeration, thermoelectric (Peltier) coolers, and liquid nitrogen (LN_2). Closed-cycle refrigerators are bulky, and require cooling lines to carry the refrigerant to and from the CCD camera head; they are therefore impractical for an instrument that is mounted on a moving telescope. Joule-Thomsen refrigerators (see Lauer *et al.* 1985 for a CCD camera design that uses these coolers) have limited heat-pumping capabilities and a host of other problems (e.g., if the narrow channels in these refrigerators clog, they can explode, destroying the CCD detector as well as the refrigerator). Thermoelectric (Peltier) coolers (hereafter TE-coolers) also have limited heat-pumping capability, but scientific cameras incorporating TE-coolers have been successfully used in applications where where exposure times are relatively short (a few seconds) such as x-ray detection (Luppino *et al.* 1987) or in an instrument such as the Explosive Transient Camera (Vanderspek 1985). It is very difficult, if not impossible, to build a TE-cooled camera that can cool a detector as large as the CCD mosaics described here to temperatures lower than -100^{o}C. Liquid nitrogen cooling is the only remaining alternative. A number of astronomical CCD dewar designs are described in the literature (Abraham and Robinson 1986; Gunn *et al.* 1987).

The first attempt at a dewar design for this instrument followed the design in Luppino (1989) for the simple side-mount dewar used in the BRICC for the TI-4849 CCD (see Figure 4.3). This simple dewar is similar in design to a commercial unit supplied by Dr. Frank Melsheimer of DFM Engineering. The design is an inversion of the traditional astronomical dewar, and is very easy to fabricate and use. Instead of mounting the cryogen vessel inside the vacuum container, a portion of the vacuum chamber is immersed in a vessel of LN_2. In this case, the immersed part is a thin-wall stainless-steel tube brazed onto a copper rod. The copper rod is

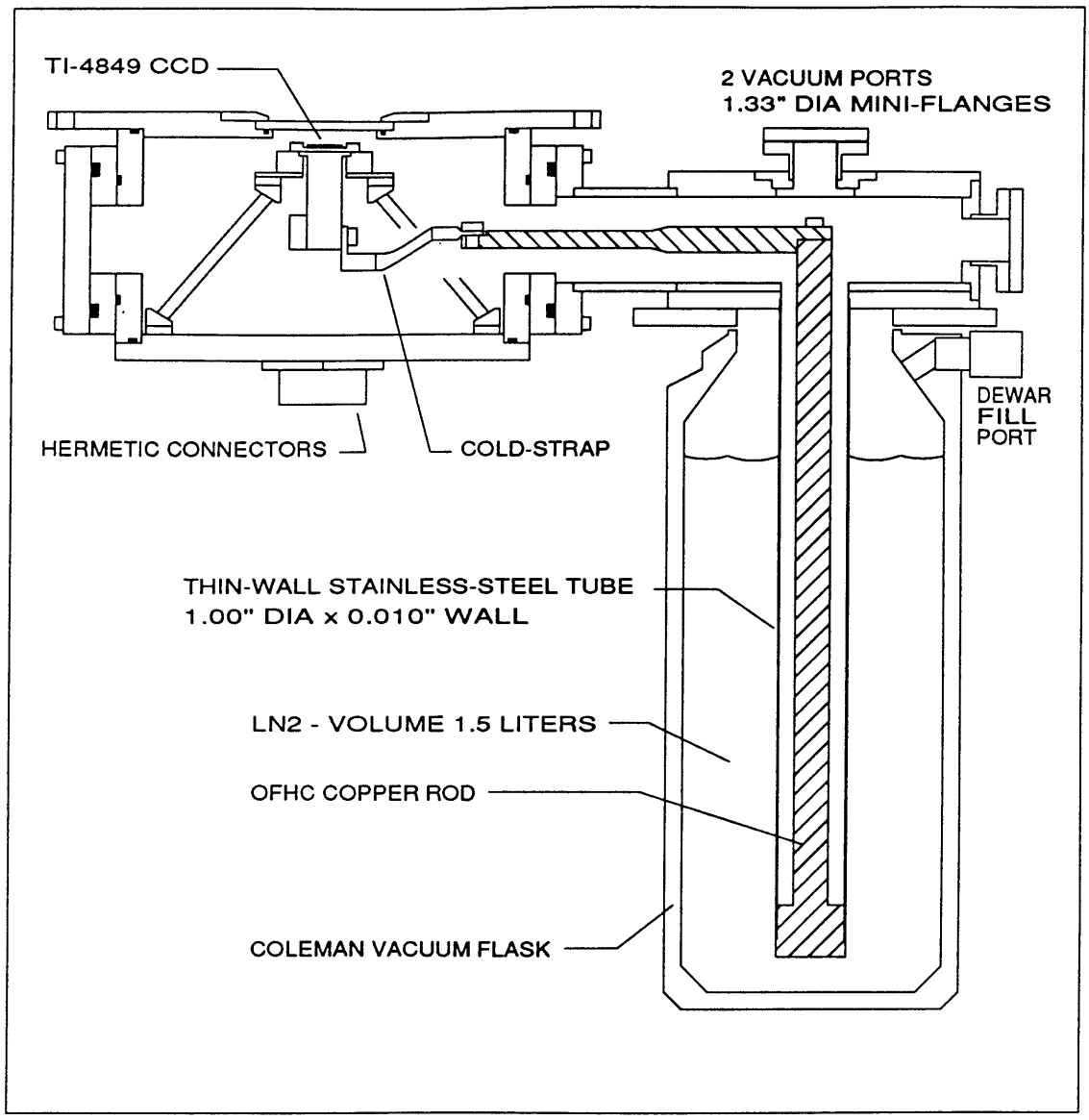

FIGURE 4.3 Assembly drawing of the side-mount dewar attached to the TI-4849 CCD camera head

thermally connected to the CCD through the cold-finger and a flexible copper-braid strap as shown in Figure 4.3. The actual LN_2 container is an inexpensive (~$40) Coleman stainless-steel flask. It was slightly modified to allow it to be filled and mounted to the camera head. The vacuum ports are industry-standard, stainless-steel, knife-edge flanges that utilize copper or viton gaskets. Two of these flanges are attached to the camera head: the dewar mounts on one, the other is blanked off. A high-vacuum valve and Granville-Phillips convectron vacuum gauge are attached to the a smaller knife-edge mini-flange on the dewar. Molecular sieve (zeolite) fills the lower section of the thin-wall tube structure that is dunked into the LN_2. This cryosorb material keeps the camera evacuated at a pressure less than 10^{-5} Torr as long as cryogen remains in the dewar. The simplicity and reliability of this dewar design makes it an attractive choice for many instrument applications. However, this design cannot be used in a look-down position (such as prime focus) without cumbersome modifications. In principle, the dewar could be rotated on its mounting flange, but then it would probably interfere with the CCD camera mounting fixtures and other apparatus typically located at prime focus. We have built a number of these dewars for our laboratory applications, and for dedicated instruments such as the BRICC. We decided, however, to make the large-format camera as versatile as possible to permit its possible use on other telescopes where it could be used at prime focus. We therefore designed and built the large-format coaxial dewar described below.

An assembly drawing for the large-format CCD coaxial dewar is shown in Figure 4.4. Some parts of this design are based on our TE-cooled camera designs we have used for our x-ray CCDs, while other parts are based on good ideas borrowed from other dewar designs. The dewar is 8.0 inches in diameter and ~18 inches long from the front plate surface to the LN_2 fill and vent port. Light enters the dewar through a 4.0 inch diameter quartz window mounted in the front plate. The surface of the CCD is 0.75 inches behind the outer surface of the front plate; this places the detector only 0.20 inches behind the back of the window. The CCD focal-plane and cold finger are mounted on a stiff spider made from four, low thermal-conductivity, thin-wall stainless-steel tubes (0.16 inches diameter by 0.005 inch wall thickness). These tubes are attached to the cold finger and the camera-head back plate by specially machined delrin feet that clamp firmly onto the tubes when tightened, but allow a small amount of adjustability when the tension screw is released. The CCD focal plane is free from flexure induced by the motion or thermal expansion of the dewar cryogen can. A harness made of constantan and copper wires connects the CCD focal plane to the two hermetic connectors mounted on the sidewalls of the camera-head portion of the dewar. Constantan wire (30 gauge) is used for all signal wires, since it has much higher thermal resistivity than copper, while maintaining reasonable electrical conductivity. All ground wires are 28 gauge copper to avoid any ground loops. A total of 30 constantan and 8 grounds are needed for the TI four CCD mosaic focal plane (this number is increased significantly for a multiphase CCD compared to a virtual-phase CCD - the LL 840 × 840 CCD needs 66 constantan wires and 16 grounds unless some clock sharing is done - see Section 4.3). There is no active circuitry inside the dewar. Our experience with all of our CCDs to date has shown us that it is unnecessary to mount electronics where they cannot be easily repaired or replaced. The outgassing of electronic components inside the vacuum is also a concern. Connections to the

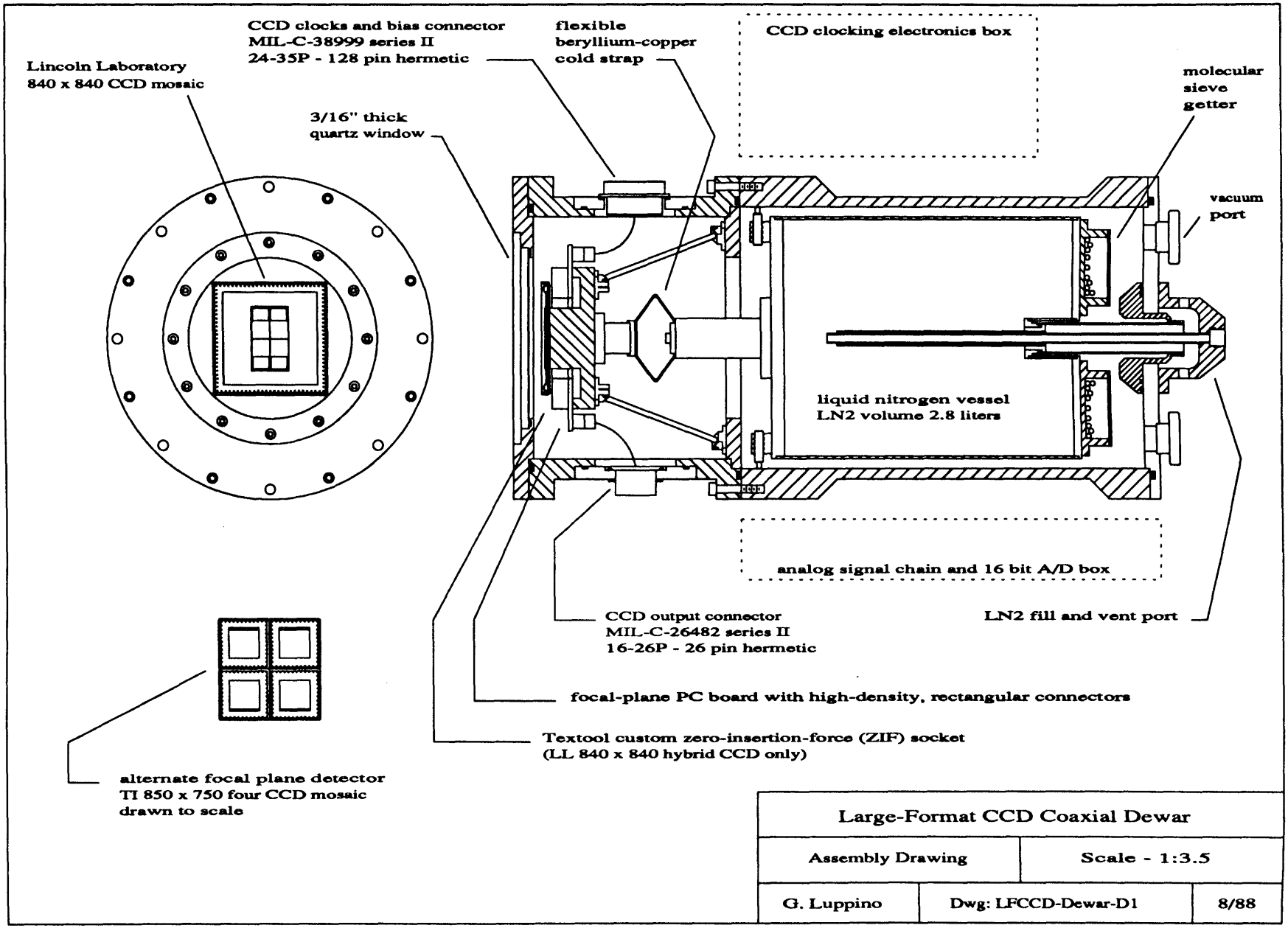

FIGURE 4.4 Assembly drawing of large-format CCD coaxial dewar

CCD output amplifiers (video output, drain bias voltage, and signal ground) of all four chips are made through a 26 pin hermetic connector (MIL-C-26482 series II 16-26P). All other electrical signals required in the dewar, such as the CCD clocks and biases and the temperature measurement and control circuitry, are made through a 128 pin hermetic connector (MIL-C-38999 Series II 24-35P).

The back half of the dewar cylinder contains the LN_2 cryogen can and the fill and vent tube support structure. The cryogen can has an OFHC copper front plate brazed onto the welded stainless steel sidewall and backplate structure. Three 0.5 inch diameter solid copper rods are attached to the copper front plate and span the full length of the inside of the cryogen can (these are not shown in the assembly drawing). This assures that the temperature of the front of the can does not vary with dewar orientation. The active volume of the dewar is ~2.8 liters of LN_2. The can is supported radially at the front by three teflon-tipped, high tension, ball plungers which act somewhat as shock absorbers and freely allow the cryogen can to thermally expand and contract both radially and axially. The can is supported in the back by a welded, thin-wall, stainless-steel tube structure that allows the liquid nitrogen to both fill and vent through the central coaxial tubes. An extension fill tube can be screwed into the tube support fixture to allow the full volume of the dewar to be used when it is mounted in a look-up position (such as Cassegrain focus): when this tube is removed, the full volume of the dewar can be used in a look-down position (such as prime focus). The entire can is nickel plated and highly polished. Additional radiation shielding is provided by a layer of aluminized mylar wrapped around the can and along the interior wall of the outer aluminum housing. A semicircular container mounted on the back plate of the cryogen can contains molecular-sieve getter material (zeolite) that keeps the dewar evacuated to a pressure less than 10^{-5} Torr as long as it is filled with LN_2. The cryogen can is thermally attached to the CCD cold finger by a flexible cold strap made of a berylium-copper leaf spring. One side of this strap is attached to a copper post screwed onto the cold surface of the cryogen can. The other side contains a copper recepticle that mates with the back of the CCD cold finger. An indium gasket ensures good thermal contact. The cross-section of the spring material is chosen so that the CCD equilibrium temperature (without external heat input) is just a few degrees below the desired operating temperature. A heater resistor mounted on the CCD cold finger is then used to regulate the CCD temperature to within 0.1°C of the optimal value. Note from Figure 4.4 that the front cylinder of the dewar containing the CCDs and the electrical connectors can be separated from the back cylinder containing the cryogen can by removing the eight #10-32 socket head screws that hold the two sections together. This allows one to easily work on either of the two halves, or to interchange front portions containing different CCD arrays. An internal view of the front of the dewar, showing the CCDs is shown in Figure 4.5. Figure 4.6 is a photograph of the disassembled dewar showing most of the major parts.

One major design requirement was that the dewar have a hold-time of at least 12 hours. Since liquid nitrogen has a heat of vaporization of 160 J/ml, and the dewar cryogen volume is 2.8 liters, the dewar has a hold-time coefficient of 124 watt-hours; *i.e.* the dewar will hold for 12.4 hours if the total heat load is 10 watts.. The

actual heat load can be calculated by considering all of the heat gained by conduction and radiation. Conduction losses are simple: for the most of the geometry in the dewar, the heat conduction Q_c (in watts) through a plane-parallel structure of cross-sectional area A, and length L, is given by

$$Q_c = \frac{kA}{L}(T_h - T_c) \tag{4.1}$$

where k is the thermal conduction coefficient (in W cm^{-1} K^{-1}), and T_h and T_c are the hot and cold sides respectively. Thermal conduction coefficients for various materials used in the dewar are listed in the following table.

Table 4.1
Thermal Properties of Dewar Materials

Material	k (W cm^{-1} K^{-1}) at 80K[a]	k (W cm^{-1} K^{-1}) at 150K	Total Emissivity ε [b]
Bright Aluminum	2.15	2.00	0.08
Bright Copper	4.57	4.50	0.15
304 Stainless-Steel	0.08	0.11	0.10
Teflon	0.0023		
Constantan	0.18	0.20	
Nickel			0.12

(a) Numbers taken from Cryogenics section of Donnely, R.J. 1981, in *Physics Vade Mecum*, ed. H.L. Anderson (New York: AIP), p. 131.
(b) Numbers taken from *CRC Handbook of Chemistry and Physics*

Conduction heat gain by residual gas present in the dewar is negligible for pressures less than 10^{-3} Torr. The approximate radiative warming of the dewar can be calculated assuming a simple geometry where the cold surfaces are parallel to their warm counterparts. In this case, a cold surface at temperature T_c, and of surface area A_c, and with emissivity ε_c, experiences a radiative heat load

$$Q_r = \sigma A_c \varepsilon_c \varepsilon_h (T_h^4 - T_c^4) \tag{4.2}$$

from the warm surface at temperature T_h, and with emissivity ε_h. The factor σ has a value of 5.67×10^{-12} W cm^{-2} K^{-4}. Values for the emissivities of the various materials used in the dewar are listed in Table 4.1. A worst case calculation gives a total radiative heat load on the dewar (without any radiation shielding) of less than 2 watts.

The dewar is evacuated through a high-vacuum valve located on one of the three vacuum ports welded onto the stainless-steel back plate. These ports are industry-standard, 1.33 inch diameter knife-edge, high vacuum mini-flanges. The pressure in the dewar is measured with a Granville-Phillips convectron gauge mounted on

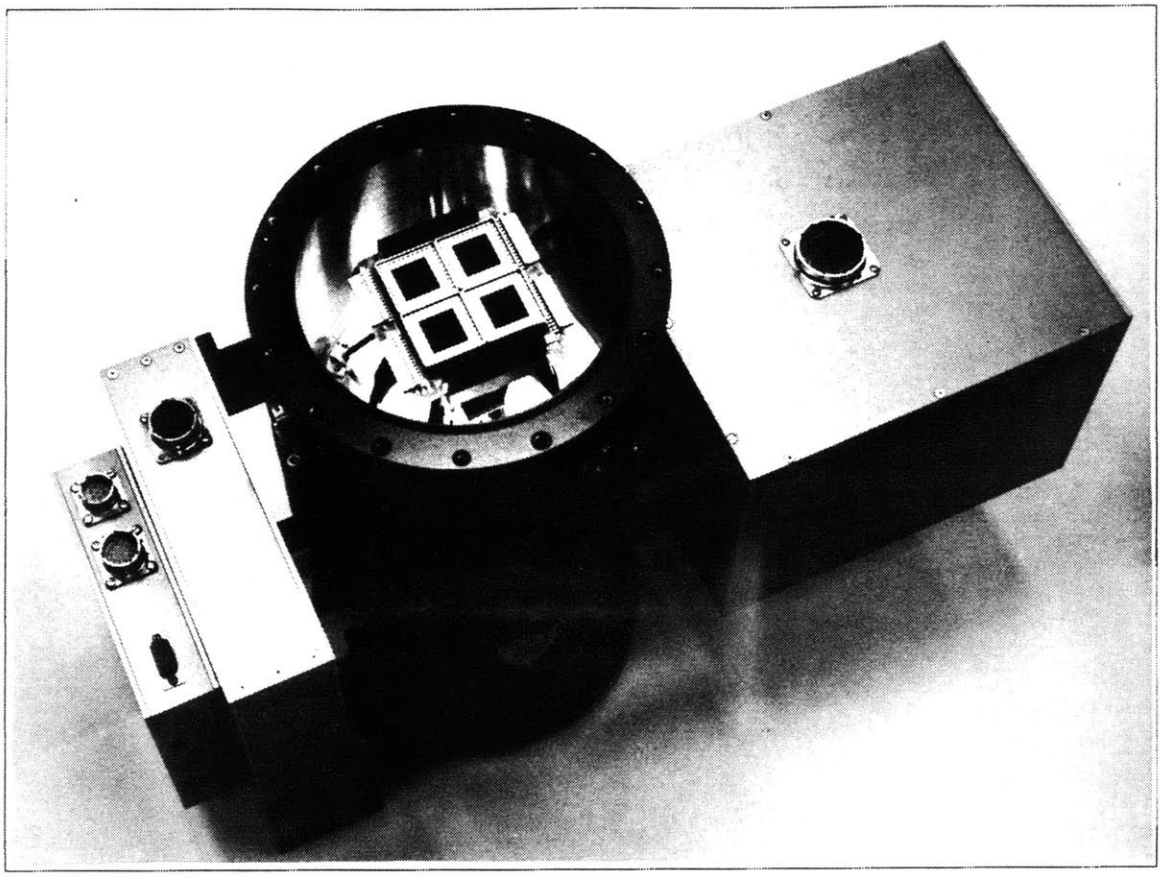

FIGURE 4.5 Internal view of dewar showing the TI 850 x 750 four CCD mosaic installed

FIGURE 4.6 Photograph of disassembled dewar showing details of the internal design.

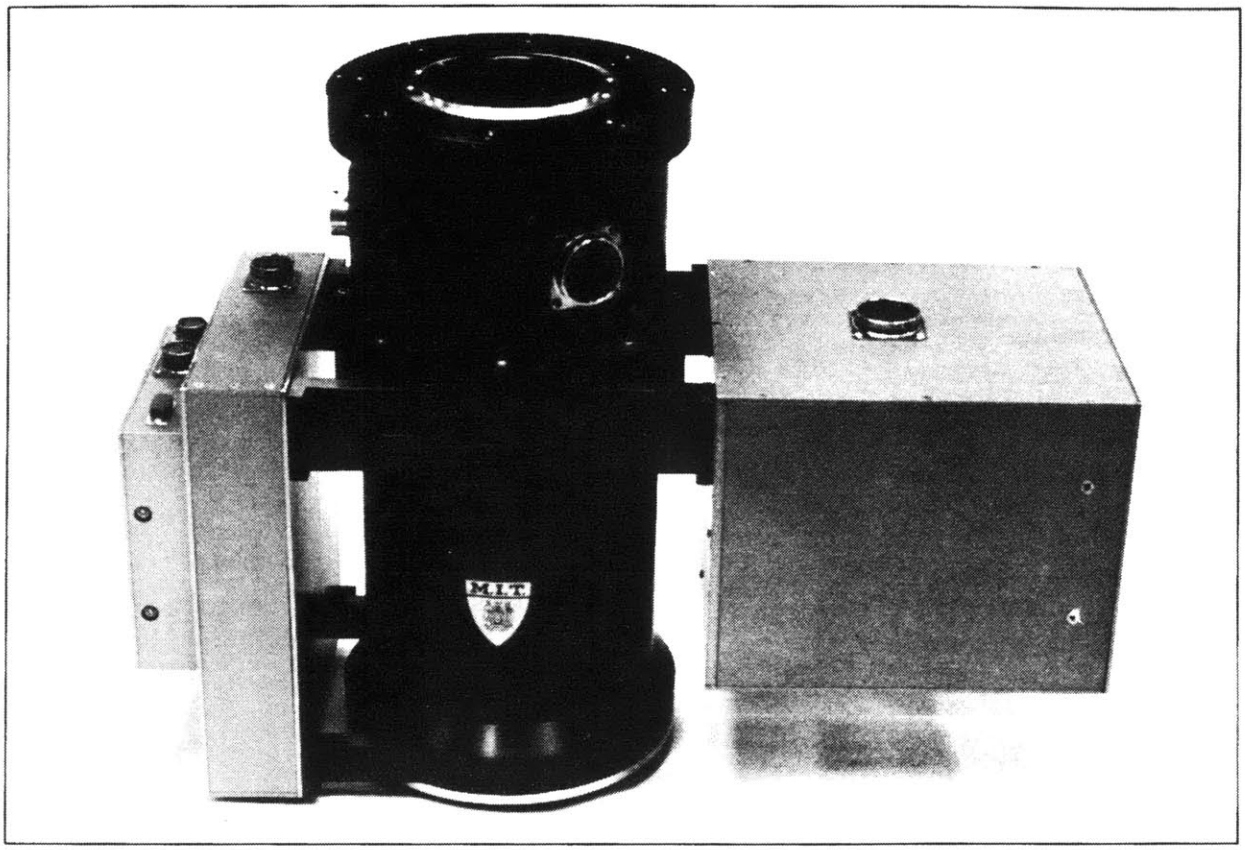

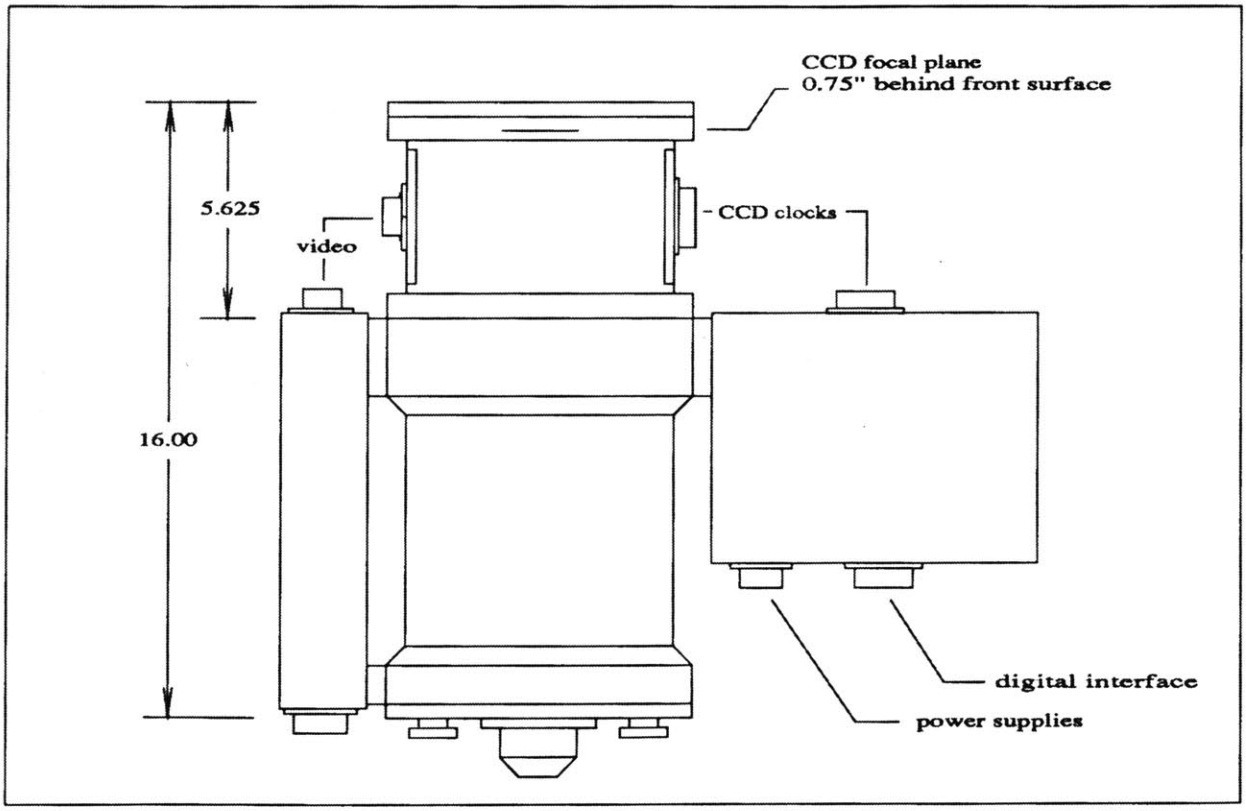

FIGURE 4.7 Drawing and photograph showing an external view of the dewar and electronics boxes.

one of the other two ports. Careful high-vacuum techniques were used throughout the construction of the dewar: all parts were cleaned, high-outgassing components were avoided, and vented screws were always used in blind holes inside the vacuum vessel. To preserve the clean environment of the CCD, only a turbomolecular pump or cryo-sorption pump are used to pump-out the dewar; this avoids the possibility of backstreaming-oil contamination from a mechanical or diffusion pump.

The front of the dewar can be attached to a telescope or instrument by eight 1/4 × 20 captive socket-head cap screws on a 7.50 inch diameter bolt circle. A drawing and photograph showing the an external view of the dewar is shown in Figure 4.7. Two electronics boxes are mounted on posts attached to the dewar cylinder. The smaller of the two boxes houses the preamplifier and analog signal chain. The larger box contains the tri-level clocking electronics to operate four virtual-phase CCDs, and the temperature control electronics. This larger box can be replaced by another (mechanically identical) box that will generate the multiphase clocks for the Lincoln-Laboratory CCDs - the analog signal chain box remains unchanged (see Section 4.3). Details of the CCD electronic design are described later in this section.

c) Virtual-phase CCD Electronics

This section describes the electronics controller that operates the virtual-phase TI mosaic. The controller is divided into two main portions: the off-telescope electronics and the on-telescope electronics. A microprocessor CPU with a FORTH-like operating system resident in ROM memory forms the heart of the off-telescope electronics. Other boards are connected to this microprocessor through a digital bus. These other boards consist of a programmable, digital clock sequencer (which generates the clock timing for the CCD), a digital interface board (which sends the digital timing and control signals from the off-telescope electronics to the on-telescope electronics), and other circuits such as a filter-wheel controller and a shutter timer. Commands are sent to the microprocessor from a SUN Microsystems workstation across an RS-232C serial line. The configuration of the off-telescope electronics is independent of the number or type of CCDs in the camera so long as only one CCD is read-out at a time. A block diagram showing the organization of the complete controller is shown in Figure 4.8. The on-telescope electronics is physically and schematically divided into two sections: the CCD clocking and temperature control electronics, and the analog signal chain electronics. These two sections live in separate, shielded aluminum boxes attached to the dewar body (see Figure 4.7). Three shielded cables run from the computer room (housing both the off-telescope electronics and the SUN workstation) to the on-telescope electronics: the first is the digital interface cable (50 wires), the second is the power supply cable (10 wires), and the third is the data cable (37 wires - sending the 16 bit A/D output to the SUN workstation). In the following discussion, the particular requirements for high-performance operation of the virtual-phase CCDs will be stressed.

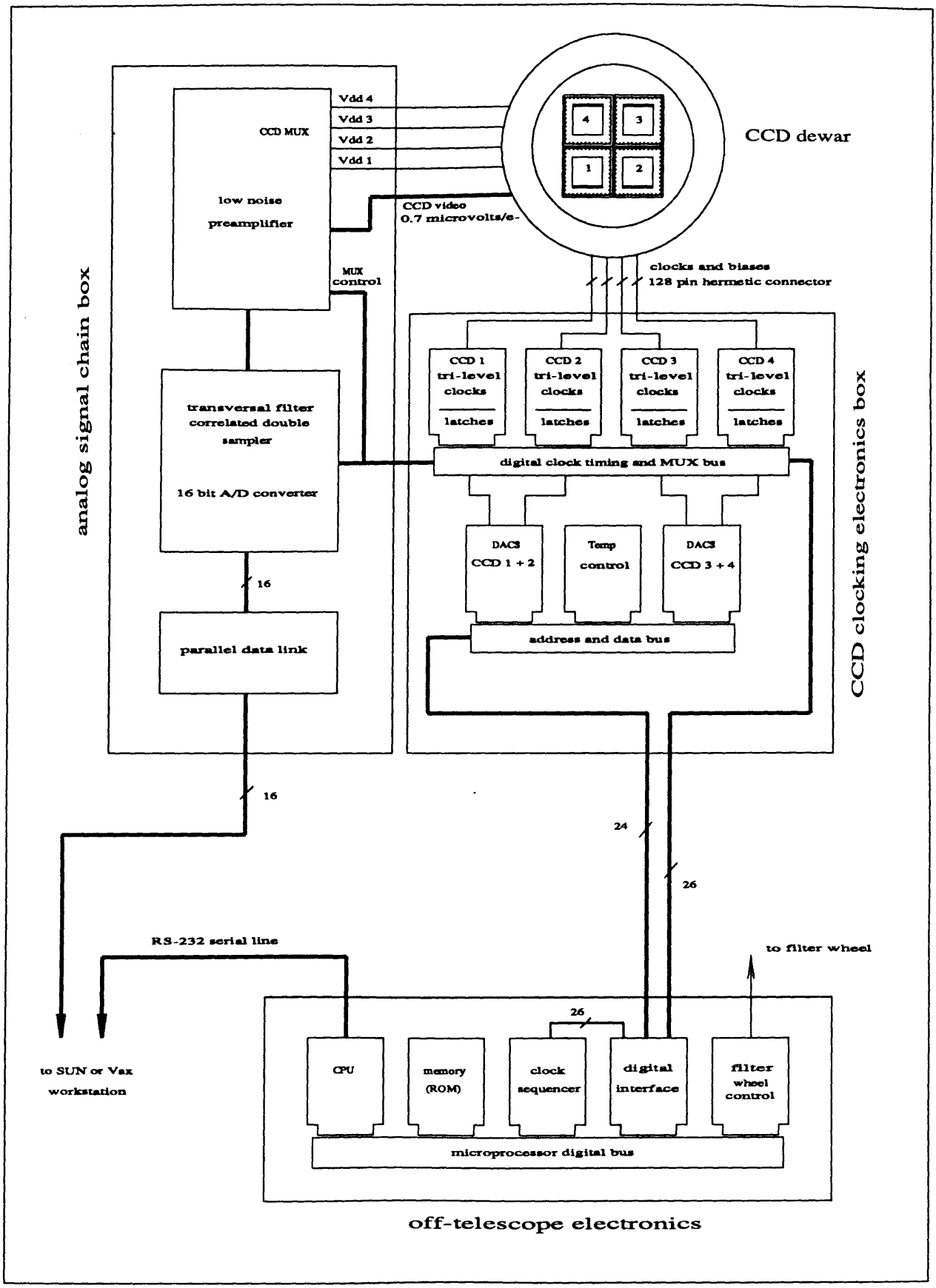

FIGURE 4.8 Electronic controller block diagram for the TI 850 × 750 mosaic

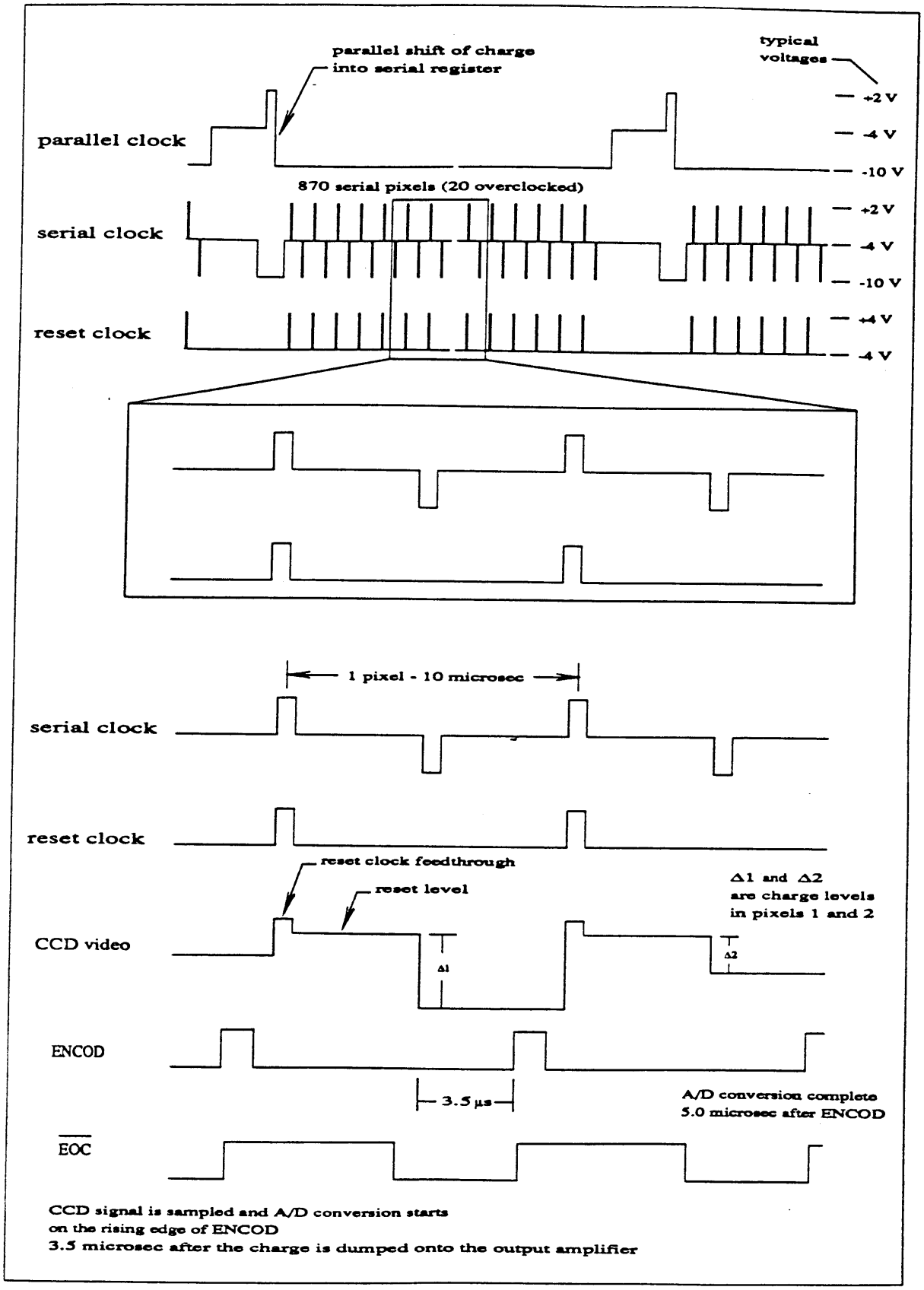

FIGURE 4.9 Virtual-phase CCD timing diagram for tri-level delta clocking.

(i) Tri-Level Clocks

Virtual-phase CCDs used for low-noise, scientific applications must be clocked using tri-level clocks in order to eliminate an extra noise source generated by high internal fields in the device and colloquially referred to as "spurious charge." Each CCD requires three clocks: two tri-level, and one bi-level. One tri-level clock is required for the imaging portion of the CCD, and the other is needed for the serial shift register. The third clock controls the reset gate for the on-chip output amplifier. Figure 4.9 is a timing diagram showing the operation of these clocks. A schematic of the design for a single tri-level clock is shown in Figure 4.10. The waveform is generated using two digital (0 to +5 V) timing signals generated by the programmable sequencer, and three bias voltages. Note that digital-to-analog converters (DACs) are used to set the actual clock voltages. A description of the circuit shown in Figure 4.10 follows. The filtered DAC inputs, Va and Vb, shown on the non-inverting inputs of the right-pointing, opamps, are amplified by the opamp stages and tied to the emitters of transistor pairs Q1 and Q2, and Q4 and Q5. The bases of these transistors are biased at 1.3V by the +12V input shorted across two diode drops to ground. Q1 and Q4 form shunts to ground while Q2 and Q5 provide a current to the HA-2525 summing and inverting amplifier. The baseline and offset level of this final stage is provided by the Vo DAC connected through a resistor network to the inverting input of the final stage. When ϕa is clocked high, Q1 is turned off and current flows through Q2 and into the summing amplifier. There is a voltage drop across Q2 which is exactly compensated for by Q3 and R5 which are connected in a feedback loop to the first opamp stage. When ϕa goes low, Q1 is turned on and shunts the contribution from the input opamps to ground. A cartoon showing how these two timing signals and three voltages combine to from the resulting tri-level clock is shown in the upper right of the schematic in Figure 4.10.

(ii) Transversal Filter Correlated-Double Sampler and 16 bit A/D Converter

The front-end of the A/D board consists of a tapped delay-line transversal filter configured for correlated double-sampling (CDS) of the amplified CCD signal. This circuit is a modification of the design by John Doty (Doty, Luppino, and Ricker 1987). The amplified CCD video is fed into a 20-tap analog delay line (see Figure 4.11). The signals that appear on the last 10 taps are weighted by the summing resistors and integrated by the passive summing network. This integrated signal is connected to the inverting input of the Harris HA-2525 differential amplifier. The signals on the first 10 taps of the delay line are similarly weighted and integrated and connected to the non-inverting input of the HA-2525. At the proper instant in time, when the edge of the serial clock that shifts the charge under the output amplifier is centered on the delay line, the right half of the delay line contains the amplifier reset voltage and left half contains the signal-charge voltage. The output of the differential amplifier reflects the integrated difference between the two voltages.

When all of the summing resistors are equal, the transversal filter is a matched filter for detecting the CCD signal against a background of white noise (Doty, Luppino, and Ricker 1987). The resistors can be changed,

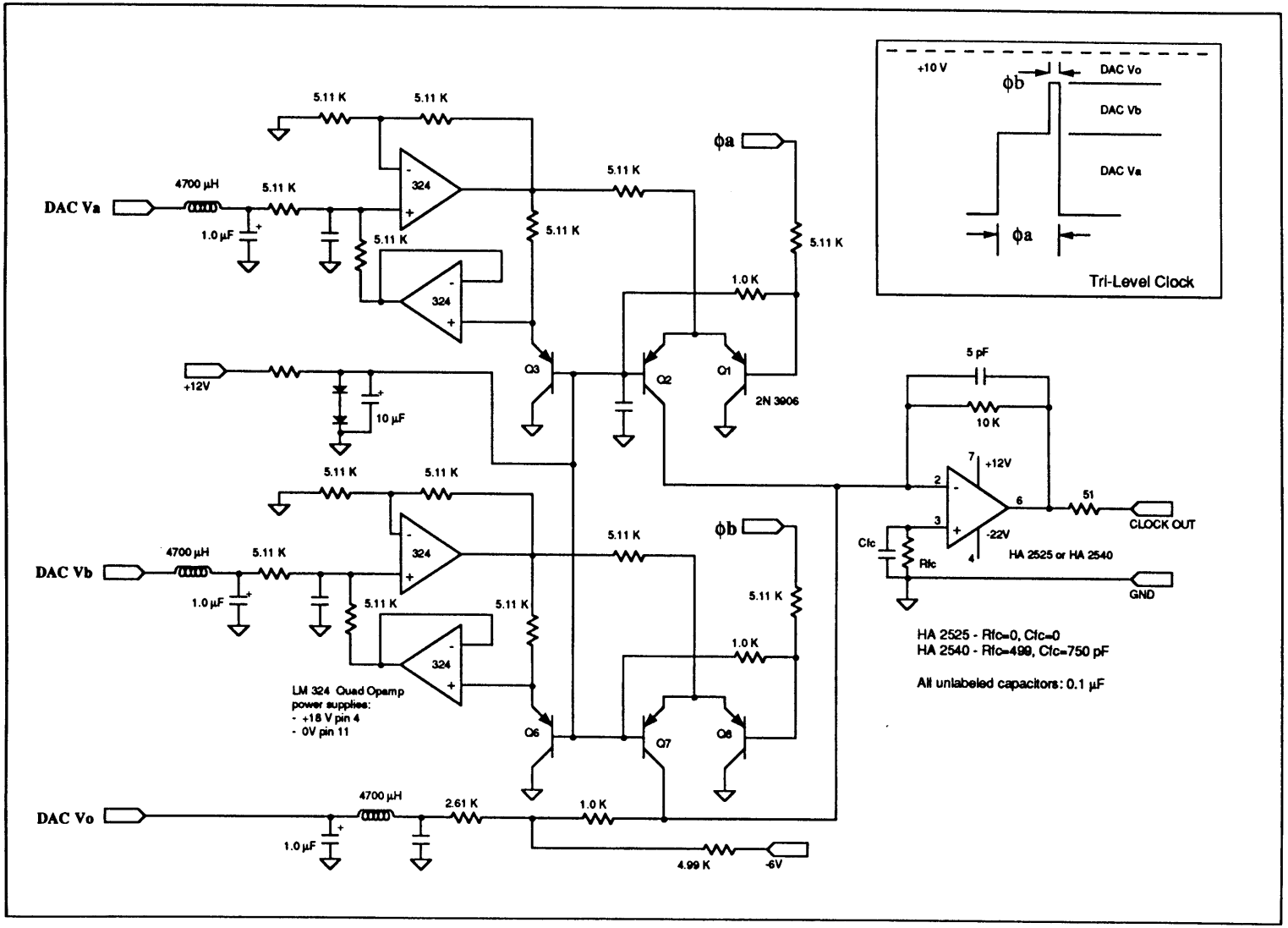

FIGURE 4.10 Schematic of the Tri-level clock driver circuit for clocking virtual-phase CCDs. The two digital clock signals, ϕ_a and ϕ_b, and three DAC voltages, V_a, V_b, and V_o, are used to generate each tri-level clock.

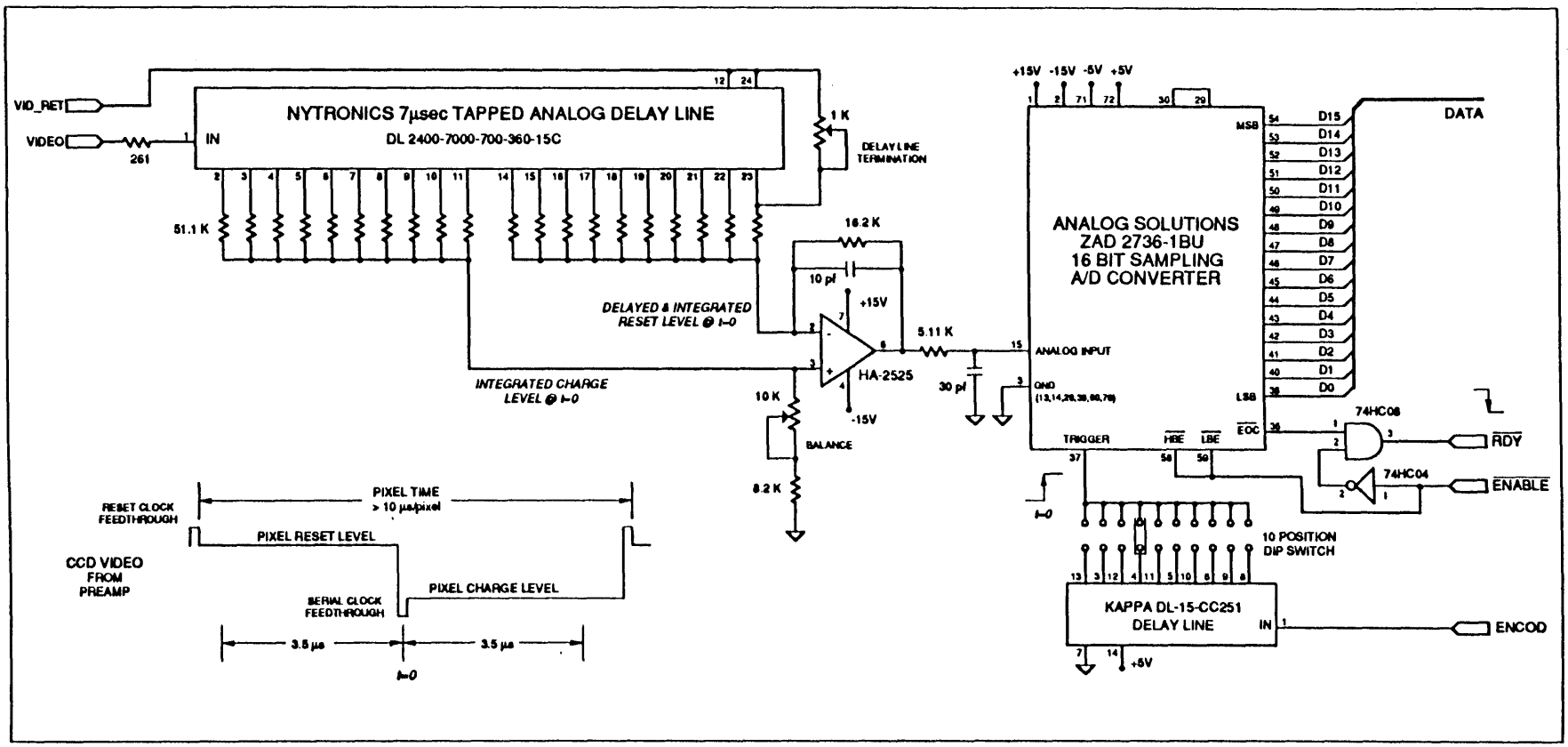

FIGURE 4.11 Schematic of the delay-line transversal filter correlated double sampler and 16 bit A/D converter circuit. The preamplified CCD video (the waveform for a typical pixel is shown at the lower left) enters the delay line at the left. At the proper instant in time (indicated by t=0 in this drawing), the sampling ADC converts the output of the transversal filter into a 16-bit quantity. The gain of the preamplifier and transversal filter are chosen so that the system gain constant is less than the system readnoise while preserving as much of the dynamic range of the CCD as possible. With the TI-4849 CCD, the dynamic range is limited by the ~65000 values of the ADC.

however, to synthesize a matched filter for a different noise spectrum (such as 1/f noise). The filter is the principal bandwidth limit in the system, and we currently use a 7 μsec delay line (Nytronics) which limits our pixel rate to ~ 140 kHz. In contrast to clamp-sample CDS circuits, and dual-slope integrator circuits, this circuit is extremely simple, draws little power, and uses only a few, inexpensive, easily-obtained components. Only one critical timing signal is required.

The output of the transversal filter is connected to the input of a hybrid 16-bit sampling A/D converter manufactured by Analog Solutions (ZAD 2736-1BU). The filter gain is set to match the 0V to +10V range of the A/D. The timing for this circuit is simple: the A/D merely requires a rising-edge trigger to start conversion. This trigger is generated by the programmable sequencer. Since the sequencer has a time resolution of 250 ns, a switch-selectable, 10-tap digital delay line is used to allow 25 ns precision in the placement of the trigger edge. This way the A/D conversion can be initiated at the proper instant when the delayed, integrated reset signal and the integrated charge level are at the proper location in the delay line. The digital delay line allows compensation for signal propagation delays in the signal chain, but, we have found that the A/D trigger can vary by as much as ± 100 ns from the optimal location with no detectable deterioration of the system signal-to-noise ratio.

4.3 CCD Camera System Design for the MIT-Lincoln Laboratory 840 × 840 Hybrid CCD

a) CCD Focal Plane

The Lincoln-Laboratories 840 × 840 CCD mosaic is built using four of the 840 × 420 CCID-7 framestore CCDs developed by Dr. Barry Burke and his co-workers in Group 87 at MIT Lincoln-Laboratory. The CCID-7 is described in Section 4.1. These CCDs have an active area made up of 420 × 420, 27 μm square pixels: the total size of the quad mosaic is therefore 0.89 in. × 0.89 in. (22.7mm × 22.7mm). Figure 4.1 shows one of the CCID-7 devices, while Figures 4.12 and 4.13 show a drawing and photograph of the larger-format, hybrid sensor. These figures illustrate a number of features of the Lincoln-Laboratory design: each hybrid CCD is mounted on a ceramic substrate containing the gold traces that electrically connect the CCD pads to the kovar package pins. A temperature sensor (MAT-02 transistor), four separate JFET preamplifiers (U-309), and four separate load resistors (passive loads for the on-chip MOSFETs that form the first stage of the dual source follower output amplifier) are also mounted onto this substrate. The ceramic substrate is epoxied into a 104 pin, 2.8 inch square kovar package manufactured by Airpax.

The principal requirements for the construction of the CCD mosaic are as follows: the gaps between the devices must be an integral number of the 27 μm pixel spacing, and must be aligned to within a fraction of a pixel so that all of the pixels of the hybrid sensor occupy a common grid. These gaps should be as small as possible (subject to the above constraint), and the resulting mosaic must be flat to within a few microns. The

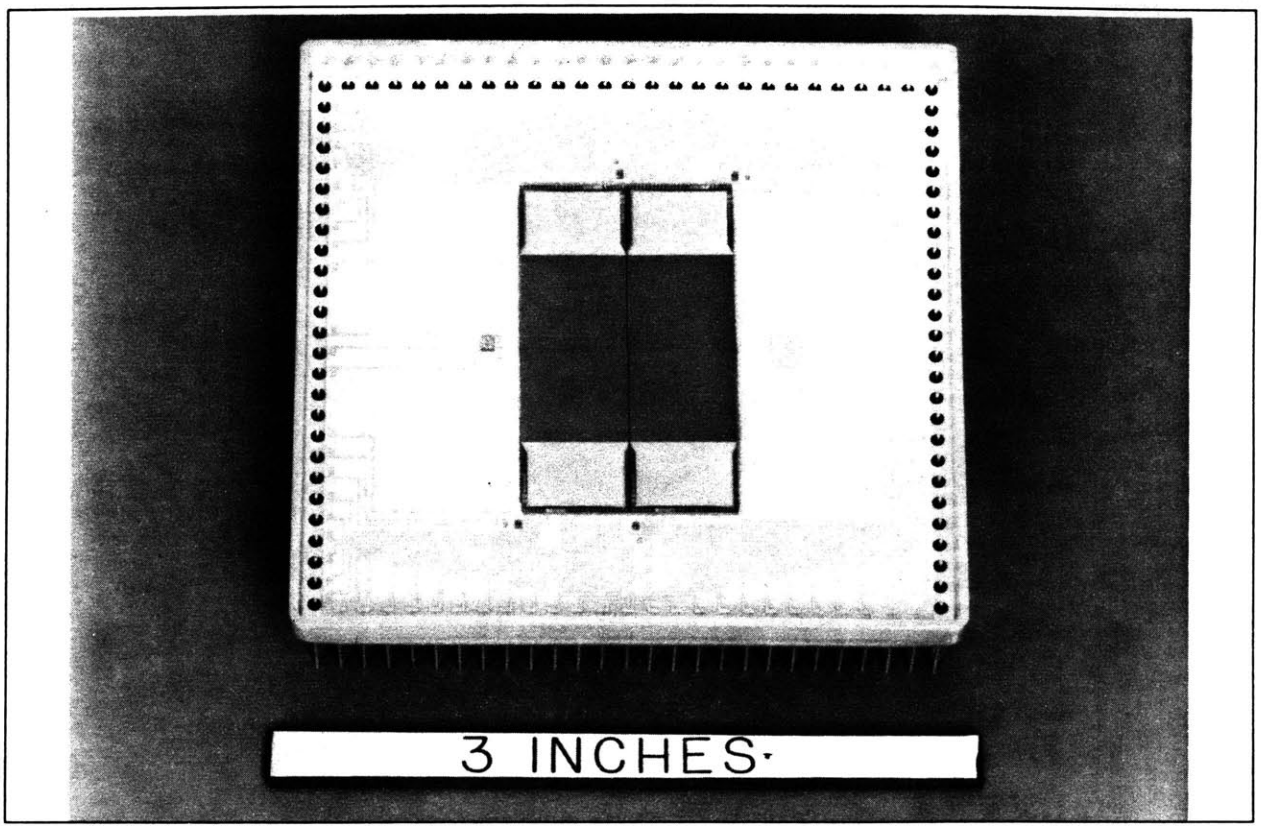

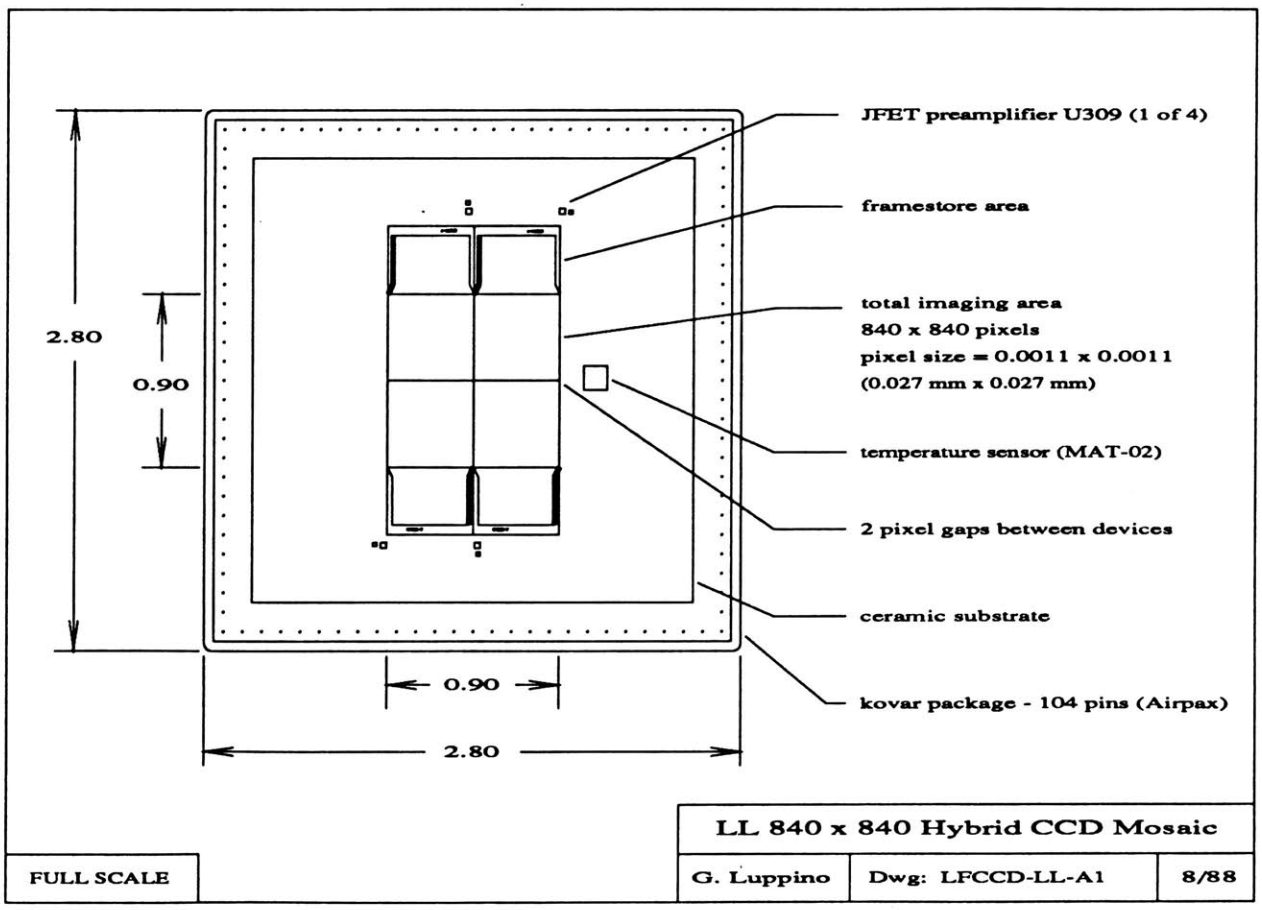

FIGURE 4.12 Drawing and photograph showing the MIT-Lincoln Laboratory 840 x 840 CCD mosaic

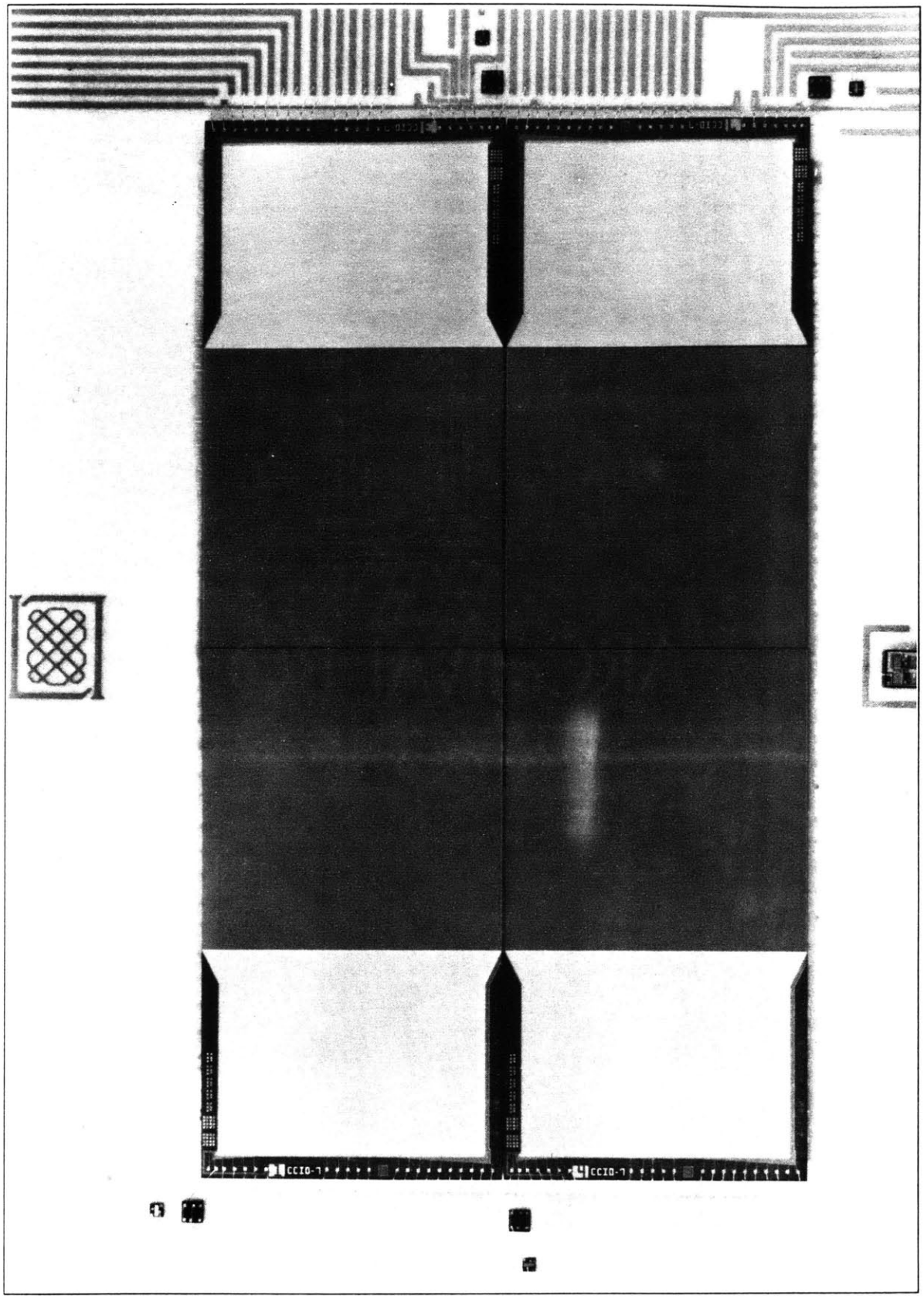

FIGURE 4.13 Close-up photograph of the Lincoln Laboratory Quad CCID-7 CCD mosaic. (Photograph courtesy of Dr. Barry Burke - MIT Lincoln Laboratory).

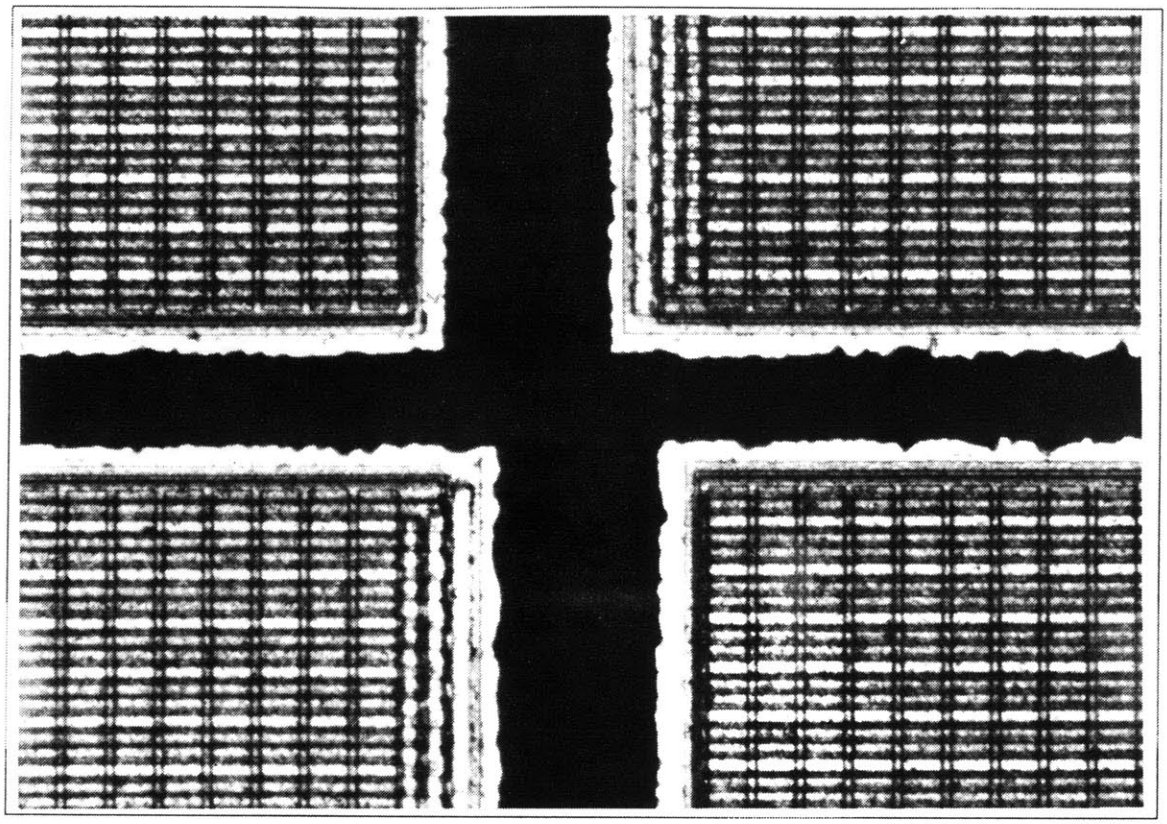

FIGURE 4.14 Micrograph of the central portion of the Quad CCID-7 mosaic showing the small gaps between the devices and the accurate *pixel* registration. Notice the parallel-clock busses on the sides of two of the devices: the gaps are not symmetric since room has to be left for these clock busses. The seams are 4 pixels wide in the vertical direction and 6 pixels wide in the horizontal direction (Photograph courtesy of Barry Burke - MIT Lincoln Laboratory).

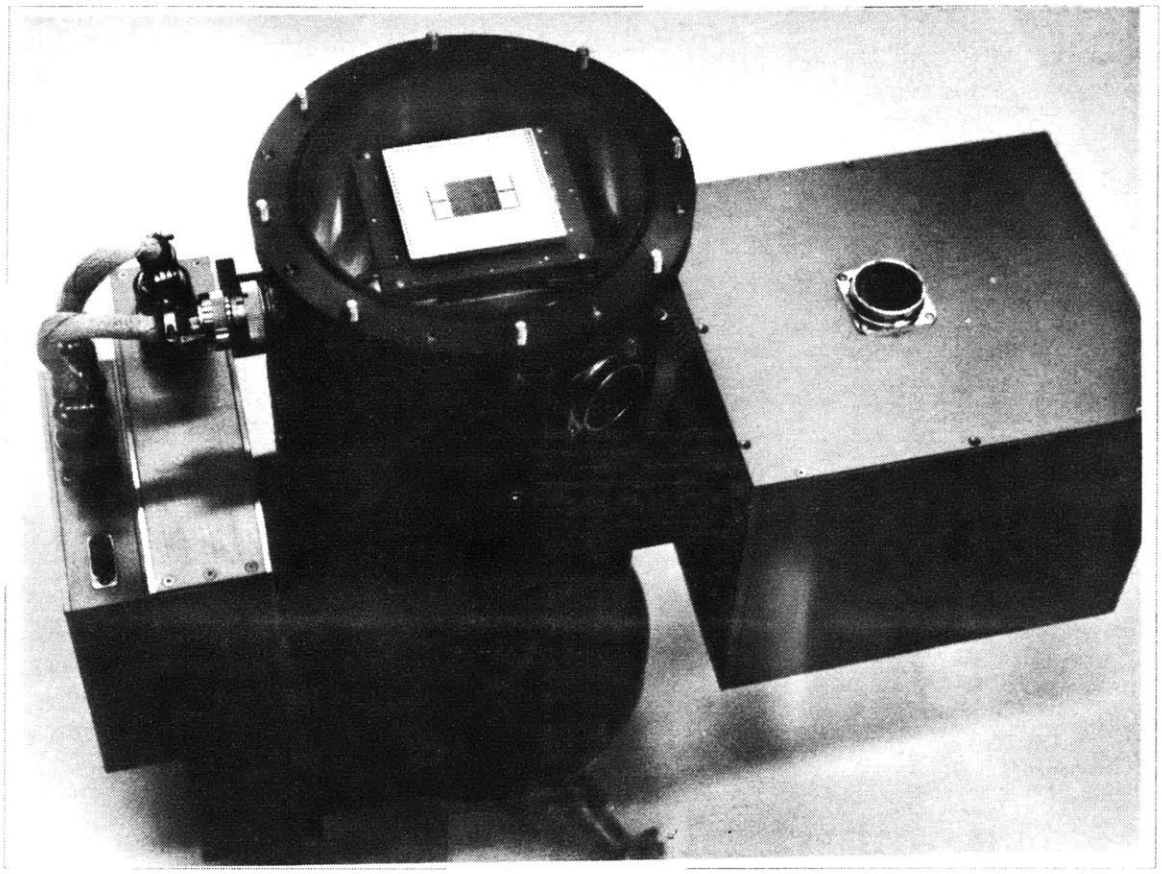

FIGURE 4.15 Internal view of dewar showing the LL 840 × 840 hybrid CCD mosaic installed

hybrid focal-plane assembly technique developed by the Lincoln-Laboratory group is described by Burke *et al.* (1987): this technique is briefly outlined here. The first step in the fabrication of a CCD mosaic is the proper design of the individual CCDs. In order for the device to be three-side abuttable, the clock busses and other structures on the edges of the device have to be kept to a minimum. The top edge and the left side of each device have no structures other than a narrow n^+ diode strip which is used to intercept edge-generated dark current. The clock busses for the three-phase parallel clocks, as well as the n^+ diode, are run up the right side. Each device is sawed out of the wafer within 27 μm of the the pixel edges on the top and left sides, and within 27 μm of the edge of the clock busses on the right side. The saw cut is made as close as possible to the edge diode. Each CCD is held in a vacuum chuck mounted on a precision translation/rotation stage. A glass plate with Cr registration marks is positioned directly over the front surface of the CCD, and the chuck is slowly raised until it almost comes in contact with the glass plate. An operator precisely aligns the n^+ perimeter diode with the registration marks on the glass plate by looking down on the whole assembly through a microscope and adjusting the controls on the translation/rotation stage. When the device is properly positioned, the chuck is raised slightly, bringing the CCD into contact with the plate, and a small drop of cyanoacrylate cement is applied to the device through a small hole in the glass plate. The cement wicks across the surface of the CCD and firmly bonds it to the glass plate. When all four of the CCDs are bonded to the plate, non-conductive epoxy is applied to the back sides of the CCDs and the whole assembly is mounted onto the ceramic substrate. The glass plate is then removed from the front side of the CCDs by dissolving the cyanoacrylate cement in acetone.

The final assembled mosaic has gaps that are 4 pixels wide along the tops of the devices and 6 pixels wide along the sides. A micrograph of the center of the CCD mosaic is shown in Figure 4.14.

The packaged CCD is mounted in a custom zero-insertion-force (ZIF) socket manufactured by 3M/Textool and subsequently modified to permit the inclusion of a cold finger, chip hold-down fixture, and radiation shielding. A view of the CCD mounted in the dewar is shown in Figure 4.15.

b) Multi-phase CCD Electronics

The electronic controller built to operate the four 3-phase, Lincoln Laboratories devices is described in this section. This controller is divided into two main portions, on-telescope electronics and off-telescope electronics, just as the TI virtual-phase controller described in Section 4.2. The off-telescope electronics for the LL 840 × 840 mosaic is identical to that for the TI mosaic, and will not be discussed here. The transversal filter, correlated-double-sampler and 16 bit A/D converter are also unchanged. A block diagram in Figure 4.16 illustrates the layout of the controller electronics for this CCD.

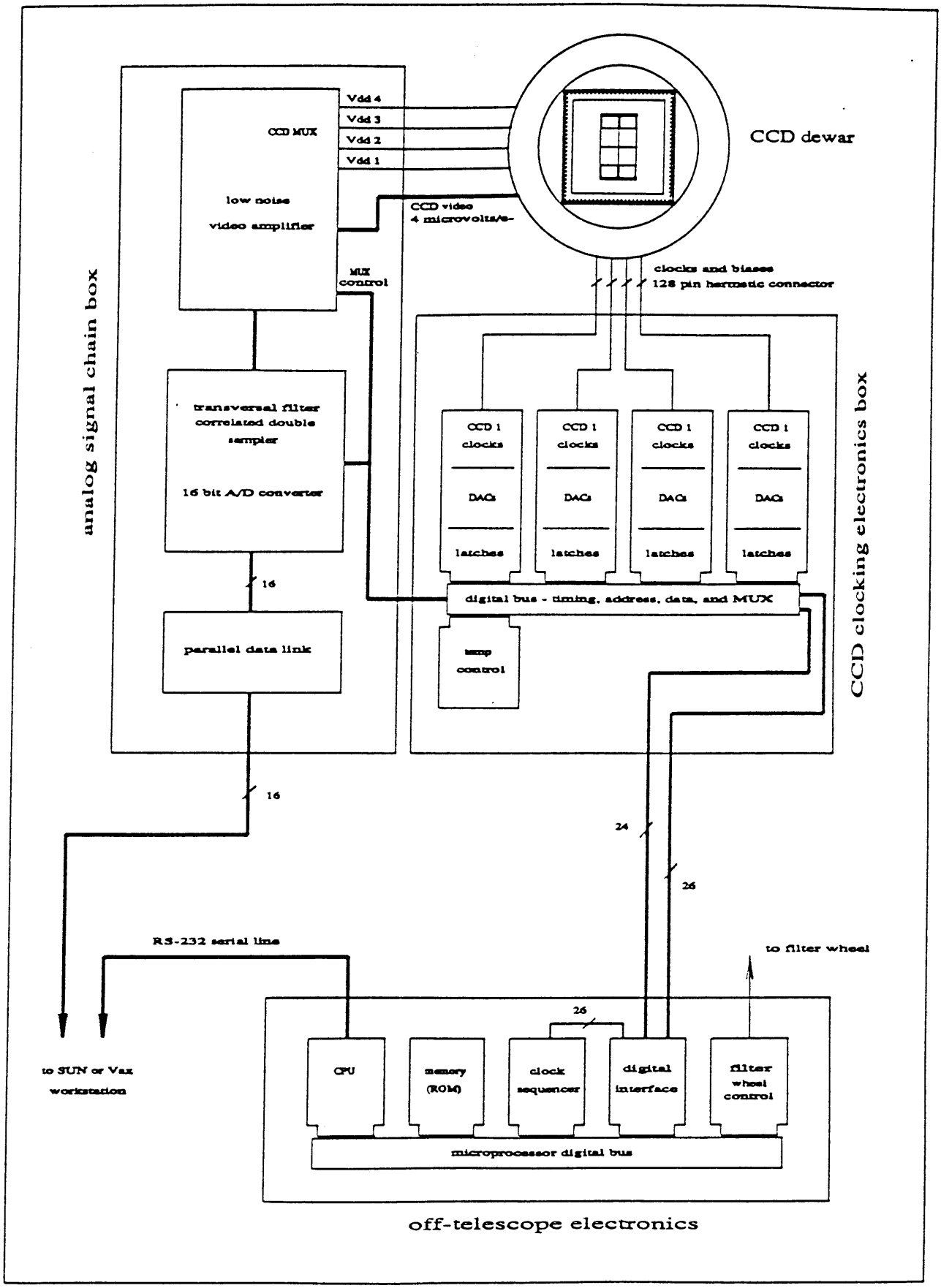

FIGURE 4.16 Electronic controller block diagram for the LL 840 x 840 mosaic

REFERENCES:

Abraham, A.A., and Robinson, W.G. 1986, "Integration of Visible CCDs into Cryogenically Cooled Dewars for Astronomical Applications," in *Proceedings of the SPIE 627, Instrumentation in Astronomy VI*, ed. Crawford, D.L., p.176.

Blouke, M.M., Corrie, B., Heidtmann, D.L., Yang, F., Winzenread, M., Lust, M., Marsh, H., and Janesick, J.R. 1987, "Large Format, High Resolution Image Sensors," *Optical Engineering*, **26**, 837.

Burke, B., Mountain, R., Daniels, P., and Harrison, D. 1987, "420 x 420 CCD Imager and Four-Chip Hybrid Focal Plane," *Optical Engineering*, **26**, 890.

Doty, J.P., Luppino, G.A., and Ricker, G.R. 1987b, "Design of Low Noise, High Performance X-ray CCD Cameras," *Optical Engineering*, **26**, 1055.

Gunn, J.E., Emory, E., Harris, F., and Oke, J.B. 1987, "The Palomar Observatory CCD Camera," *P.A.S.P.*, **99**, 518.

Gunn, J.E., Carr, M., Danielson, G., Lorenz, E., Lucinio, R., Nenow, V., Smith, J., Westphal, J., Schneider, D., and Zimmerman, B. 1987, "Four-Shooter: A Large Format Charge-Coupled Device Camera for the Hale Telescope," *Optical Engineering*, **26**, 779.

Hynecek, J. 1981, "Virtual Phase Technology: A New Approach to Fabrication of Large Area CCDs," *IEEE Trans. Electron Devices*, **ED-28**, 483.

Janesick, J.R., Hynecek, J., and Blouke, M. 1981, "Virtual Phase Imager for Galileo," in *Proceedings of the SPIE 290, Solid State Imagers for Astronomy*, ed. Geary, J., and Latham, D., p. 165.

Janesick, J., Elliot, T., Collins, S., Blouke, M., and Freeman, J. 1987, "Scientific Charge-Coupled Devices," *Optical Engineering*, **26**, 692.

Janesick, J., Elliot, T., Bredthauer, R., Chandler, C., and Burke, B. 1988, "Fano-Noise-Limiter CCDs," in *Optical and Optoelectronic Applied Science and Engineering Symposium*

Lauer, T., Miller, J., Osborne, J., Robinson, L., and Stover, R. 1985, "CCD Use at Lick Observatory," in *Proceedings of the SPIE 445, Instrumentation in Astronomy V*, ed. Boksenburg, p. 132.

Luppino, G.A. 1989, "A Virtual-Phase CCD Camera for The MDM Observatory," *P.A.S.P.*, in press.

Luppino, G.A., Ceglio, N.M., Doty, J.P., Ricker, G.R., and Vallerga, J.V. 1987b, "Imaging and Nondispersive Spectroscopy of Soft X-rays Using a Laboratory X-ray CCD System," *Optical Engineering*, **26**, 1048.

Mackay, C.D. 1986, "Charge-Coupled Devices in Astronomy," *Ann. Rev. Astron. Astrophys.*, **24**, 255.

Nousek, J., Garmire, G., Ricker, G.R., Collins, S.A., and Riegler, G. 1987, "The AXAF CCD Imaging Spectrometer Experiment (ACIS)," *Astro. Lett. and Communications*, **26**, 35.

Chapter 5

CCD Instrument Calibration

This Chapter describes the procedure used to select and characterize the CCDs and the instrument presented in the previous Chapter. Section 5.1 outines the methods used for CCD selection and calibration and Section 5.2 presents the results of these measurements for the five selected CCDs. The photometric calibration of the instrument is described in Section 5.3. There is no calibration data for a Lincoln Laboratory 840 × 840 CCD since the control electronics for this device are in the final stage of construction, and no functioning devices have been delivered before the completion of this thesis. Future plans and expected performance for these LL CCDs are described in Chapter 8.

5.1 CCD Selection and Characterization Methods

The instrument CCDs were selected from a large number of devices built by Texas Instruments for x-ray astronomy use. Five detectors were eventually selected: the TI-4849 device used in the prototype camera and the four TI 850 × 750 devices destined for the large-format camera. The properties of approximately 50 TI-4849 sensors and 20 TI 850 × 750 sensors were measured initially using the x-ray calibration methods described below. Optical light calibration was carried out at the telescope for the selected detectors.

a) X-ray Calibration

When tuning a particular CCD detector for astronomical use, all the device properties, such as readout noise, linearity, dynamic range, cosmetics, charge-transfer-efficiency (CTE), quantum-efficiency (QE), and gain constant (e^-/ADU) can be measured, and optimized using optical light. This section describes an alternative method that uses soft x-rays to evaluate and optimize CCD operation. This method is not meant to replace, but rather to supplement, existing optical techniques.

(i) X-ray detection with CCDs

When an optical photon is absorbed in a silicon CCD, the photon energy is enough to excite a valence band electron into the conduction band. Consequently, a single electron-hole pair is produced, independent of the energy of the photon. An x-ray photon, however, has enough energy to be photoelectrically absorbed by a Si atom, liberating a primary photoelectron with a large excess of kinetic energy. This electron moves through the silicon and loses energy through ionizing collisions with bound electrons. Meanwhile, the ionized Si atom will decay by ejection of Auger electrons which also surrender their kinetic energy to other bound atomic electrons,

or by radiative transistions which result in the emission of Si characteristic x-rays. Eventually, a small (d~0.4 μm) charge cloud containing [$E_{x\text{-}ray}$/3.65 eV] electrons appears at the point in the CCD where the x-ray was absorbed (Bautz *et al.* 1987). Consider a simplified description of the interaction of 5.9 keV x-rays (Mn K_α x-rays produced by a radioactive, K-capture ^{55}Fe source). A 5.9 keV photon is absorbed by a CCD Si atom, liberating a K-shell electron. This primary photoelectron has a kinetic energy equal to the difference between the 5.9 keV photon energy and the 1.8 keV needed to ionize the Si atom, and produces a charge cloud of ~1223 electrons (4100 eV/3.65 eV). The excited silicon atom decays by radiative transitions, or, more likely (Knoll 1979), by ejection of Auger electrons. These Auger electrons carry off kinetic energy equal to the atomic transition energy, and produce e^--h pairs in the same way as the primary photoelectron, so that, ultimately, a charge cloud of ~ 1616 electrons is produced by the absorption of the 5.9 keV x-ray. If the atom does decay radiatively, the photons often escape since Si is relatively transparent to its own radiation. Consequently, some small number of the x-ray events produce a charge cloud of only 1123 e^- corresponding to the 4.1 keV deposited by the primary photoelectron (this can be seen in the x-ray histogram at the bottom of Figure 5.1 - this small peak at 4.1 keV is called the Mn Kα escape peak).

The generation of the electron charge cloud is not a noiseless process. The variance in the number of electrons produced by a photon of energy E_x is given by

$$\sigma_s^{\,2} = F\left(\frac{E_x}{3.65\ eV}\right) \tag{5.1}$$

where F, the Fano factor, has a typical value of 0.1 for Silicon (Knoll 1979; Stern, Liewer and Janesick 1983). Notice that a Fano factor with a value less than unity actually reduces the variance one would expect if this process were described purely by Poisson statistics, where the variance in the number of electrons would just be equal to the number. Therefore, one can measure 5.9 keV (^{55}Fe again) x-rays with a limiting precision of σ_s=13 e^-=46 eV or a limiting energy resolution of 46 eV × 2.35=109 eV FWHM, which corresponds to $E/\delta E$=54.

(ii) determination of system gain using x-rays

There are obvious advantages in using monoenergetic x-rays to characterize CCD performance. Each absorbed x-ray produces a localized charge packet of known size, and the CCD's collection, transfer, and readout of this packet can be monitored. These x-ray photon calibration techniques have been used for a number of years by our group and others (Janesick *et al.* 1987; Chowanietz, Lumb, and Wells 1986). In practice, a shuttered ^{55}Fe source illuminates the CCD, and the exposure time is adjusted to assure that there is low probability of getting more than one photon in a single pixel. The CCD is read out, a bias frame (or bias level) is subtracted, and the ADU (analog-to-digital unit) value in each pixel is binned in a histogram A number of such exposures

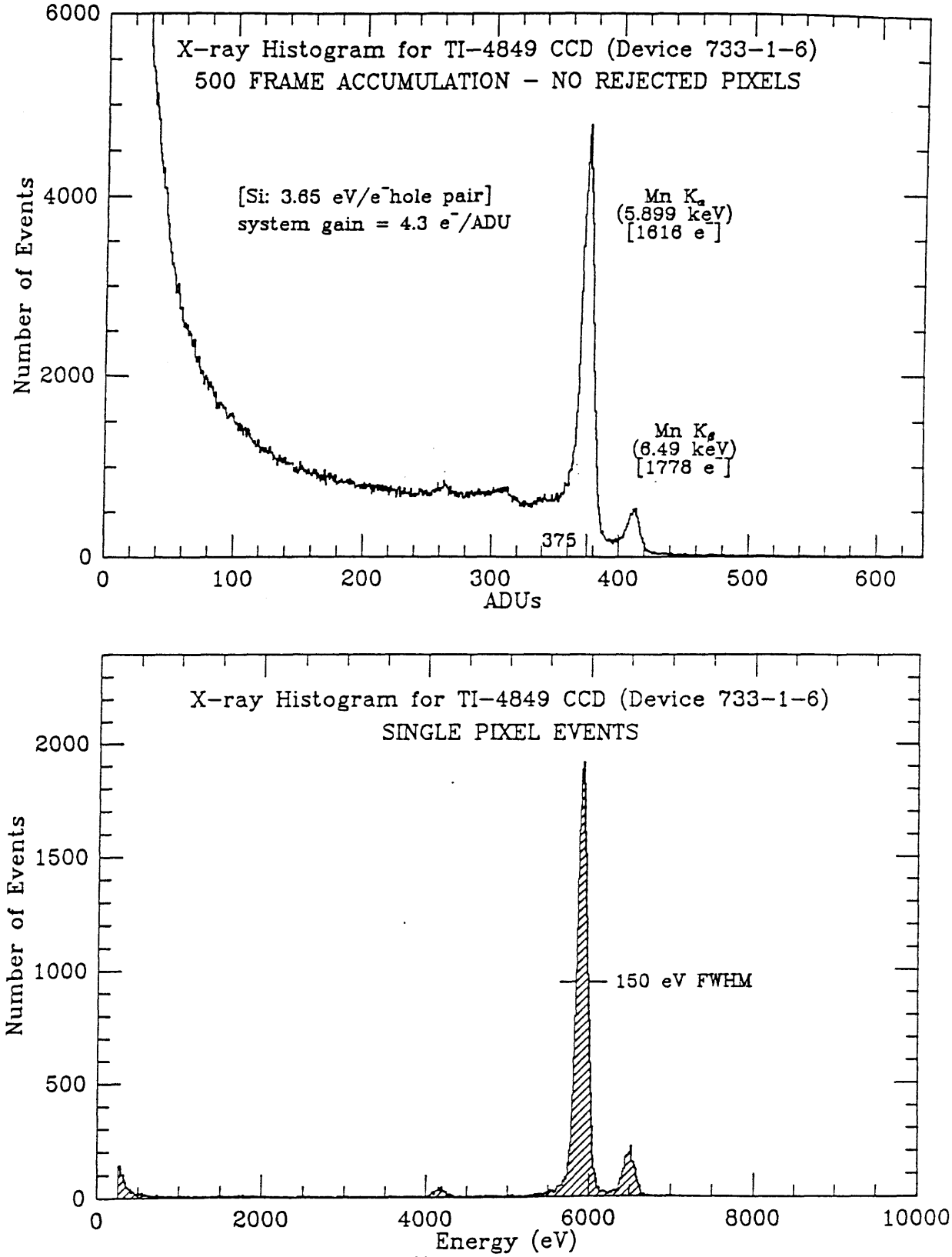

FIGURE 5.1 Histogram of events from an ^{55}Fe x-ray source. All of the pixels in 500 one-second exposures of the TI-4849 CCD were binned to generate the top plot. Ideally, each Mn Kα x-ray produces a charge cloud of 1616 ± 13 electrons. The 5.9 keV peak at 375 ADU indicates a system gain of 4.3 electrons/ADU. The bottom plot was derived from the same exposures; here, events were binned only if the charge was confined to a single pixel.

are taken until enough x-ray events are accumulated in the histogram to allow identification of the x-ray lines. The resulting histogram (for a very good CCD) will look like that in the top of Figure 5.1. Here, no attempt has been made to eliminate partially collected charge events (*partial events*) or charge split between two or more pixels (*split events*). The pixels can be examined to see if any charge splitting has occurred. If only the events that occurred in single pixels are binned, a single-pixel-event histogram, such as that shown at the bottom of Figure 5.1 is generated.

A great deal of information can be extracted from a CCD x-ray histogram. One of the most important numbers for any CCD system is the system gain constant (e^-/ADU). The gain constant can simply be read off of the x-ray histogram by just looking at the position of the Mn K_α x-ray peak on the ADU axis (assuming there are no charge losses during readout - *an important assumption*). Since each Mn K_α x-ray produces ~1616 electrons, the gain constant is just 1616 divided by the peak position in ADU (see Figure 5.1). The quick evaluation of the system gain constant (assuming the software exists for binning and generating x-ray histograms) is a powerful tool when tuning CCDs for optimal noise performance. The CCD readout noise is a sensitive function of a number of operating parameters, particularly the output amplifier drain voltage V_{DD}, which also affects the gain of the output amplifier. Consequently, after each adjustment of V_{DD}, both the noise *and* the gain constant must be remeasured.

(iii) charge transfer properties

Good charge transfer is critical for high-performance scientific CCDs. The charge-transfer properties is often characterized in terms of 1) an overall pixel-to-pixel charge transfer efficiency (*CTE*) which is a measure of the amount of charge transferred each time the device is clocked, and 2) discrete charge traps, or pockets, which have a fixed charge capacity. The *CTE* of a CCD can be measured easily using monoenergetic x-rays, since we know how many electrons are being generated for each absorbed photon. In practice, one accumulates an x-ray histogram using a small (50 × 50) subarray on the CCD near the output FET. In this case, the number of transfers is small, and *CTE* effects are essentially negligible. If another histogram is accumulated using a subarray N pixels away from the mean location of the first, then the position of the x-ray peak, S_O, in the resulting histogram will be shifted by

$$S_o = (CTE)^N \, S_i \tag{5.2}$$

from the initial position, S_i. This effect is easy to measure, even for devices with very good *CTE*. For example, if one accumulates a histogram in opposite corners of a TI-4849 CCD (584 × 390 pixels - N=874 between the centers of two 50 × 50 subarrays in the corners) with a *CTE* of 0.99999 and a gain of 4 e^-/ADU, then the peak will be shifted by 4 ADU between the two histograms. In many cases, devices with poor *CTE* (<0.99995) can have their transfer efficiency significantly improved with the introduction of a *fat zero* of ~100

electrons. This fat zero can be optically injected by flashing the CCD with a uniform light source before exposing the detector to the scene being imaged. In most cases of broad-band optical imaging, however, the night sky itself provides enough of a fat zero to ensure adequate charge transfer.

Charge traps (or pockets) are a far more insidious problem than overall *CTE*. These traps, which can be scattered all over some devices, have capacities ranging from a few electrons to voracious buckets which need thousands of electrons to fill them. A trap in a pixel will affect the charge in pixels "behind" the trap since this charge must be clocked through the trap during readout. Traps in the imaging portion (parallel register) of the device will affect only the columns in which the traps are located; however, all of the pixels in the CCD eventually are clocked down the serial register, and a large trap here can render the device useless for low-light-level applications. Small pockets with maximum capacity of no more than a few hundred electrons (again, not in the serial register) are tolerable if the CCD can be provided with a large enough fat zero (either by flashing or from the night sky).

b) Optical Light Calibration

(i) gain and noise measurement by mean-variance calibration

The total variance in a portion of a CCD image exposed to a uniform light source is simply the sum of three variance terms,

$$\sigma_T^{\,2} = \sigma_S^{\,2} + \sigma_R^{\,2} + \sigma_{qe}^{\,2} \tag{5.3}$$

where σ_S is the Poisson shot noise, σ_R is the readout noise and σ_{qe} is a (small) noise term coming from pixel-to-pixel quantum efficiency fluctuations over the area of the chip being used for the measurement. Each of the above terms is in units of *number of detected photons* (or just electrons since each detected photon produces one electron). If the total variance is written in ADUs, then the shot noise variance is equal to the signal, S, divided by the gain constant, g, and the readout variance is simply σ_R^2/g^2. In order to extract a value for g, one measures S and σ_T^2 by exposing the CCD to the uniform light source for various lengths of time. If there were no pixel-to-pixel sensitivity variations, then one could simply fit a line to the data where the inverse of the slope is the gain constant, and the y-intercept is the system noise (in ADU). The σ_{qe}^2 term, however, is proportional to S^2, so one must fit a second-order polynomial of the form

$$\sigma_T^{\,2} = \frac{S}{g} + \frac{\sigma_R^{\,2}}{g^2} + k\,S^2 \tag{5.4}$$

An example of such a fit is given in Figure 5.3, where the mean-variance technique was used to calibrate the TI 850 × 750 CCD.

(ii) linearity

CCDs are extremely linear optical transducers. If the output signal, S_o, is expressed as some power of the input signal, S_i,

$$S_o = K\, S_i^{\gamma} \tag{5.5}$$

then CCDs typically have values for γ of 1.000 ±0.002. The conversion of an incident photon to an electron-hole pair is a linear process, so any nonlinearity is usually due to the CCD output amplifier. Figures 5.2 and 5.4 illustrate the linearity of two of the CCDs used in this instrument.

(iii) dynamic range

The dynamic range of a CCD is defined as its full well capacity divided by the system readout noise. The full well capacity for TI virtual-phase devices is typically 200,000 electrons, so the full dynamic range of the chip can be spanned easily by a 16-bit A/D converter for devices with readout noise greater than ~3 electrons.

5.2 CCD Selection and Optimization

a) TI-4849

The best selected TI-4849 CCD (device 733-1-6) was characterized in our laboratory using the x-ray calibration methods described above; the instrument was also characterized at the telescope using optical light. The x-ray histograms shown in Figure 5.1 was generated for the TI-4849 device in the BRICC. This histogram indicates a system gain constant of 4.3 e^-/ADU. The noise of the CCD was measured by taking two bias frames, subtracting them, and computing the standard deviation of the resulting numbers, or by taking a single bias frame and computing the standard deviation of its pixel values (the second method will, in general, produce a higher number if the device has readout-generated column-to-column structure or cosmetic defects). Both methods yield approximately the same result for the TI-4849 CCD of ~ 2.0 ADU which is equivalent to ~ 8.6 e^- noise.

The linearity of the system equipped with the TI-4849 was measured on the telescope by illuminating the CCD with a flat-field lamp and taking exposures for successively longer integration times. The average charge per pixel in a 100 × 100 box centered on the device was measured and is shown plotted against the integration time in Figure 5.2. The system is linear up to a well depth of at least 180,000 e^-. The upper limit on the low-level non-linearity is 0.5%. This value is dominated by uncertainties in the short-exposure shutter timing. The gain of the system is set such that 1 ADU equals approximately half the readout noise while the 16 bits span the full useable dynamic range of the CCD.

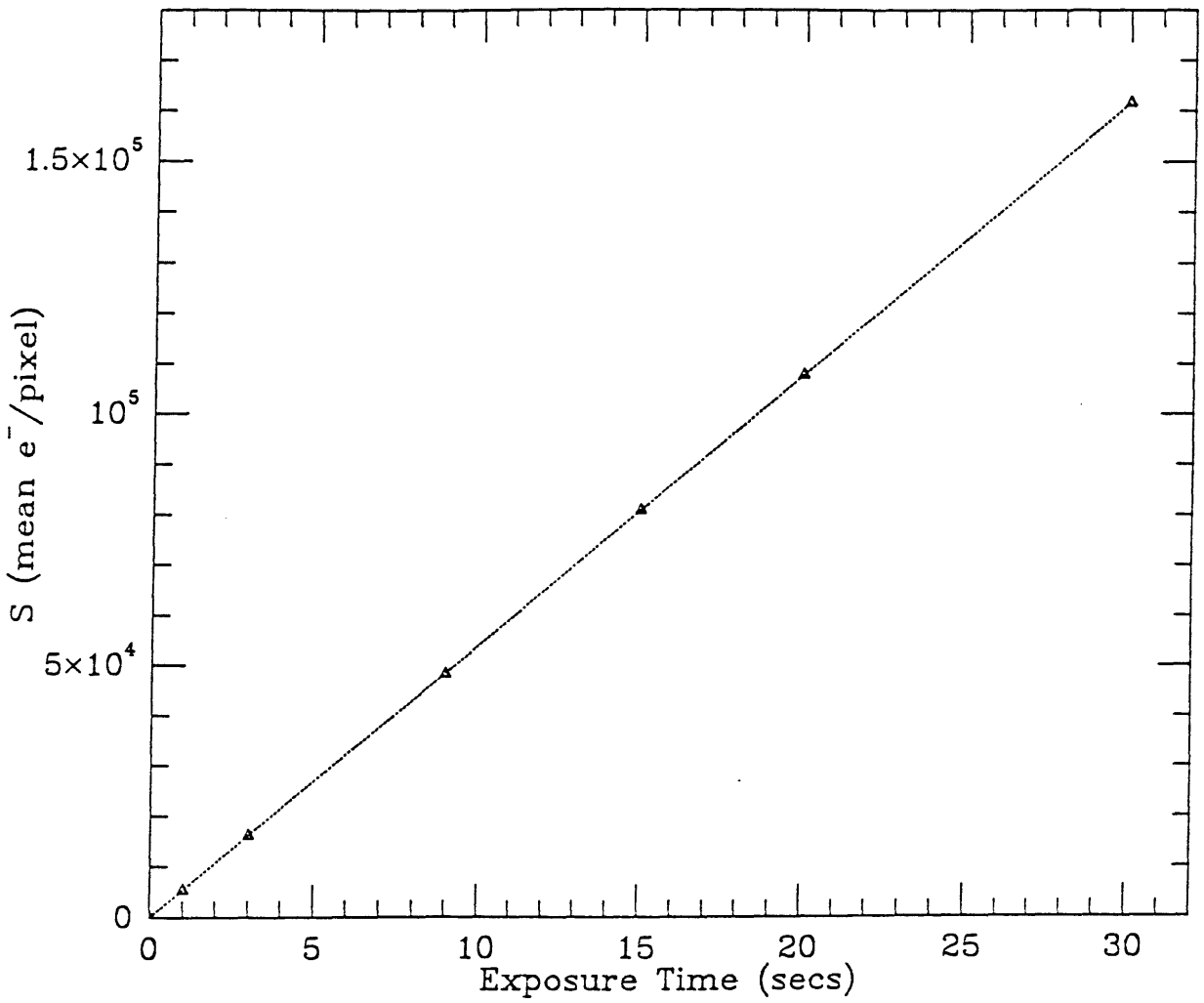

FIGURE 5.2 Plot of the mean signal level as a function of integration time for the TI-4849 CCD in the BRICC. The CCD was exposed to a constant brightness flat-field lamp. The plot shows the CCD is linear to a well depth of at least 180,000 electrons.

TI-4849 device 733-1-6 has excellent cosmetic properties. There are no hot columns or gross blemishes, and the CCD does not suffer from any interference fringing. There are a few (~ 100) charge traps (pockets) scattered around the device, but they are confined to the imaging area, and there are no traps in the serial register. Ignoring the few charge traps, the peak-to-peak non-uniformity of the device sensitivity is less than 4 percent in *R*-band (*i.e.* a normalized flat field has all pixels with values between 0.98 and 1.02). This CCD suffers somewhat from a glowing, on-chip FET; however, only the 50 × 50 pixels nearest the FET are contaminated in exposures as long as two hours. A flat-field image for this device is shown in Figure 5.5a. At the normal operating temperature of −100°C, the average dark current is less than one electron per pixel in ten minutes.

All of the virtual phase CCDs we have tested have had a troublesome problem with pixel-to-pixel crosstalk - sometimes called amplifier *undershoot*. This problem becomes obvious when the CCD is exposed to a bright, compact object, such as a standard star. The pixels immediately following the star (in the readout direction) have values a few percent *below* the bias level, which we believe is caused by incomplete reset of the on-chip amplifier (this effect can cause apparent "charge trails" or "undershoot" depending on how the transversal filter is balanced). The effect goes away completely if the signal in the background is a few hundred electrons above bias, so it is not a problem for broad-band imaging where the sky provides the necessary signal pedestal. However, for short exposures of bright objects (such as standard stars), where the sky value is negligible, it is recommended that an optical pedestal (fat zero) be injected by flashing the CCD before the exposure. This undershoot problem is a strong function of the levels of the CCD reset gate clock voltage and the reset voltage V_{ref}, so tuning these values can minimize the problem, but not eliminate it.

Table 5.1
Measured Performance of Instrument CCDs

Device Type	Device Number	Readout Noise e^-	Gain Constant e^-/ADU	Full Well e^-	CTE	EPI Resistivity Ω - cm
4849H	733-6-1	8.5	4.3	250,000	0.999995	100
TI 850 × 750	4598-17-9	18.0	1.8	200,000	0.9999	10
TI 850 × 750	4598-17-7	18.0	1.8	200,000	0.9999	10
TI 850 × 750	4598-17-2	18.0	1.8	200,000	0.9999	10
TI 850 × 750	4598-17-11	18.0	1.8	200,000	0.9999	10

b) TI 850 × 750 CCDs

Four TI 850 × 750 CCDs were selected for use in the large-format camera. The properties of all four were carefully measured in the laboratory using x-rays; only one of these devices, however, was used at the telescope

for optical imaging. It turned out that all four of the selected devices came from the same lot *and* slice (lot 4598 slice 17): therefore they all have very similar properties A detailed description of each of the TI 850 × 750 CCDs is given below.

TI 850 × 750 DEVICE 4598-17-9 This may be the best of the four big TI chips. This was the device used for most of the cluster observations described later, and this is the only one of the four devices that has been fully characterized with optical light. As listed in Table 5.1, this chip was built on 10 Ω-cm silicon and has 18 electrons rms noise and poor charge transfer properties (many charge traps and a *CTE* of ~0.9999). Nevertheless, this CCD is good for broad-band optical imaging. It has quantum efficiency comparable to that of the TI-4849 CCD, and response non-uniformities are less than 5 percent peak-to-peak across the chip. There are no hot columns, but there are four columns that have significantly lower response than the rest of the device. A flat-field image of this CCD is shown in Figure 5.5b. Although the average dark current on all four of the TI 850 × 750 CCDs is less than one electron per minute per pixel at –80 degrees C, they must be operated at –100 degrees C in order to reduce the charge generated by a large number of hot pixels (dark spikes). At this temperature, the signal in the hot pixels is dominated by the shot noise in the sky.

The linearity of the system with this larger chip was measured using the same method as described for the TI-4849. The CCD was exposed to a flat-field lamp, and the average signal per pixel in a 100 × 100 box is plotted against exposure time in Figure 5.4. There is some indication of high-level non-linearity, but this could be due to brightness variations in the flat-field lamp and not the CCD. If the linearity is real, it is best fit to a power law of the form of equation 5.5 with γ=0.983. Unfortunately, this effect was not noticed in time to check the lamp stability independently.

Initially, measurement the ^{55}Fe x-ray peak at ~700 ADU indicated a system gain of 2.3 e^-/ADU. Most of the cluster observations were carried out with this system gain. After some recent electronic modifications, the system was recalibrated at the telescope using optical light and the mean-variance technique: the system gain is now 1.8 e^-/ADU (see Figure 5.3) and the noise is 10 ADU or 18 e^- rms.

Unlike the TI-4849 device, there is very little FET glow from the output amplifiers on any of the four TI 850 × 750 chips, primarily because their amplifiers are biased with a V_{DD} 3 volts lower than the TI-4849. This CCD suffers from the same pixel-to-pixel crosstalk problem as that described for the TI-4849 CCD.

TI 850 × 750 DEVICE 4598-17-7 For optical imaging, this CCD may be as good as, or better than 4598-17-9. It has only two bad columns and fewer traps, but the overall CTE measured using x-rays appeared to be slightly poorer than that of the first device. This CCD has not been carefully characterized using optical light, but the x-ray measurements show the system gain and CTE are the same as those for device 4598-17-9.

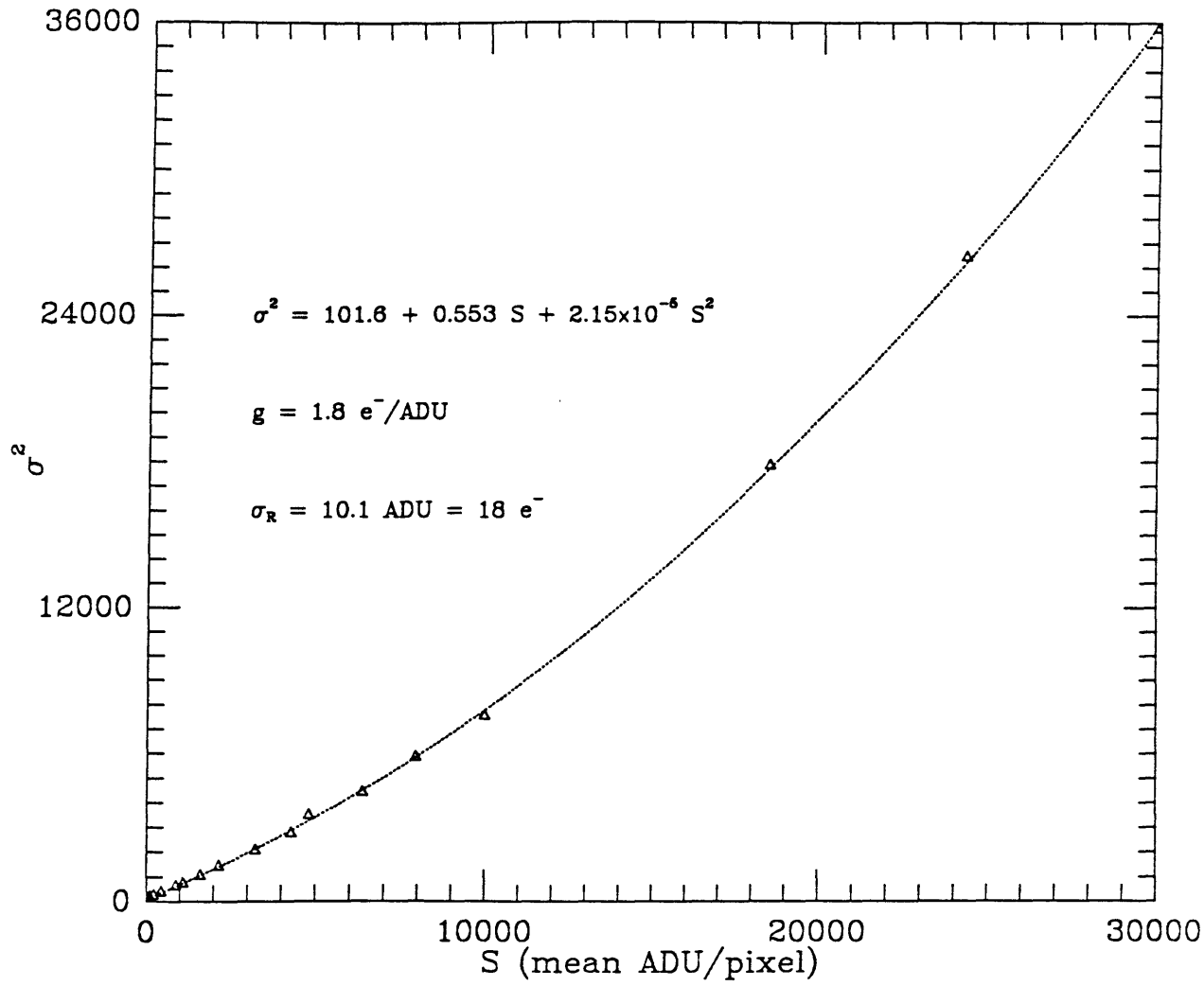

FIGURE 5.3 Plot of the variance versus the mean signal per pixel in a 100 × 100 box centered on the TI 850 × 750 CCD. This plot allows measurement of the system gain constant, as well as the readout noise. The quadratic variance term comes from pixel-to-pixel sensitivity (quantum efficiency) variations. From this measurement, one derives a system gain constant of 1.8 electrons/ADU and a readout noise of 10.1 ADU = 18 electrons.

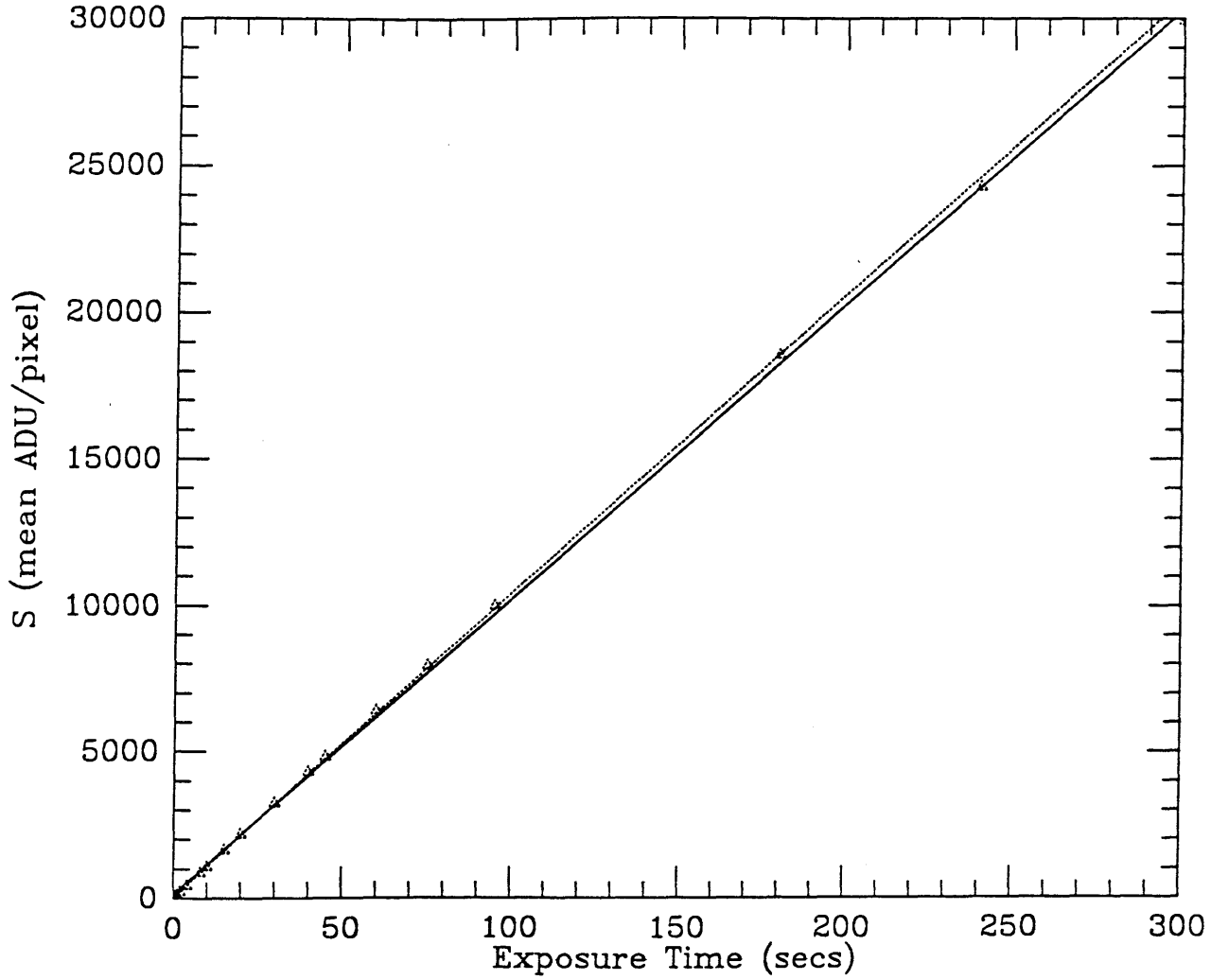

FIGURE 5.4 Plot of the mean signal per pixel as a function of integration time for the TI 850 × 750 CCD. The CCD was illuminated by a flat-field lamp whose brightness may not have been constant over time. Assuming the apparent non-linearity is real, it was fit with a function of the form $S=KT^{\gamma}$ where K is a constant. The fit, shown by the dotted line in the plot above, used a value of 0.983 for γ.

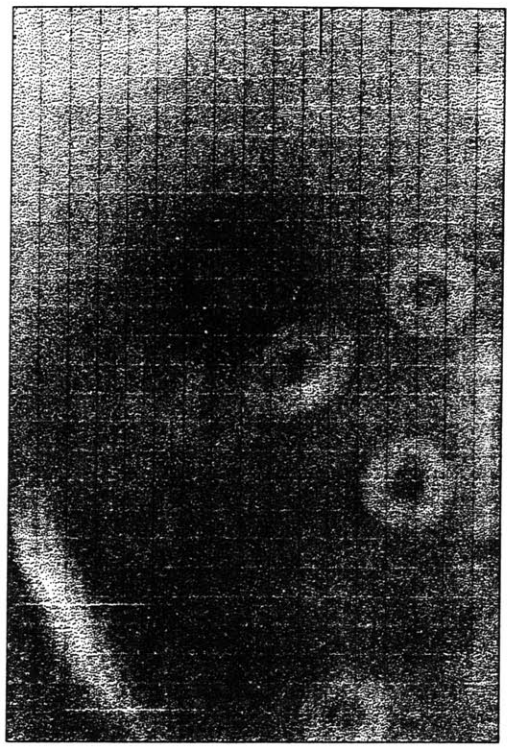

FIGURE 5.5a Flat field (R-band) for the TI-4849 CCD. The bias level has been subtracted and the image has been normalized by dividing it by its mean. This negative grey-scale picture is displayed with a linear stretch so that black represents 1.025 and white represents 0.975. As can be seen, this CCD is quite flat; maximum deviations are only a few percent. The obvoius grid pattern is an artifact of the step-and-repeat process used to make the CCD mask; this pattern, along with all of the other structure seen, is completely eliminated from CCD images when they are flattened (divided by a frame such as this). The white donuts are just shadows of dirt specks on the dewar window.

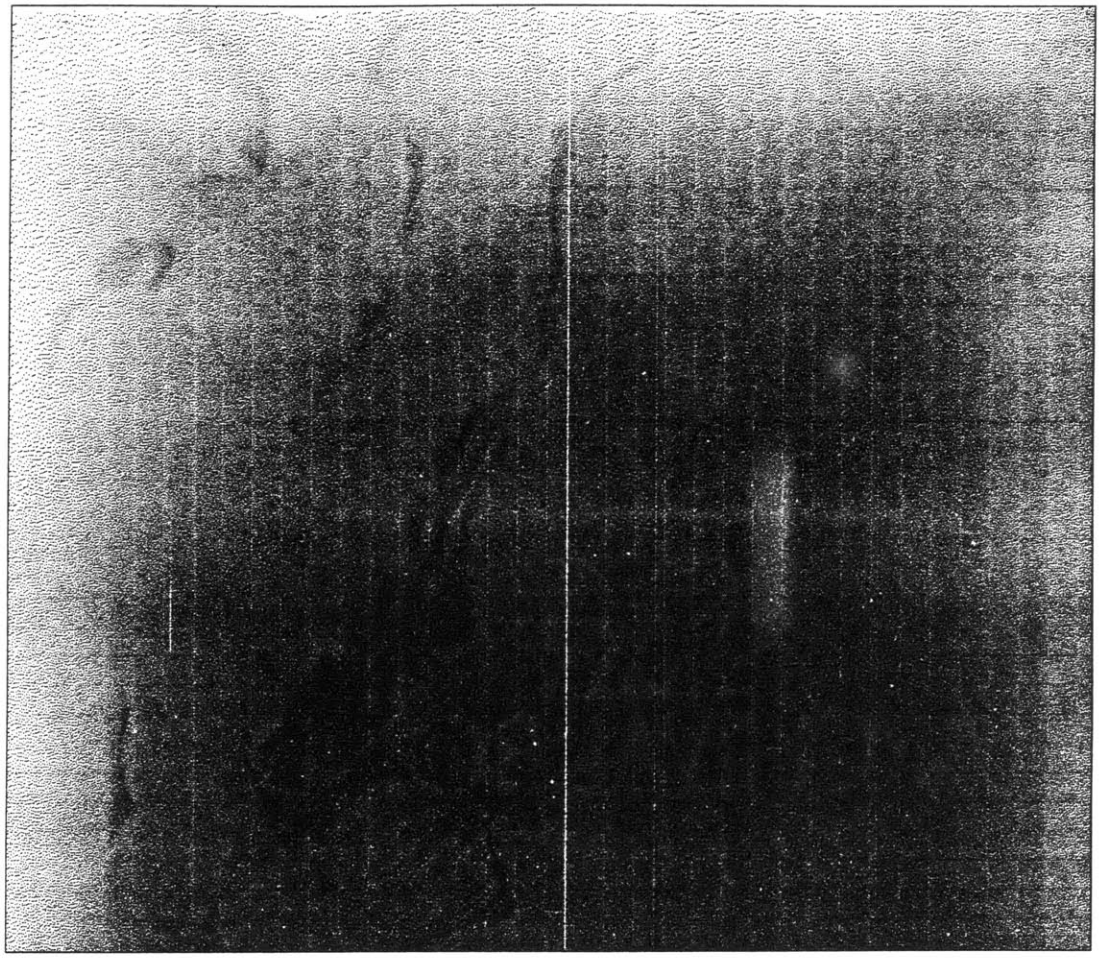

FIGURE 5.5b Flat field (R-band) for the TI 850 × 750 CCD. The frame has been prepared and displayed the same as Figure 5.5a (0.975 to 1.025 stretch). As with the TI-4849 CCD, the response is uniform to within a few percent over the entire array.

TI 850 × 750 DEVICE 4598-17-2 The properties of this chip are very similar to those of the two described above. There is one blocked column on the right side of the device (away from the output amplifier). The noise, CTE and gain are the same as 4598-17-9.

TI 850 × 750 DEVICE 4598-17-11 Other than a single hot column at the far right of the device, this CCD is identical to the three sensors described above. The noise, CTE and gain are the same as 4598-17-9.

5.3 Instrument Photometric Calibration

A set of standard KPNO broad-band (Mould) *BVRI* filters were purchased from Omega Optical and installed in the instrument filter wheel. The photometric response of the instrument was calibrated using the standard stars of Landolt (1983) and Christian *et al.* (1985). The photometric calibration has been tied to the Johnson *UBV* and Kron-Cousins *R* and *I* bandpasses (Bessel 1986).

a) Color Transformations

From the photometry and listed colors of the photometric standard stars, the following color transformations were computed for the TI 850 × 750 CCD on the 1.3m telescope.

$$R = R_i - 0.058\,(V - R)$$

$$(V - R) = 1.107\,(V - R)_i$$

$$B = B_i + 0.177\,(B - V)$$

$$I = I_i - 0.461\,(R - I) \qquad (5.6)$$

The instrumental magnitudes, subscripted with i, are a good match for *V* and *R* bands, but there are significant color terms for *B* and *I* bands.

b) System Efficiency

In order to calculate the system efficiencies, the following expression for *AB* magnitude (see Oke and Gunn 1983) was used to convert magnitudes to number of incident photons

$$n_\lambda = 1.5 \times 10^{23} \left(\frac{1000\ \text{Å}}{\lambda}\right) 10^{-0.4\,(AB + 48.64)} \text{ photons cm}^{-2}\,\text{s}^{-1}\,\text{Å}^{-1} \qquad (5.7)$$

where $n\lambda$ was measured by Hayes and Latham (1975) to be 948 photons $\text{cm}^{-2}\,\text{s}^{-1}\,\text{Å}^{-1}$ at the top of the atmosphere for Vega, an A0V star with $AB(\lambda{=}5556\text{Å}){=}V{=}0$. This equation yields the well known conversion

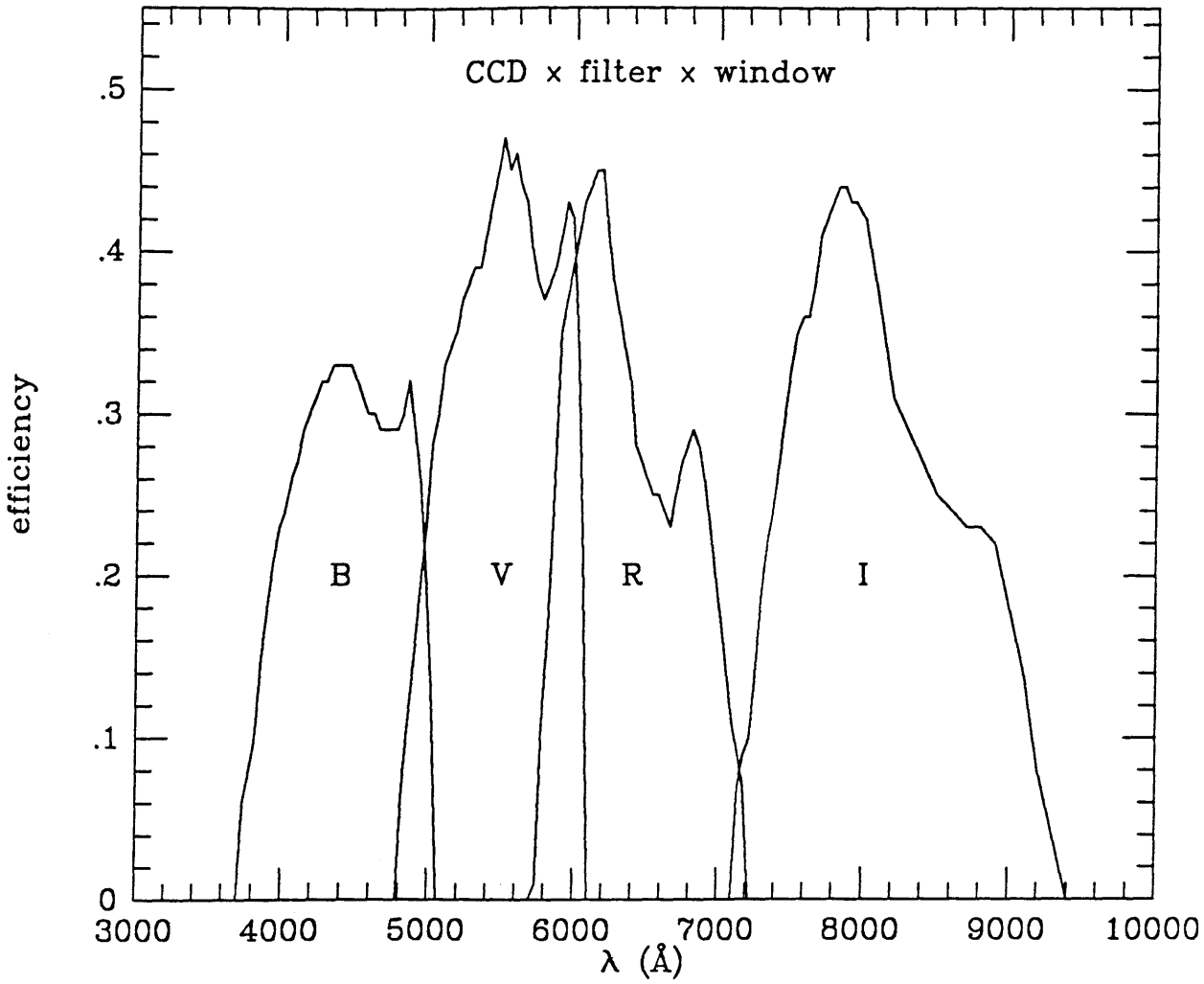

FIGURE 5.6 System efficiency for the broadband photometric bandpasses. The efficiency curves are the product of the TI-4849 CCD quantum efficiency (measured by Texas Instruments), a standard KPNO set of Mould BVRI filters (transmission curves provided by the manufacturer - Omega Optical), and the transmission of the S1-UV quartz window in the dewar. The transmission of the atmosphere and the reflections from aluminum have not been included in this plot.

that a V=7.5 star has a photon flux of 1 photon cm^{-2} s^{-1} $Å^{-1}$ at the top of the atmosphere. The following Table lists the measured efficiencies, and m_1's (magnitude of an object that yields 1 electron per second) for the TI-4849 CCD and the TI-850 × 750 CCD on the 1.3m and 2.4m MDM telescopes.

Table 5.2
System Efficiencies

	TI-4849 CCD			TI 850 × 750 CCD		
	ε	m_1 (1.3m)	m_1 (2.4m)	ε	m_1 (1.3m)	m_1 (2.4m)
B	0.18	23.28	24.59	0.20	23.39	24.73
V	0.22	23.50	24.81	0.23	23.56	24.94
R	0.24	23.54	24.88	0.15	22.89	24.28
I	0.14	23.40	24.71	0.08	22.76	24.09

The average efficiencies have been calculated with help from equation 5.3 for a number of Landolt standard stars and faint standard stars from Christian *et al.* (1985). These efficiencies, which include the telescope (2 reflections from aluminum) and the transmission through one airmass, should be compared to the calculated system efficiency shown in Figure 5.6. This plot was generated using the measured transmission curves for the Mould *BVRI* filters (provided by the manufacturer), the transmission of the quartz dewar window, and the measured quantum efficiency of the TI-4849 CCD (provided by Texas Instruments). If a reasonable value of ~0.8 is chosen for the reflectivity of the telescope mirrors, and if one includes the absorption of one atmosphere, then the average efficiencies for the bandpasses shown in Figure 5.6 agree with the values listed in Table 5.2. No quantum efficiency measurements were available for the TI 850 × 750 CCD, however both CCDs were manufactured in a similar way and should have similar efficiency. The TI-4849 CCD was a special prototype built on 100 Ω-cm silicon (compared to 5-10 Ω-cm for typical devices). Since the width of the depletion region increases with epitaxial layer resistivity for a given gate voltage, this 100 Ω-cm CCD has a thicker active area for detection of near-infrared photons, and this translates into the higher quantum efficiency in *R* and *I* bands compared to the TI 850 × 750 CCD which was built on 10 Ω-cm silicon. On the other hand, the TI 850 × 750 CCD was built with slightly thinner gates and gate oxide, so it has correspondingly better blue response than the TI-4849.

REFERENCES:

Bessel, M.S. 1979, "UBVRI Photometry II: The Cousins VRI System, Its Temperature and Absolute Flux Calibration, and Relevence for Two-Dimensional Photometry," *P.A>S.P.*, **91**, 589.

Bessel, M.S. 1986, "VRI Photometry III: Photographic and CCD R and I Bands and the Kron-Cousins RI System," *P.A.S.P.*, **98**, 1303.

Christian, C.A., Barnes, J.V., Butcher, H., Hayes, D.S., Mould, J.R., and Siegel, M. 1985, "Video Camera/CCD Standard Stars," *P.A.S.P.*, **97**, 363.

Hayes, D. and Latham, D. 1975,"Atmospheric Extinction and the Absolute Spectral Energy Distribution of Vega," *Ap.J.*, **197**, 593.

Landolt, A. 1983, "*UBVRI* Photometric Standard Stars Around the Celestial Equator," *Astron. J.*, **88**, 439.

Oke, J.B., and Gunn, J.E. 1983, "Secondary Standard Stars for Absolute Spectrophotometry," *Ap.J.*, **266**, 713.

Schild R. 1983, "CCD Photometry of M67 Stars Useful as *BVRI* Standards," *P.A.S.P.*, **95**, 1021.

Schild, R. 1985, "CCD Observations of M67 Stars Useful as Photometric Standards," *P.A.S.P.*, **97**, 824.

Stern, R.A., Liewer, K., and Janesick, J. 1983,"Evaluation of a virtual-phase charged-coupled-device as an imaging x-ray spectrometer," *Rev.Sci.Instrum.*, **54**, 198.

Thuan, T.X., and Gunn, J.E. 1976, *P.A.S.P.*, **88**, 543.

Wade, R.A., Hoessel, J.G., Elias, J.H., and Huchra, J.P. 1979, "A Two-Color Photometric System for the Near Infrared," *P.A.S.P.*, **91**, 35.

Chapter 6

Observations and Analysis of the Steep-Spectrum Radio Source Sample

This chapter describes the observations of the galaxy cluster candidate fields and presents the results of these observations. Section 6.1 outlines the history of the CCD instrument development and presents a summary of the observations carried out while the instrument was under construction. Section 6.2 explains the techniques used to analyze the CCD data. Optical identifications for the steep-spectrum radio sources, including reproductions of some of the CCD images and *VLA* maps, are presented in Section 6.3. This section also presents detailed descriptions of the cluster properties, and compares existing radio and optical data on the cluster fields. Section 6.4 presents additional observations of three interesting distant clusters that were not part of the steep-spectrum sample. Some of the global properties of the radio-selected sample are discussed in Section 6.5, and a summary follows in Section 6.6.

6.1 Instrument Development and Observations

The instrument described in the last two chapters was actually built in a number of stages during the years of 1986, 1987, and 1988. During all of this instrument development, observations of the cluster candidate fields were made whenever possible with whatever instrument and telescope configuration was then available. The first instrument configuration, a precursor to the current large-format CCD camera and now a stand-alone instrument called the *BRICC* (Big Red Imaging CCD Camera), was fabricated in 1986 to operate a single TI-4849 (584 x 390) virtual-phase CCD. The *BRICC* consists of a simple filter-wheel, shutter, and a bare CCD (no reimaging optics) mounted at the cassegrain focus of either the 1.3m or 2.4m telescope. The original CCD camera portion of this instrument was very similar to our laboratory x-ray CCD system described in Luppino, *et al.* (1987); a primary ehancement being the installation (in early Spring of 1987) of a new analog signal chain incorporating a 16-bit analog-to-digital converter, which allowed full use of the CCD dynamic range. The *BRICC* is now in regular use at MDM Observatory, and is described in detail in Luppino (1989). A number of cluster observations were made with this instrument.

When the TI 850 x 750 CCDs became available, the camera head and dewar was designed and built to hold four of these imagers as described in Chapters 4 and 5. Initially, however, only *one* of these larger-format virtual-phase chips was operated with the *BRICC* electronics. The CCD camera head housing the four TI 850 x 750 CCDs was mounted in place of the TI-4849 camera head on the *BRICC* mounting plate, offset so that the optical axis was centered on the best of the four big CCDs. This instrument arrangement was used for the bulk

Table 6.1
Summary of Observations

Dates	Telescope	CCD	Pixel Size	Field Size	Remarks
Aug 1987	1.3m	TI 4849	.47" × .47"	4.6' × 3.0'	Engineering - initial checkout of the BRICC and the TI 4849 CCD camera
Dec 1987	2.4m	TI 4849	.25" × .25"	2.4' × 1.6'	First planned SSRS observations - run plagued by bad weather and problems with scattered light from the improperly baffled 2.4m telescope.
March 1988	1.3m	TI 4849	.47" × .47"	4.6' × 3.0'	Engineering checkout of the upgraded 16-bit system and first light for a TI 850 × 750 chip - some observations made with TI 4849 chip.
April 1988	1.3m	TI 850 × 750	.47" × .47"	6.7' × 5.9'	Observations with *best* single TI 850 × 750 CCD - major portion of the dark time used to acquire 4-color images of Cl 1358+6245.
May 1988	2.4m	TI 850 × 750	.25" × .25"	3.5' × 3.1'	Limited field of view and poor seeing - nevertheless, some new clusters discovered
Dec 1988	2.4m	TI 850 × 750	.25" × .25"	3.5' × 3.1'	Faulty 2.4m mirror support system repaired midway through run - extremely poor quality data acquired at the beginning of run. After telescope was repaired, the weather was terrible, and the CCD camera window suffered dewing problems that contaminated the few images that were obtained .
March 1989	2.4m	TI-4849	.72" × .72"	5.0' × 6.7'	Some cluster images were acquired during an observing run for a different program. The TI 4849 CCD camera was mounted behind the Mk III spectrograph used as a 2.8:1 focal reducer - corners of the field were somewhat vignetted.
March 1989	4m	TI-2 800 × 800	.29" × .29"	4.0' × 4.0'	CCD images of 5 clusters were acquired during an observing run for a different program. KPNO TI-2 CCD was used at the prime focus of the 4 meter telescope. The weather conditions for this run were excellent with clear, photometric sky and subarcsecond seeing throughout the run.
April 1989	1.3m	TI 850 × 750	.47" × .47"	6.7' × 5.9'	Large amount of high quality, three color (*VRI*) images acquired for confirmed clusters identified last Spring.

of cluster observations in this thesis. During the Summer of 1988, the electronics for controlling all four of the TI 850 × 750 CCDs were completed. At the same time, work started on the design and construction of the new system for the Lincoln Laboratory 840 × 840 CCD. The Lincoln Laboratory camera head has been completed, but the electronic controller is still under construction, and no galaxy cluster observations have been carried out with this CCD system. See Chapter 8 for a discussion of future observing plans and instrument development.

A summary of the observations is listed in Table 6.1. Additional CCD images of five cluster fields were obtained in March of 1989 with the TI-2 prime-focus CCD on the Kitt Peak 4m telescope. This data was taken in spectacular conditions under photometric skies with sub-arcsecond seeing. Further observations were carried out in April 1989 on the MDM 1.3m telescope. Overall, the CCD data is of widely varying quality: some of the images were acquired in photometric conditions when both the telescope and instrument were working perfectly. Others were taken under good sky conditions with a malfunctioning instrument, or under poor sky conditions with a properly-functioning instrument.

6.2 Data Acquisition, Reduction and Analysis Techniques

In order to aid in flattening and cosmic ray removal, multiple images, with the telescope slightly displaced between exposures, were taken for most of the observed cluster fields. These CCD images were then analyzed using, for the most part, data reduction tools developed, supported, and kindly provided by John Tonry. The primary reduction program was Tonry's modification of *VISTA*, a program originally supplied by Todd Lauer. The following reduction procedure was followed on clusters for which the data was good enough to warrant thorough analysis.

An image first had its bias level removed and then an appropriately scaled dark current frame was subtracted. The image was then flattened using high signal-to-noise pictures of the twilight sky. The flattened frame was trimmed to remove the overclocked pixels and multiplied by a mask which flagged all known cosmetic defects. After each frame making up a *stack* was prepared in this way, all of the frames were shifted into registration (by integer pixel shifts) and fed to *autoclean* , a program (again, written by John Tonry) designed to remove cosmic rays automatically from a number (N>3) of identical images. *Autoclean* assumes that each successive image in the stack can be represented as a linear combination of the first image in the stack, so that pictures with different exposure times or sky backgrounds can be compared. At each position (x,y), *autoclean* looks at the stack of pixels, and determines whether one of the pixels in the stack deviates significantly from the median of the stack (this identifies cosmic rays). The program then removes any bad pixels from the stack. An average, cleaned image is created by averaging each image's contribution to a pixel, while ignoring any pixels flagged as bad. Since *autoclean* creates an average picture made up of all of the shifted images, it automatically deals with matching the background when building a mosaic picture of a field larger than the size of the detector. Once a stacked picture was created, photometry was accomplished using the aperture photometry tools of *VISTA*. In

addition, some of the fields containing obvious rich clusters were processed using *FOCAS*, the *Faint Object Classification and Analysis System* (Jarvis and Tyson 1981; Valdes 1982).

6.3 Optical Identification of the Steep-Spectrum Radio Source Fields

A total of 52 fields were observed: 46 were SSRSs and 6 were other sources that contained a possible or known distant cluster of galaxies. Of the 46 SSRS fields, 16 were removed from the following analysis because the data were extremely poor. Of the remaining 30 SSRSs, 15 have certain optical identifications (as a galaxy, group cluster or quasar) and another 11 have probable IDs (the candidate ID is within 15 arcseconds of the center or one of the lobes of the radio source). Four of the sources, 4C 23.39, 0936+26, 4C 67.17.1 and 1623+25, have no apparent optical counterpart (down to the limiting magnitude of the observations). In addition, a very distant cluster of galaxies was serendipitously discovered in the CCD images of 4C 67.17.1 (well away from the position of the radio source).

Detailed descriptions of all 30 of the SSRS fields follow. The optical ID was called a cluster of galaxies if the number of galaxies in the CCD field exceeded a 3σ fluctuation in the number of background galaxies expected based on the limiting magnitude of the observation. In other words, a source was identified as a cluster of galaxies if $N_{CCD} > N_{expected} + 3\ (N_{expected})^{1/2}$. The number of background galaxies was estimated by integrating the *R*-band number counts of Tyson (1988) down to the limiting magnitude of the observation. The limiting magnitude was computed by measuring the noise/pixel in the sky (σ_{sky}) for each CCD frame. The limiting magnitude for a 5σ detection is then $m_{lim} = m_0 - 2.5 \log (5\ N^{1/2}\ \sigma_{sky})$ where N is the number of pixels in the aperture used for the photometry, and m_0 is the magnitude zero point for the observations.

CCD images for some of the radio sources identified with clusters are shown in Figure 6.1 (included at the end of this section), and *VLA* maps for the SSRS fields seen with the *VLA* are shown in Figure 6.2 (also included at the end of this section). All of the radio data (*VLA* maps, spectral indices and flux densities) were kindly provided by Ian McHardy and Brin Cooke. For each radio source, the position of the optical ID (or at least the nearest galaxy) is shown plotted on the *VLA* map. Table 6.2 lists all of the radio information on the observed SSRS sample. Column (1) lists the SSRS name. Often the radio maps have double-lobed or complex structure, so the 1950.0 coordinates of the lobes or knots of highest surface brightness are listed in columns (2) and (3) and the component is labeled (N,S,E,W,C) in column (4). The *VLA* radio flux (in mJy) at 1411 MHz for each of these lobes or knots can be found in column (5) and the total radio flux from the source in column (6). Column (7) contains the spectral index. Note that α was measured between 38 and 178 MHz for the 4C sources (as determined by Slingo and Baldwin and Scott), and α was measured between 80 and 160 MHz for the other sources. The classification of the optical ID (galaxy, quasar, group or cluster) is listed in column (8) and column (9) identifies the feature of the radio source with which the optical galaxy is associated. In column (8), uncertain identifications are indicated by leading (?) while uncertain classifications are indicated by trailing (?).

The celestial coordinates of the optical ID can be found in columns (10) and (11). The angular separation (Δ) between the nearest component of the radio source (either one of the radio lobes of the center of a double-lobed source) and the optical ID is listed in column (12). Note the optical positions are good to ± 3 arcseconds. Finally, the R magnitude of the optical ID is listed in column (13).

Table 6.2
Steep-Spectrum Radio Source Positions and Optical IDs

(1) SS RADIO SOURCE	(2) RADIO COORDINATES α (1950.0)	(3) RADIO COORDINATES δ (1950.0)	(4)	(5) $S_{1.4}$	(6) $S_{1.4(tot)}$	(7) α	(8) OPT[6] ID	(9) ID POS	(10) OPTICAL ID COORDINATES α (1950.0)	(11) OPTICAL ID COORDINATES δ (1950.0)	(12) Δ	(13) R_{ID}[1]
0047–03	00 47 11.3	–02 59 14.1	W	810	1052	1.88	Cl	W	00 47 11.6	–02 59 14.7	4	22.4♦
	00 47 13.9	–02 59 23.9	E	252								
0059+01	00 59 39.8	01 47 41.4	N	350	725	2.15	Cl	C	00 59 41.2	01 47 03	2	21.3♦
	00 59 42.1	01 46 29.9	S	375								
0251+00	02 51 07.0	00 48 27.0	S	471	703	1.58	?Cl	S?	02 51 06.7	00 48 21	7	21.2
	02 51 07.6	00 48 46.2	N	232								
0717+17	07 17 34.3	17 04 08.6	W	607	807	1.81	?G	W?	07 17 33.6	17 04 11	6	19.9
	07 17 40.9	17 04 50.1	E	200								
0745–19[2]	07 45 18.4	–19 10 11.4	C	2410	2410	1.3[2]	Cl	C	07 45 18.4	–19 10 11.4	0.5	15.88
0752+18	07 52 51.2	18 31 45.0	C	590	590	1.62	?Cl	C?	07 52 50.9	18 31 39	7	21.3♦
0825+01	08 25 24.8	01 22 32.2	N	420	601	1.91	?G?	C?	08 25 25.9	01 22 27	12	19.6
	08 25 25.1	01 22 22.9	S	181								
0829+14	08 29 09.6	14 02 25.2	S	315	562	1.63	?Q	C?	08 29 13.6	14 02 49.0	14	V=19.8
	08 29 10.8	14 02 58.0	C	3								
	08 29 12.4	14 03 31.6	N	244								
0840+29	08 40 06.2	29 54 15.3	S	478	959	1.54	Grp	C	08 40 07.1	29 54 57.2	2	18.9
	08 40 07.0	29 54 54.1	C	16								
	08 40 07.8	29 55 33.8	N	465								
0903+25	09 03 17.9	25 49 26.6	S	290	600	2.10	Cl	C	09 03 19.5	25 49 43	6	19.31♦
	09 03 18.8	25 49 37.9	C	20								
	09 03 20.1	25 49 54.4	N	290								
0910+23	09 10 42.6	23 50 05.0	S	702	1135	1.67	G	C	09 10 42.9	23 50 10	2	I=18.4
	09 10 43.1	23 50 15.8	N	433								
0936+26	09 35 59.2	26 11 39.6	...	61	61	2.08	?Grp	...	?09 36 01.0	26 12 35.8	...	?19.0
4C 67.17.1	09 42 39	67 40 25		...	...	1.32	?Grp		09 42 31.3	67 40 36	...	19.0
0942.1+67[3]	...	...	...	...	...	...	Cl	...	09 42 07.3	67 39 00	...	21.5

0950+25	09 50 47.5	25 30 19.1	S	230	1039	1.71	?G?Q?	S	09 50 47.4	25 30 19	2	V=20.4
	09 50 48.7	25 30 38.3	N	809								
1057+30	10 57 17.4	30 43 53.4	N	388	891	1.62	G	C	10 57 20.4	30 43 16.9	2	21.2
	10 57 23.5	30 42 35.3	S	503								
1127−03	11 27 36.1	−03 12 34.2	S	314	632	2.00	?Cl	N?	11 27 35.8	−03 12 43.7	10	21.0♦
	11 27 36.4	−03 13 22.2	N	318								
1139+18	11 39 00.2	18 48 39.9	C	734	734	1.60	G	C	11 39 00.3	18 48 42	2	22.5
4C 58.22	11 40 07.1	58 24 33.0	S	504	613	1.29	Cl	C	11 40 07.8	58 24 38.6	3	19.04♦
	11 40 08.0	58 24 39.1	C	87								
	11 40 14	58 25 06	N	22								
1150+26	11 50 11.7	26 30 50.5	W	140	385	1.74	Q?G?	C	11 50 13.9	26 30 53	5	19.5
	11 50 15.3	26 30 52.9	E	245								
1222+26	12 22 01.3	26 29 48.6	W	307	675	1.51	Cl	C	12 22 02.9	26 29 50	0.5	19.42
	12 22 02.9	26 29 51.8	C	10								
	12 22 04.1	26 29 54.0	E	358								
1234+26	12 34 02.0	26 51 51.0	N	243	562	1.57	?Cl	S?	12 34 03	26 51 38	5	20.32♦
	12 34 03.1	26 51 33.7	S	319								
1358+24	13 58 49.4	24 27 13.1	S	197	792	1.84	Cl	C	13 58 49.9	24 27 23.5	3	18.26
	13 58 50.1	24 27 26.9	N	595								
4C 23.37	14 13 38.8	23 21 10.0	S	95	194	1.31	Cl	C	14 13 38.8	23 21 22.7	1	18.66
	14 13 38.8	23 21 21.6	C1	5								
	14 13 38.8	23 21 25.3	C2	6								
	14 13 38.5	23 21 40	N	88								
1436+03[4]	...	...	...	...	...	1.55	Cl	...	14 36 06	03 53 00	...	16.9
1437+22	14 37 38.0	22 03 39.6	S	226	456	1.74	Grp	C	14 37 38.0	22 03 45	2	17.1
	14 37 38.1	22 03 46.1	C	16								
	14 37 38.2	22 03 49.6	N	214								
4C 23.39	14 43 21.6	24 03 16.7	...	119	119	1.20	...	...	...	...	...	...
4C 7.38	14 44 02.6	07 41 37.6	W	330	667	1.22	G?Cl?	W?	14 44 02.5	07 41 33.3	5	20.9
	14 44 03.5	07 41 34.1	C	17								
	14 44 04.9	07 41 27.5	E	320								
1623+25	16 23 01.9	25 12 04.8	...	396	689	1.86	...	...	...	...	...	...
	16 23 02.2	25 12 11.8		293								
1643+13	16 43 08.7	13 27 10.7	S	469	851	2.62	?Cl	C?	16 43 08.4	13 27 37.2	20	21.4
	16 43 11.4	13 28 10.2	N	382								

2325+04[5]	23	25	30.4	04	19	09.4	N1	160	219	1.83	?Cl	N1?	23	25	30.3	04	19	43.2	20	21.9♦
	23	25	31.4	04	18	38.7	S1	59												
	23	25	34.9	04	23	07.3	N2	163												

1 Diamond superscripts signify that the radio ID, if a member of a cluster, is not the brightest galaxy in the cluster.

2 0745−19 is also PKS0745−191 which is described in Fabian *et al.* (1985). This x-ray luminous cluster is at a redshift of z=0.103 and shows evidence of a massive cooling flow in excess of 1000 $M_{\odot}$ yr^{-1}.

3 This potentially very distant cluster was discovered serendipitously in the field of 4C 67.17.1 about 3' E by 2' S of the galaxy assumed to be the optical ID of the SSRS. This cluster can be seen as a faint group of galaxies near the bright star in the SW corner of Figure 6.1-Plate 1.

4 1435+03 is also Abell 1942. Since this is a well known cluster of galaxies, it is was not subsequently observed with the *VLA*. The listed redshift and coordinates are taken from Abell, Corwin and Olowin (1989).

5 The low resolution radio map for 2325+04 shows what is probably two separate radio sources separated by ~4 arcminutes. A cluster of galaxies may be associated with the southernmost component. The total radio flux was computed using only the two southernmost (first two) entries in this table.

6 The following notation is used to indicate how confident we are of the optical identification (although the reader should look at the positions plotted on the radio maps) and classification. A leading (?) indicates the identification is uncertain. A trailing (?) indicates the classification is uncertain, e.g. ?Cl would mean there is a cluster in the field but the ID'ed galaxy in the cluster is not certain; Cl? would mean the ID is certain, but the classification as a cluster is uncertain.

0047–03 This SSRS has classical double-lobed radio structure as shown in the *VLA* map in Figure 6.2. The optical CCD image was taken during the December 1988 run when there were problems with the weather, telescope and instrument. The CCD data is of very poor quality and only covers a field of view of ~2'. Nevertheless, the optical ID is a faint R=22.4 galaxy which appears to be a member of a cluster dominated by two brighter members with R~20.7 The position of the optical ID is associated with the western lobe of the radio source and is shown plotted on the *VLA* map in Figure 6.2. We estimate this cluster to have z=0.62.

0059+01 The radio map of this SSRS shown in Figure 6.2 is typical of a classical double-lobed radio galaxy with two bright radio lobes but no central compact core. One of the radio lobes has a low surface brightness tail extending along the axis of the source. The optical CCD image was taken during the December 1988 run when there were problems with the weather, telescope and instrument. The CCD data are of very poor quality and only covers a field of view of ~2'. There are two candidates for the optical ID. The first is a R=19.8 galaxy plotted as B on the *VLA* map. This galaxy appears to be the brightest member of a clusters of galaxies. Another galaxy, however, is closer to the center of the two radio lobes and is shown plotted as A on the *VLA* map. This fainter galaxy has R=21.3. We estimate this cluster to be at redshift z=0.51.

0251+00 The radio map of this SSRS shown in Figure 6.2 is typical of a classical double-lobed radio galaxy with two bright radio lobes but no central compact core. Again, the optical CCD image was taken during the December 1988 run when there were problems with the weather, telescope and instrument. The CCD data are of very poor quality and only covers a field of view of ~2'. The optical ID for the radio source appears to be an R=21.2 galaxy which is the brightest member of a cluster. This galaxy is not centered between the radio lobes, but appears to be located near the SW lobe as shown plotted on the *VLA* map. We estimate this cluster is at redshift z=0.69.

0717+17 While the low-resolution radio map shows a hint of classical double-lobed structure, the high-resolution *VLA* map shown in Figure 6.2 indicates the source is fairly complex with a brighter southwestern knot. A CCD image taken with the TI 4849 CCD on the 1.3m telescope reveals a faint R=19.9 galaxy located near the brighter radio knot. There is another faint R=21.5 galaxy NE of this position. The brighter galaxy is labeled B on the *VLA* map in Figure 6.2. The fainter is labeled A.

0745–19 This source is a well-known x-ray cluster of galaxies described by Fabian *et al.* (1985). The steep-spectrum radio source is compact and lies in the core of a cluster of galaxies containing a massive cooling flow of 1000 $M_\odot$ yr^{-1}. The cluster is at a redshift of z=0.103 and has an x-ray luminosity of L_x (2-10 keV) = 1.8×10^{45} erg s^{-1}.

0752+18 This radio source has a bright circular core with a faint extension to the northeast. A CCD image taken with the TI 4849 CCD on the 1.3m telescope reveals a very faint R=21.3 galaxy some 7" SW of the radio position. The location of this identification is shown on Figure 6.2. There are 38 galaxies in this field down to a limiting magnitude of R_{lim}=22.5 which classifies this as a cluster, although not a very rich cluster. The brightest cluster member is a triple nucleus R=18.8 galaxy located 68" to the NE. This galaxy is estimated to have a redshift of z=0.39.

0825+01 The radio source has classical double-lobed structure but shows no central compact core. The optical counterpart appears to be an isolated R=19.5 galaxy although this optical position is 10-15" E of the radio position as shown on the *VLA* map. There is no evidence for a cluster down to a limiting magnitude of R_{lim}=20.4 (note: the CCD image was taken while the moon was up).

0829+14 This steep-spectrum radio source shows classical double-lobed structure with a compact central core. The optical CCD images reveal a compact group near the radio source. The actual ID is a star-like blue object that appears to be a quasar located ~15" E of the center of the radio lobes. A spectrum was obtained (by McHardy) for this object with the 4.2m William Herschel Telescope (WHT) on LaPalma indicating the object is a quasar with redshift z=0.6.

0840+29 The *VLA* maps (shown in Figure 6.2) of this steep-spectrum radio source show it to have classical double-lobed structure with a compact central component. The optical images reveal three closely-spaced galaxies that may be part of a faint, compact group. One of these galaxies is positionally coincident with the compact radio core shown on the *VLA* map. There is no evidence of a rich cluster of galaxies down to the limiting magnitude of R_{lim}=21.7. A spectrum obtained (by McHardy with the 4.2m WHT) for the brightest (R=18.9) galaxy coincident with the radio source indicates this galaxy is at z=0.4.

0903+25 The *VLA* map indicates this radio source again has complex low surface brightness structure similar to a classical double with a compact core. The optical counterpart is an R=19.3 galaxy that is the member of a rich cluster. The ID galaxy is not the brightest cluster member. In fact, it is located 64" away from the center of the cluster which is dominated by the double galaxy shown in Figure 6.1-Plate 5. This CCD image was taken with the 2.4m telescope in December 1988 in "less than ideal" conditions. Subsequent imaging in April 1989 with the 1.3m telescope revealed a large cluster dominated by a "dumbell" central galaxy whose components are separated by only 7.2 arcseconds. The brighter of the galaxies has R=18.6, but the aperture is certainly including light from the nearby companion. We classify this rich cluster as BM type II and RS Type B and estimate it to be at redshift z=0.36.

0910+23 The low-resolution *VLA* map (B Array) of this radio source shows classical double-lobed structure. Optical images of this field were obtained with the 1.3m telescope in *I* band. The optical ID is an I=18.4 isolated galaxy with a few small, faint satellite galaxies. This may be a distant cD group. There is no indication of a rich cluster down to a limiting magnitude of I_{lim}=20.4. We estimate this source to be at redshift z=0.40.

0936+26 A *VLA* map for this SSRS is not included in Figure 6.2. The source was barely seen, having a flux of only 61 mJy at 1411 MHz. The radio source has a very steep spectrum (α=2.08) and may be identified optically with a small, compact group located northwest of the very bright star shown in Figure 6.1-Plate 5. This ID is questionable, however, since the group of galaxies is located nearly an arcminute N of the radio position. The brightest galaxy in this group has R=19.0. There is no evidence of a "rich cluster" down to a limiting magnitude of R_{lim}=21.8.

4C 67.17.1 This radio source was detected by Slingo (1974) at 408 MHz, but not at 1400 MHz (with the Cambridge One-Mile telescope). This source was also not seen with the *VLA* A-array at 1411 MHz. A deep *R* CCD image of this field was acquired with the TI-2 800 × 800 PFCCD on the Kitt Peak 4m telescope in March 1989. The image was taken in sub-arcsecond seeing with 0.29" pixels A reproduction of this CCD image is shown in Figure 6.1-Plate 2. There are no galaxies at the position of the radio source (at about the left center of the field in the CCD image); however, there is a faint cluster of galaxies near the saturated star in the SW corner, and there is brighter galaxy with a few smaller companions in the NE portion of the frame. The brighter galaxy has R=19.0 and appears to be a cD group which we estimate to have a redshift of z=0.42; this group is closer to the radio position than the faint cluster which we believe is a serendipitous discovery. The magnitude of the brightest galaxy in the faint cluster is R=21.5 and we estimate the cluster has a redshift of z=0.73.

0950+25 The *VLA* map for this SSRS is shown in Figure 6.2. *V* band CCD images were acquired on the 1.3m telescope and indicate the optical counterpart is a blue star-like object coincident with the SW radio lobe. This object has V=20.4 and may be a quasar.

1057+30 A *VLA* map of this cluster shown in Figure 6.2 is again typical of a classical double-lobed radio source. CCD images taken with the 2.4m telescope reveal a R=21.2 galaxy at the radio position. The position of this optical ID is plotted on the *VLA* map an is situated exactly at the center of the double radio lobes. In addition, there are ~50 faint galaxies spread over the ~2' × 3' CCD field, however this number is less than a 3σ fluctuation in the number of expected background galaxies so we do not classifiy this SSRS as a cluster of galaxies.

1127-03 A *VLA* map of this SSRS is shown in Figure 6.2. This cluster was discovered by McHardy and Cooke from images taken on the AAT. An additional CCD image acquired with the 1.3m telescope is shown in Figure 6.1-Plate 5. The brightest cluster member has R=19.38, but this galaxy is not the optical ID for the SSRS. There are three fainter galaxies that could be the optical IDs and they are shown plotted on the *VLA* map in Figure 6.2. The best choice is the ID marked A on the plot. This galaxy is associated with the northern lobe of the double-lobed radio source. We estimate this cluster to be at a redshift z=0.43.

1139+18 The *VLA* map for this SSRS is not included in Figure 6.2. However, the optical ID (based on the radio position) appears to be a faint galaxy at R~22.5. There is no evidence of a cluster of galaxies down to a limiting magnitude of R_{lim}=23.8.

4C 58.22 The *VLA* map for this SSRS is shown in Figure 6.2. The optical ID is a R=19.0 galaxy that is the second brightest member of a compact cluster. The position of this galaxy is indicated on the radio map and the CCD image is shown in Figure 6.1-Plate 2. The obvious spiral galaxy is undoubtedly a foreground galaxy since it as bright as the brightest cluster galaxy (R=18.92). There are ~90 galaxies in the frame, but only ~30 in the central portion. We estimate this cluster to have a redshift of z=0.41.

1150+26 This SSRS is identified with a star-like R=19.5 object that may be a quasar. The *VLA* map is shown in Figure 6.2 and the position of the optical counterpart is shown plotted on the map. There is also a nearby R=20.8 galaxy to the east of the QSO and this is plotted on the radio map and labeled by E. The QSO is nearly coincident with the center of the double-lobed radio source. There is not an obvious rich cluster of galaxies present down to a limiting magnitude of R_{lim}=23.5.

1222+26 A *VLA* map for this SSRS is typical of a double-lobed radio source with a compact nucleus. The eastern lobe shows some complex structure. A single I CCD image of this field was taken with the PFCCD on the 4m telescope during morning twilight. A cluster was apparent and a reproduction of this image is shown in Figure 6.1-Plate 5. Follow-up observations were carried out on the 1.3m telescope in V and R in April 1989. The optical ID is the R=19.4 brightest cluster member which is coincident with the compact nucleus of the radio source. We estimate the redshift of this cluster to be z=0.47.

1234+26 This SSRS is identified with a small R=20.3 galaxy which may be an outlying member of a very rich, large cluster of galaxies whose center is about 2' north of the radio source. The *VLA* map can be seen in Figure 6.2 which shows the position of the optical ID galaxy. A small portion of this cluster is shown in Figure 6.1-Plate 5. This image was taken with the 2.4m telescope in "less than ideal" conditions, and the

frame does not cover the center of the cluster. Subsequent observations carried out in April on the 1.3m reveal >100 galaxies scattered over a ~7' × 7' field with the brightest member having R=18.8. When seen close-up, the wierd object at the SE corner appears to be tight group of four interacting spiral galaxies (or perhaps just a chance superposition). The cluster of galaxies is classified as BM Type III and at least Richness Class 1. *Einstein* x-ray observations were carried out near this field during observations of N4565. 6 IPC x-ray sources were detected within 30' of the radio position. None of these sources, however, are included in the CCD frame. The positions of these sources are listed in Table 6.4. We estimate this cluster to be at redshift z=0.39.

1358+24 The optical ID for this SSRS is the R=18.26 brightest cluster member in a rich cluster of galaxies. A portion of this rich cluster is shown in Figure 6.1-Plate 5, and a *VLA* map is included in Figure 6.2. The image shown in the Figure was taken with the 2.4m telescope and a small field of view (Note: the image in Figure 6.1-Plate 5 is actually oriented with North to the right and East up). Subsequent images taken with the 1.3m telescope reveal an elongated condensation of ~100 galaxies surrounding the cD galaxy. We classify this cluster BM Type I and RS Type cD. The redshift is estimated to be z=0.35.

4C 23.37 Slingo (1974) suggested this steep-spectrum radio source originated in a faint group. Deep V and I CCD images were obtained for this field with the TI-2 800 × 800 PFCCD on the Kitt Peak 4m telescope in March 1989. The images were taken in sub-arcsecond seeing with 0.29" pixels. The V image is shown in Figure 6.1-Plate 4, and a *VLA* map is shown in Figure 6.2. A few of the brighter galaxies, which are just visible on the POSS, are probably the foreground group that Slingo thought was the steep spectrum radio source. However, the deep CCD images reveal a very rich cluster in the background. Additional R CCD images were acquired with the TI 850 × 750 CCD on the MDM 1.3m telescope in April 1989. The brightest cluster galaxy has R=18.72 and its position is coincident with the center of the double-lobed radio source shown plotted on the *VLA* map. We classify this cluster as BM Type I and RS Type cD. These classifications were based on judicious exclusion of foreground group members. Spectroscopic observations (carried out by McHardy) of the brightest galaxy in this cluster were obtained with the 4.2m William Herschel Telescope (WHT) on LaPalma. These observations yielded an absorption-line redshift of z=0.45 and confirmed the foreground group is at z<0.2).

1453+03 This SSRS is associated with the well-known cluster of galaxies Abell 1942 at z=0.21 and therefore was not observed with the *VLA*. A1942 is a BM Type III cluster with 83 galaxies making it Richness Class 3.

1437+22 The optical ID for this SSRS is an isolated R=17.1 cD galaxy that forms the center of a small group. The position of the ID is at the center of the double-lobed radio source and is shown plotted on the *VLA* map in Figure 6.2. A spectrum of this galaxy indicates it is at a redshift of z=0.20.

4C 23.39 This is one of two of the 30 observed SSRS fields that does not have an obvious optical counterpart down to a limiting magnitude of $R_{\rm lim}$=22.8. The radio map is shown in Figure 6.2.

4C 7.38 A *VLA* map for this SSRS is shown in Figure 6.2. The optical ID is an R=20.9 galaxy. The ID is associated with the western knot of the radio source and its position is shown plotted on the *VLA* map. There are ~65 galaxies in the field down to the limiting magnitude of $R_{\rm lim}$=22.2. This number exceeds the number of expected background galaxies, but there are not enough galaxies to call this a cluster.

1623+25 This SSRS does not have an obvious optical ID. There is a star-like object at the correct Declination but 14" to the east and this objects position is listed in Table 6.2 as the "ID" for the SSRS. There is no evidence of any faint galaxies near the radio source down to a limiting magnitude of $R_{\rm lim}$=22.0.

1643+13 This is another SSRS with classical double-lobed structure and no central source. The *VLA* map is shown in Figure 6.2 and the position of the optical ID is plotted on the map. Optical images taken with the 2.4m telescope reveal a double galaxy near the radio position. The eastern galaxy is closest to the center of the radio lobes but the western galaxy is the brighter with R=21.4. These galaxies are the brightest members of a cluster of galaxies whose redshift we estimate to be z=0.71.

2325+04 The *VLA* map for this SSRS is shown in Figure 6.2. Again, the optical CCD image was taken during the December 1988 run when there were problems with the weather, telescope and instrument. The CCD data are of very poor quality and only covers a field of view of ~2'. The optical ID is a R=21.9 galaxy which is a member of a cluster of galaxies whose brightest member has R=20.0. We estimate this cluster to have redshift z=0.53. The position of the optical ID is shown plotted on the *VLA* map. Note on the radio map there is an additional radio knot ~5 arcminutes to the NE. The position of this knot and its flux is listed in Table 6.2, but the total radio flux does not include this since it is probably a separate radio source.

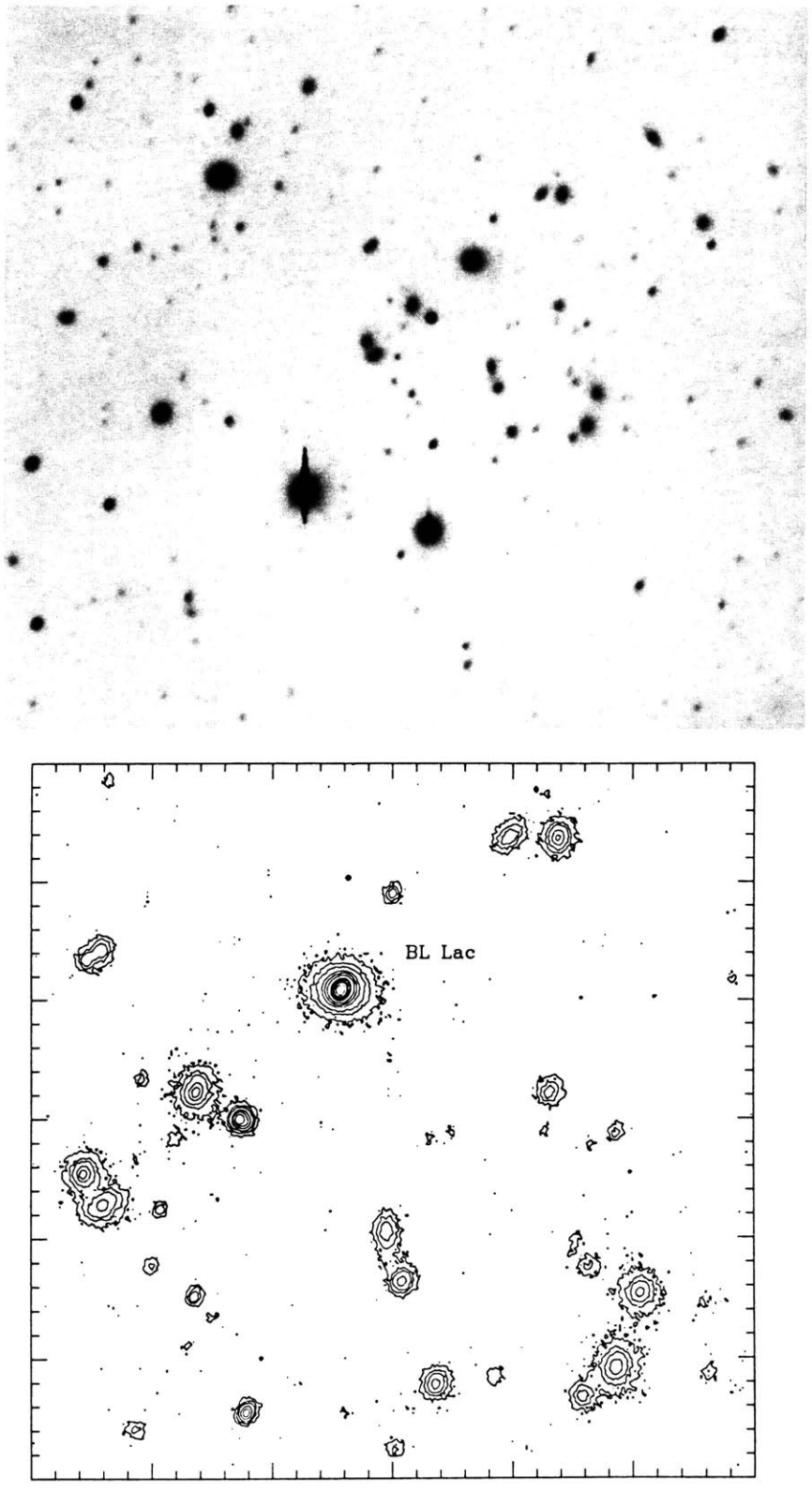

FIGURE 6.1 - **PLATE 1** - CCD images of distant clusters of galaxies. The CCD image at the top shows cluster *Cl 0414+009* which contains a bright x-ray BL Lac object. The BL Lac is the ~ 16.5 mag object located near the upper right center of the frame. The bottom frame is a contour plot of the core of the cluster. This R band image was taken with the prime focus CCD (TI-2) on the Kitt Peak 4m telescope in 0.7 arcsecond seeing. North is up and East is to the left this and all of the following images.

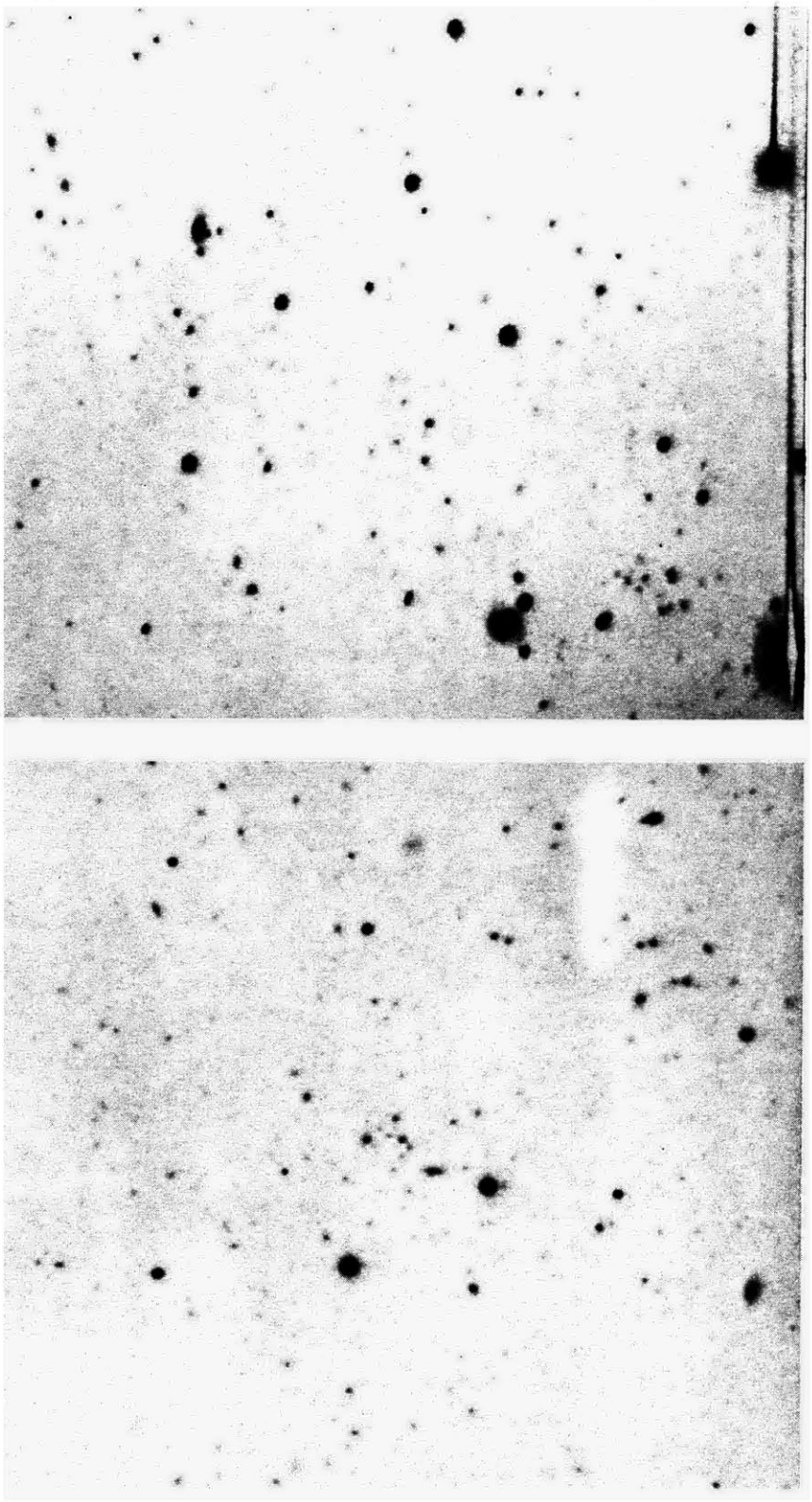

FIGURE 6.1 - **PLATE 2** - CCD images of distant clusters of galaxies. The image at the top shows a faint cluster associated with the steep-spectrum radio source 4C 67.17.1. This image was taken with the prime-focus CCD (TI-2) on the Kitt Peak 4m telescope. The compact cluster shown in the bottom image is coincident with the steep-spectrum radio source *4C 58.22*. This image was taken with the instrument described in this thesis.

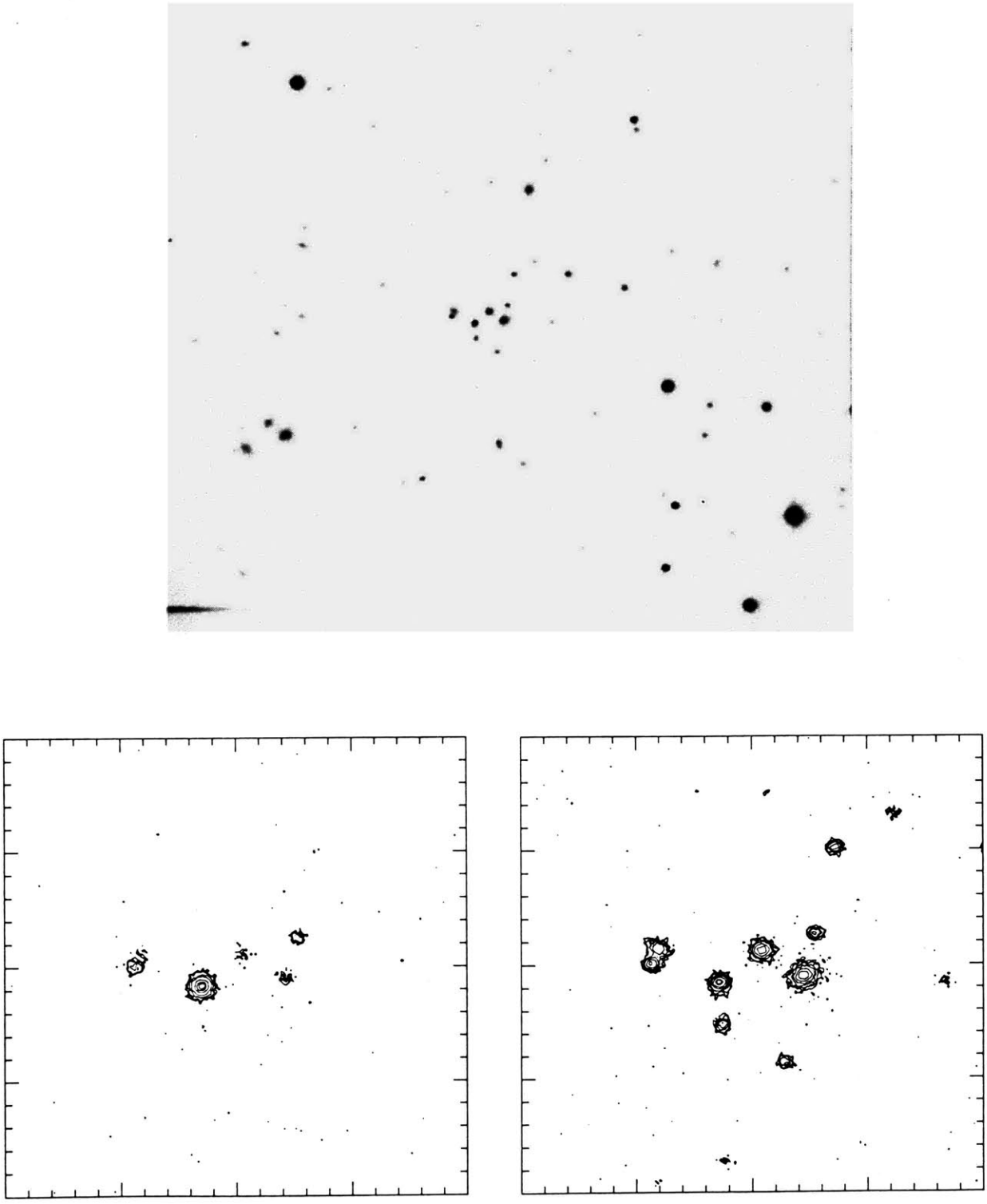

FIGURE 6.1 - **PLATE 3** - CCD images of distant clusters of galaxies. This compact cluster of galaxies, Cl 1217+1006, was discovered surrounding a very blue stellar object believed to be a quasar. The redshift of this object has not been measured. The contour plots in the lower portion of this frame show the core of this cluster in blue (B-band at the left) and red (R-band at the right) light.

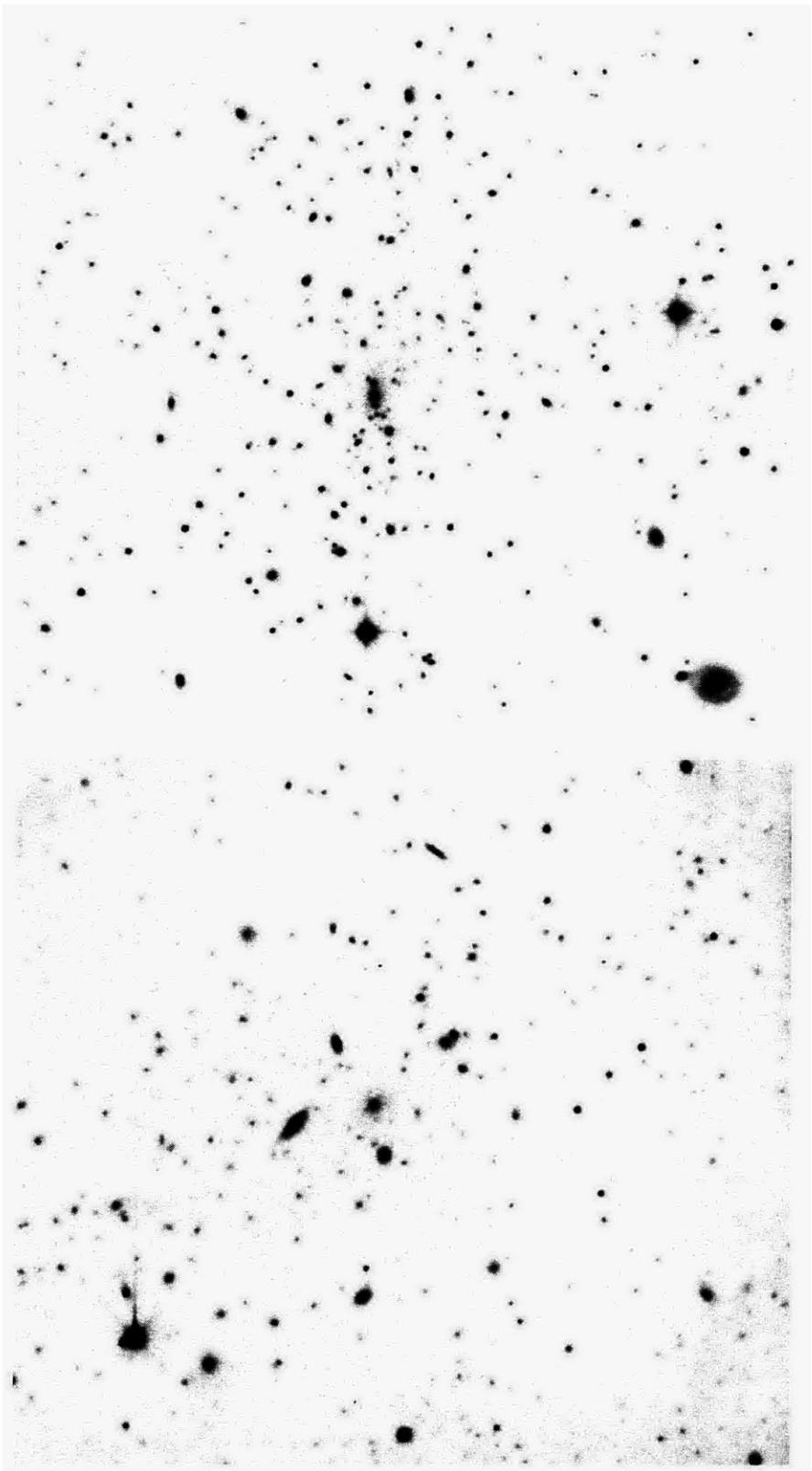

FIGURE 6.1 - **PLATE 4** - CCD images of distant clusters of galaxies. The extremely rich cluster *Cl 1358+6245* is shown in the top image. This cluster, which is at a redshift of z=0.32, was discovered as the optical counterpart of a slightly extended Einstein IPC x-ray source (see Chapter 7 for a detailed study of this object). This image was taken using the instrument described in this thesis. The cluster in the bottom image is coincident with the steep spectrum radio source *4C 23.37*. This V-band image was taken using the prime focus CCD (TI-2) on the Kitt Peak 4m telescope.

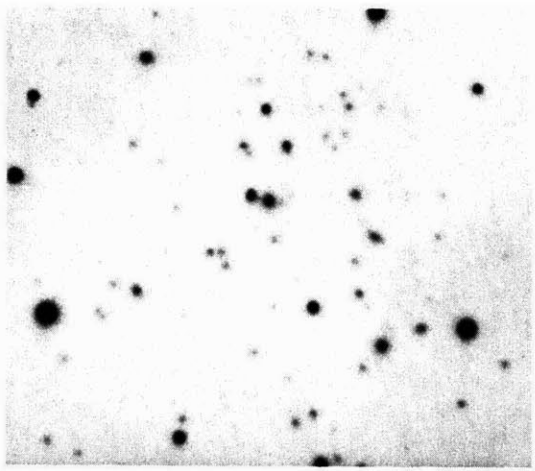

Cl 0903+25

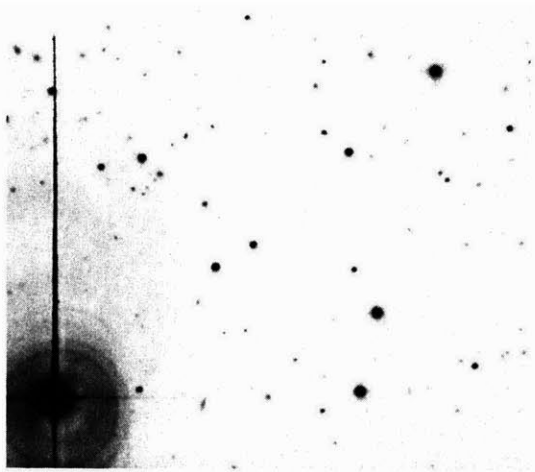

Cl 0936+26

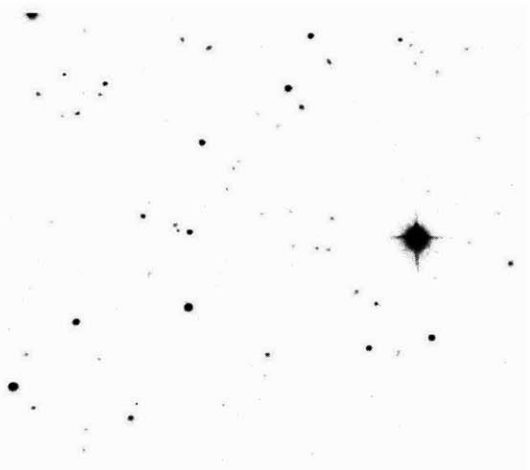

Cl 1127-03

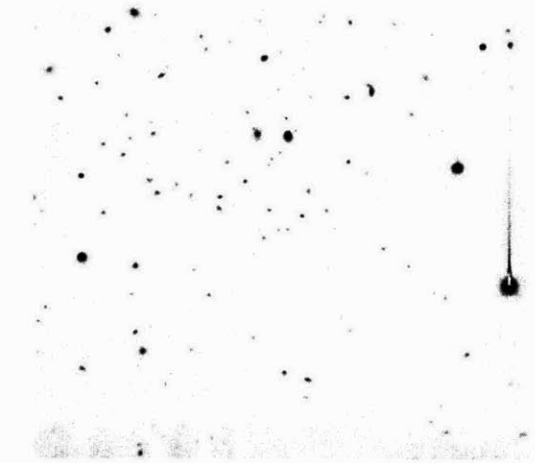

Cl 1222+26

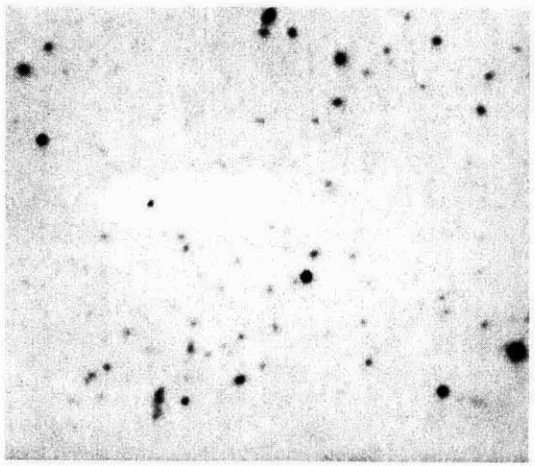

Cl 1234+26

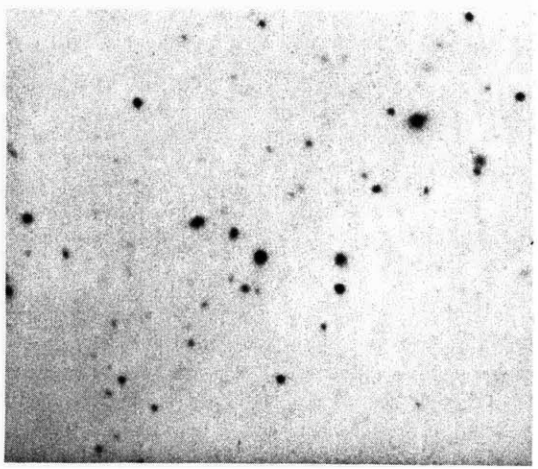

Cl 1358+24

FIGURE 6.2 (cont.) - **PLATE 5** - CCD Images of distant clusters of galaxies. See text for a detailed description of each cluster.

Radio sources: 0047–03 0059+01 0251+00 0717+17

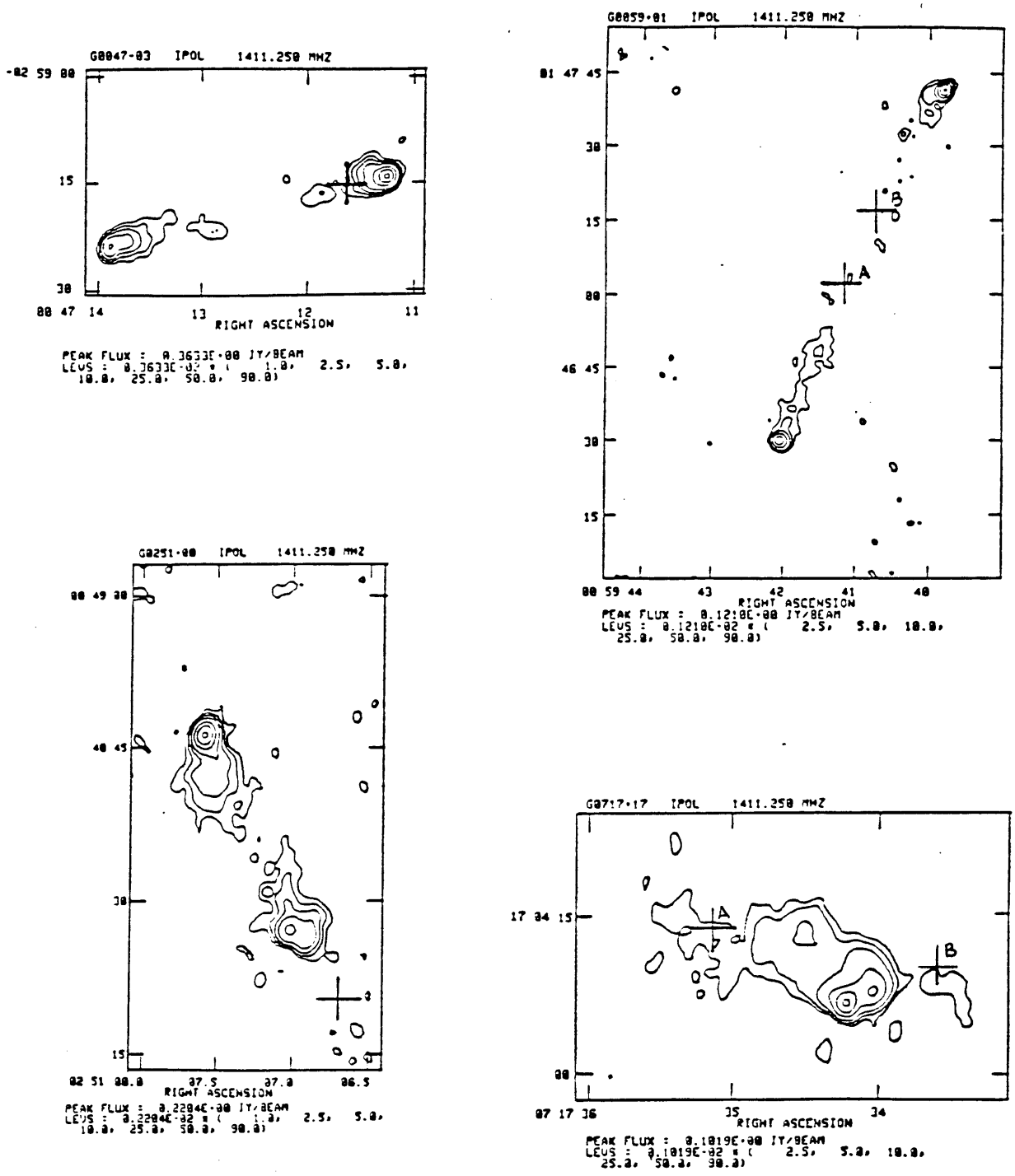

FIGURE 6.2 *VLA* maps and optical IDs of observed steep-spectrum radio sources

Radio sources: 0752+18 0825+01 0829+14 0840+29

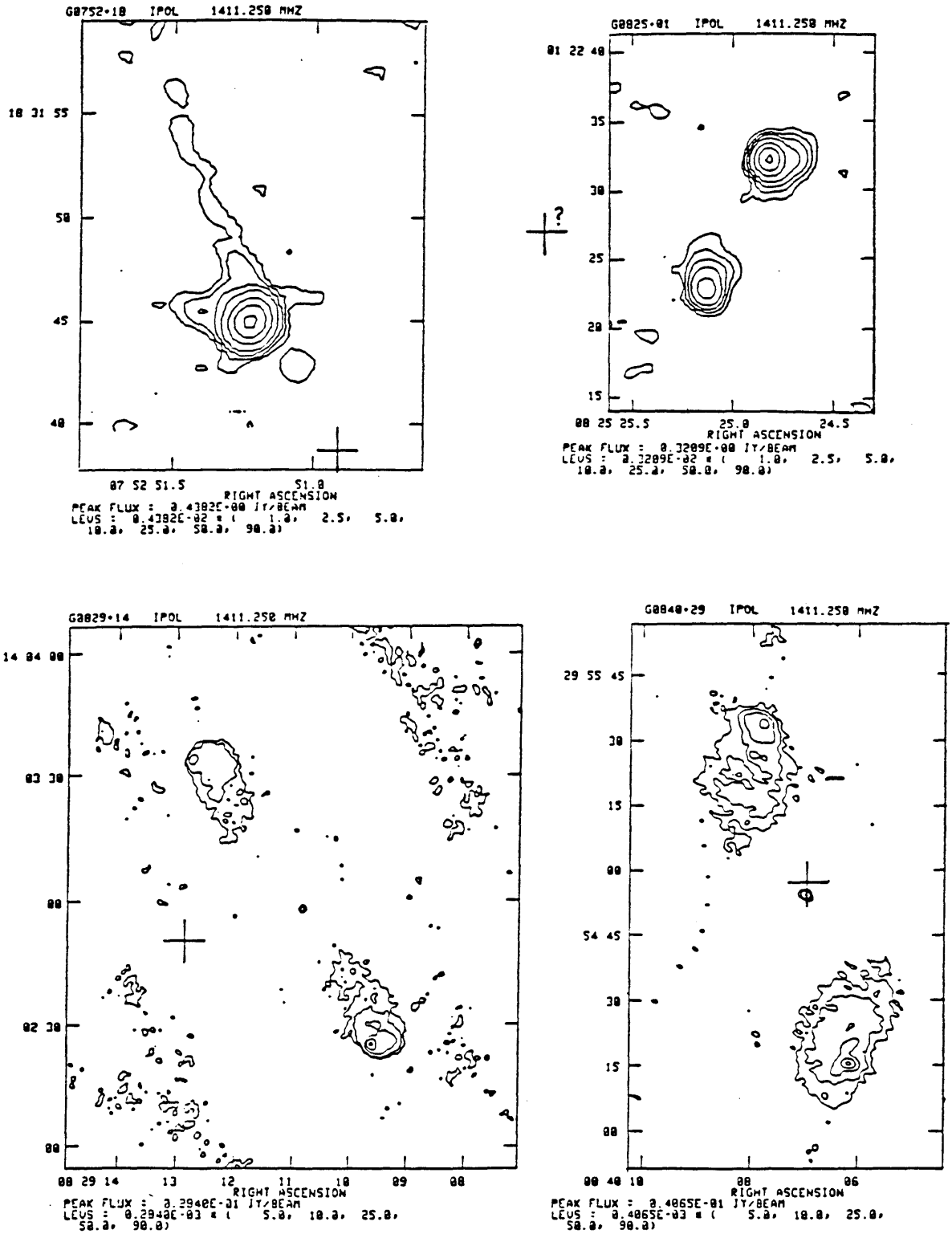

FIGURE 6.2 (continued) *VLA* maps and optical IDs of observed steep-spectrum radio sources

Radio sources: 0903+25 0910+23 0950+25 1057+30

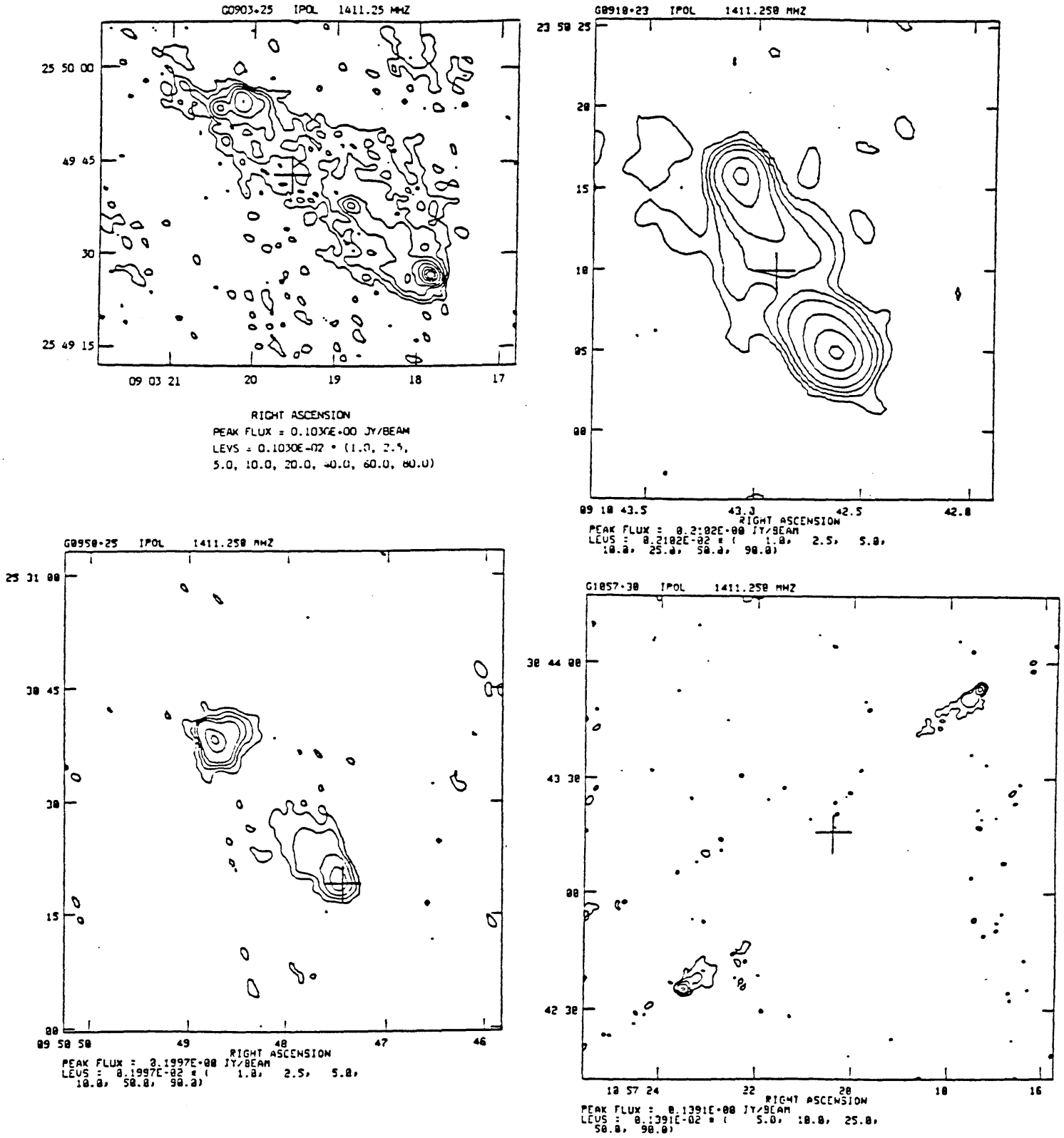

FIGURE 6.2 (continued) *VLA* maps and optical IDs of observed steep-spectrum radio sources

Radio sources: 1127–03 4C 58.22 1150+26

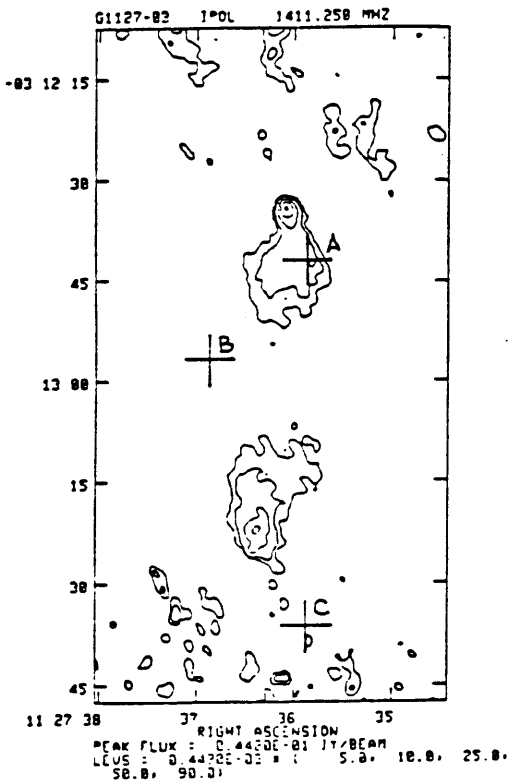

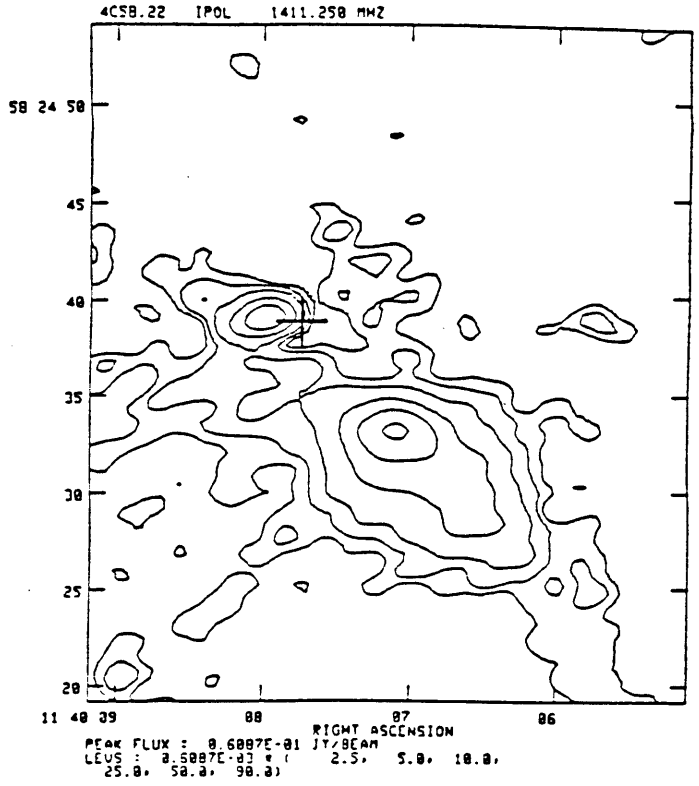

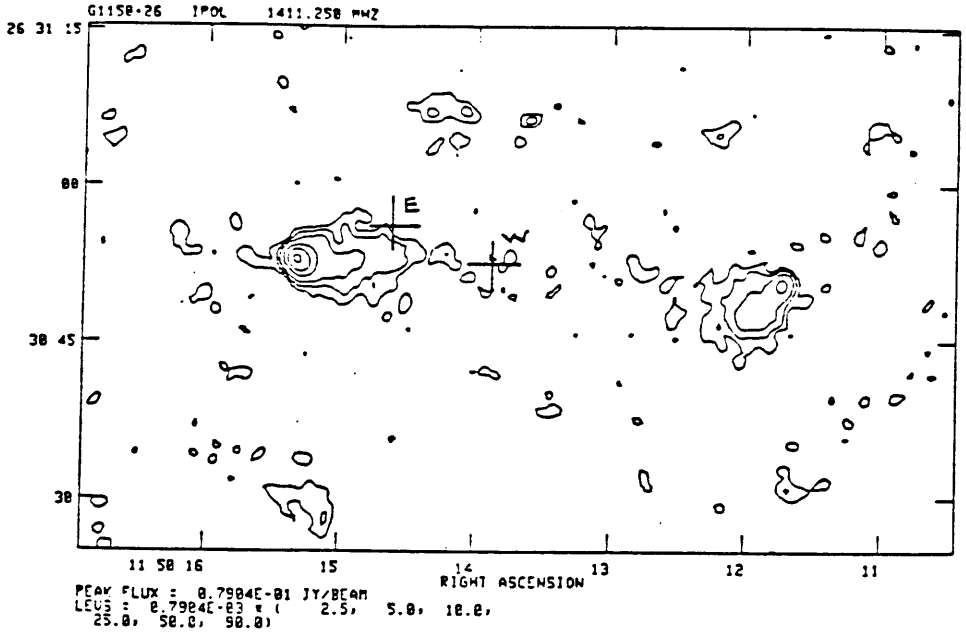

FIGURE 6.2 (continued) *VLA* maps and optical IDs of observed steep-spectrum radio sources

Radio sources: 1222+26 1234+26 1358+24

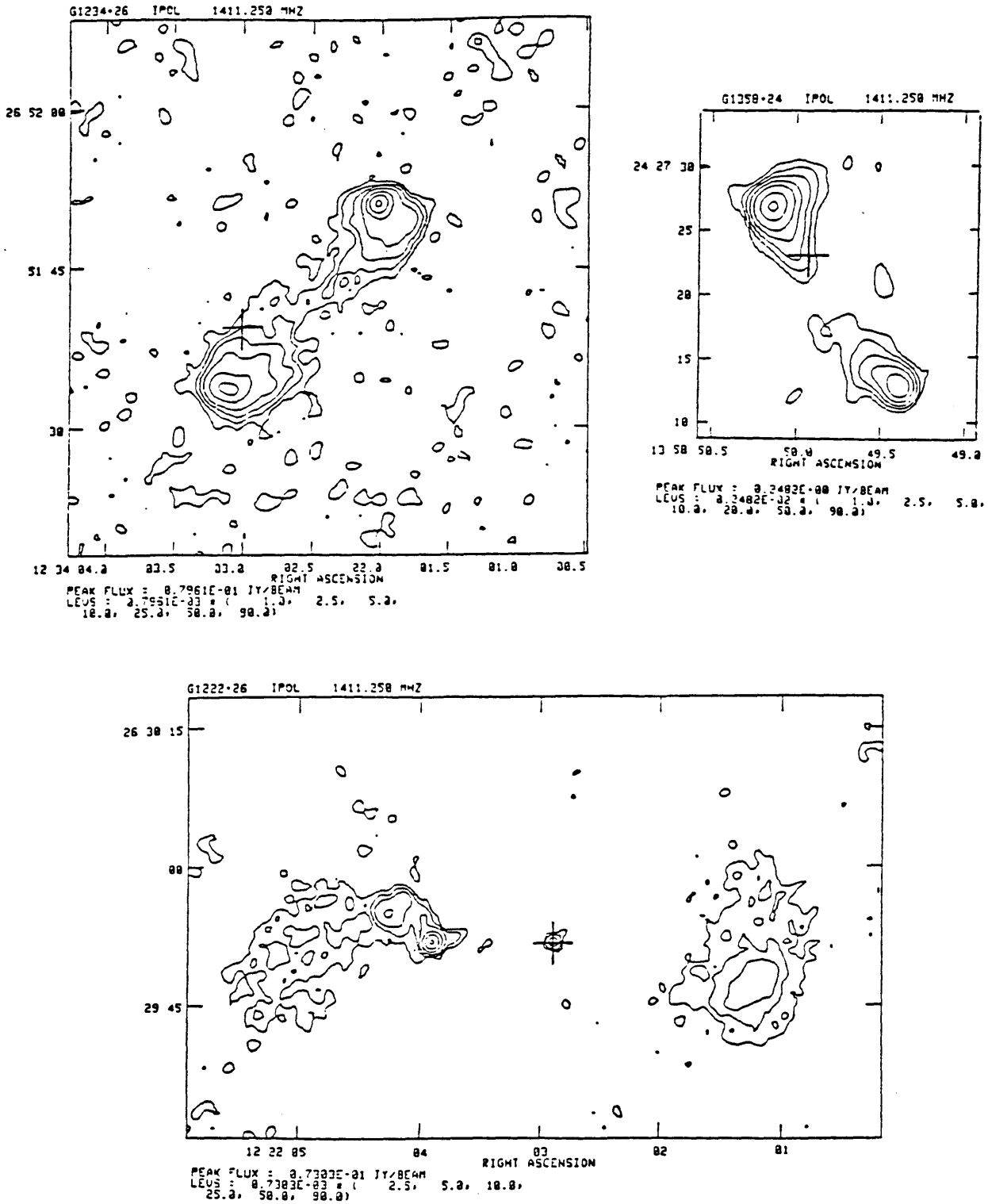

FIGURE 6.2 (continued) *VLA* maps and optical IDs of observed steep-spectrum radio sources

Radio sources: 4C 23.37 1437+22 4C 7.38

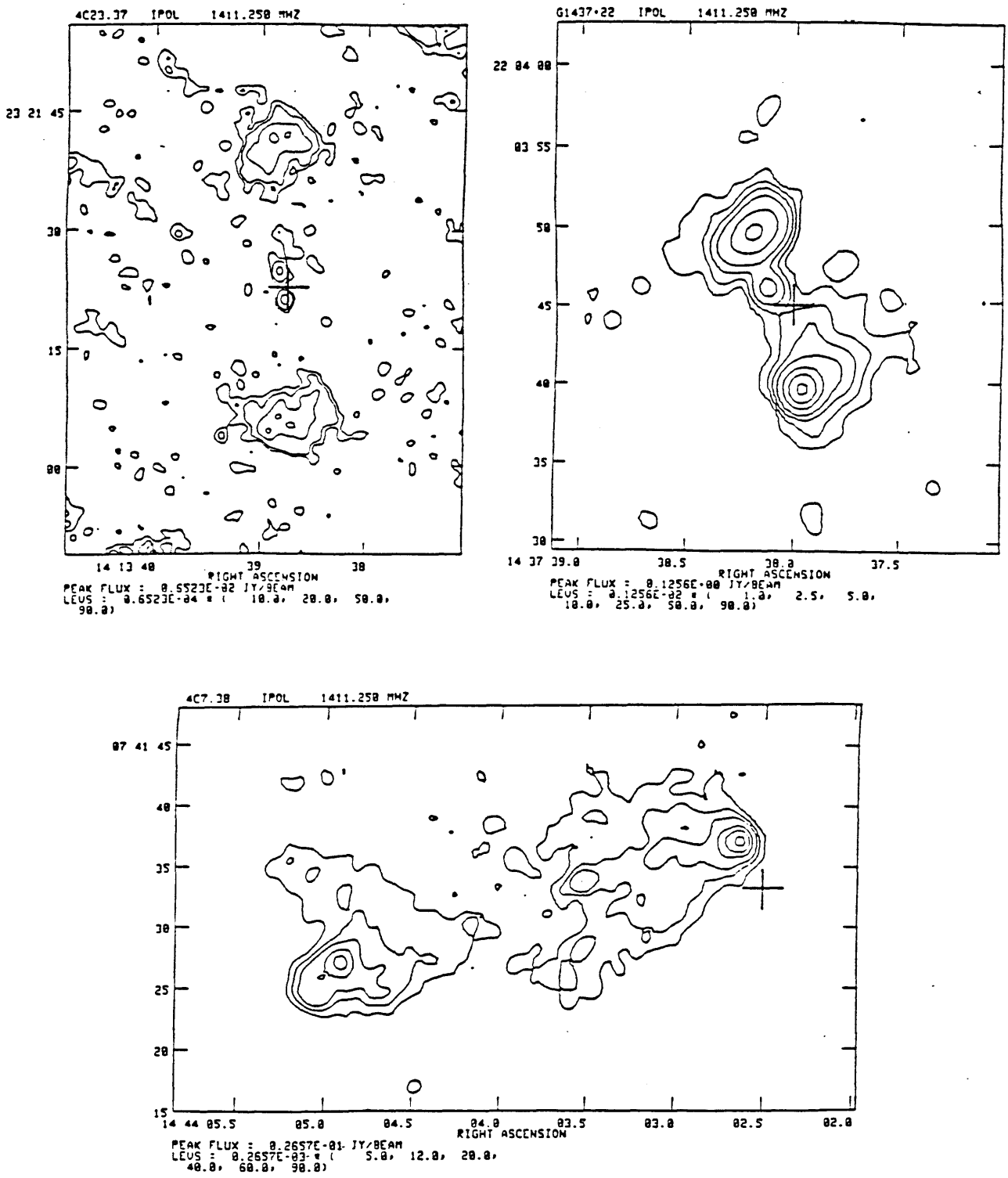

FIGURE 6.2 (continued) *VLA* maps and optical IDs of observed steep-spectrum radio sources

Radio sources:	4C 23.39	1623+25	1643+13	2325+04

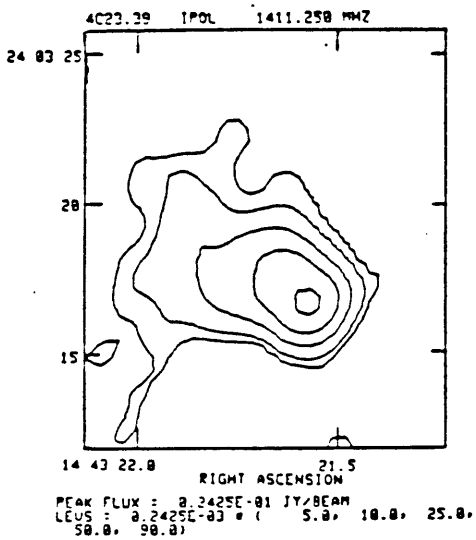

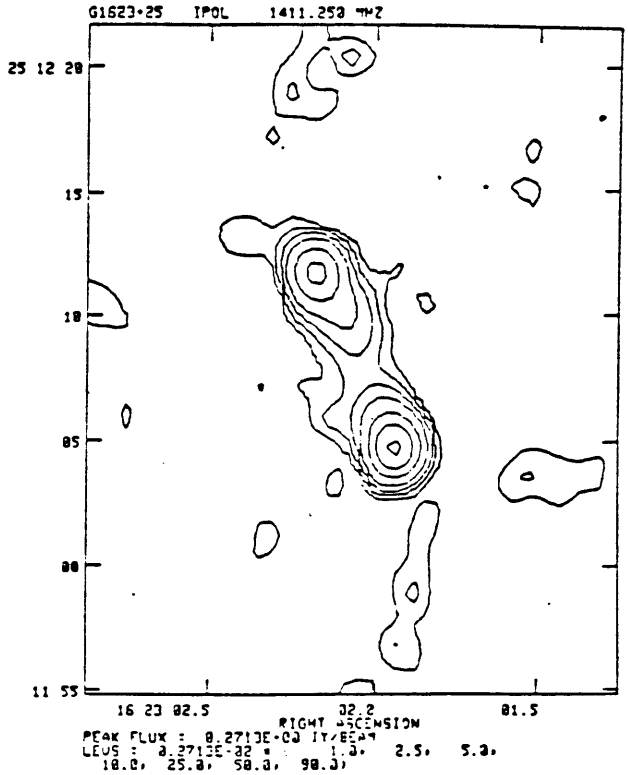

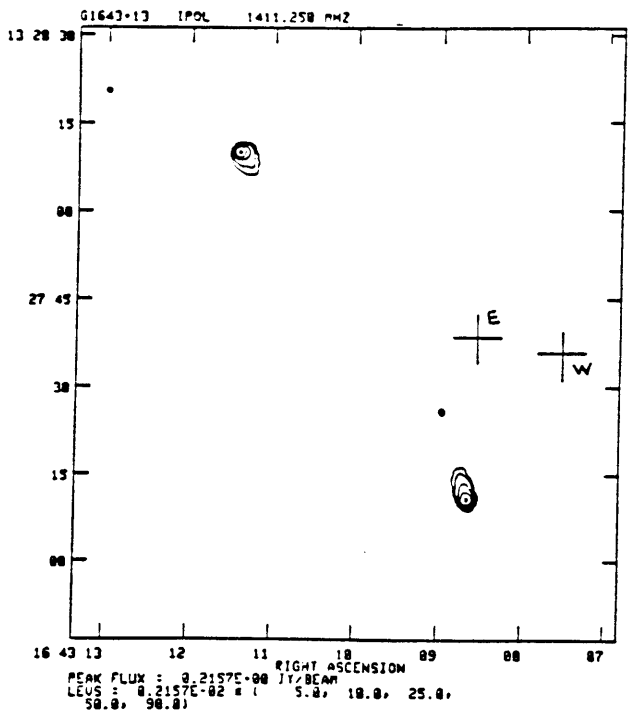

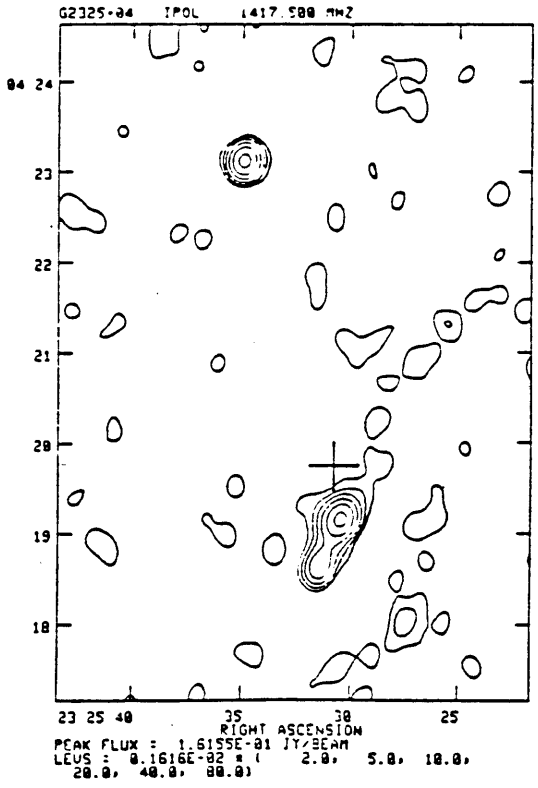

FIGURE 6.2 (continued) *VLA* maps and optical IDs of observed steep-spectrum radio sources

6.4 Additional Non-Radio-Selected Cluster Fields

In addition to the steep-spectrum radio source fields, a number of other interesting objects that might possibly be distant clusters of galaxies were also observed. Three such clusters are listed in Table 6.4 below. Two of the clusters were x-ray selected, and one was optically selected. A detailed description of each cluster is also presented below.

0414+009 This field contains a bright x-ray source coincident with a BL Lac object described in Ulmer *et al.* (1983). These authors observed this object with *HEAO-1* and with the IPC and HRI on *Einstein*. The *HEAO-1* x-ray source was originally thought to be associated with the Abell 480 cluster of galaxies (Ulmer 1980). The Einstein observations, however, showed that the x-ray source was pointlike with a position well away from the Abell cluster. Subsequent *VLA* radio observations revealed a compact source with a flat, nonthermal spectrum coincident with the x-ray source. The authors identified a $V \approx 16.3$ starlike object from the POSS which was coincident with the x-ray and radio sources. An optical spectrum, acquired over the wavelength range between 3900 to 5300 Å was featureless and did not allow measurement of a redshift for the source.

Deep *VRI* CCD images of this field were taken in the with the TI-2 800 × 800 prime focus CCD (PFCCD) on the Kitt Peak 4m telescope in March 1989. The images, which were acquired in sub-arcsecond seeing with 0.29" pixels, reveal a faint, rich cluster of galaxies surrounding the BL Lac object; see Figure 6.1-Plate 1.

The magnitude of the BL Lac is R=16.47. The bright galaxy to the northeast has R=16.91. The brightest of the faint galaxies surrounding the BL Lac have R = 18.76. There are ~35 galaxies in the magnitude range m_3 and m_3+2 making this cluster at least Abell Richness Class 0.

1217+1006 The CCD image in Figure 6.1-Plate 3 shows a faint group (cluster?) of galaxies surrounding an extremely blue object. The blue object was found as part of the APM QSO survey (Foltz *et al.* 1987), and the cluster was brought to my attention by Gordon MacAlpine, who noticed the large number of galaxies present in the guider field while he was attempting to take a spectrum of the quasar. The extreme blue excess of this object is apparent on the B and R contour plots at the bottom of Figure 6.1-Plate 3 [Note: the CCD image in Figure 6.1 has been rotated 180°: North is down and East is to the right].

The magnitude of the blue object (quasar? - BL Lac?) is R=18.08 and the color is $B-R$ = –0.05. The brightest galaxy in the group has R=17.83 and is very red with B–R =

1.84. Note that in R, the blue object is not the brightest object in the cluster. We estimate this group has a redshift $z = 0.3$.

1358+6245 This x-ray selected cluster is was discovered in the field of an *Einstein* IPC x-ray source. Deep, *BVRI* CCD images have been obtained for this object, and the results of this photometry are described in Chapter 7. A spectrum obtained for the central galaxy yields an absorption-line redshift of z=0.32. A CCD image of this spectacular rich cluster is shown in Figure 6.1-Plate 4. This cluster is at least Richness Class 3, BM Type II and RS Type B (although a convincing case can be made for BM Type I and RS Type cD), and exhibits the Butcher-Oemler effect with a blue galaxy fraction f_b=0.18 or f_b=0.10 depending on the background galaxy correction. This cluster is also a luminous x-ray source.

Table 6.4
Properties of Non-Radio-Selected Clusters of Galaxies

CLUSTER	α (1950.0)	δ (1950.0)	z	R	Comments
0414+009	04 14 17.7	00 58 03	0.20	16.47	X-ray BL Lac in a rich cluster of galaxies.
1217+1006	12 17 06.8	10 06 31.9	0.30	18.08	Compact group (cluster?) containing a blue stellar-like object with $B-R$ = –0.05. Object could be a QSO or BL Lac.
1358+6245	13 58 21.0	62 45 33	0.32	18.45	Extremely rich, x-ray luminous cluster.

6.5 Analysis of Steep-Spectrum Radio Sample Properties

a) SSRSs associated with clusters of galaxies: their redshifts and richnesses

Table 6.2 lists the optical IDs for the 30 observed SSRSs. In most cases, the optical ID is coincident with some feature of the radio source (either a radio lobe or the center of a double-lobed source). The offsets Δ for the suspected IDs have been binned in a histogram shown in Figure 6.4a. The measurement error for the optical astrometry was ±3 arcseconds. Looking at Figure 6.4a, we can see that most of the optical IDs are good to within the measurement error. A few of the Δs, however, are greater than 10 arcseconds and these IDs are questionable. It is possible to estimate the probability of finding a cluster of galaxies by chance in the field of a SSRS. If we assume a density of clusters of galaxies of ~2 clusters per square degree with redshifts less than ~0.6 (Gunn, Hoessel, and Oke 1986), and we assume that each SSRS has a characteristic size of ~1 square arcminute, and we suppose that the spatial coincidence of the two will gaurantee an ID (although we actually use a stricter criterion here), then there is a 6×10^{-4} probability of randomly identifying a cluster of galaxies with a SSRS. Since there are ~125 SSRSs in the McHardy and Cooke sample, we can expect 0.07 probability of one of the sample to be a chance alignment of a SSRS with a clusters of galaxies with redshift $z<0.6$.

In order to compare the properties of the SSRSs associated with clusters of galaxies, redshifts were required. The cluster redshifts were estimated using the method of Sandage (1976) assuming that the brightest cluster galaxy has $M_V = -23.3 \pm 0.35$ for a rich cluster of galaxies. For such a galaxy, the R apparent magnitude was computed as a function of redshift $q_0 = 1/2$ and $H_0 = 50$ and is shown plotted in Figure 6.3. The K-corrections were calculated by integrating the spectral-energy distributions (SEDs) of Coleman, Wu and Weedman (1980) for the four types of galaxies E/S0, Sba, Scd and Im (see also Chapter 7 for a plot of these SEDs) through the instrument bandpasses shown in Chapter 6. For a given cluster having a brightest cluster member with apparent magnitude R_{bcg}, the estimated redshifts listed in Table 6.3 were read off of this graph. No attempt at evolutionary correction was made for this rough redshift estimate. Distances determined in this fashion are probably good to no better than ±40% (also assuming the correct galaxy has been identified as the brightest cluster member - not necessarily true for some of the poor data!).

One goal of these observations is to estimate the richness of the discovered clusters of galaxies. This was accomplished using the following procedure. Once the redshift has been estimated, the actual size of the cluster covered by the CCD image can be calculated. In all cases, the CCD images are significantly smaller than the 3Mpc Abell radius (this illustrates the need for a truly "large-format" chip which is properly matched to the seeing). The observed number of galaxies within the CCD field of view can be used to estimate the number within one Abell radius assuming the surface density of galaxies Σ in the cluster can be modelled by some function. For simplicity, we have chosen

$$\Sigma = \frac{1}{r^2 + r_c^{\,2}} \tag{6.1}$$

where r_c is a "core radius" which we assume to be $250 h_{50}^{-1}$ kpc. The number within radius R is then

$$N(<R) = \int 2\pi r\, \Sigma(r)\, dr = \pi \ln\left(1 + \frac{R^2}{r_c^{\,2}}\right) \tag{6.2}$$

and we can determine a scaling factor f_A

$$f_A = \frac{\ln\left(1 + \frac{3Mpc^2}{0.25\,Mpc^2}\right)}{\ln\left(1 + \frac{R^2}{0.25\,Mpc^2}\right)} \tag{6.3}$$

which we will use to convert our observed number of galaxies to the corrected number within a 3Mpc radius.

We are not only sampling a limited portion of the angular extent of these clusters, we are also sampling different portions of their luminosity functions depending on the brightness of the galaxies in the clusters and the limiting magnitude of the observations. We can assume these clusters are described by a universal luminosity function which we will assume is a Schechter (1976) function (see also §2.1 and equation 2.1.1)

$$\phi(m) = N^* (0.4 \ln 10) 10^{-0.4(\alpha+1)(m-m^*)}\, e^{-10^{-0.4(m-m^*)}}\, d(m - m^*) \tag{6.4}$$

Assuming the CCD data is complete down to the limiting magnitude, we can integrate the luminosity function

$$\Phi(m) = \int_{-\infty}^{m} \phi(m)\, dm \tag{6.5}$$

also assuming $M_V(1)$=–23.3 (Sandage 1976), M_V^*=–21.5 (Lugger 1988), and α=–1.25. This "luminosity function correction" can then be applied to the background-subtracted and scaled galaxy counts to determine N* for each cluster. Note that this correction is very sensitive to the limiting magnitude of the observation. A 0.5 magnitude change in the limiting magnitude can alter the associated richness by one Abell Class. If the source confinement model for steep-spectrum radio sources is correct, we would expect to see a correlation between the cluster richness and the spectral index α. In Figure 6.4b the log of the richness (N*) is plotted against the spectral index; however, no correlation is apparent.

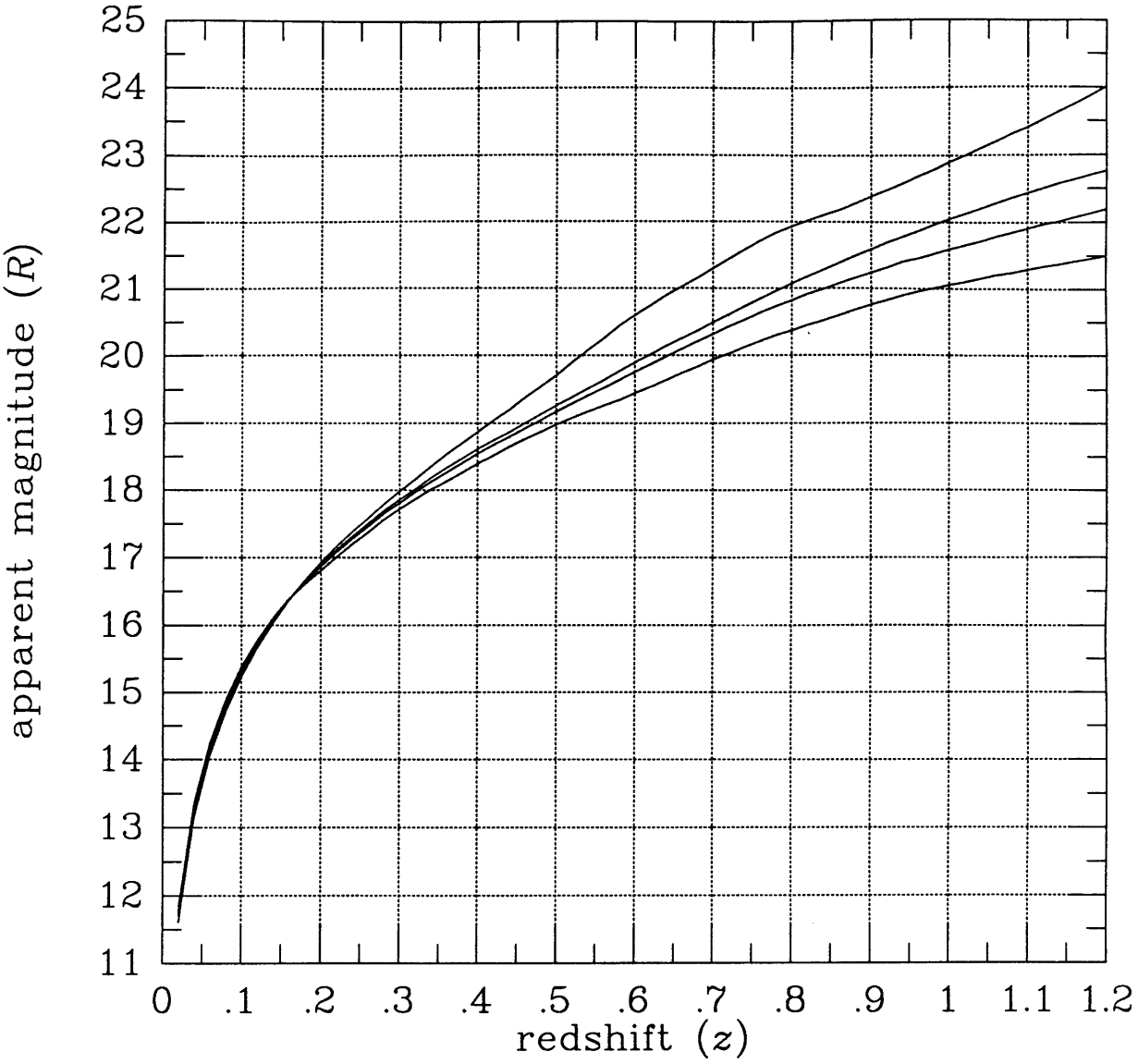

FIGURE 6.3 R apparent magnitude as a function of redshift z for a galaxy with $M_V = -23.3 \pm 0.35$. The K-corrections were computed by integrating the SEDs of Coleman, Wu and Weedman (1980) through the instrument bandpasses. The apparent magnitude was computed assuming H_0=50 km s^{-1} Mpc^{-1} q_0 = 1/2. The top line corresponds to an E/S0 galaxy, the second to a Sbc, the third to a Scd and the bottom to an Im galaxy. No evolutionary corrections have been included.

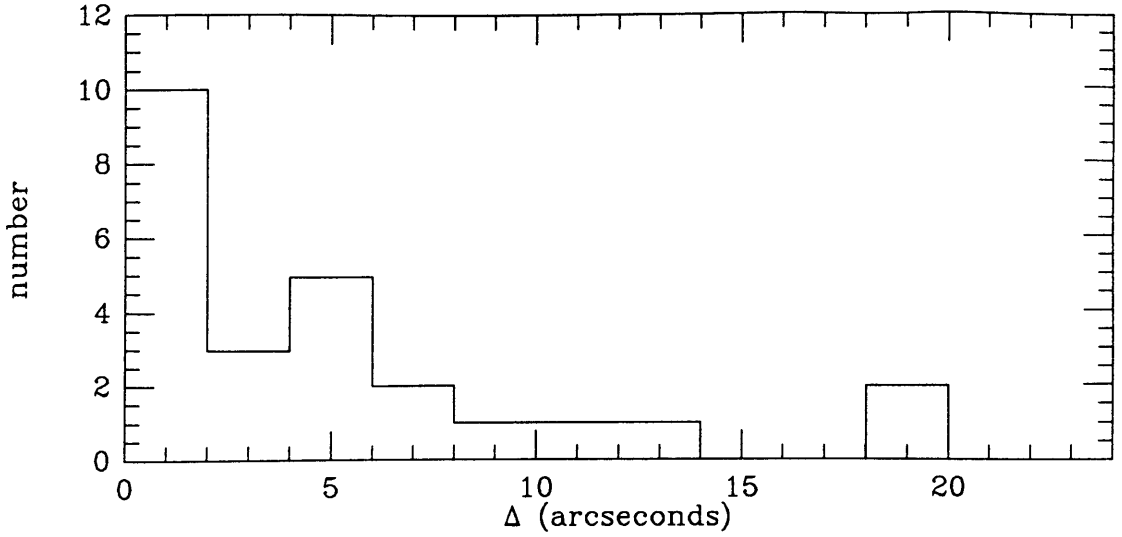

FIGURE 6.4a Histogram of the angular separations of the radio sources and their optical IDs. The measurement error for the optical astrometry was ±3 arcseconds.

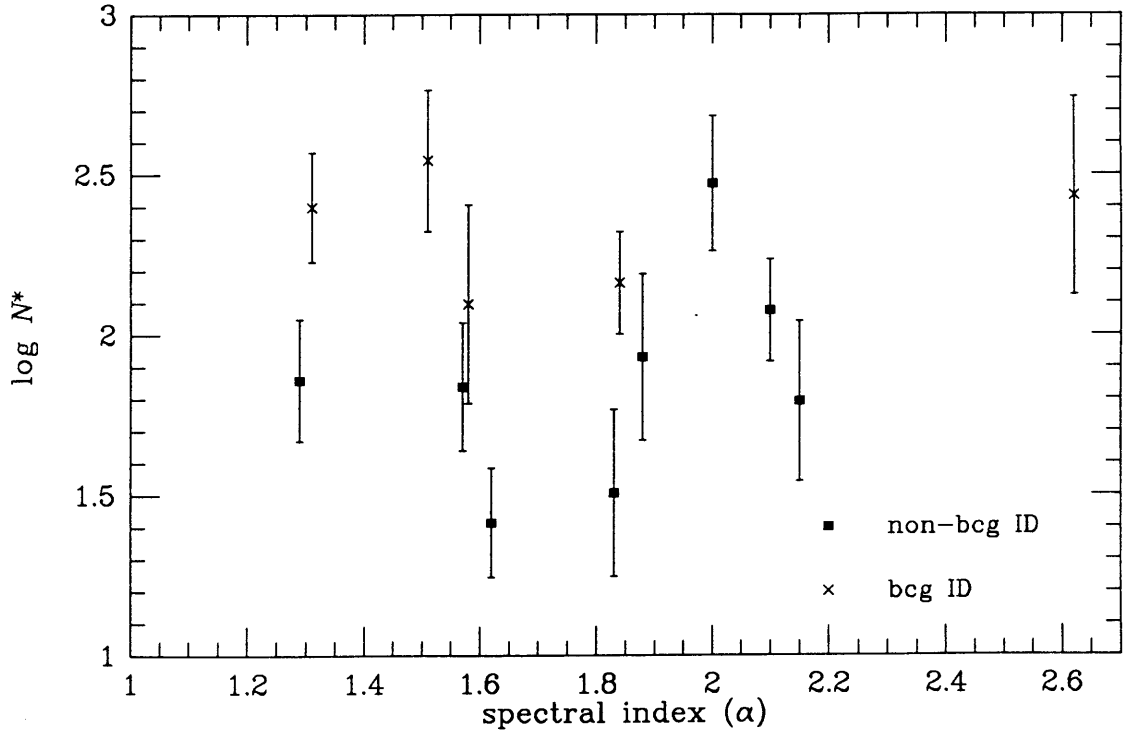

FIGURE 6.4b Correlation of cluster richness with the SSRS spectral index. The clusters have been divided into clusters where the radio source is coincident with the optically dominant galaxy and clusters where the radio source is identified with a fainter cluster member.

The parameters discussed above have been tabulated for the 30 SSRSs and are presented in Table 6.3. The table is divided into two sections: the 15 SSRSs associated with clusters of galaxies, and the remaining 15 sources. In the top portion of the table the radio source name can be found in column (1) and the magnitude limit (5σ – determined as described earlier) of the observation is listed in column (2). The R magnitude of the brightest cluster galaxy is listed in column (3) and the estimated redshift (based on Rbcg) is listed in column (4). If the cluster has a measured redshift, it is given in column (5). Next, the field of view (F.O.V.) of the CCD is listed in column (6) and the number of galaxies counted on the CCD frame is listed in column (7). The expected number of galaxies (based on Tyson counts down to the limiting magnitude of the observations in the CCD field of view) is listed in column (8). A factor which corrects the observed number of galaxies to the number within a 3Mpc radius is listed in column (9) and the total corrected count, $N_{CORR} = f_A(N_{CCD} - N_{expect})$ can be found in column (10). The uncertainty in N_{CORR} is listed in column (11). The value for the Schechter luminosity function integrated to the limiting magnitude is listed in column (12) and the resulting value for $N^* = N_{CORR}/\Phi(R_{lim})$ is listed in column (13). The error estimate $\Delta N^*/N^*$ listed in column (14) was computed by propagating an assumed 0.3 mag increase in the limiting magnitude and the uncertainties in N_{CCD} and N_{expect} (counting statistics) through the calculation of N^*. The relationship between N^* and the Abell richness of a cluster was determined from Figure 5 of Schechter (1976) and the Abell Richness Class for the clusters in Table 6.3 is listed in column (15). Finally, the Bautz-Morgan Type is listed in column (16).

b) radio morphology

The morphologies of all 30 of the steep-spectrum radio sources show remarkable similarity. They are often classical double-lobed radio sources. Some have central sources centered between the radio lobes and some show diffuse, complex structure along the radio axis separating the lobes. There are also sources with some hotspots such as 0717+17 and 1222+26. Conspicuously absent, however, are the types of radio sources commonly associated with clusters of galaxies: head-tail or radio trail sources. "Conventional wisdom" contends that classical double radio sources are rarely associated with clusters of galaxies (Eales 1985; Longair and Seldner 1979); however, there have been some exceptions such as 3C 295 (Baum and Heckman 1986). In this study, however, nearly all of the radio sources found to be associated with clusters have classical double-lobed structure.

c) radio and optical correlations for the SSRS sample

In order to investigate possible correlations among the optical and radio properties of the SSRS sample, the rest frame radio luminosity of the SSRS is required. It is easy to show (with the help of equations 2.2.18 and 2.2.8) that radio luminosity between frequencies ν_1 and ν_2 of a radio source at redshift z with spectral index α is given by

Table 6.3
Properties of the Steep Spectrum Radio Sources

(1)	(2)	(3)	(4)	(5)	(6)	(7)	(8)	(9)	(10)	(11)	(12)	(13)	(14)	(15)	(16)
							CLUSTERS OF GALAXIES								
SSRS	R_{lim}	R_{bcg}	z_{est}	z_{meas}	F.O.V.	N_{CCD}	N_{expect}	f_A	N_{CORR}	±	$\Phi(R_{lim})$.	N*	$\Delta N^*/N^*$	Rich	BM Type
0047–03	23.3	20.7	0.62	...	2' × 1.5'	33	18	3.4	51	24	0.60	85	0.61	1	...
0059+01	22.8	19.8	0.51	...	2' × 1.5'	30	15	3.7	56	25	0.91	62	0.58	1	...
0251+00	23.3	21.2	0.69	...	2' × 1.5'	30	18	3.3	40	23	0.32	125	0.72	2	...
0745–19	...	15.9	0.14	0.10	...	...	...	...	...	...	...	...	...	...	I
0752+18	22.5	18.8	0.39	...	3' × 5'	38	17	2.0	42	15	1.64	26	0.39	0	II
0903+25	21.5	18.6	0.36	...	6' × 5'	95	33	1.6	99	18	0.83	119	0.38	2	II
1127–03	21.4	19.4	0.46	...	6' × 5'	85	32	1.5	80	16	0.27	296	0.49	3	III
4C 58.22	21.8	18.9	0.41	...	6' × 5'	75	35	1.5	60	16	0.83	72	0.44	1	II
1222+26	21.2	19.4	0.47	...	6' × 5'	80	30	1.4	70	15	0.20	350	0.51	3	I
1234+26	21.9	18.8	0.39	...	6' × 5'	100	54	1.5	69	19	1.00	69	0.45	1	III
1358+24	21.2	18.3	0.35	...	6' × 5'	105	30	1.6	120	19	0.83	145	0.37	2	I
4C 23.37	21.2	18.7	0.40	0.45	6' × 5'	120	30	1.5	135	18	0.54	250	0.38	3	I
1436+03	...	16.9	0.21	0.21	...	...	...	...	...	...	...	...	...	3	III
1643+13	23.0	21.4	0.71	...	3' × 3.5'	65	45	1.9	38	20	0.14	271	0.71	3	III
2325+04	23.0	20.0	0.53	...	2' × 1.5'	29	16	2.0	29	13	0.91	32	0.59	0	...

(1)	(2)	(3)	(4)	(5)	(6)	(7)	(8)	(9)
					OTHERS (GROUPS, ISOLATED GALAXIES, QUASARS)			
SSRS	R_{lim}	R_{ID}	z_{est}	z_{meas}	F.O.V.	N_{CCD}	N_{expect}	Comments
0717+17	22.3	19.9	...	...	3' × 5'	30	43	
0825+01	20.4	21.3	...	...	6' × 5'	20	13	moon was up
0829+14	*V*=21.5	*V*=19.8	...	0.60	6' × 5'	35	35	quasar
0840+29	21.7	18.9	...	0.40	6' × 5'	25	48	group
0910+23	*I*=20.4	*I*=18.4	0.40	...	6' × 5'	25	13	cD group
0936+26	21.8	...	...	...	6' × 5'	35	54	**no ID** although group in field
4C 67.17.1	23.0	...	...	...	4' × 4'	70	72	**no ID** - serendipitous(?) z>0.8 cluster in field
0950+25	*V*=21.9	*V*=20.4	...	...	3' × 3.5'	22	13	quasar?
1057+30	23.1	21.2	...	...	3' × 3.5'	50	48	lots of galaxies - cluster?
1139+18	23.8	22.5	...	...	3' × 3.5'	27	110	
1150+26	23.5	19.5	...	...	3' × 3.5'	25	70	
1437+22	20.7	17.1	...	0.2	3' × 3.5'	18	10	image contaminated by streaks - cD group
4C 23.39	22.8	...	...	...	6' × 5'	60	130	**no ID**
4C 7.38	22.2	20.9	...	...	6' × 5'	65	54	maybe a cluster - hard to tell with this data
1623+25	22.0	...	...	...	6' × 5'	32	54	**no ID**

$$L = \frac{4\pi\, d_L^{\,2}\, S_{\nu_o}}{(1-\alpha)\,\nu_o^{\,-\alpha}\,(1+z)^{1-\alpha}}\left[\nu_2^{\,1-\alpha} - \nu_1^{\,1-\alpha}\right] \tag{6.6}$$

where ν_o is the observing frequency and $S_{\nu o}$ is the observed flux density at this frequency (see also Hewitt 1986). "Radio luminosity" is often defined as the portion of the spectrum between 10 MHz and 100 GHz. For example, 4C 23.37 at z=0.45 has an observed flux density at 1411 MHz of 194 mJy and a spectral index of 1.31. The resulting radio luminosity is 4.4×10^{43} ergs s^{-1}. Figure 6.5a plots the log of the radio luminosity as a function of the spectral index. A strong correlation is obvious from the data. This correlation is consistent with the results of Blumenthal and Miley (1979) who noted that sources with the steepest radio spectra are on average more luminous radio emitters and located further away. Since the radio emission is believed to occur in the radio lobes at the boundary of the source and the intracluster medium, and we believe this medium is likely to change systematically with redshift, it is plausible that the correlation of radio luminosity with spectral index is simply a manifestation of a changing intracluster medium with redshift. Figure 6.5b plots the log of the radio flux density at 1411 MHz as a function of the apparent magnitude of the optical ID. In this case, no correlation is apparent.

c) known x-ray sources in the SSRS fields

Since we expect clusters of galaxies selected by the presence of a SSRS to be bright x-ray sources, we searched the *Einstein* database for x-ray sources in the fields of all the objects listed in Table 6.2. Table 6.5 lists the SSRS fields that contain one or more x-ray sources within 30 arcminutes of the SSRS center. Only 5 of the 30 entries in Table 6.2 are listed in Table 6.5; however, this does not mean most of the SSRS sources do not contain x-ray sources. In most of the cases, there were simply no *Einstein* observations of these fields. One cluster, 1234+26, contains 6 x-ray sources within 30' of the radio position. The catalog of observations indicates that this sequence number was part of a program to look for x-ray sources in the halo of N4565 and these sources are probably part of this galaxy. None of the x-ray positions are covered by the CCD images.

Table 6.5
X-ray sources in Observed Steep-Spectrum Radio Source Fields

SS FIELD	X-ray Position α (1950.0)	δ (1950.0)	Seq.#	Counts/s	±
0059+01	01 00 40	02 05 21	2086	2.14×10^{-2}	0.32
0745−19[1]	07 45 18	−19 10 11	...	...	...
0840+29	08 39 53	29 38 47	3033	4.94×10^{-2}	0.67

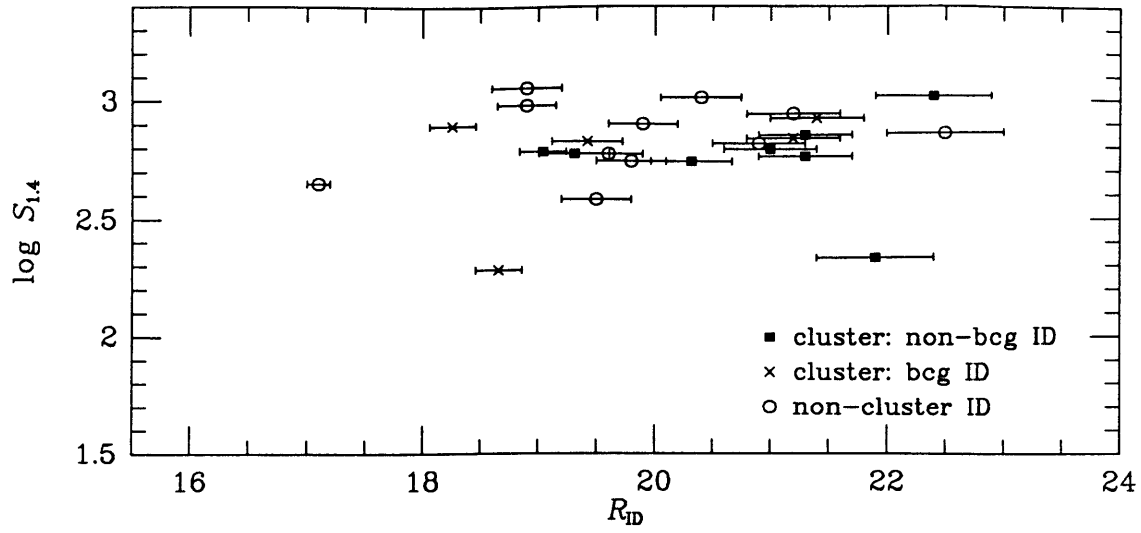

FIGURE 6.5b Log of the radio flux density at 1411 MHz plotted against the *R* apparent magnitude of the optical identification for the radio source.The radio IDs have been subdivided into clusters where the radio source is the brightest cluster galaxy, clusters where the radio source is not the brightest cluster galaxy, and non-cluster IDs.

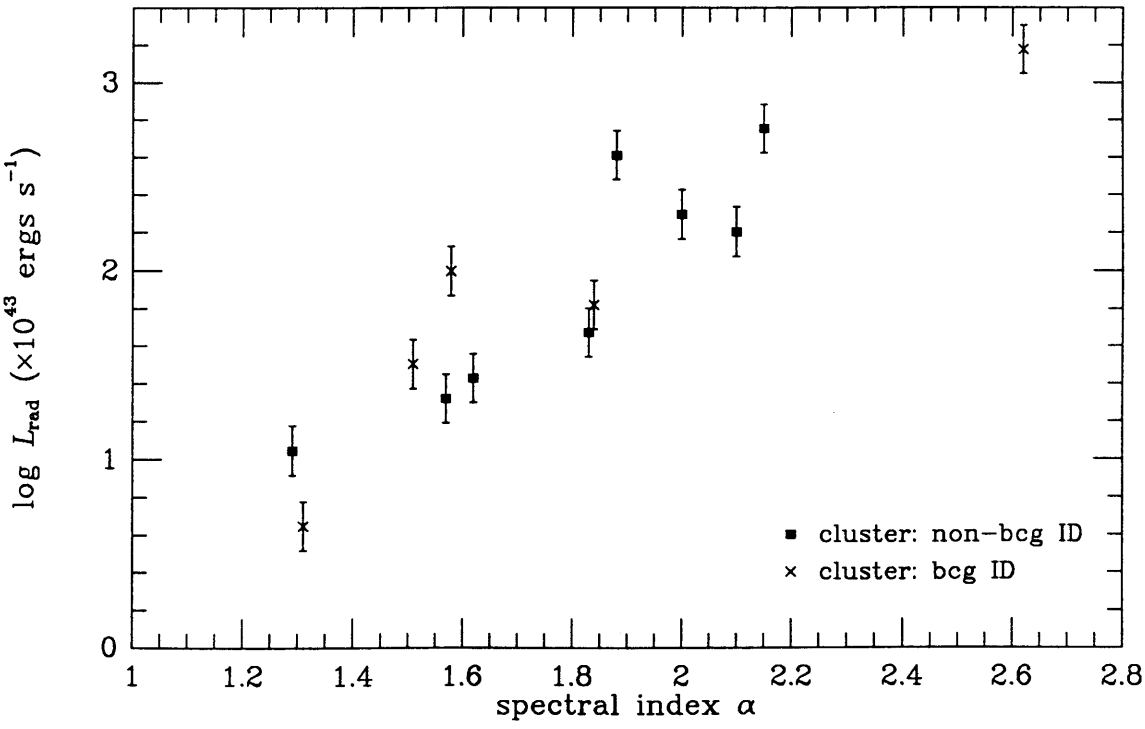

FIGURE 6.5a Plot of the radio luminosity (10 MHz to 100 GHz) as a function of the spectral index for the radio sources associated with clusters of galaxies. The estimated redshift was used to compute the radio luminosity.

1234+26	12 33 00	26 29 00	9974	4.12×10^{-3}	0.95
	12 33 37	26 29 57	9974	3.35×10^{-3}	0.83
	12 34 32	26 25 34	9974	2.70×10^{-3}	0.74
	12 34 32	26 32 25	9974	4.36×10^{-3}	0.86
	12 34 56	26 37 24	9974	5.10×10^{-3}	0.98
	12 34 31	26 36 49	9974	4.60×10^{-3}	1.0
4C 23.37	14 14 11	23 29 03	3037	1.66×10^{-2}	0.41

[1] X-ray observations of 0745–19 were carried out with the *HRI* on *Einstein* and are described in Fabian *et al.* (1985) who report L_x (2-10 keV) = 1.8×10^{45} erg s^{-1}.

6.5 Summary

In this section, the observations and properties of the SSRS sample have been presented. A total of 30 SSRS fields were included in the above analysis. Of these 30 sources, 15 have certain optical identifications (as a galaxy, group, cluster or quasar; as listed in Table 6.2) and another 11 have probable IDs (the nearest galaxy is no more than 15 arcseconds from the center of the double-lobed radio source). Four of the sources, 0936+26, 4C23.39, and 1623+25, and 4C 67.17.1 have no obvious optical counterparts, although there is a faint group in the field of 0936+26 (well away from the radio position), there is a blue, star-like object in the field of 1623+25 (again, well away from the radio position) and there is a (serendipitous?) distant (z_{est}~0.8) cluster in the field of 4C 67.17.1. A total of 15 of the SSRSs are associated with clusters of galaxies (as defined earlier in §6.3): for 9 of these cluster SSRSs, the optical ID is unambiguous, and for 6, the optical ID is less certain (the identified galaxy is not exactly centered between the radio lobes: see the radio maps in Figure 6.2) but there is certainly a cluster of galaxies in the field.

It is interesting to consider the four SSRSs that have not been optically identified. In three of these cases, a cluster of galaxies with z>0.7 could be present in the field since it would be undetectable at the limiting magnitude of the observations. Granted, the brightest cluster galaxy would be detectable, but there would not be enough galaxies above the magnitude limit to identify a cluster in the field, and there may be no optical ID since the radio source may not be associated with the brightest cluster galaxy. Consequently, it is possible that clusters with z>0.7 are hiding in three of the unidentified fields where the radio source is associated with a fainter member galaxy in these clusters. The fourth unidentified SSRS, 4C 67.17.1, contains two candidate optical IDs, a faint group and a distant cluster, although both are at least an arcminute away from the position of the radio source. Since the angular size of a cluster of galaxies can exceed the CCD field of view, even at z>1, it is impossible to guarantee that the radio source is not associated with a faint member of the z~0.8 cluster.

One unexpected and important result of this work is the identification of clusters of galaxies containing radio sources associated with galaxies *other* than the optically dominant member. McHardy (1979) has shown that 4C

radio sources occur more often in BM Type I clusters than in clusters with either BM Types, and the radio source is usually associated with the giant cD galaxy. However, in 8 of the 15 clusters in this sub-sample, the radio source is identified with a member galaxy of the cluster which is not the brightest cluster galaxy. None of these 8 clusters is BM Type I, and the mean absolute magnitude of the radio galaxy compared to the brightest cluster galaxy is $\langle M_V(\mathrm{ID})-M_V(1)\rangle=1.37$ making the radio galaxies typical L* galaxies rather than bright, optically dominant galaxies. In addition, these galaxies are often located as much as an arcminute away from the center of the cluster (as defined by the optically dominant galaxy). One might argue that these could be background clusters and the radio source is indeed associated with the brightest member in these clusters. This is unlikely, however, since the probability of having two such superposed clusters in the field is quite low and in this sample we see 8 such occurrances. There is also the more serious possibility that the brightest cluster galaxy has been mis-identified with a foreground galaxy and the redshift estimate is also wrong. This problem will only be solved with spectroscopic observations of the suspected optically dominant galaxies as well as the radio IDs. Nevertheless, the lack of an expected correlation of cluster richness with radio spectral index coupled with the observation of SSRSs associated with average cluster galaxies located some distance from the cluster center raises some questions about the validity of the source-confinement model for steep-spectrum radio sources. Note, however, that we do not see any BM Type I clusters where the radio source is associated with a cluster member other than the optically dominant galaxy.

Six of the SSRSs have measured redshifts. Three of these sources are not obviously associated with rich clusters of galaxies: 0829+14 at z=0.6 appears to be associated with a quasar (although the optical ID is ~15 arcseconds from the center of the double-lobed radio source), 0840+29 at z=0.40 with a faint group, and 1437+22 at z=0.2 with a cD group (or poor cluster). The other 3 sources, 0745–19 at z=0.10, 4C23.37 at z=0.45, and 1436+03 (A1942) at z=0.21, are all identified with rich clusters. Redshifts were estimated for the remainder of the SSRSs associated with clusters by using the magnitude of the brightest cluster galaxy (as described earlier in §6.4). The 15 clusters lie in the redshift range $0.1<z<0.75$ with a median redshift of z=0.43. As described in the last section, the richness of the clusters was estimated by applying surface density profile and luminosity function corrections to the observed galaxy counts. When these corrections are included, the clusters turn out to be quite rich with a median richness coresponding to Abell Richness Class 2 (e.g. Coma) although the uncertainty in the richness corresponds roughly to one Abell Richness Class.

From this work, it is evident that steep-spectrum radio sources are excellent pointers to rich clusters of galaxies. We have shown, however, that Slingo's strong statement that "steep spectrum radio sources occur *exclusively* in rich clusters of galaxies and that many of those previously unidentified are in clusters having z>0.2" is certainly not true. There are excellent examples such as 1437+22 and 0840+29 where the optical ID lies within one arcsecond of the center of the double-lobed radio source and the magnitude of the ID (an isolated galaxy or a very small group) is bright enough that many other cluster galaxies would also have been seen if a

cluster were present in the field. Nevertheless, at least half of the observed fields *do* contain rich clusters, and these objects are not optically selected and should therefore be free of many potential selection biases introduced when correlating and comparing the optical properties of an optically selected sample.

REFERENCES:

Abell, G.O., Corwin, H.G., and Olowin, R.P. 1989, "A Catalog of Rich Clusters of Galaxies," *Ap.J.Supp.*, **70**, 1. ACO

Baum, S., and Heckman, T. 1986, in *Radio Continuum Processes in Clusters of Galaxies*, ed. C. O'Dea and J. Uson (Green Bank: NRAO), p. 119.

Blumenthal, G., and Miley, G. 1979, "Spectral Index Dependent Properties of Steep Spectrum Radio Sources," *Astron.Ap.*, **80**, 13.

Coleman, G.D., Wu, C.C., and Weedman, D.W. 1980, "Colors and Magnitudes Predicted for High-Redshift Galaxies," *Ap.J.Supp.*, **43**, 393.

Baldwin, J.E., and Scott, P.F. 1973, "Extragalactic Radio Sources with Steep, Low Frequency Spectra," *M.N.R.A.S.*, **165**, 259.

Eales, S. 1985, "CCD Observations of a rich, distant cluster of galaxies (1046+35) containing a classical double radio source," *M.N.R.A.S.*, **214**, 27.

Fabian, A.C., Arnaud, K.A., Nulsen, P., Watson, M., Stewart, G., McHardy, I., Smith, A., Cooke, B., Elvis, M., and Mushotzky, R. 1985, "An X-ray, optical and radio study of PKS 0745-191: a massive cooling flow," *M.N.R.A.S.*, **216**, 923.

Fanaroff, B.L., and Riley, J.M. 1974, "The Morphology of Extragalactic Radio Sources of High and Low Luminosity," *M.N.R.A.S.*, **167**, 31P.

Foltz, C.B., Chaffee, F., Hewett, P., MacAlpine, G., Turnshek, D., Weymann, R., and Anderson, S. 1987, "The APM QSO Survey. I. Initial MMT Results," *Astron.J.*, **94**, 1423.

Gunn, J.E., Hoessel, J.G., and Oke, J.B. 1986, "A Systematic Survey for Distant Galaxy Clusters," *Ap.J.*, **306**, 37.

Hewitt, J.N. 1986, Ph.D. Thesis, Massachusetts Institute of Technology, p. 138.

Jarvis, J.F., and Tyson, J.A. 1981, "FOCAS: Faint Object Classification and Analysis System," *Astron.J.*, **86**, 476.

Longair, M., and Seldner, M., 1979, *M.N.R.A.S.*, **189**, 433.

Luppino, G. A. 1989, "A Virtual-Phase CCD Camera for The MDM Observatory," *P.A.S.P.* in press.

Luppino, G.A., Ceglio, N.M., Doty, J.P., Ricker, G.R., and Vallerga, J.V. 1987b, "Imaging and Nondispersive Spectroscopy of Soft X-rays Using a Laboratory X-ray CCD System," *Optical Engineering*, **26**, 1048.

Sandage, A. 1976, *Ap.J.*, **205**, 6.

Shanks, T., Couch, W., McHardy, I., Cooke, B., and Pence, W. 1987, "Observations of High Redshift Galaxy Clusters: Implications for Cosmology," in *High Redshift and Primeval Galaxies* (Paris: Editions Frontieres), 1987.

Slingo, A. 1974, "Observations of Ten Extragalactic Radio Sources with Very Steep Spectra," *M.N.R.A.S.*, **166**, 101.

Slingo, A. 1974, "The Structure and Origin of Radio Sources with Very Steep Spectra," *M.N.R.A.S.*, **168**, 307.

Tyson, J.A. 1988, "Deep CCD Survey: Galaxy Luminosity and Color Evolution," *Astron.J.*, **96**, 1.

Ulmer, M.P. 1980, "An X-ray Survey of Distant Rich Clusters of Galaxies with HEAO 1," *Ap.J.*, **235**, 351.

Ulmer, M.P., Brown, R.L., Schwartz, D.A., Patterson, J., and Cruddace, R.G. 1983, "The Discovery of an X-ray Bright BL Lacertae Object: 0414+009," *Ap.J.*, **270**, L1.

Valdes, F 1982, *KPNO FOCAS Users Manual.*

Chapter 7

CCD Photometry of Cl 1358+6245 at z=0.32: an X-ray Selected, Distant, Rich Cluster of Galaxies

Cluster 1358+6245 was discovered by McHardy in an *Einstein* x-ray observation of a previously unidentified *Ariel-V* x-ray source. An optical CCD image of this field obtained in 1986 by Ricker with the *MASCOT* (Ricker *et al.* 1981) revealed an exceptionally rich, compact, and apparently distant cluster of galaxies. Deep, four-color (*BVRI*) CCD images of this cluster, as well as a spectrum of the optically dominant galaxy which places the cluster at a redshift of z=0.32, were acquired in order to investigate, in detail, the nature of this extraordinary object.

It turns out that Cl 1358+6245 was, in fact, identified by Zwicky and is listed in the *Catalogue of Galaxies and of Clusters of Galaxies* (Zwicky and Herzog 1968) as extremely distant containing 235 galaxies. Zwicky also highlighted this cluster's entry in the catalog with a footnote claiming Zw 1358.1+6245 was very compact and rich: the only such designation in the entire catalog.

7.1 Observations

a) CCD Photometry and Data Reduction

Photometric observations of Cl 1358+6245 were carried out with the TI 850 × 750 CCD controlled by the *BRICC* (Luppino 1989) electronics. During the nights of 18-20 April 1988, the instrument was mounted at the f/7.5 cassegrain focus of the 1.3m McGraw-Hill telescope at the MDM (Michigan-Dartmouth-MIT) Observatory on Kitt Peak. The image scale was 0".465 per pixel, resulting in a CCD field of view of 6'.7 × 5'.9; the seeing was typically 1".5 to 2".0. Images were taken through Mould *BVRI* filters (KPNO 1983). These filter passbands, when combined with the CCD sensitivity, provide a reasonable approximation of the Johnson *B* and *V* and Kron-Cousins *R* and *I* bands (Schild 1983 and references therein). A number of the standard stars of Landolt (1983) were observed on the nights that the cluster images were taken. These standards were used to calibrate the CCD photometry, and to monitor the transparency of the sky throughout the observations. The equations necessary to transform observations in these filters to the standard *BVRI* photometric system are listed in Chapter 5 (see §5.3).

The CCD images were de-biased, flattened and stacked as described in the last chapter. Seven 1800-second exposures were stacked to make the resultant *R* frame. Four 1800s *B* images, two 1800s *V* images and two 1800s *I* images were used to construct the other three colors. All objects in the field were photometered and

classified in all four colors using the *Faint Object Classification and Analysis System* (*FOCAS*: Jarvis and Tyson 1981; Valdes 1982).

FOCAS classified objects as stars, galaxies, diffuse or extended objects, and noise, based on the shape of the object as compared to the stellar point-spread-function determined from bright stars in the field. Galaxies could be separated from stars down to magnitudes where it doesn't matter anymore. (At *R* fainter than ~21, essentially all of the objects in the field are galaxies). All objects in the catalog, particularly those classified as diffuse or noise, were visually inspected to be certain that the objects were real. In some cases, *FOCAS* found pieces of a satellite trail or diffraction spikes of bright stars, and these spurious objects were filtered from the catalog.

In order to compare the four *FOCAS* catalogs, a common coordinate system (*i.e.* celestial coordinates) was needed so that the catalogs could be matched. The celestial coordinates of the detected galaxies were calculated in a two-step procedure from the coordinates of SAO stars near the field. First, the positions of ~25 SAO stars and ~15 field stars visible on the *R* CCD image were measured from the POSS E print using a Mann Precision Instruments measuring table equipped with Bausch and Lomb absolute position encoders. A linear least-squares fit of the known positions of the SAO stars to their measured positions was used to determine the celestial coordinates of the CCD field stars to within ±0.5". The celestial coordinates of the field stars were then used to derive the transformation from CCD coordinates to celestial coordinates for the faint galaxies with a precision of ±0.5".

The matched catalog for Cl 1358+6245 has 332 entries which are all classified as galaxies. To be included in this matched catalog, each entry must have at least one match with the other three colors. The *BVRI* aperture magnitudes ($32h_{50}^{-1}$ kpc diameter; q_0=1/2) and colors for the galaxies are listed in Table 7.1 (Table 7.1 is located at the end of the chapter). These magnitudes have been corrected for atmospheric absorption and galactic reddening (see §7.1a). The coordinates for the 322 galaxies are also listed in Table 7.1 as offsets in arcseconds with respect to the brightest galaxy in the cluster at position $\alpha(1950.0) = 13^h\ 58^m\ 21^s.0$ and $\delta(1950.0) = +62^o\ 45'\ 33".7$.

The unmatched *R* catalog contains many more entries (a total of 404) than the matched catalog because the *R* data goes much fainter than the other colors (the total exposure time for the *R* images was greater and the galaxies are brighter in this waveband).

(i) photometric errors

The statistical errors in the magnitudes were calculated in the following way. The magnitude of a object with total flux *F* e^-/s can be written as

$$m = m_0 - 2.5 \log F$$
$$= m_0 - \frac{2.5}{\ln 10} \ln F = m_0 - 1.086 \ln F \qquad (7.1.1)$$

where m_0 is the magnitude zero point determined from measurements of standard stars (note: m_0 also absorbs the exposure time). The uncertainty in magnitude measurement δm is then

$$\delta m^2 = \left(\frac{\partial m}{\partial F} \delta F \right)^2 + \left(\frac{\partial m}{\partial m_0} \delta m_0 \right)^2$$
$$= \left(\frac{1.086}{F} \delta F \right)^2 + \delta m_0{}^2 \qquad (7.1.2)$$

where δF is the total noise in the object being photometered *i.e.* $\delta F^2 = (shotnoise^2 + skyshot^2 + readnoise^2)$, and δm_0 is the measurement error in the zero point magnitude[1] . Magnitudes are calculated by *FOCAS* using instrumental intensity in ADUs, so in order to compute the true magnitude, the system gain constant e^-/ADU must be known. At the time of these observations, the system gain constant for the TI 850 × 750 CCD was 2.3 e^-/ADU. Using the above equation, and the fact that $F = gS_{ADU}$ where g is the gain constant, the errors in the measured magnitudes were calculated using

$$\delta m^2 = \left[\frac{1.086}{L_{fca}} \sqrt{587.2\ S_{sbr} + 2.3\ L_{fca}} \right]^2 + \delta m_0{}^2 \qquad (7.1.3)$$

where L_{fca} and S_{sbr} are the *FOCAS* variables for the total signal in an aperture (Luminosity fixed circular aperture) and sky noise per pixel (Sigma sky background) respectively. This equation was derived using the fact that $\delta F^2 = N(\delta_{RN}{}^2 + \delta_{SKY}{}^2) + \delta S^2 = N(g\ S_{sbr})^2 + g\ L_{fca}$ where N is the number of pixels in the aperture used to compute L_{fca}: N = 111 pixels for the 5.95 pixel radius aperture used for these observations ($16 h_{50}{}^{-1}$ kpc at z=0.32). The zero point errors were δm_{0B} = 0.050, δm_{0V} = 0.027, δm_{0R} = 0.023, and δm_{0I} = 0.091. For example, the R-band observations described in this chapter have internal 1σ errors of σ=0.023 mag for the bright galaxies (R<19; error is just the zero point error), and σ=0.25 mag for the faintest galaxies (R~23.5). The corresponding errors in the colors are σ_{V-R} = 0.03 mag for the bright galaxies and σ_{V-R} = 0.4 for the faintest galaxies.

(ii) reddening

The photometric observations were corrected for galactic absorption using the values for galactic reddening given by Burstein and Heiles (1978). At the galactic coordinates (l = 109.95 and b = 52.84) of Cl 1358+6245,

[1] The first term in equation 7.1.2 illustrates the useful approximation that the photometric error, in magnitudes, is approximately equal to the inverse of the signal-to-noise ratio (assuming the zero point errors are small).

$E(B-V) = 0.03\pm0.01$. The following equations, which give the extinction in the *BVRI* bandpasses as a function of $E(B-V)$,

$$\begin{aligned} A_B &= 4.05\ E(B-V) \\ A_V &= 3.05\ E(B-V) \\ A_R &= 2.25\ E(B-V) \\ A_I &= 1.55\ E(B-V) \end{aligned} \qquad (7.1.4)$$

were derived using van de Hulst's curve 15 (Johnson 1968). The galactic reddening, at these galactic coordinates, has a small effect on the measured galaxy colors since $\Delta(V-R) = 0.024$ mag and $\Delta(B-R) = 0.054$ mag.

b) Spectroscopic Measurements

Spectroscopic observations of the brightest cluster galaxy in Cl 1358+6245 were carried out using the MDM Observatory 2.4m Hiltner telescope equipped with the *MASCOT* CCD spectrograph (Ricker *et al.*1982). This instrument has been modified significantly from that described in the earlier papers (Luppino 1985). The old TI 328 × 490 CCDs (which were operated in framestore mode, an active area of only 328 × 245 pixels) were replaced with higher quality TI-4849 (584 × 390) CCDs and new CCD control electronics in 1985. The TI-4849 CCD in the spectrograph channel is oriented so that the spectrum is dispersed along the device columns, resulting in 584 wavelength channels; the dispersion was 5.4 Å/pixel and the CCD image scale was ~1.3"/pixel. A rather large (3 arcsecond) slit width was used, but the seeing was never much better than this value. At the time of these observations, the spectrograph CCD suffered from a bad hot-column defect that contaminated the columns greater than column 130. This defect limited the unvignetted field-of-view along the slit to 100 pixels roughly centered on column 80; however, the slit length was still long enough (130 arcseconds) to allow adequate sky subtraction for compact objects such as the central galaxies in the core of Cl 1358+6245. Two one-hour exposures were taken on the night of 10 May 1988. The sky conditions were mostly clear with intermitant clouds throughout the night. The CCD spectra were reduced using the *IRAF* ONEDSPEC and APEXTRACT packages.

7.2 Analysis of Cluster Properties

a) Redshift

The spectrum of the central galaxy in Cl 1358+6245 is shown in Figure 7.1. The spectrograph slit was oriented N-S, and an aperture of ~20 pixels, centered on galaxies 154 and 161 (see Table 7.1), was summed for the extraction of the sky-subtracted spectrum. An absorption-line redshift of 0.323 ± 0.001 is determined from the Ca *H* and *K* and *G*-band features. A weak *OII* (3727) feature is also discernable. There is some indication that the *OII* feature is extended and this may signal the presence of cooling flow. Unfortunately, nothing can be

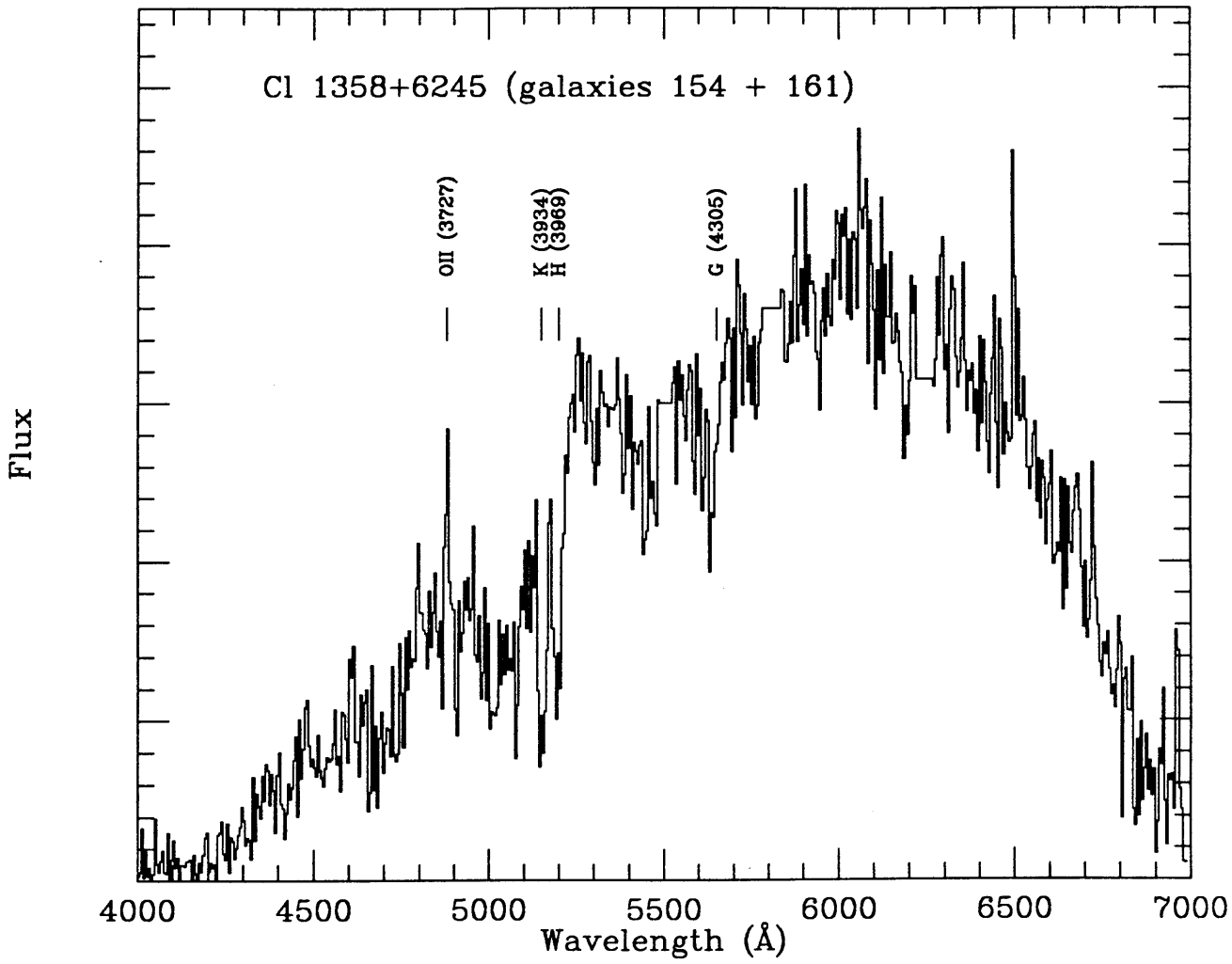

FIGURE 7.1 Spectrum of the brightest cluster galaxy at the core of Cl 1358+6245. Unambiguous identification of the absorption features Ca H and K and the G band along with a weak OII (3727) emission line yield a redshift of z=0.32 for the cluster.

said about the shape of the continuum or the equivalent width of the lines because this spectrum was not flux calibrated.

b) Cluster Morphology

A composite CCD image of Cl 1358+6245 is shown in Figure 7.2. This mosaic image was formed from seven 1800 second *R* images which were shifted and stacked as described in the last section. The image covers an angular diameter of ~7' × 8' arcmin, which corresponds to a metric size of $\sim 2.4 h_{50}^{-1} \times 2.8 h_{50}^{-1}$ Mpc at the cluster redshift ($5.7 h_{50}^{-1}$ kpc/arcsecond at z=0.32). The center of Cl 1358+6245 is dominated by galaxies 154 (the brightest cluster galaxy) 161, 145, 164, 135, 136, and 137 (see Figure 7.4). These may physically associated and form a multiple nucleus central cD galaxy, or they may just be chance superpositions of the large number of galaxies in the condensed core. These seven galaxies seem to be surrounded by a low surface brightness halo which is apparent in the contour plot in Figure 7.4 (see also §7.3.a and Figure 7.13). The core appears to be elongated N-S.

The Bautz-Morgan type of the cluster was estimated using the method of Dressler (1978; see §2.1.b). Unfortunately, this estimate is very sensitive to the choice of m_1, m_2, and m_3. At z>0.2, the brightest cluster galaxy (hereafter G1) is often easy to identify, but m_2 and m_3 are quite uncertain because of significant background contamination from field galaxies. If one blindly follows the Dressler prescription, Cl 1358+6245 is classified as BM Type III. However, the galaxies used for m_2 and m_3 are probably not cluster members since they are well removed from the core and have magnitudes close to that of G1. The cluster becomes BM Type II with a better choice of m_2 (galaxy #130; G2) and m_3 (galaxy #81; G3). Unfortunately, the only way to be certain that the classification is correct is to verify with spectra the cluster membership of G2 and G3 (G2, which is only $110 h_{50}^{-1}$ kpc from G1, is almost certainly a cluster member. The membership of G3, however, is less certain; see Figure 7.4). Another possible source of confusion is the use of aperture magnitudes for the above calculation. If total magnitudes are used the three brightest galaxies (as they were by Dressler 1978), and the central conglomeration of galaxies is called a multiple nucleus cD with all the light from this group integrated to obtain m_1, then this cluster becomes BM Type I. The nature of the central galaxy is discussed in §7.3.a. For now, we will be conservative and classify Cl 1358+6245 as Bautz-Morgan Type II.

The Revised Rood-Sastry (RS) classification (Struble and Rood 1982), based on the spatial arrangement of the ten brightest cluster galaxies, can also be determined for this cluster. Unfortunately, at these faint magnitudes, this method also suffers from contamination by field galaxies. Based on the relative (aperture) magnitudes of G1 and G2, and their close separation of $110 h_{50}^{-1}$ kpc, Cl 1358+6245 is classified as RS Type B (supergiant binary galaxies; see Struble and Rood 1982). This classification could easily be revised to cD if G1 was, in fact, a multiple nucleus cD galaxy. This is discussed further in §7.3

FIGURE 7.2 This composite CCD image of the rich cluster of galaxies Cl 1358.1+6245 was formed from seven separate 1800 second R-band exposures taken on the MDM Observatory 1.3m telescope in April 1988 with a single TI 850 × 750 CCD in the instrument described in this thesis. A spectrum of the 18.5 R magnitude central galaxy indicates the cluster is at a redshift of 0.32. The field of view of this mosaic image is 8 arcminutes NS by 7 arcminutes EW - north is up and east is to the left. The image scale is 0.465"/pixel. A faint satellite trail is visible extending from the northeast to the southwest corner of the frame.

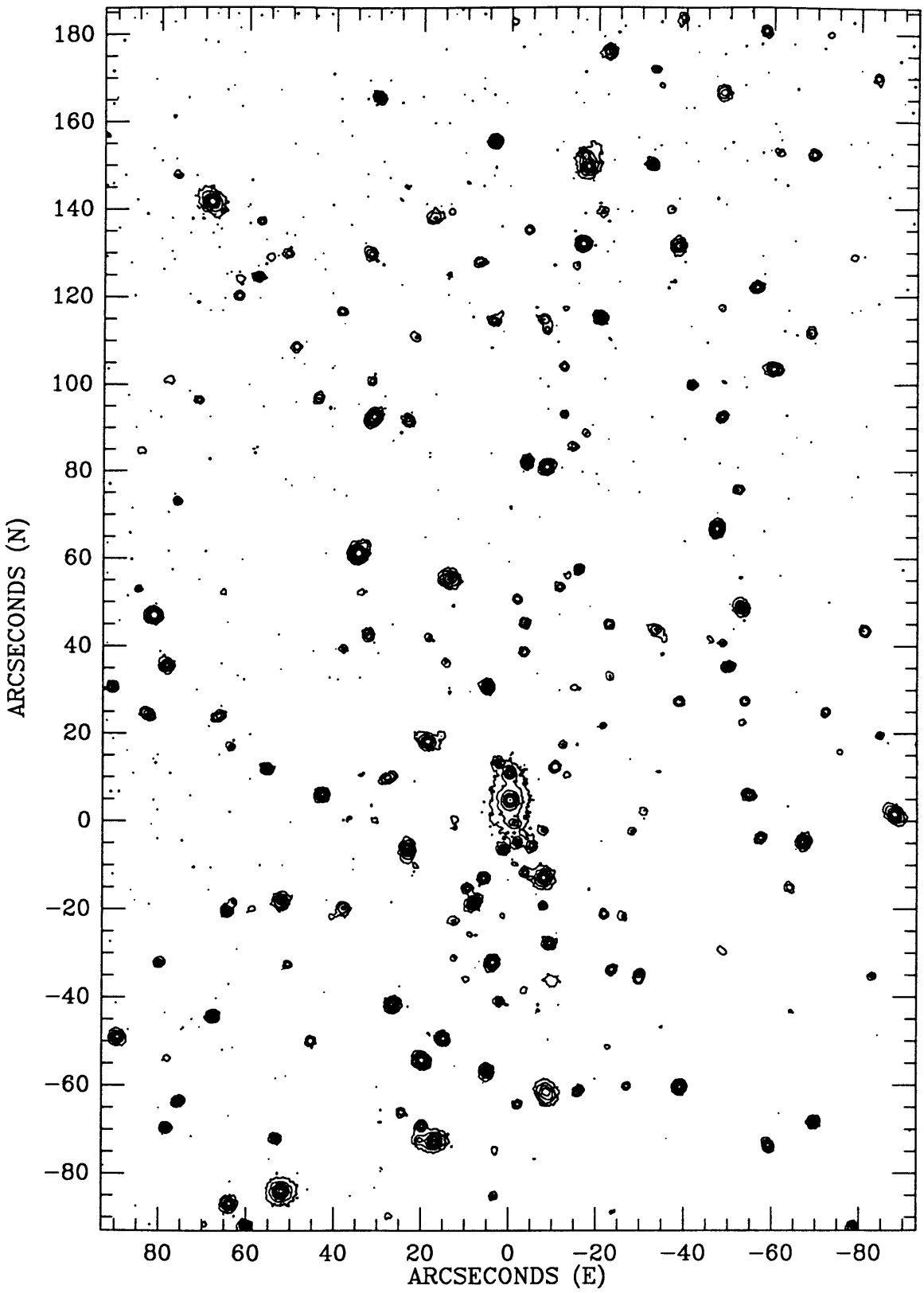

FIGURE 7.3 Contour plot of Cl 1358+6245

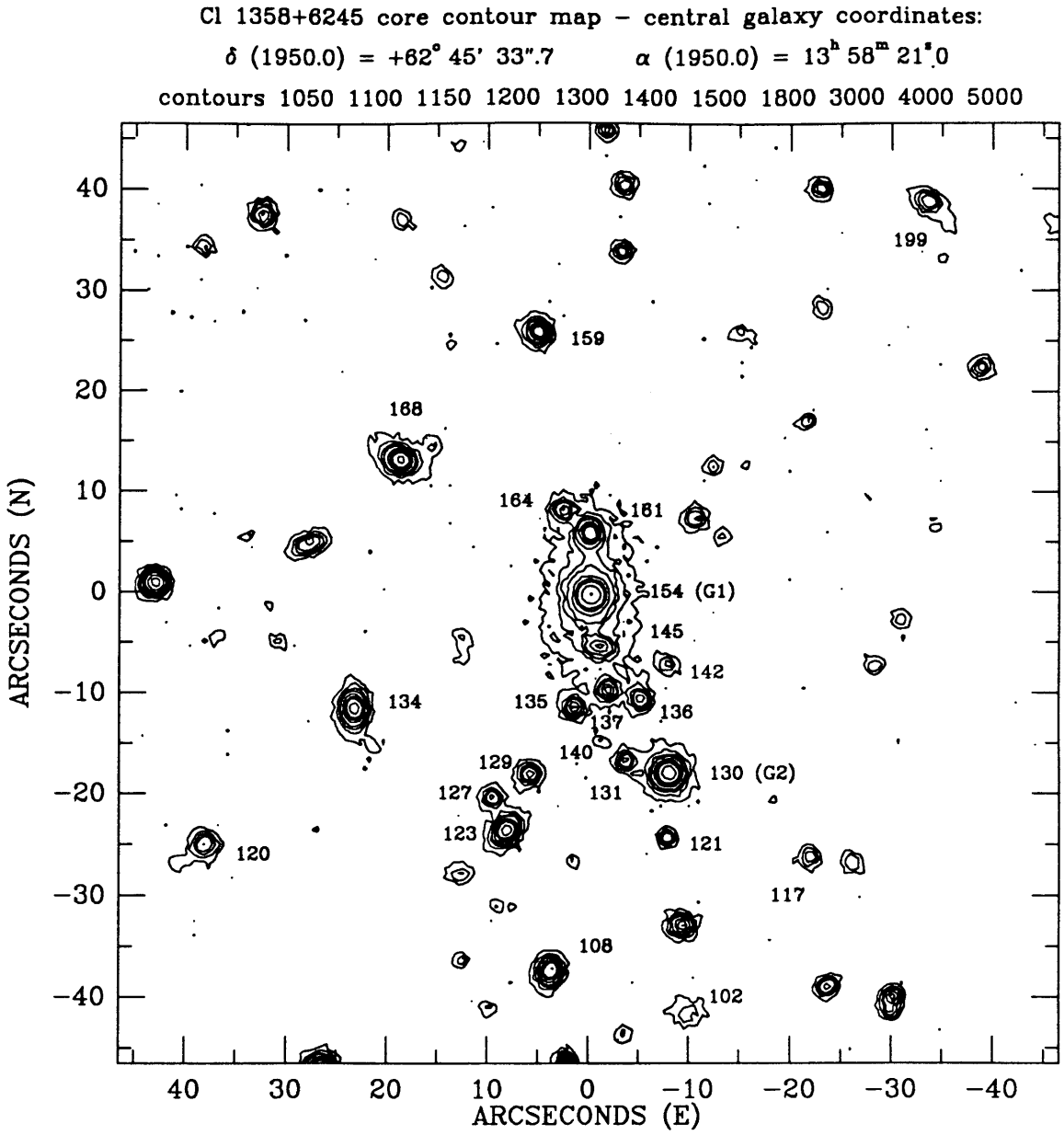

FIGURE 7.4 Contour plot of the $250h_{50}^{-1}$ kpc radius core of Cl 1358+6245. Some of the brighter galaxies are labeled with the numbers listed in Table 7.1 The two brightest cluster galaxies, G1 and G2, can be seen in this plot, as well as some of the blue galaxies discussed in §7.2.

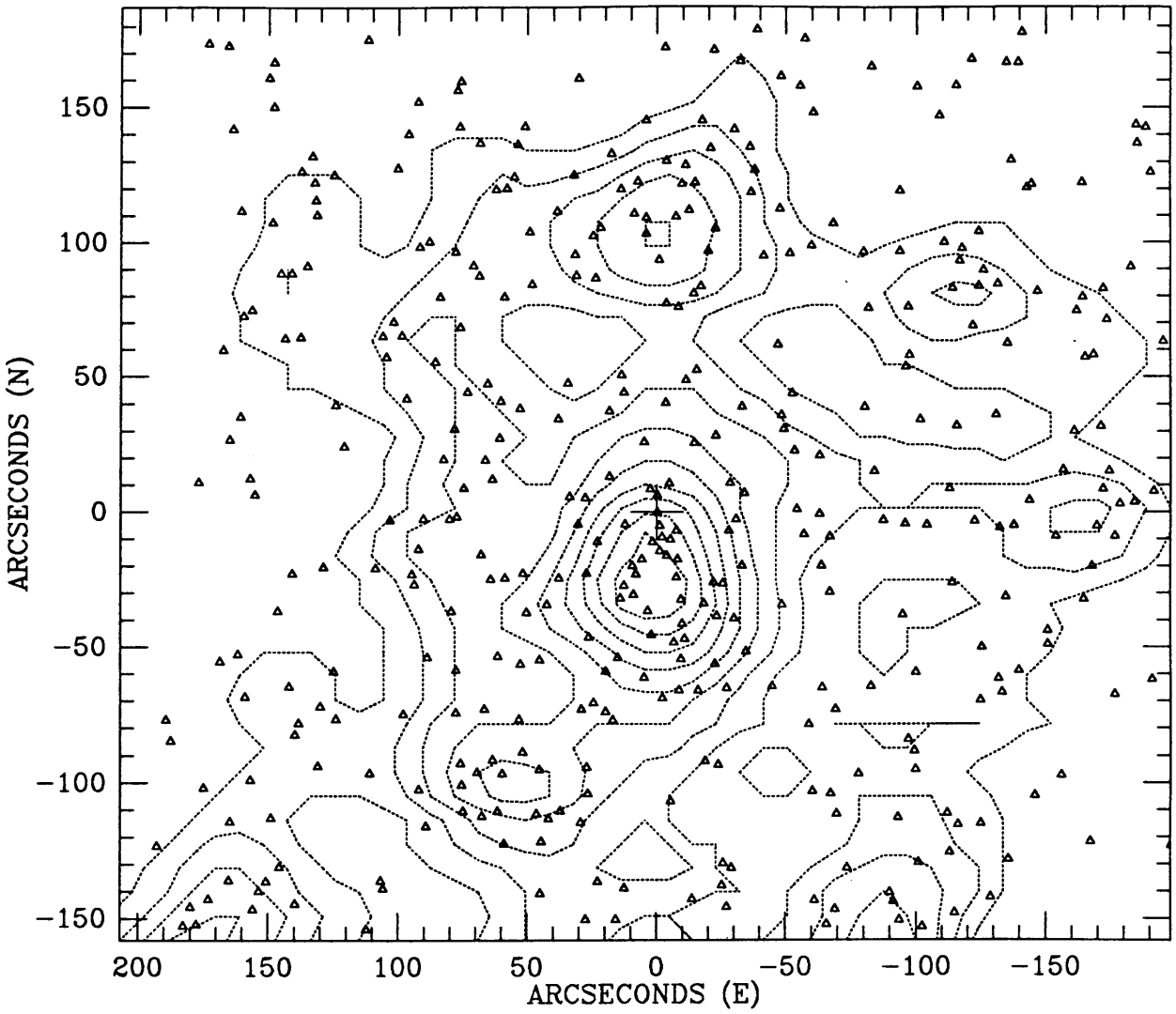

FIGURE 7.5 Galaxy surface number density contour plot of the 6' × 5' field centered on Cl 1358+6245. The galaxies were counted in 20 × 20 pixel bins and the resulting coarse plot was smoothed over an area of 100 × 100 pixels. The lowest contour level corresponds to a surface density of 10 galaxies arcmin^{-2}. The contours are spaced at intervals of 3 galaxies arcmin^{-2}. The position of the brightest cluster member is indicated by the cross near the center. The actual positions of the 404 galaxies that were used to generate this plot are indicated by the triangles.

The cluster field was examined for low surface brightness extended structures or luminous arcs that might be produced by gravitational lensing of background galaxies by the cluster potential well (Lynds and Petrosian 1989; Soucail *et al.* 1988). Thusfar, spectacular arcs with surface brightness ~23.5 V mag arcsec^{-2} have been discovered in A370 (z=0.37), A2218 (z=0.17), A963 (z=0.21), and Cl 2244-02 (z=0.33). Fainter, arclike structures have also been detected in Cl 0024+16 (z=0.39), Cl 0500-24 (z=0.32), and A2390 (z=0.23) (Mellier 1989). Although it may only be a coincidence, luminous arcs seem to be found preferentially in clusters with very high central concentrations (C>0.5; see §7.2) at redshifts of z~0.2–0.4. In the field of Cl 1358+6245, however, which has a central concentration of C=0.51, there are no obvious extended structures or luminous arcs down to a limiting magnitude of 25.5 R mag arcsec^{-2}.

c) Richness and Luminosity Function

The richness of Cl 1358+6245 was estimated using a variety of methods. As described in §2.1, the Abell richness class was determined by counting the number of galaxies within a $3h_{50}^{-1}$ Mpc radius in the magnitude range m_3 and m_3+2. However, as mentioned above, it is quite difficult to be certain that m_3 is truly the magnitude of the third brightest *cluster* galaxy because of significant background contamination from field galaxies. Nevertheless, any richness measurement based on an incorrect field galaxy m_3 will *underestimate* the richness since $(m_3)_{\rm field} < (m_3)_{\rm true}$. Cl 1358+6245 is at least an Abell Richness Class 3 cluster. There are $N(<m_3+2=21.3)$=140 galaxies in the CCD field after correction for background (Tyson 1988). This is certainly an underestimate since the CCD field only covers a radius of ~$1h_{50}^{-1}$ Mpc instead of the $3h_{50}^{-1}$ Mpc used by Abell, and the m_3 used is probably less than the true m_3. Bahcall (1981) has proposed a richness measurement thatis relatively insensitive to uncertainties in the background correction or the exact position of the cluster center. The Bahcall richness is based on the average central density of galaxies $N_{0.5}$ brighter than m_3+2 within a $0.5h_{50}^{-1}$ Mpc radius of the cluster center. Unfortunately, this method is still very sensitive to the choice of m_3. Cl 1358+6245 has $N_{0.5}$=50 galaxies after correction for background and the magnitude-richness correlation (see Bahcall 1981). For comparison, Coma is an Abell Richness Class 2 cluster and has $N_{0.5}$(coma)=28 (Bahcall 1981), although Couch *et al.* (1985) argue for a larger value of $N_{0.5}$(coma)=48 galaxies based on more careful photometry. In either case, it appears that Cl 1358+6245 is richer than Coma, maybe by as much as a factor of two, and is at least as rich as the most spectacular distant Abell clusters such as A370, at z=0.373, which is also Richness Class 3 (Kristian, Sandage and Westphal 1978), and A1689, at z=0.18, which is Richness Class 4. Since Cl 1358+6245 is very x-ray luminous (the x-ray properties will be discussed later in this chapter), it is instructive to compare it to the archetypal high-redshift x-ray cluster , Cl 0016+16, at z=0.54. Koo (1981) initially determined $N_{0.5}$(0016+16)=46 galaxies; however, Ellis *et al.* (1985) have shown, based on intermediate-bandwidth multicolor photometry, that the field of Cl 0016+16 is contaminated by a foreground component at z~0.3, and have revised the number of core galaxies to $N_{0.5}$=27 (but the data is somewhat

Table 7.2 Galaxy Counts for Cl 1358+6245 Field

R Mag	N_{CCD}			N (r<1h_{50}^{-1} Mpc)			N (r<0.5h_{50}^{-1} Mpc)		
	N_{tot}	N_{back}	N_{corr}	N_{tot}	N_{back}	N_{corr}	N_{tot}	N_{back}	N_{corr}
18.0 - 18.5	1	0	1	1	0	1	1	0	1
18.5 - 19.0	5	2	3	5	1	4	1	0	1
19.0 - 19.5	15	3	12	14	2	12	9	0	9
19.5 - 20.0	22	4	18	20	3	17	11	1	10
20.0 - 20.5	37	7	30	31	5	26	16	1	15
20.5 - 21.0	42	10	32	33	7	26	12	2	10
21.0 - 21.5	60	16	44	44	11	33	15	3	12
21.5 - 22.0	59	26	33	43	18	25	18	4	14
22.0 - 22.5	53	40	13	42	28	14	7	7	
22.5 - 23.0	64	63	1	54	44	10	13	11	2
23.0 - 23.5	40	99		34	69		8	17	
23.5 - 24.0	5	154		5	108		1	27	

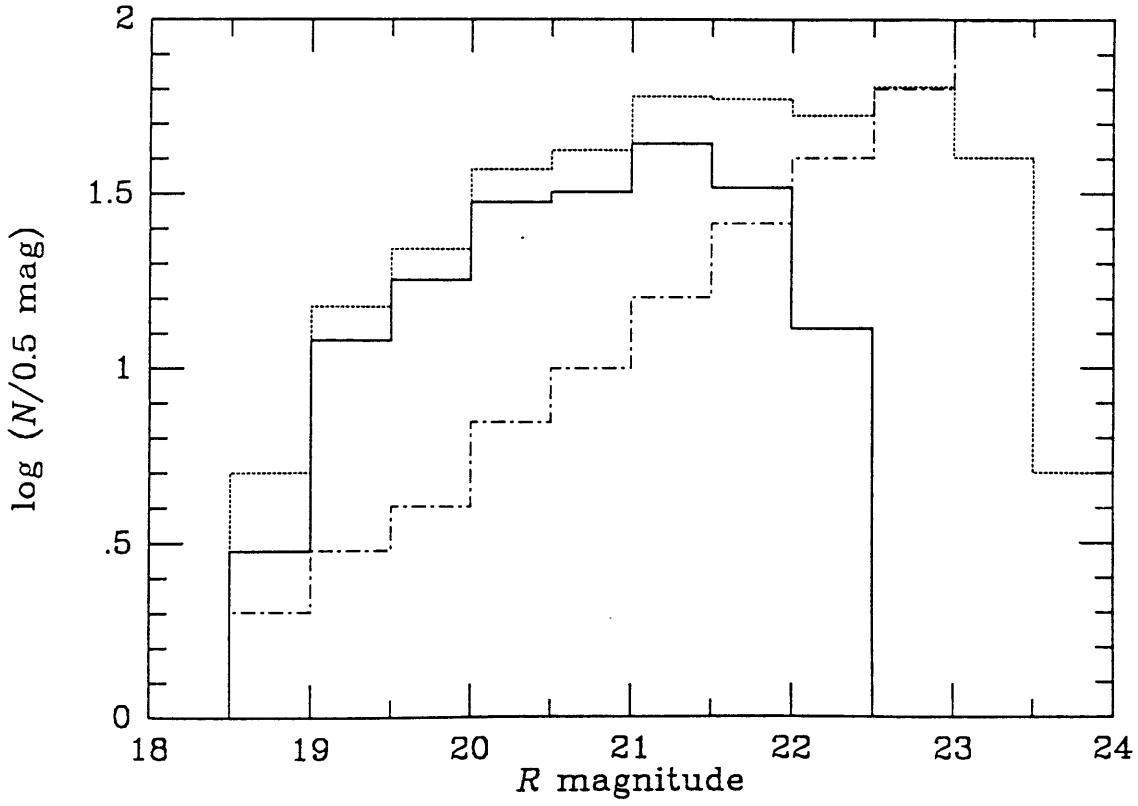

FIGURE 7.6 Luminosity function for Cl 1358+6245. All of the galaxies in the CCD frame (N_{CCD} portion of Table 7.2) were used to generate this plot. The dotted line represents the total counts N_{tot}, the dashed line represents the background counts N_{back} calculated from Tyson (1988) and the heavy solid line is the difference N_{corr}.

incomplete and the true number may be a bit larger than this). Nevertheless, we see that Cl 1358+6245 is indeed richer than Cl 0016+16.

The luminosity function for this cluster, tabulated in Table 7.2 and shown plotted in Figure 7.6, was generated from the entire R CCD image by counting the number of galaxies in half-magnitude bins. The background counts are taken from Tyson (1988) who derived the following expression for the differential surface number density (N = number deg^{-2} mag^{-1}) of background galaxies

$$\log N(R) = 0.39\,R - 4.80 \qquad (7.2.1)$$

as a function of total R magnitude.

d) Colors of the Cluster Galaxies

(i) transformation to the cluster rest frame

In order to compare properties of cluster galaxies at different redshifts, a standard passband in the rest frame of the galaxy must be used. This is particularly important when galaxies in different clusters are selected to some limiting magnitude: this magnitude should be the same rest frame magnitude for each of the clusters, independent of color or redshift. Traditionally, two passbands, more or less centered in the optical portion of the spectrum, have been used for this purpose: the V band (Butcher and Oemler 1984; BOV) and the g band of Thuan and Gunn (1976)(SGHI). Following BOV, galaxies were selected with an absolute magnitude M_V brighter than −20. We must therefore transform our photometric observations to the cluster rest frame at z=0.32. Clearly, one could measure the apparent V magnitude and redshift it back to the cluster rest frame by applying the appropriate K-correction (see §2.2). At redshifts larger than 0.1, however, the K-correction becomes quite large and rest frame magnitudes computed using K-corrections are prone to error since the intrinsic spectral energy distribution of the observed galaxy is, in principle, unknown. The magnitude of this problem can be appreciated by looking at the spectral energy distributions (SEDs) of Coleman, Wu and Weedman (1980; CWW) for E/S0, Sbc, Scd, and Im galaxies shown in Figure 7.7. The rest frame *BVRI* bandpasses (solid lines; subscripted *rf* on the plot) and the observed *BVRI* bandpasses for z=0.32 (dashed lines) are plotted on the same wavelength scale as the SEDs. Rest frame V and observed V do not even overlap. Clearly, to determine rest frame V, one would like to use either the R or I bandpasses, or some combination of the two. Since the R data for Cl 1358+6245 is of higher quality than that for the other three colors, we transformed to the cluster rest frame V using the observed R magnitude by writing the identity

$$M_V - M_R = (V - R)_0 \qquad (7.2.2)$$

where $(V-R)_0$ is the rest frame color. It follows from (Eq. 2.2.26)

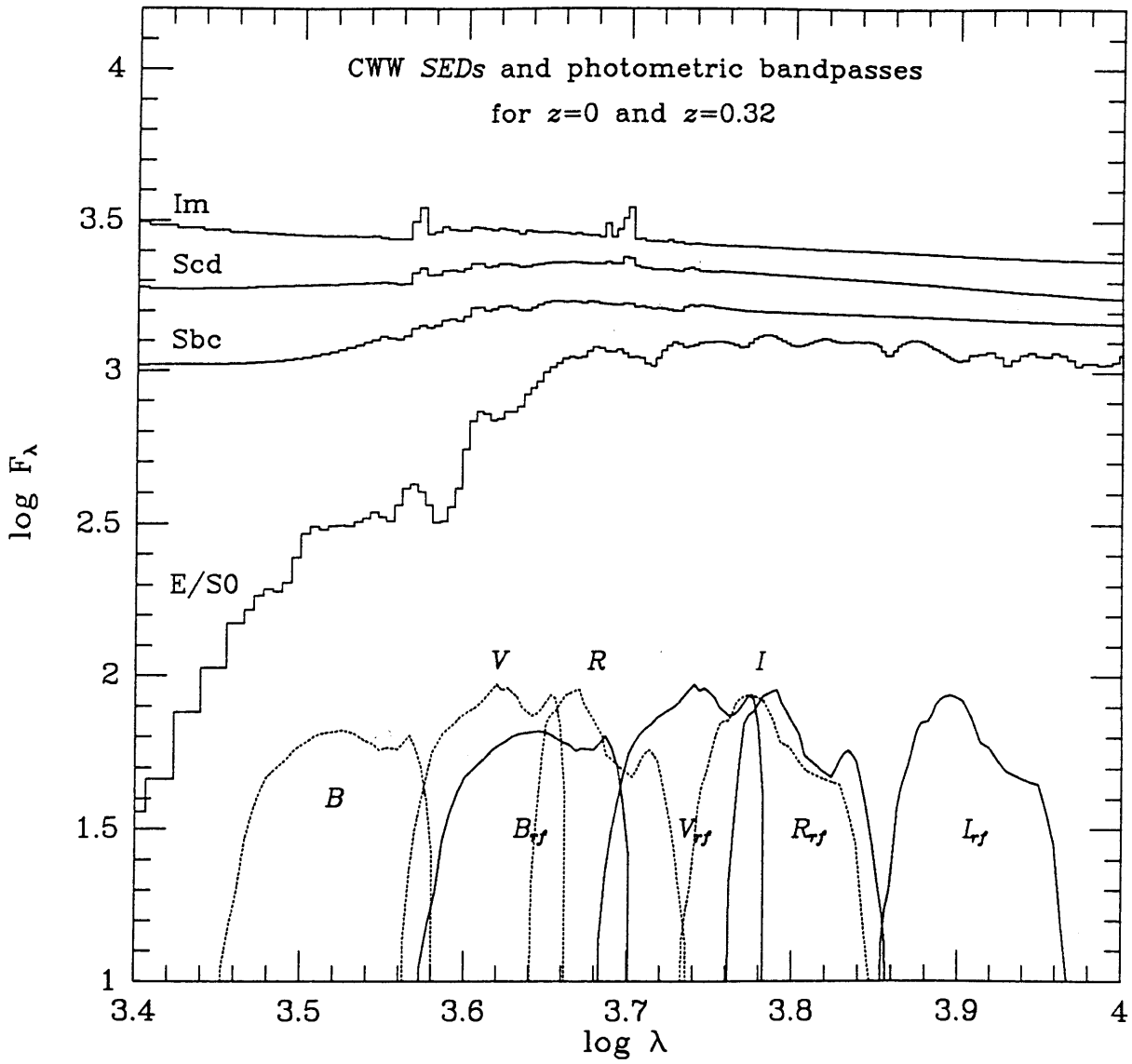

FIGURE 7.7 Spectral energy distributions for E/S0, Sbc, Scd, and Im galaxies from Coleman, Wu and Weedman (1980). The relative shapes of the instrument *BVRI* bandpasses in the observer rest frame and in the cluster rest frame at z=0.32 are shown plotted on the bottom of the graph. The cluster rest frame bandpasses are subscripted *rf*. Clearly, to determine rest frame *V* at *z*=0.32, one would ideally like to use a combination of observations in the *R* and *I* bandpasses.

$$R - M_R = 5\log d_L + 25 + 2.5\log(1+z) + 2.5\log \frac{\int_0^\infty L_\lambda S_R(\lambda)\, d\lambda}{\int_0^\infty L_{\lambda(1+z)} S_R(\lambda)\, d\lambda}$$

$$= 5\log d_L + 25 + K_R(z) \qquad (7.2.3)$$

that

$$M_V = R - 5\log d_L - 25 - K_R(z) + (V-R)_0 \,. \qquad (7.2.4)$$

The K-correction, $K_R(z)$=0.35, was computed by convolving the SEDs of CWW for the E/S0 galaxy spectral energy distribution with the filter bandpasses shown in Figure 7.7. The E/S0 rest frame color is also computed to be $(V-R)_0$=0.55. Therefore, $M_V = R - 41.36$, and galaxies are selected at z=0.32 (luminosity distance of $2053h_{50}^{-1}$ Mpc) with M_V brighter than −20 if R<21.36. Since it appears that the R data is complete to R~22.0 (see Figure 7.6), we are certain we are selecting all of the galaxies brighter than this required rest frame absolute magnitude.

We transformed to rest frame B using the observed V magnitude, again using the SEDs of CWW to compute, in this case, the K-correction, $K_V(z)$=0.885, and the rest frame color, $(B-V)_0$=0.93. The resulting transformation is

$$\begin{aligned} M_B &= V - 5\log d_L - 25 - K_V(z) + (B-V)_0 \\ &= V - 41.52 \end{aligned} \qquad (7.2.5)$$

(ii) color magnitude and color-color diagrams

The $V-R$ vs. R color magnitude diagram is shown plotted in Figure 7.8. All galaxies with $V-R$ colors (202 galaxies) in the matched catalog have been plotted, the vertical line at R=21.36 indicates the position of the M_V<−20 cutoff. The well known E/S0 color-magnitude (C-M) relation (Visvanathan and Sandage 1977), which represents decreasing color with increasing magnitude (*i.e.* bluer colors for fainter galaxies), can be seen in this diagram. This effect typically has a slope of ~0.02 to 0.1 magnitudes per magnitude, and, since we are trying to compare the colors of galaxies over a range of ~4 magnitudes, the C-M effect, if not removed, could bias the galaxy color distribution toward bluer galaxies. The C-M effect in Cl 1358+6245 was measured from the data for the galaxies brighter than the cutoff magnitude. Following Couch *et al.* (1983), galaxies were corrected using the following relation

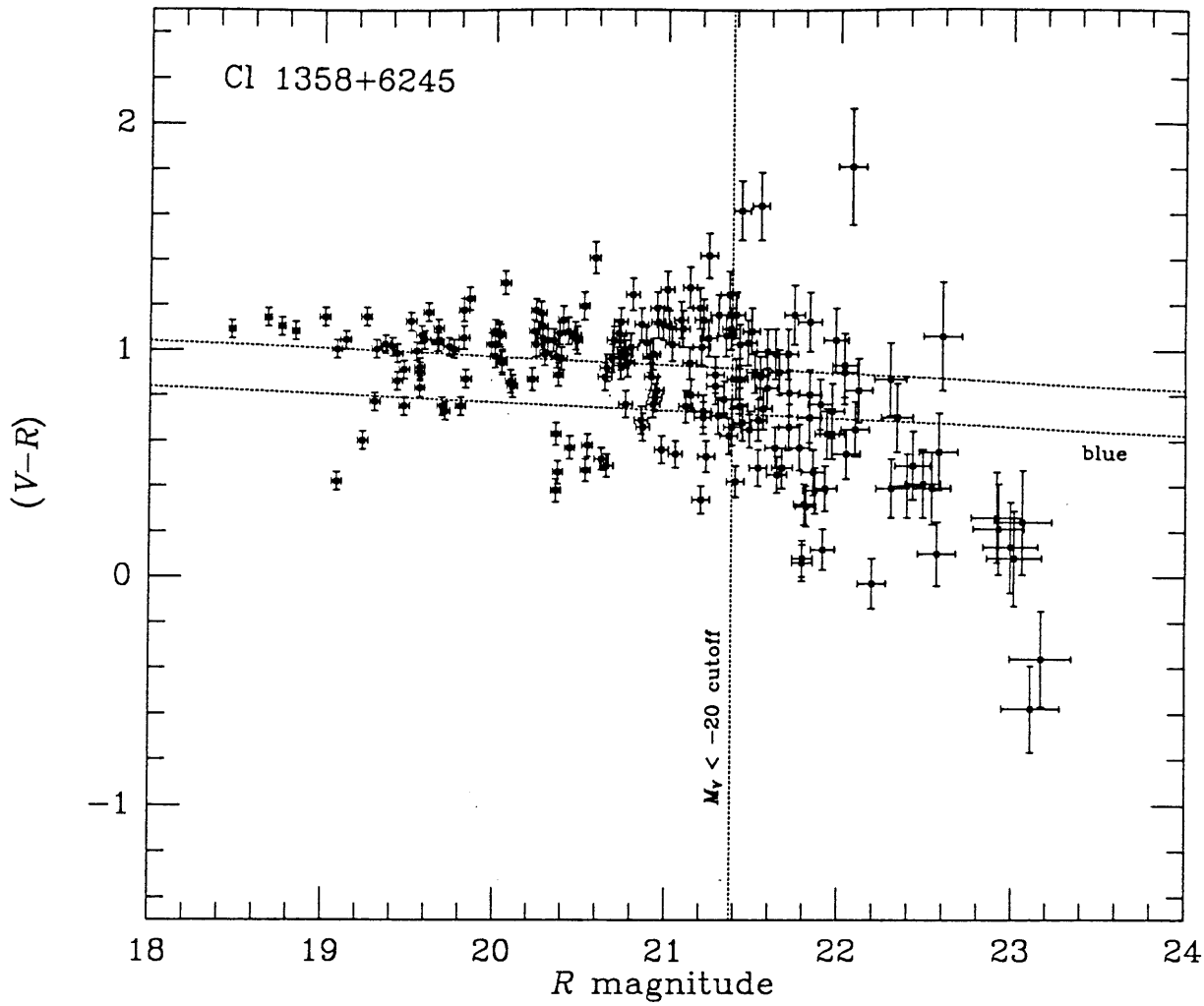

FIGURE 7.8 (V–R) vs R color magnitude diagram for all of the galaxies listed in Table 7.1 having V–R colors (202). The vertical line represents the M_V<–20 magnitude limit. The upper horizontal line is the mean color of the distribution determined from the galaxies brighter than R=21.37. Blue galaxies are located below the lower horizontal line.

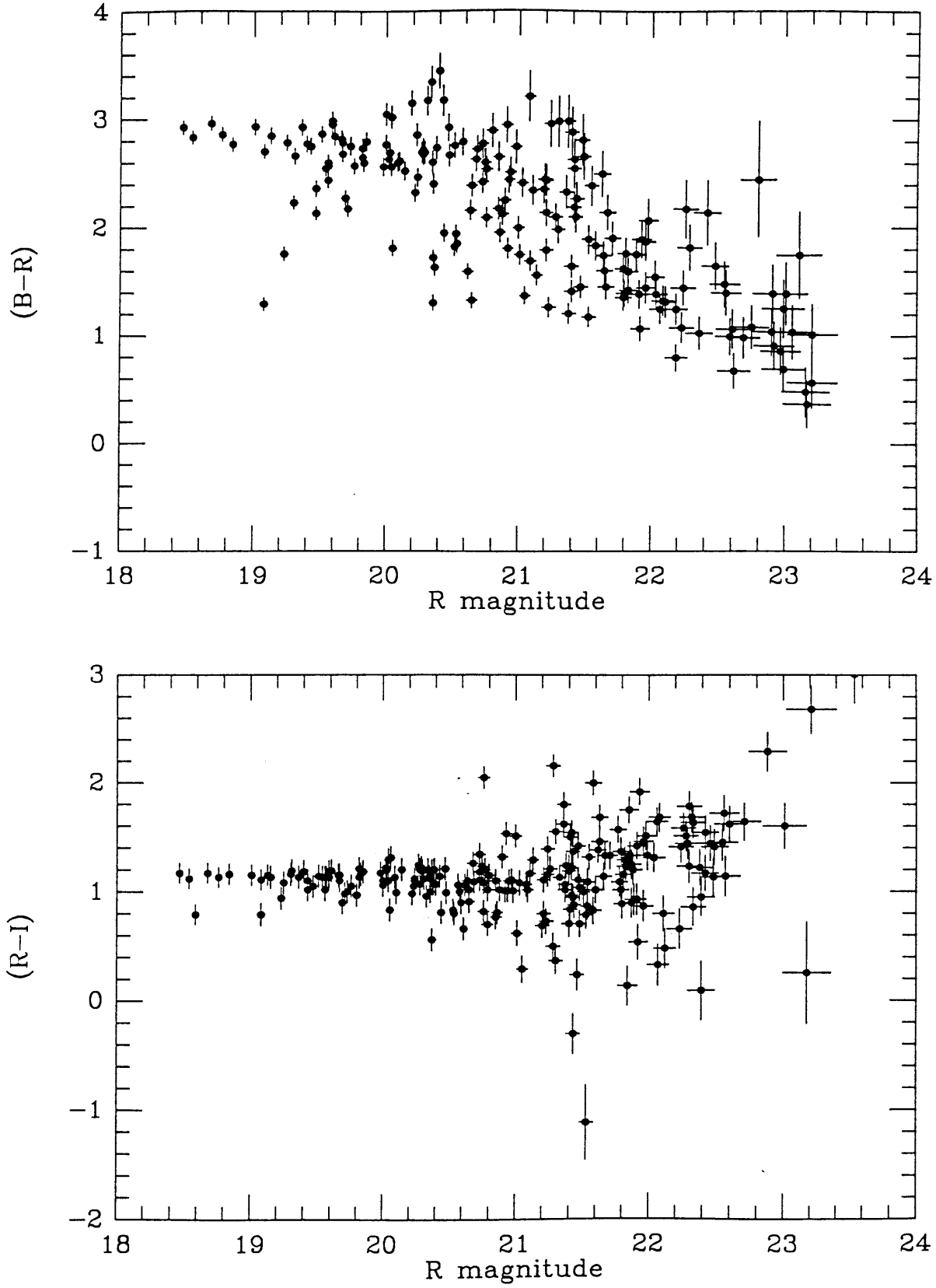

FIGURE 7.9 Color-Magnitude Diagrams for Cl 1358+6245

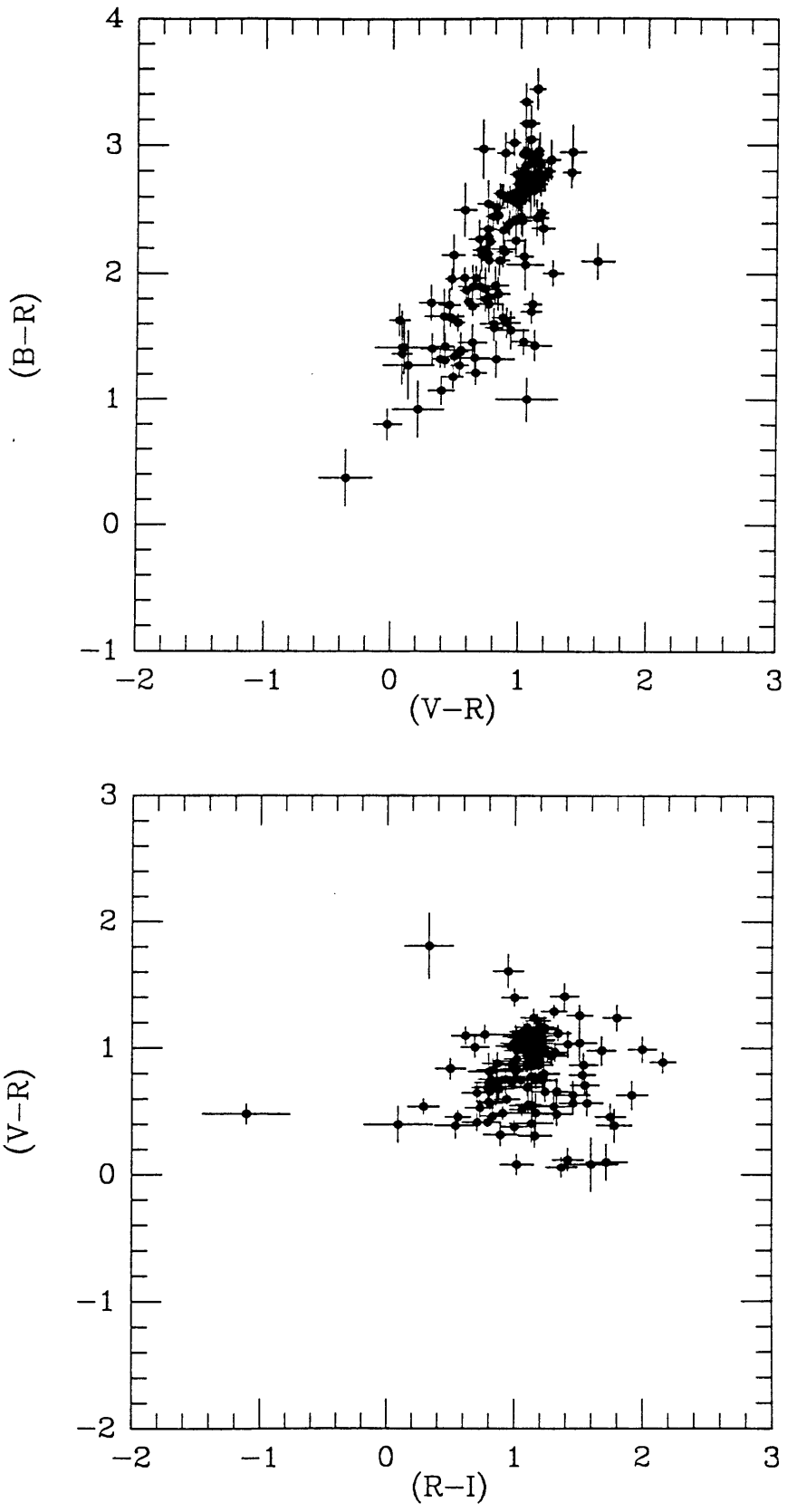

FIGURE 7.10 Color-Color Plots for Cl 1358+6245

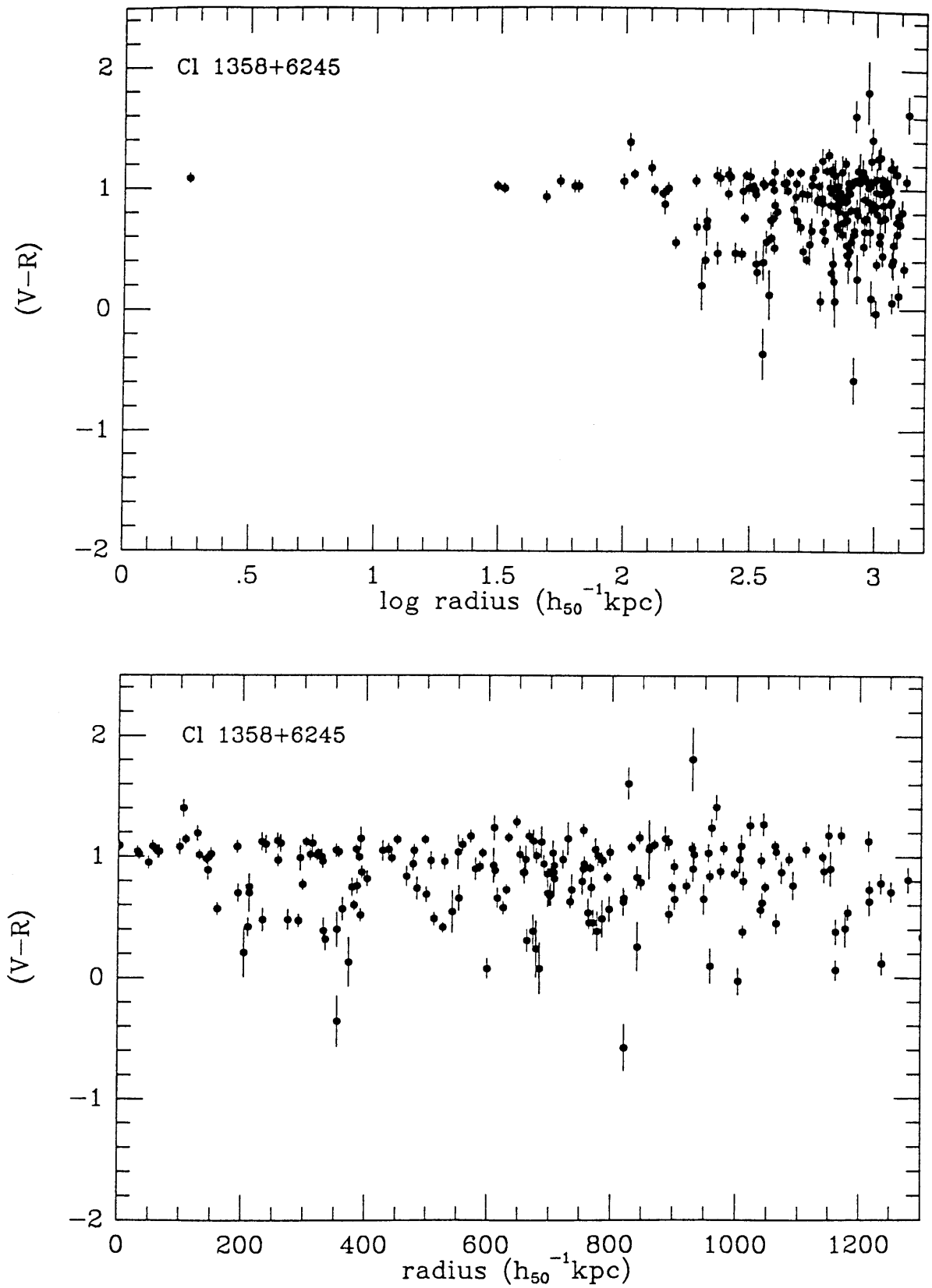

FIGURE 7.11 Radial Distribution of Galaxy Colors

$$(V - R)^c = (V - R) + \eta(z)(R - R_p) \qquad (7.2.6)$$

where $(V-R)^c$ is the corrected color, R_p is the "pivot" magnitude selected to be midway between the brightest cluster galaxy magnitude and the cutoff magnitude (R_p=19.5), and $\eta(z)$ is the slope. The measured slope of $\eta(z)$=–0.036 agrees quite well with the slope predicted from Figure 2 of Visvanathan and Sandage (1977). The upper horizontal line in Figure 7.8 indicates the point about which the colors of E/SO galaxies are symmetrically distributed. Galaxies falling below the lower line are classified as blue (0.2 mag bluer than the mean color of the distribution; see BOV). For completeness, Figure 7.9 shows the color magnitude diagrams for the B–R and R–I colors as a function of R magnitude.

Color-color diagrams are shown plotted in Figure 7.10. The top panel shows B–R plotted against V–R and the bottom panel shows V–R plotted against R–I. These plots serve as an aid in helping distinguish cluster members from field galaxies. We expect a clump of points on either plot to correspond to the location of the red E/S0 galaxies. On the top plot, this clump occurs around (B–R)=2.7 and (V–R)=1.1, while on the bottom plot it occurs at (V–R)=1.1 and (R–I)=1.1.

(iii) spatial distribution of colors

Figure 7.11 displays the V–R color as a function of radial distance from the center of the cluster. The colors are plotted against log radius (top) and against radius (bottom) in h_{50}^{-1}kpc (at z=0.32 with q_0=1/2, the scale is 5.7kpc/arcsec). As expected, virtually all of the galaxies in the core of the cluster (within 200 kpc) are red.

(iv) blue galaxy fraction - Butcher-Oemler Effect

In order to comapre Cl 1358+6245 to the galaxy clusters studied by Butcher and Oemler, we have tried to follow their analysis procedure described in BOV. Defining R_{20}, R_{30}, R_{60} and R_{100} as the radii of circles containing 20, 30, 60, and 100% of the cluster's projected galaxy distribution, the concentration index is defined as

$$C \equiv \log(R_{60}/R_{20}) . \qquad (7.2.7)$$

Butcher and Oemler selected centrally concentrated clusters with $C \geq 0.4$.. In order to measure the radii, BO used radial surface density profiles obtained by counting galaxies on the plates used for the photometry. They certainly had enough field of view to determine properly the radius at which the surface density of cluster galaxies blended in with the surface density of the local background. In addition, BO used their plate material to measure the local background, rather than use a global number derived from galaxy counts in a different part of the sky. Unfortunately, we have no data for Cl 1358+6245 extending more than $1h_{50}^{-1}$Mpc (~3') from the cluster center. We have therefore set R_{100} equal to the radius at the edge of the CCD field. The curve of

growth of the total number of galaxies, N ($m<M_V=-20$), within radius r as a function of r is shown in Figure 7.12a. The values for R_n and N_n (the number of galaxies contained within R_n after subtraction of the background) are listed in Table 7.3 and are shown on Figure 7.12a. We see that Cl 1358+6245 is centrally compact with C=0.52. There are 36 galaxies within R_{30} before correcting for the background. Only 3 of these 36 are not in the matched catalog (because they are missing from the V catalog), and these are not included in the following analysis. The area encircled by R_{30} is 2.9 arcmin^2, so we expect ~3 background galaxies down to the R<21.36 magnitude cutoff.

The blue galaxy fraction as defined in BOV is the number of blue *cluster* galaxies within R_{30} divided by the total number of *cluster* galaxies within R_{30},

$$f_b \equiv \frac{N_b(r < R_{30})}{N\ (r < R_{30})} \tag{7.2.8}$$

where blue galaxies are defined to have rest frame $(B-V)_{rf}$ colors 0.2 mag less (bluer) than the mean cluster $(B-V)_{rf}$. A difficult problem in determining f_b is the proper correction for the background, so that $N_b(r<R_{30})$ represents the number of blue cluster members and does not include (preferentially blue) galaxies from the field. In Cl 1358+6245, $\langle B-V\rangle_{rf}$= 0.89, so galaxies with rest frame $B-V$ < 0.690 are classified as blue. All 33 galaxies within R_{30} have been binned in the color histogram shown in Figure 7.12b. The rest frame color has been corrected for C-M effect described earlier. There are 6 blue galaxies that meet the above criteria. They are galaxies 108, 117, 121, 159, 199, 212 (121 just barely qualifies with $B-V$ of .67). The background has not been subtracted. The blue galaxy fraction is f_b=0.18±0.07 assuming all 33 galaxies are cluster members. If we assume 3 of the galaxies are not cluster galaxies, and, in addition, that these 3 galaxies are blue, the blue fraction drops to f_b=0.10±0.06. In Figure 3 of BOV, Butcher and Oemler show how the blue galaxy fraction increases with redshift. If the BO effect is a universal phenomenon for rich, concentrated clusters, then we expect Cl 1358+6245 at z=0.32 to have f_b between 0.1 and 0.2, consistent with the value we measure.

e) X-ray Properties

The field containing Cl 1358+6245 was observed on three separate occasions with the *Imaging Proportional Counter* (*IPC*) on the *Einstein* satellite: sequence numbers 9227, 7304 and 7305. In each case, the integration time was ~1.5 ksecs and a weak source (<100 counts) was detected near the position of the cluster, about 30' from the center of the field of view of the telescope. The source appeared to be slightly extended, but there were not enough photons to perform any detailed surface brightness analysis. The following count rates for the three observations were determined using data obtained from the Harvard Center for Astrophysics *Einstein* On-Line Service: CR(#9227)=2.83(±0.59)×10^{-2} counts s^{-1}, CR(#7304)=5.61(±0.99)×10^{-2} counts s^{-1}, and CR(#7305)=4.19(±0.76)×10^{-2} counts s^{-1}. In order to decide which count rate is correct, we examined possible

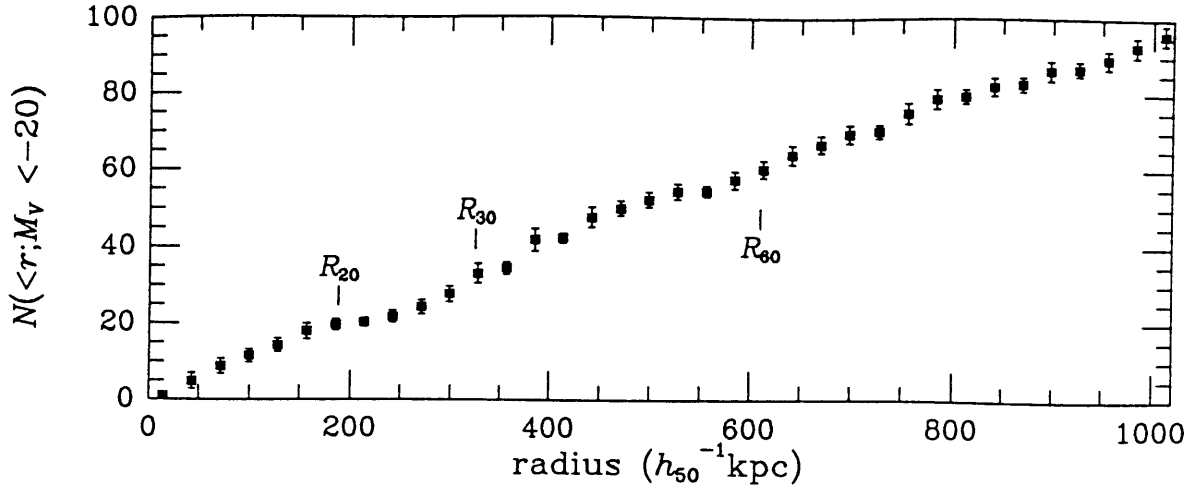

FIGURE 7.12a Curve of growth of the total number of galaxies brighter than M_V=−20 within radius r corrected for the expected number of background galaxies. At the edge of the CCD field (~1 Mpc radius) we have not reached the point where the number of cluster galaxies blends into the background. Nevertheless, R_{100} was chosen as 1Mpc and R_{20}, R_{30}, and R_{60} were computed and are shown on this plot.

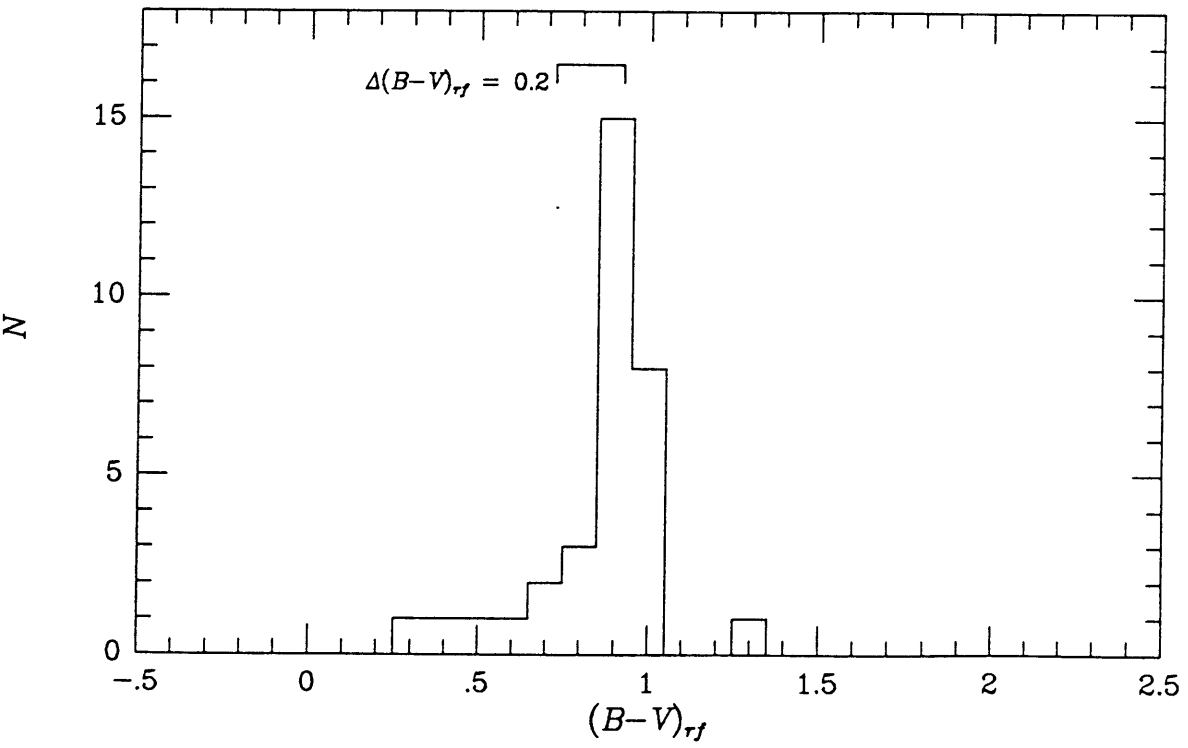

FIGURE 7.12b Color histogram for all of the galaxies brighter than M_V=−20 within R_{30}, corrected for the C-M effect but not for the background. Blue galaxies (those with rest frame $\Delta(B-V)$=0.2 mag less than the mean) are located to the left of the bracket at the top.

systematic instrumental errors, and we compared the positions of the detected sources to the position of the optically dominant galaxy. Sequence number 7305 was rejected because a significant portion (~50%) of the frame and detection subcells were shadowed by the detector ribs. There was only slight obscuration in #7304, however, and none in #9227. In both of these observations, the x-ray source was detected at about the same distance (~1') from the optical position of the cluster. We computed the source flux in the 0.3–3.5 keV band assuming the emission is thermal bremmstrahlung from T=7 keV gas. The fluxes are $8.49(\pm1.8)\times10^{-13}$ ergs cm^{-2} s^{-1}, and $1.68(\pm0.3)\times10^{-12}$ ergs cm^{-2} s^{-1}, after correcting for galactic absorption from a column density of N_H=2.0×10^{20} cm^{-2} in the direction of Cl 1358+6245. At a redshift of z=0.32, the luminosity distance is $2053h_{50}^{-1}$ Mpc (q_0=1/2) and the above fluxes correspond to an x-ray luminosity ranging from L_x(0.5–4.5keV)=4.3×10^{44} h_{50}^{-2} ergs s^{-1} to L_x(0.5–4.5keV)=8.4×10^{44} h_{50}^{-2} ergs s^{-1} (L_x=1.0×10^{45} h_{50}^{-2} ergs s^{-1} if q_0=0). For comparison, Cl 0016+16 has an x-ray luminosity of L_x(0.5–4.5keV)=1.9×10^{45} h_{50}^{-2} ergs s^{-1} (Henry *et al.* 1982) if q_0=1/2. Note that luminosity reported in Henry *et al.* (L_x=2.5×10^{45} h_{50}^{-2} ergs s^{-1}) was computed for q_0=0.

The factor of two discrepancy in luminosity could indicate the presence of a variable x-ray source, such as a quasar or active galaxy, but the required increase in luminosity of ~4×10^{44} h_{50}^{-2} ergs s^{-1} would make this a bright source indeed, and no evidence for such an object exists in the optical data.

f) Summary

We have described the observed optical and x-ray properties of Cl 1358+6245. This cluster is exceedingly rich: it qualifies as Abell Richness Class 3 by counting only the galaxies within a $1h_{50}^{-1}$ Mpc radius rather than the $3h_{50}^{-1}$Mpc used by Abell. When data is obtained that covers a larger field of view, the cluster will certainly become Richness Class 4. At a redshift of z=0.32, the cluster is a bright x-ray source, and may have an x-ray luminosity comparable to the Perseus cluster and a significant fraction (40%) of Cl 0016+16, the most luminous known x-ray cluster. We have classified Cl 1358+6245 as BM Type II and RS Type B. However, these classifications could be changed readily to BM Type I and RS Type cD if it turns out G1 is a cD galaxy (this is discussed further in the next section). We have measured the blue galaxy fraction and find that Cl 1358+6245 exhibits the BO effect at the ~2σ level with the blue fraction ranging from f_b=0.18±0.07 to f_b=0.10±0.06 depending on the background correction. A summary of the properties of Cl 1358+6245 are listed in Table 7.3.

Table 7.3 Summary of the Properties of Cl 1358+6245

cD coordinates	α (1950.0) = $13^h58^m21^s.0$	δ (1950.0) = $62^o45'33''$
Galactic coordinates	l = 109.95	b = 52.84
Extinction	$E(B-V)$ = 0.03±0.01	
Redshift	z = 0.323±0.001	
m_1	18.47	[q_0=0.5, $32h_{50}^{-1}$ kpc aperture]
m_2	19.01	
m_3[a]	19.23	
m_{10}[a]	19.57	
Bautz-Morgan Classification	II (possibly I)[b]	
Rood-Sastry Classification	B (possibly cD)[b]	
$N_{0.5}$[c]	50	
N_{CCD}[c]($m<m_3+2$)	140	
Abell Richness Class	3	
M_V (cD)	−22.89	[q_0=0.5, $32h_{50}^{-1}$ kpc aperture]
$(B-V)_{rf}$(cD)	0.93	
X-ray Luminosity	L_x (0.5-4.5 KeV) = 8.4×10^{44} erg cm^{-2} s^{-1}	

Butcher-Oemler properties[d]

N_{100}	=	99	R_{100}	=	180
N_{20}	=	19	R_{20}	=	32
N_{30}	=	30	R_{30}	=	58
N_{60}	=	58	R_{60}	=	107

Concentration $C = \log(R_{60}/R_{20})$ = 0.52

Blue Galaxy Fraction[e] f_b = 0.18 ± 0.07 (no background correction)

0.10 ± 0.06 (background removed)

[a] High probability of error due to field galaxy contamination.

[b] Classification sensitive to field galaxy contamination and the inability to detect a faint cD envelope around the central galaxy even if it exists.

[c] Corrected for background.

[d] BO properties derived using a radius of 1Mpc (limited by the size of the CCD) which is not the point at which the cluster galaxy density merges into the background galaxy density.

[e] 6 of 33 galaxies brighter than $M_V < -20$ within R_{30} are blue. We expect 3 field galaxies within this region. The second value listed for f_b assumes 3 of the 6 blue galaxies were not cluster members.

7.3 Discussion

a) Nature of central galaxy

The brightest galaxy in rich clusters (G1) is often used as a standard candle in classical cosmological tests such as the Hubble diagram (see §2.3); therefore, a large amount of data exists on these objects as a class (Sandage and Hardy 1973; Schneider, Gunn and Hoessel 1983b [SGHII]; Hoessel and Schneider 1985; Hoessel, Gunn and Thuan 1980 [HGT]). HGT have presented the absolute magnitudes (M_V) of the brightest cluster galaxy in 116 nearby Abell clusters. Their absolute magnitudes were measured in an aperture ($32h_{60}^{-1}$ kpc diameter) similar to that used in this study, so we will compare our results to those of HGT. The brightest cluster galaxy, G1, in Cl 1358+6245 has an absolute visual magnitude of M_V=–22.89 in a $32h_{50}^{-1}$ kpc diameter aperture, and the absolute magnitude increases to M_V ($32h_{60}^{-1}$ kpc) = –23.09 when the magnitude is measured in the HGT aperture (HGT assume q_0=1/2). HGT find that $\langle M_V \rangle_{BCG}$=–22.93±0.27 for BM Type I clusters, and $\langle M_V \rangle_{BCG}$=–22.81±0.28 for BM Type II clusters; therefore, we see that G1 is rather bright for a BM Type II cluster but is well within the dispersion quoted for BM Type I clusters.

The rest frame color of G1 is $(B-V)_{rf}$=0.93. We looked for a color gradient in G1 by measuring the colors in 5 different apertures: $10h_{50}^{-1}$ kpc, $20h_{50}^{-1}$ kpc, $32h_{50}^{-1}$ kpc, $53h_{50}^{-1}$ kpc, and $86h_{50}^{-1}$ kpc (the largest aperture includes some contribution from some of the nearby galaxies). The V–R colors for these apertures were 1.105, 1.095, 1.086, 1.049, and 1.034 respectively. Even though there appears to be a systematic decrease in the color as the aperture size increases, the total amplitude of the color change, $\Delta(V-R)$=–0.07 mag, is only at the 2σ level and we conclude this is not significant enough to say there a real color gradient present in the central galaxy. This value of $\Delta(V-R)$ is consistent with the color gradient seen in the present day giant ellipticals studied by Sandage and Visvanathan (1978).

Galaxy G1 certainly has the color and magnitude of a giant elliptical such as N4472 in the Virgo cluster. The question remains whether G1 is, in fact, a cD galaxy or just part of the compact group in the core of the cluster (similar to the core of A1689). The limiting surface brightness of these observations is 25.5 R mag arcsec^{-2} (see Figure 7.13 for a surface brightness contour map). When this is transferred to the cluster rest frame, after the K-correction and $(1+z)^4$ surface brightness dimming, the limiting surface brightness becomes ~24 V_{rf} mag arcsec^{-2}. Consequently, it is impossible to see the extended envelope of a cD galaxy even if it exists.

b) Substructure

Cl 1358+6245 appears elongated NS (see Figures 7.2 and 7.3) with at least two distinct subclumps ~150" N by ~20" E and ~50" W by ~100 " S. These subclumps become more pronounced when we look at the galaxy

isopleths in Figure 7.5. Such substructure is often seen in rich clusters, and we may be seeing objects that have not been fully virialized, or the secondary infall of groups of galaxies into already virialized clusters. Of course, we may also be seeing chance projections of smaller goups of galaxies that are in no way physically related. It is worth noting an interesting clump of 8-10 faint galaxies (R>22.5) that can barely be seen ~100" E by ~65" N (see Figure 6.2 Plate 4 where this faint group stands out just a bit better than in Figure 7.2). These galaxies are quite red and they may, in fact, be the brightest galaxies in a very distant (z>1) background cluster of galaxies.

c) Significance of BO-effect

Cl 1358+6245, although x-ray selected, seems to fit into the generally accepted picture that (optically selected) clusters with z>0.2 have bluer galaxy populations than clusters today. This picture is reinforced by the results of spectroscopic surveys (Dressler and Gunn 1982; Couch and Sharples 1987; Dressler 1987) which often confirm the cluster membership of the blue galaxies, and suggest the presence of numerous galaxies that have undergone a recent burst of star formation ("E+A" galaxies)[1] and some emission line galaxies. The popular assumption is that we are witnessing dramatic evolution of the galaxies in the cores of these distant clusters, but the exact cause of the evolution is still uncertain. Koo *et al.* (1988), however, caution us not to be too eager or quick to accept this interpretation since the optical selection of clusters is poorly understood at best, and there are a number of examples of clusters with z>0.2 where the BO effect is not seen including A2397, A2645, II Zw 1305+2941 (Koo *et al.* 1988), and Cl 0016+16, the cluster with the largest redshift in the BO sample (z=0.54). Nevertheless, recent work by Gunn and collaborators (Gunn 1989) suggest evolution is present in clusters with redshifts greater than z=0.5, where they see the number of blue galaxies, particularly E+A galaxies (the active fraction) increase with redshift out to z~1. In particular, Dressler and Gunn (Dressler 1987) have examined Cl 0016+16 and found a large number of E+A galaxies that were "missed" in the photometric study since they were not especially "blue" and were not not classified as such by Koo (1981) or Butcher and Oemler (1984).

d) Future Observations

Cl 1358+6245 is certainly an interesting object and worthy of detailed optical, x-ray and radio observations. We plan to obtain deep CCD photometry covering at least the $3h_{50}^{-1}$ Mpc radius of the cluster. We also plan to measure directly the local background, rather than rely on a global value for the background determined from a different part of the sky. Multi-object spectroscopy of a large number (~50) of galaxies in the field is critical, and will enable us to: 1) measure the velocity dispersion and study the dynamics of the cluster, 2) determine

---

[1] Active galaxies labelled "E+A", and also called "post-starburst" or PSB galaxies, were first discovered by Dressler and Gunn (1982) in their spectroscopic observations of 3C 295 cluster. These galaxies have spectra typical of an old stellar population (KIII stars), but with strong Balmer absorption lines and no emission lines. They are called "E+A" because their spectra are indicative of a population of "A" stars added to an older elliptical "E" type population. They are typically 0.2 to 0.3 mag bluer than their "passive" elliptical counterparts.

cluster membership, especially for the blue galaxies, and for galaxies at the bright end of the luminosity function, and 3) investigate the physical nature of the blue galaxies that turn out to be cluster members: are they ellipticals with signs of a recent burst of star formation (the E+A galaxies of Dressler and Gunn)? Are the blue galaxies situated close to other galaxies that may have triggered bursts of star formation through dynamical interactions as suggested by Lavery and Henry (1988)? Could the blue galaxies simply be spiral galaxies akin to what we see today, or possibly emission line galaxies with Seyfert type nuclei?

In addition to the optical observation, imaging x-ray observations (with *ROSAT* or *AXAF*) will allow us to map the x-ray surface brightness and measure directly the local gas density which serves as a tracer of the cluster potential well. We will search for cooler gas near the optically dominant galaxy, a possible signature of a cluster cooling flow. Finally, Cl 1358+6245 is an excellent target in which to look for the Sunyaev-Zel'dovich Effect (see §2.3c), since VLA observations indicate the cluster contains no intrinsic radio source (McHardy 1989) that can contaminate measurements of the microwave decrement.

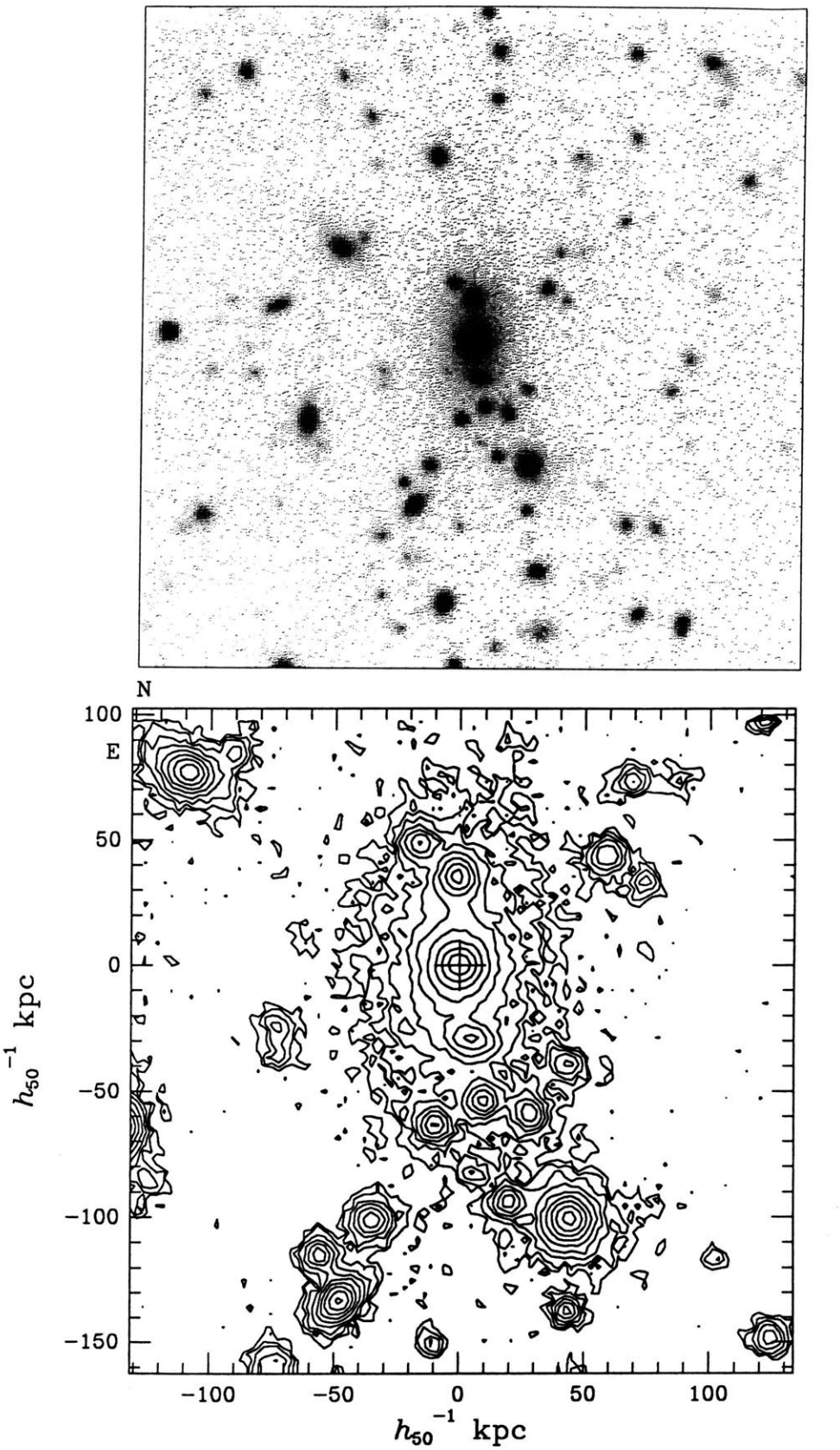

FIGURE 7.13 Surface brightness image (200 × 200 pixels) and contour plot (100 × 100 pixels) of the core of Cl 1358+6245. Contours are drawn from 20 R mag arcsec^{-2} to 25 R mag arcsec^{-2} at intervals of 1 R mag arcsec^{-2}

Table 7.1 Photometry of Cl 1358+6245 galaxies

galaxy	Δα (arcsec)	Δδ (arcsec)	B	V	R	I	(B–R)	(V–R)	(R–I)
1	1.40	−156.00	21.87	...	...	19.33	...	...	...
2	112.70	−153.70	23.11	...	21.66	20.52	1.45	...	1.14
3	177.10	−152.30	...	21.79	20.72	...	...	1.07	...
4	−93.10	−151.70	23.78	...	23.21	20.54	0.57	...	2.68
5	−65.80	−152.20	...	...	20.33	19.37	...	...	0.96
6	−69.90	−147.50	24.45	...	22.26	20.69	2.18	...	1.58
7	155.40	−147.30	23.82	22.56	21.93	20.00	1.89	0.63	1.92
8	139.50	−144.90	...	22.42	21.54	20.67	...	0.88	0.87
9	182.60	−151.90	...	23.17	21.54	...	...	1.63	...
10	−27.10	−145.80	...	23.17	22.91	...	...	0.26	...
11	−13.80	−143.80	22.82	21.52	20.86	20.05	1.96	0.66	0.81
12	−61.10	−143.80	24.28	22.55	21.40	20.17	2.88	1.15	1.23
13	173.50	−143.50	23.61	22.52	21.71	...	1.90	0.81	...
14	−128.80	−142.80	23.63	22.65	21.89	20.96	1.75	0.76	0.93
15	−89.40	−142.40	20.35	...	21.41	20.57	−1.06	...	0.84
16	45.10	−141.10	23.41	22.40	21.58	20.74	1.83	0.83	0.83
17	153.50	−140.30	22.42	21.59	21.05	20.75	1.37	0.54	0.29
18	97.90	−140.00	...	...	18.59	17.80	...	...	0.79
19	106.20	−139.30	23.43	...	22.19	...	1.24	...	...
20	21.40	−139.20	24.56	...	22.42	20.88	2.15	...	1.54
21	12.60	−139.20	22.02	20.40	19.56	18.54	2.46	0.83	1.02
22	−24.90	−138.20	23.16	21.53	20.48	19.50	2.68	1.04	0.99
23	165.10	−136.00	...	22.21	21.08	20.00	...	1.13	1.07
24	150.70	−136.00	...	22.93	22.03	...	...	0.90	...
25	106.70	−136.30	...	...	21.47	20.37	...	...	1.11
26	−29.10	−131.70	21.85	20.39	19.47	...	2.38	0.91	...
27	145.70	−131.30	...	...	21.87	20.96	...	...	0.90
28	−26.30	−130.30	22.15	20.46	19.56	...	2.59	0.90	...
29	−135.70	−128.80	22.37	20.77	19.67	18.52	2.70	1.09	1.15
30	−28.90	−128.10	...	21.15	...	18.80	...	...	...
31	−19.80	−128.00	23.87	22.98	...	...	...	...	...
32	179.50	−124.90	23.26	22.12	...	...	...	...	...
33	192.90	−123.90	...	21.55	21.20	...	...	0.34	...
34	−198.80	−123.60	23.29	...	21.91	20.99	1.38	...	0.93
35	59.30	−123.40	...	22.91	22.53	...	...	0.39	...
36	89.10	−116.90	24.03	....	22.55	21.11	1.48	...	1.45
37	−116.70	−115.80	24.05	22.44	21.42	20.45	2.63	1.02	0.97
38	164.70	−114.60	21.80	20.08	19.08	17.97	2.72	1.00	1.11
39	46.80	−112.20	...	22.07	21.13	19.84	...	0.94	1.29
40	−112.10	−111.60	21.62	20.22	19.47	18.42	2.15	0.75	1.05
41	37.20	−111.30	22.57	20.99	19.82	18.61	2.75	1.17	1.21
42	60.90	−110.80	24.31	...	22.91	...	1.40	...	...
43	41.90	−113.40	...	...	22.06	20.43	...	...	1.64
44	−5.40	−107.00	23.56	22.95	22.03	...	1.54	0.93	...
45	26.40	−104.30	...	21.27	20.37	19.18	...	0.89	1.19
46	91.80	−103.40	...	22.91	22.42	21.25	...	0.49	1.17
47	−143.60	−103.20	22.98	22.16	22.19	...	0.79	−0.03	...
48	174.50	−102.50	23.54	22.36	21.19	...	2.36	1.18	...
49	−64.30	−101.80	24.41	23.10	23.01	21.41	1.40	0.08	1.60
50	−155.90	−97.30	...	22.40	21.13	...	...	1.27	...
51	−78.40	−96.80	...	21.66	20.73	19.55	...	0.93	1.18

galaxy	Δα (arcsec)	Δδ (arcsec)	B	V	R	I	(B–R)	(V–R)	(R–I)
52	69.10	−96.40	...	22.69	22.30	20.51	...	0.39	1.78
53	59.40	−96.90	...	21.35	20.06	18.75	...	1.29	1.31
54	156.90	−99.20	...	...	22.38	21.17	...	...	1.22
55	111.00	−96.80	...	...	20.76	18.71	...	...	2.05
56	27.10	−94.30	...	...	21.62	20.24	...	...	1.38
57	−23.90	−94.00	24.05	23.02	21.98	20.47	2.07	1.04	1.51
58	63.20	−91.70	22.46	20.76	19.61	18.42	2.86	1.16	1.19
59	51.60	−88.90	21.38	...	18.54	17.42	2.84	...	1.12
60	−99.00	−88.30	23.42	22.62	21.83	20.60	1.59	0.80	1.23
61	187.50	−85.30	...	22.12	20.94	...	...	1.18	...
62	−97.00	−84.30	...	22.88	21.74	...	...	1.15	...
63	152.70	−80.60	24.06	22.60	...	...	...	...	...
64	−11.90	−80.40	23.50	22.89	...	22.40	...	...	...
65	−59.10	−78.50	23.01	21.37	20.28	19.08	2.73	1.10	1.20
66	138.30	−78.30	...	22.13	21.48	20.77	...	0.65	0.71
67	16.40	−77.70	21.64	19.82	18.68	17.51	2.97	1.14	1.17
68	189.40	−77.30	...	22.24	21.86	...	...	0.38	...
69	52.60	−76.80	23.32	21.64	20.68	19.42	2.64	0.96	1.26
70	98.00	−75.40	23.42	22.22	21.53	20.74	1.89	0.69	0.79
71	77.60	−74.50	22.35	...	20.52	...	1.83	...	...
72	19.70	−74.40	22.74	21.09	20.03	18.83	2.71	1.06	1.20
73	−69.30	−72.90	22.72	21.41	20.24	19.14	2.48	1.17	1.10
74	176.40	−72.70	22.99	21.02	...	...	...	...	...
75	24.20	−71.20	...	22.29	21.24	...	...	1.05	...
76	−2.20	−68.90	...	22.45	21.30	...	...	1.15	...
77	28.90	−73.00	...	...	21.99	20.65	...	...	1.33
78	−125.00	−69.40	...	...	23.54	20.54	...	...	3.01
79	−176.40	−67.70	23.03	22.27	21.40	20.21	1.64	0.87	1.19
80	−133.30	−67.30	23.38	21.72	20.93	19.40	2.45	0.79	1.53
81	−8.60	−66.50	21.00	19.83	19.23	18.29	1.77	0.60	0.94
82	−16.00	−66.00	22.86	21.52	20.76	19.94	2.10	0.76	0.82
83	95.70	−65.60	20.92	...	...	17.41	...	...	...
84	−27.10	−65.00	...	...	21.43	20.06	...	...	1.37
85	4.90	−61.80	22.48	20.87	19.82	18.69	2.67	1.05	1.13
86	−131.90	−61.70	23.53	23.04	21.43	20.48	2.10	1.61	0.95
87	19.70	−59.50	21.99	20.17	19.13	17.98	2.86	1.04	1.15
88	77.60	−58.70	...	22.36	21.71	20.38	...	0.66	1.33
89	168.60	−55.90	...	22.47	21.37	20.30	...	1.09	1.07
90	−22.50	−56.10	...	...	21.87	20.62	...	...	1.25
91	44.70	−54.90	23.46	21.76	20.94	19.93	2.52	0.82	1.01
92	15.10	−54.40	22.50	20.74	19.73	18.73	2.77	1.01	1.00
93	88.80	−54.00	22.49	20.70	19.66	18.51	2.83	1.03	1.15
94	162.00	−53.10	24.20	22.65	21.24	19.85	2.96	1.41	1.39
95	−34.70	−51.70	...	22.79	22.39	22.30	...	0.40	0.09
96	−150.90	−49.60	23.05	21.57	20.65	19.63	2.40	0.92	1.02
97	−6.70	−47.80	22.69	22.01	21.53	22.64	1.17	0.48	−1.11
98	−64.20	−47.80	23.93	23.52	...	...	...	...	...
99	26.20	−46.40	22.39	20.63	19.51	18.37	2.88	1.12	1.14
100	2.10	−46.00	23.73	22.09	20.98	19.97	2.75	1.11	1.01
101	−150.90	−44.40	22.49	21.76	21.23	20.50	1.26	0.53	0.73
102	−9.90	−40.80	22.76	22.11	21.01	20.38	1.75	1.10	0.62
103	−82.30	−39.80	24.76	22.67	...	...	...	...	...
104	−23.80	−38.50	23.85	21.53	20.40	19.34	3.45	1.13	1.07

galaxy	Δα (arcsec)	Δδ (arcsec)	B	V	R	I	(B–R)	(V–R)	(R–I)
105	–95.20	–37.50	23.64	...	23.16	...	0.48	...	...
106	50.30	–37.20	...	...	21.41	19.91	...	...	1.50
107	79.50	–37.20	23.04	21.55	20.85	19.76	2.18	0.69	1.10
108	3.50	–37.10	21.97	20.43	19.69	18.78	2.29	0.75	0.90
109	–199.50	–35.50	22.98	...	20.35	19.21	2.62	...	1.14
110	–47.90	–34.30	23.19	22.12	21.80	20.91	1.39	0.32	0.89
111	–9.50	–32.40	23.10	21.31	20.23	19.18	2.87	1.08	1.05
112	–165.20	–32.30	23.01	21.91	20.88	19.86	2.13	1.03	1.02
113	–134.60	–31.40	23.31	21.74	20.76	19.68	2.55	0.98	1.08
114	9.10	–30.60	...	...	22.60	20.98	...	...	1.62
115	–25.70	–26.40	22.81	21.82	21.40	20.69	1.41	0.42	0.71
116	–113.80	–26.30	23.56	22.12	21.81	20.65	1.76	0.31	1.16
117	–22.00	–25.90	23.35	21.91	21.21	20.10	2.14	0.70	1.11
118	64.30	–25.50	22.55	21.09	20.22	19.24	2.34	0.87	0.98
119	58.70	–25.00	24.13	22.20	21.63	20.17	2.50	0.57	1.46
120	37.80	–25.00	22.77	21.32	20.36	19.24	2.42	0.97	1.12
121	–7.70	–24.20	...	22.17	21.28	19.12	...	0.89	2.16
122	95.80	–23.70	24.23	...	23.21	...	1.02	...	...
123	8.20	–23.60	22.20	20.41	19.43	18.41	2.77	0.98	1.02
124	51.80	–23.20	22.47	20.71	19.67	18.57	2.80	1.03	1.10
125	27.20	–23.10	23.83	23.13	22.92	...	0.91	0.21	...
126	108.80	–20.90	21.90	20.44	19.71	18.73	2.19	0.73	0.98
127	9.60	–20.30	23.29	21.71	20.52	...	2.77	1.19	...
128	–63.70	–19.30	23.46	21.86	21.11	19.94	2.35	0.75	1.17
129	5.90	–17.50	23.38	21.98	20.58	19.58	2.80	1.40	1.00
130	–8.00	–17.50	21.95	20.15	19.01	17.86	2.94	1.14	1.15
131	–3.40	–17.10	23.61	21.52	20.43	19.30	3.18	1.08	1.14
132	68.00	–15.90	...	...	22.49	21.07	...	...	1.41
133	92.10	–15.30	23.95	...	22.90	...	1.04	...	...
134	23.00	–11.50	22.00	20.32	19.31	18.12	2.68	1.00	1.19
135	1.70	–11.00	23.69	21.38	20.34	19.14	3.35	1.04	1.20
136	–4.80	–10.50	23.50	21.35	20.31	19.19	3.18	1.04	1.12
137	–1.50	–9.60	23.06	21.08	20.00	18.94	3.06	1.08	1.06
138	–67.00	–9.30	...	20.63	19.57	18.44	...	1.06	1.13
139	–177.00	–8.80	...	22.68	21.70	...	...	0.98	...
140	–1.10	–14.40	...	...	21.24	20.08	...	...	1.16
141	–57.20	–8.60	23.37	21.75	20.75	19.52	2.61	1.00	1.23
142	–7.60	–6.80	24.30	...	21.08	20.01	3.21	...	1.07
143	–132.30	–6.20	23.31	...	22.07	...	1.24	...	...
144	–168.90	–5.70	23.97	22.66	22.56	20.84	1.40	0.10	1.72
145	–0.60	–5.40	22.56	20.63	19.59	18.46	2.97	1.04	1.13
146	–138.30	–5.30	22.78	20.97	20.00	18.90	2.78	0.97	1.10
147	36.90	–4.60	...	23.03	22.33	21.47	...	0.70	0.86
148	–95.30	–5.10	...	23.13	22.57	21.44	...	0.55	1.14
149	103.20	–3.60	22.18	20.47	19.56	18.43	2.62	0.92	1.13
150	–122.50	–3.40	22.71	20.95	20.09	18.96	2.62	0.86	1.13
151	–87.30	–3.00	22.05	20.38	19.25	18.16	2.80	1.14	1.08
152	90.30	–2.90	...	...	22.46	21.02	...	...	1.44
153	77.30	–1.70	24.09	...	23.06	...	1.04	...	...
154	–0.10	–0.30	21.40	19.56	18.47	17.30	2.93	1.09	1.17
155	–62.30	0.20	23.55	22.81	23.17	...	0.37	–0.36	...
156	–54.50	1.50	...	21.26	20.24	19.12	...	1.02	1.12
157	–184.40	3.40	...	20.55	19.80	18.83	...	0.75	0.97

galaxy	Δα (arcsec)	Δδ (arcsec)	B	V	R	I	(B–R)	(V–R)	(R–I)
158	−144.30	4.50	23.40	22.59	21.96	20.50	1.44	0.63	1.46
159	27.70	4.80	22.39	21.01	20.44	19.63	1.96	0.57	0.81
160	−12.70	5.60	...	22.60	...	19.83	...	...	...
161	−0.10	5.80	22.30	20.37	19.36	18.23	2.94	1.02	1.13
162	−34.00	7.10	...	...	22.39	21.45	...	...	0.95
163	−191.60	7.80	...	...	20.79	20.09	...	...	0.70
164	2.70	8.10	23.07	20.99	20.04	18.75	3.03	0.95	1.29
165	−112.80	8.60	...	...	22.32	20.63	...	...	1.68
166	−74.70	11.00	24.03	22.36	...	21.05	...	...	...
167	−93.30	12.90	23.72	...	...	20.86	...	...	...
168	18.90	13.20	22.19	20.41	19.40	18.23	2.79	1.01	1.18
169	−84.00	14.70	23.94	...	21.55	20.23	2.39	...	1.32
170	−173.50	17.10	23.68	...	22.24	20.83	1.44	...	1.41
171	−52.50	17.50	23.28	...	21.30	20.92	1.98	...	0.37
172	161.70	19.20	23.82	...	22.97	...	0.86	...	...
173	82.00	19.20	22.97	21.33	20.28	19.20	2.69	1.05	1.07
174	66.20	19.20	22.22	21.13	20.62	19.55	1.60	0.52	1.06
175	−110.40	19.90	23.45	22.28	...	...	...	...	...
176	120.90	24.30	23.71	22.12	21.44	20.56	2.27	0.68	0.88
177	−111.50	25.70	...	21.92	...	20.18	...	...	...
178	89.40	25.80	23.70	21.98	...	19.76	...	...	...
179	5.00	25.80	22.56	21.00	19.98	18.81	2.58	1.02	1.17
180	128.40	27.00	...	23.12	...	20.49	...	...	...
181	−14.50	25.60	...	...	21.84	21.70	...	...	0.14
182	78.30	30.40	22.62	20.98	20.04	18.94	2.58	0.94	1.10
183	−49.30	30.80	...	21.35	20.39	19.19	...	0.96	1.20
184	−115.20	31.30	...	21.80	20.79	19.77	...	1.01	1.02
185	−161.10	29.90	...	23.88	22.07	21.74	...	1.81	0.33
186	−168.80	32.00	22.82	21.53	20.64	19.54	2.17	0.88	1.10
187	111.20	32.70	21.42	...	...	18.85	...	...	...
188	−2.90	33.80	23.84	22.40	...	20.20	...	...	...
189	−101.70	34.10	...	22.60	21.36	19.56	...	1.24	1.80
190	160.30	35.00	23.25	22.55	21.65	...	1.60	0.90	...
191	−130.90	36.00	...	22.31	21.85	20.10	...	0.46	1.75
192	14.80	31.70	...	22.65	...	20.78	...	...	...
193	38.40	34.50	...	22.57	21.58	19.58	...	0.99	2.00
194	18.90	36.50	23.81	22.15	21.67	20.34	2.14	0.48	1.33
195	31.90	37.50	23.33	21.66	...	19.04	...	...	...
196	53.30	38.40	24.25	23.11	22.99	...	1.26	0.13	...
197	−80.30	38.50	23.15	21.86	20.90	19.58	2.26	0.97	1.32
198	123.70	38.80	23.84	22.70	21.96	21.09	1.87	0.73	0.87
199	−33.40	38.90	22.48	21.00	20.53	19.70	1.95	0.47	0.83
200	−22.80	40.30	21.90	21.49	...	...	...	...	...
201	−48.30	35.90	...	...	21.86	20.53	...	...	1.33
202	96.80	41.60	23.14	21.87	21.79	20.76	1.35	0.08	1.02
203	72.70	44.00	23.69	...	22.99	...	0.69	...	...
204	−52.40	44.10	22.35	20.76	19.76	18.71	2.59	1.00	1.05
205	−130.00	44.80	...	22.55	...	20.34	...	...	...
206	−2.80	40.60	...	22.07	20.95	19.85	...	1.12	1.10
207	−1.40	45.90	23.98	22.50	...	...	...	...	...
208	34.30	47.20	22.99	22.31	21.92	21.38	1.06	0.39	0.54
209	65.30	47.30	...	...	22.12	21.64	...	...	0.48
210	−115.90	49.70	23.17	22.75	...	...	...	...	...

galaxy	Δα (arcsec)	Δδ (arcsec)	B	V	R	I	(B–R)	(V–R)	(R–I)
211	120.50	50.40	23.32	21.65	...	19.80	...	...	...
212	13.90	50.50	21.55	20.06	19.30	18.14	2.25	0.77	1.16
213	–52.90	51.10	24.20	23.36	...	20.84	...	...	...
214	99.60	52.30	23.43	22.28	...	...	...	...	...
215	–15.30	52.90	23.51	21.96	20.85	20.07	2.66	1.11	0.77
216	169.20	54.10	23.55	22.37	...	20.58	...	...	...
217	–165.10	57.50	...	...	20.30	19.11	...	...	1.19
218	–96.90	58.10	24.29	...	21.48	20.44	2.81	...	1.04
219	–168.30	58.20	21.67	20.74	20.36	19.36	1.31	0.38	1.00
220	167.80	60.20	22.70	21.94	21.14	...	1.56	0.80	...
221	–46.80	62.20	22.11	20.53	19.54	18.40	2.57	0.99	1.13
222	–195.20	63.30	21.88	...	20.05	19.23	1.82	...	0.83
223	143.70	63.90	23.51	21.85	20.73	19.39	2.78	1.12	1.34
224	100.70	64.30	...	23.31	23.06	...	...	0.24	...
225	137.70	64.40	25.26	...	22.80	...	2.46	...	...
226	106.30	64.80	...	23.16	22.29	...	...	0.87	...
227	76.10	68.00	...	22.41	21.51	20.51	...	0.90	1.00
228	–51.50	70.60	23.61	22.29	...	20.00	...	...	...
229	–121.90	70.70	23.29	...	22.62	...	0.67	...	...
230	–173.40	71.40	...	...	20.61	19.95	...	...	0.66
231	160.10	72.70	...	20.29	19.43	18.33	...	0.86	1.10
232	–161.30	74.50	22.78	22.19	21.09	20.07	1.69	1.09	1.02
233	–7.90	76.20	22.59	...	19.59	18.40	3.00	...	1.18
234	–3.70	77.60	23.34	...	20.19	...	3.16	...	...
235	84.50	80.20	...	22.61	21.63	19.94	...	0.98	1.68
236	–14.40	80.90	23.38	22.12	21.28	20.77	2.10	0.84	0.50
237	–172.00	83.30	23.00	21.27	20.29	19.07	2.71	0.98	1.22
238	–17.10	83.40	...	22.30	21.56	...	...	0.74	...
239	–124.20	83.90	...	...	22.28	20.78	...	...	1.51
240	–131.60	84.70	22.00	20.18	...	21.40	...	...	...
241	–131.60	84.80	...	...	19.15	18.02	...	...	1.13
242	23.70	86.90	21.98	21.14	20.65	19.73	1.33	0.49	0.91
243	31.10	87.30	20.37	19.50	19.08	18.29	1.30	0.42	0.79
244	144.70	87.70	23.70	22.04	20.80	19.65	2.90	1.24	1.15
245	141.90	88.20	23.41	22.74	22.09	...	1.32	0.65	...
246	–126.10	89.90	...	...	21.78	20.69	...	...	1.09
247	–182.20	91.30	23.83	...	22.75	...	1.08	...	...
248	71.40	91.50	23.61	22.29	21.42	19.88	2.19	0.87	1.54
249	–0.90	93.40	...	...	22.71	21.08	...	...	1.64
250	31.60	95.20	...	...	21.60	20.58	...	...	1.02
251	–80.20	95.80	24.86	...	23.11	...	1.76	...	...
252	78.40	96.20	22.92	22.50	21.47	20.05	1.45	1.03	1.42
253	–93.60	96.30	23.42	22.58	22.04	20.73	1.38	0.54	1.31
254	–117.70	97.70	24.35	...	21.37	20.35	2.98	...	1.02
255	91.80	97.90	...	...	22.88	20.59	...	...	2.29
256	–59.80	99.10	22.45	20.70	19.83	18.67	2.62	0.87	1.16
257	88.10	99.70	...	...	23.18	22.93	...	...	0.25
258	–110.30	100.10	22.97	21.42	20.27	19.03	2.71	1.16	1.24
259	49.20	103.60	23.45	22.05	21.03	19.95	2.42	1.02	1.08
260	21.80	106.00	22.58	22.04	21.38	20.14	1.20	0.66	1.24
261	–68.10	107.20	...	21.90	20.92	...	...	0.98	...
262	148.60	107.60	...	21.98	21.36	...	...	0.62	...
263	4.20	109.20	...	...	20.57	19.50	...	...	1.06

galaxy	Δα (arcsec)	Δδ (arcsec)	B	V	R	I	(B–R)	(V–R)	(R–I)
264	–7.40	109.80	22.39	21.12	20.54	19.73	1.86	0.58	0.80
265	160.50	111.90	24.11	...	22.29	20.85	1.82	...	1.44
266	39.00	112.00	23.65	22.34	21.21	...	2.44	1.13	...
267	–47.20	113.30	...	22.53	21.83	...	...	0.70	...
268	180.90	113.30	22.19	20.82	...	...	...	...	...
269	62.70	115.80	24.47	21.95	...	20.17	...	...	...
270	–56.00	117.70	22.88	21.37	...	19.11	...	...	...
271	–94.50	118.70	24.15	22.57	21.49	...	2.66	1.08	...
272	–36.50	119.10	23.42	22.93	22.11	21.31	1.31	0.82	0.80
273	58.20	119.80	...	21.71	20.77	19.57	...	0.94	1.20
274	62.20	120.00	23.97	22.17	21.42	20.20	2.55	0.75	1.22
275	14.50	120.00	23.26	22.95	21.83	...	1.42	1.12	...
276	–143.20	121.10	23.38	22.09	21.64	...	1.74	0.45	...
277	132.70	121.80	23.00	22.26	21.00	19.49	2.00	1.26	1.51
278	–144.60	122.00	...	...	21.54	20.45	...	...	1.09
279	–14.70	122.20	...	...	21.46	21.22	...	...	0.24
280	–163.60	122.90	23.42	21.85	21.79	20.42	1.62	0.06	1.37
281	7.50	123.30	23.86	21.79	20.91	...	2.95	0.88	...
282	55.90	124.40	...	22.40	21.34	...	...	1.06	...
283	32.10	125.10	22.09	20.99	20.36	...	1.73	0.63	...
284	51.70	125.40	...	22.54	...	19.69	...	...	...
285	137.30	126.40	22.68	...	20.14	18.94	2.54	...	1.20
286	–190.40	127.20	23.38	...	22.36	...	1.02	...	...
287	–37.50	127.50	22.66	21.06	19.85	18.67	2.81	1.22	1.18
288	99.80	127.80	22.73	21.69	20.92	19.91	1.81	0.76	1.01
289	–4.10	130.70	23.70	...	21.36	19.74	2.33	...	1.62
290	57.30	132.80	...	22.52	23.11	...	...	–0.58	...
291	–136.70	130.80	...	...	22.33	20.70	...	...	1.63
292	133.20	131.70	...	...	22.08	20.40	...	...	1.68
293	17.70	133.50	22.01	20.83	20.37	19.81	1.64	0.46	0.56
294	–20.70	135.40	23.65	22.21	21.20	20.51	2.45	1.01	0.69
295	–36.00	135.60	...	22.34	21.77	20.20	...	0.57	1.57
296	68.30	137.20	21.62	19.85	18.76	17.63	2.87	1.10	1.13
297	95.20	140.00	23.30	...	22.23	21.57	1.07	...	0.66
298	24.40	140.70	...	22.67	...	20.80	...	...	...
299	124.40	141.30	23.48	21.70	...	19.44	...	...	...
300	164.50	142.60	...	22.03	21.91	20.49	...	0.12	1.42
301	76.20	142.50	...	...	21.82	20.53	...	...	1.29
302	51.10	142.80	23.58	23.65	22.59	...	0.99	1.06	...
303	–17.00	145.70	21.61	19.91	18.84	17.68	2.78	1.08	1.16
304	–109.30	147.10	23.15	21.69	20.73	19.61	2.43	0.97	1.11
305	4.30	151.20	22.65	21.03	...	18.83	...	...	...
306	147.60	151.60	23.67	...	22.69	...	0.98	...	...
307	92.40	151.80	...	...	22.30	21.06	...	...	1.23
308	–100.40	158.30	23.42	21.72	20.69	19.60	2.73	1.04	1.09
309	–114.80	158.80	23.40	21.54	20.47	19.26	2.93	1.06	1.21
310	75.30	159.60	23.66	...	22.61	...	1.06	...	...
311	30.30	161.00	23.13	21.45	20.38	19.31	2.75	1.07	1.07
312	149.90	161.40	24.28	22.01	21.30	19.76	2.98	0.71	1.55
313	–47.60	162.00	22.74	20.94	20.10	19.12	2.63	0.84	0.99
314	–82.80	165.10	...	...	21.26	20.05	...	...	1.21
315	148.10	166.50	...	...	21.88	20.68	...	...	1.20
316	–134.30	166.70	23.00	21.94	21.21	20.41	1.79	0.73	0.80

galaxy	$\Delta\alpha$ (arcsec)	$\Delta\delta$ (arcsec)	B	V	R	I	(B–R)	(V–R)	(R–I)
317	–138.90	167.30	...	22.11	21.33	20.20	...	0.78	1.13
318	–32.30	166.90	...	...	21.43	21.72	...	...	–0.30
319	–121.30	168.10	24.13	22.89	22.48	21.35	1.65	0.41	1.13
320	–22.10	171.30	22.67	21.09	20.02	18.79	2.65	1.07	1.22
321	–38.20	179.00	...	21.53	20.97	19.86	...	0.56	1.11
322	–57.30	175.30	...	...	20.59	19.69	...	...	0.90

REFERENCES:

Abell, G.O. 1958, "The Distribution of Rich Clusters of Galaxies," *Ap.J. Supp.*, **3**, 211.

Abell, G.O., Corwin, H.G., and Olowin, R.P. 1989, "A Catalog of Rich Clusters of Galaxies," *Ap.J.Supp.*, **70**, 1. ACO

Bessel, M.S. 1986, "VRI Photometry III: Photographic and CCD R and I Bands and the Kron-Cousins RI System," *P.A.S.P.*, **98**, 1303.

Burstein, D., and Heiles, C. 1982, "Reddenings Derived from HI and Galaxy Counts: Accuracy and Maps," *Astron. J.*, **87**, 1165.

Butcher, H. and Oemler, A. 1984,"The Evolution of Galaxies in Clusters. V. A Study of Populations since z~0.5," *Ap.J.*, **285**, 426 (BOV).

Coleman, G.D., Wu, C.C., and Weedman, D.W. 1980, "Colors and Magnitudes Predicted for High-Redshift Galaxies," *Ap.J.Supp.*, **43**, 393.

Couch, W.J., Shanks, T., and Pence, W. 1985, "CCD Photometry of a Distant Cluster of Galaxies at a Redshift of 0.57," *M.N.R.A.S.*, **213**, 215.

Couch, W.J. and Newell, E.B. 1984, "Distant Clusters of Galaxies. I. Uniform Photometry of 14 Rich Clusters," *Ap.J.*, **56**, 143.

Couch, W., Ellis, R., Godwin, J., and Carter, D. 1983, "Spectral Energy Distributions for Galaxies in High Redshift Clusters. I: Methods and Application to Three Clusters with 0.22 <z<0.31," *M.N.R.A.S.*, **205**, 1287.

Couch, W.J., and Sharples, R.M. 1987, "A Spectroscopic Study of Three Rich Galaxy Clusters at z=0.31," *M.N.R.A.S.*, **229**, 423.

Dressler, A. 1978, "Bautz-Morgan Classes and the Luminosity Function for Clusters of Galaxies," *Ap.J.*, 222, 23.

Dressler, A. 1987, "Evolution of Cluster Galaxies Since z=1," in *Nearly Normal Galaxies: From the Planck Time to the Present*, ed. Faber (New York: Springer).

Dressler, A., and Gunn, J.E. 1982, "Spectroscopy of Galaxies in Distant Clusters. I. First Results for 3C295 and 0024+1654," *Ap.J.*, **263**, 533.

Dressler, A., and Gunn, J.E. 1983, "Spectroscopy of Galaxies in Distant Clusters. II. The Population of the 3C295 Cluster," *Ap.J.*, **270**, 7.

Dressler, A., Gunn, J.E., and Schneider, D.P. 1985, "Spectroscopy of Galaxies in Distant Clusters. III. The Population of Cl 0024+1654," *Ap.J.*, **294**, 70.

Ellis, R., Couch, W., MacLaren, I., and Koo, D., 1985, "Spectral Energy Distributions for Galaxies in High Redshift Clusters. II: 0016+16 at z=0.54," *M.N.R.A.S.*, **217**, 239.

Gunn, J.E. 1989, in *Clusters of Galaxies: STScI Workshop on Clusters of Galaxies.*

Gunn, J.E., Hoessel, J.G., and Oke, J.B. 1986, "A Systematic Survey for Distant Galaxy Clusters," *Ap.J.*, **306**, 37.

Gunn, J.E., and Oke, J.B. 1975, "Spectrophotometry of Faint Cluster Galaxies and the Hubble Diagram: An Approach to Cosmology," *Ap.J.*, **195**, 255.

Henry, J.P., Soltan, A., Briel, U., and Gunn. J.E. 1982, "Evolution of the Cluster X-Ray Luminosity Function Slope," *Ap.J.*, **262**, 1.

Hoessel, J.G., Gunn, J.E., and Thuan, T.X. 1980, "The Photometric Properties of Brightest Cluster Galaxies. I. Absolute Magnitudes in 116 Nearby Abell Clusters," *Ap.J.*, **241**, 486.

Hoessel, J.G., and Schneider, D. 1985, "CCD Observations of Abell Clusters. IV. Surface Photometry of 175 Brightest Cluster Galaxies," *Astron. J.*, **90**, 1648.

Jarvis, J.F., and Tyson, J.A. 1981, "FOCAS: Faint Object Classification and Analysis System," *Astron.J.*, **86**, 476.

Johnson, H.L. 1968, in *Nebulae and Interstellar Matter*, ed. B. Middlehurst and L. Aller (Chicago: University of Chicago Press), p.167.

Koo, D. 1981, "Multicolor Photometry of the Red Cluster 0016+16 at z=0.54," *Ap.J.*, **251**, L75.

Koo, D., Kron, R., Nanni, D., Trevese, D., and Vignato, A. 1988, "II Zw 1305.4+2941 at z=0.24: Another Rich, Red, Compact Cluster," *Ap.J.*, **333**, 586.

KPNO 1983, Kitt Peak National Observatory Newsletter No. 25.

Kristian, J., Sandage, A., and Westphal, J. 1978, "The Extension of the Hubble Diagram. II. New Redshifts and Photometry of Very Distant Galaxy Clusters: First Indication of a Deviation of the Hubble Diagram from a Straight Line," *Ap.J.*, **221**, 383.

Landolt, A. 1983, "*UBVRI* Photometric Standard Stars Around the Celestial Equator," *Astron. J.*, **88**, 439.

Lavery, R.J., and Henry, J.P. 1988, "Evidence for Galaxy-Galaxy Interactions as an Active Agent of the Butcher-Oemler Effect at a Redshift of 0.2," *Ap.J.*, **330**, 596.

Lilly, S.J. and Gunn, J.E. 1985, "Infrared Photometry of Galaxies in the Butcher-Oemler Cluster 0024+1654," *M.N.R.A.S.*, **217**, 551.

Luppino, G.A. 1985, Internal MIT memo on MASCOT Upgrade

Luppino G.A. 1989, "A Virtual-Phase CCD Camera for the MDM Observatory," *P.A.S.P.*, in press.

Lynds, R. and Petrosian, V. 1989, "Luminous Arcs in Clusters of Galaxies," *Ap.J.*, **336**, 1.

MacLaren, I., Ellis, R., and Couch, W. 1988, "Spectral Energy Distributions of Galaxies in High Redshift Clusters. III: Abell 370 at z = 0.37," *M.N.R.A.S.*, **230**, 249.

McHardy, I. 1989, in preparation.

Mellier, Y. 1989, "Arc Survey in Clusters of Galaxies," in *Clusters of Galaxies: STScI Workshop on Clusters of Galaxies*, ed. M.J.Fitchett and W.R. Oegerle (Baltimore: STScI), p.175.

Quintana, H. and Melnick, J. 1982, "The Correlation Between X-ray Luminosity and Velocity Dispersion in Clusters of Galaxies," *Astron.J.*, **87**, 972.

Ricker, G., Bautz, M., Dewey, D., and Meyer, S. 1981, "Optical studies of x-ray sources with MASCOT- a charge-coupled-device (CCD) based astronomical instrument," *S.P.I.E.*, **290**, 190.

Sandage, A. and Hardy, E. 1973, "The Redshift Distance Relation. VII. Absolute Magnitudes of the First Three Ranked Cluster Galaxies as Functions of Cluster Richness and Bautz-Morgan Cluster Type: The Effect on q_0," *Ap.J.*, **183**, 743.

Sandage , A. and Visvanathan, N. 1978, "Color and Absolute Magnitude Relation for E and S0 galaxies. III. Fully Corrected Photometry for 405 Galaxies: Comparison of Color Distributions for E and S0 Field and Cluster Galaxies," *Ap.J.*, **225**, 742.

Schild R. 1983, "CCD Photometry of M67 Stars Useful as *BVRI* Standards," *P.A.S.P.*, **95**, 1021.

Schneider, D.P., Dressler, A., and Gunn, J.E. 1986, "Three-Color CCD Photometry of the Distant Cluster of Galaxies Cl 0024+1654," *Astron.J.*, **92**, 523.

Schneider, D.P., Gunn, J.E., and Hoessel, J.G. 1983a (SGHI), "CCD Photometry of Abell Clusters. I. Magnitudes and Redshifts for 84 Brightest Cluster Galaxies," *Ap.J.*, **264**, 337.

Schneider, D.P., Gunn, J.E., and Hoessel, J.G. 1983b (SGHII), "CCD Photometry of Abell Clusters. II. Surface Photometry of 249 Cluster Galaxies," *Ap.J.*, **268**, 476.

Sharples, R., Ellis, R., Couch, W., and Gray, P. 1985, "Multi-object Spectroscopy of the Distant Cluster AC103," *M.N.R.A.S.*, **212**, 687.

Soucail, G., Fort, B., Mellier, Y., and Picat, J.P. 1987, "A Blue Ring-Like Structure in the Center of the A 370 Cluster of Galaxies," *Astron. Ap.*, **172**, L14.

Soucail, G., Mellier, Y., Fort, B., Mathez, G., and Cailloux, M. 1988, "The Giant Arc in A370: Spectroscopic Evidence for Gravitational Lensing from a Source at z=0.724," *Astron. Ap.* , **191**, L19.

Struble, M.F. and Rood, H.J. 1982, "Morphological Classifications (Revised RS) of Abell CLusters in D<4 and an Analysis of Observaed Correlations," *Astron.J.*, **87**, 7.

Thompson, L. 1986, "High-Resolution Imaging fron Mauna Kea: Surface Photometry of Galaxies in CL0024+16," *Ap.J.*, **300**, 639.

Thompson, L. 1986, "Galaxy Distribution in Butcher-Oemler Clusters," *Ap.J.*, **306**, 384.

Thompson, L. 1988, "High-Resolution Imaging from Mauna Kea: Morphology of Butcher-Oemler Galaxies," *Ap.J.*, **324**, 112.

Thuan, T.X., and Gunn, J.E. 1976, *P.A.S.P.*, **88**, 543.

Tyson, J.A. 1988, "Deep CCD Survey: Galaxy Luminosity and Color Evolution," *Astron.J.*, **96**, 1.

Valdes, F 1982, *KPNO FOCAS Users Manual.*

Visvanathan, N. and Sandage, A. 1977, "The Color-Absolute Magnitude Relation for E and S0 Galaxies. I. Calibration and Tests for Universality using Virgo and Eight other Nearby Clusters," *Ap.J.*, **216**, 214.

Zwicky, F., and Herzog, E. 1968, *Catalogue of Galaxies and of Clusters of Galaxies, Vol. IV*, (Pasadena: California Institute of Technology), p.125.

Chapter 8

Future Work

8.1 Future Cluster Observations

a) Required Imaging and Spectroscopy

The observations described in Chapter 6 reveal a number of new, distant clusters of galaxies selected on the basis of a SSRS. In order to be certain we have correctly identified the brightest cluster member and the radio ID is in fact a member of the cluster, we need spectroscopic redshifts for these galaxies. In addition, these redshifts will give us much more accurate distances to the clusters. We also need to obtain good CCD images for the fields that currently have only poor or bad data. We also need better CCD photometry in *VRI* covering a field of view large enough to encompass the whole cluster ($\theta_A > 6$ arcminutes, therefore the angular diameter is greater than 12 arcminutes – see footnote in Chapter 1). Since we want to look for the Butcher-Oemler effect in these clusters, the CCD images must be deep enough so we are certain we are complete to rest frame $M_V = -20$ (often fainter than R=22 for clusters with z>0.4). This involves the investment of a large amount of telescope time, particularly if the telescope aperture is only 1.3m. Currently, we will not gain much by using the 2.4m telescope, since the field-of-view with this telescope is limited unless we add reducing optics to match the CCD pixels to the seeing (see §8.2 below). We can also alleviate the field-of-view problem by building bigger CCDs (see §8.2c below).

b) A Case for Multi-Object Spectroscopy

CCD photometry is good, but spectroscopy is better! Spectra allow us to separate cluster members from field galaxies, and offer clues about the physics of the blue galaxies. Photometry offers tantalizing hints that distant clusters are undergoing dramatic evolution compared to clusters today. Spectroscopy confirms it (Dressler and Gunn 1982, 1983; Sharples *et al.* 1985; Lavery and Henry 1986; Newberry, Kirshner, and Boroson 1988; Couch and Sharples 1987). Moreover, spectroscopic observations of very distant clusters (z>0.5) are revealing galaxies very different than those nearby (Dressler 1987). Unfortunately, spectroscopy of faint galaxies requires an enormous amount of telescope time: a typical L^* galaxy in a z=0.75 cluster requires ~5 hours of integration time on a 5m telescope to get an absorption-line spectrum with enough signal-to-noise to measure line strengths (Gunn 1989). It is not practical to obtain spectra for many galaxies in clusters at this redshift with a 2.4m telescope, but it should be possible for clusters with 0.3<z<0.5. The amount of

information collected can be increased dramatically when the spectra of many (>10) galaxies be obtained simultaneously, using a multi-object spectrometer (see Ellis *et al.* 1988; Geary *et al.* 1986).

We plan to attempt spectroscopy of galaxies in the richest clusters described in Chapters 6 and 7 that are accessible with the 2.4m telescope. These include 4C 23.37, 4C 58.22, Cl 0414+009, Cl 1358+24, Cl 0903+26, Cl 1234+26, and certainly Cl 1358+6245. We hope to observe some of the fainter clusters with larger telescopes.

8.2 Completion of the Instrument and Planned Modifications

a) LL 840 × 840 Electronics

A functioning Quad CCD from Lincoln Laboratory has not been delivered before completion of this thesis. In any case, the multiple-CCD control electronics, which are in the final stage of construction, are not currently able to run such a device. Nevertheless, the performance of the mosaic device is expected to be comparable to that of the individual CCID-7 CCDs that have been tested in our laboratory. The x-ray histogram in Figure 8.1 illustrates the capabilities of these CCDs (this data was taken and kindly provided by Mark Bautz). Histograms of this quality, showing the low noise and excellent charge-transfer properties of these CCDs, have been taken in our laboratory using a system whose electronics are based on the design described in Chapter 4.

b) Reducing Optics for the 2.4m Telescope

When the TI CCDs (22μm pixels) and the Lincoln Laboratory CCDs (27μm pixels) are used on the 2.4m telescope (f/7.5), the resulting image scales are 0.25 arcsec/pixel and 0.30 arcsec/pixel respectively. In both cases, we are drastically oversampling the typical MDM Observatory/Kitt Peak seeing disk (1.0 to 1.5 arcsecs FWHM at best) and sacrificing useful field of view. Image reducing optics are required if we want to get back the field of view. The optical design of the reducer for this instrument is based partially on commercially available lenses used for the PFUEI at Palomar Observatory (Gunn and Westphal 1982). The optical design is a standard collimator/camera design where the collimator lens is placed its own focal length behind the telescope focal plane and the camera lens re-images the resulting parallel beam onto the CCD. The magnification (or "minification" in the case of a focal reducer) of this lens combination is simply the ratio of the collimator and camera focal lengths. Filters (or possibly a grism, see §8.2c) are placed in the parallel beam between the two lenses. The lens obtained for the collimator is a 135mm f/2.0 Nikon Xero-Nikkor. This excellent lens produces very sharp images and its field of view is large enough that a field lens near the focal plane is unnecessary. Two lenses were obtained to serve as interchangeable cameras: a 58mm f/1.2 Nikon Noct-Nikkor lens or an 85mm f'/1.2 Zeiss lens. With the 58mm Nikon lens used as the camera, the minification is 2.33:1 and the image scales become 0.58 arcsec/pixel and 0.70 arcsec/pixel for the TI and LL CCDs respectively. When the 58mm lens is replaced with the 85mm Zeiss lens, the minification becomes 1.59:1 and the image

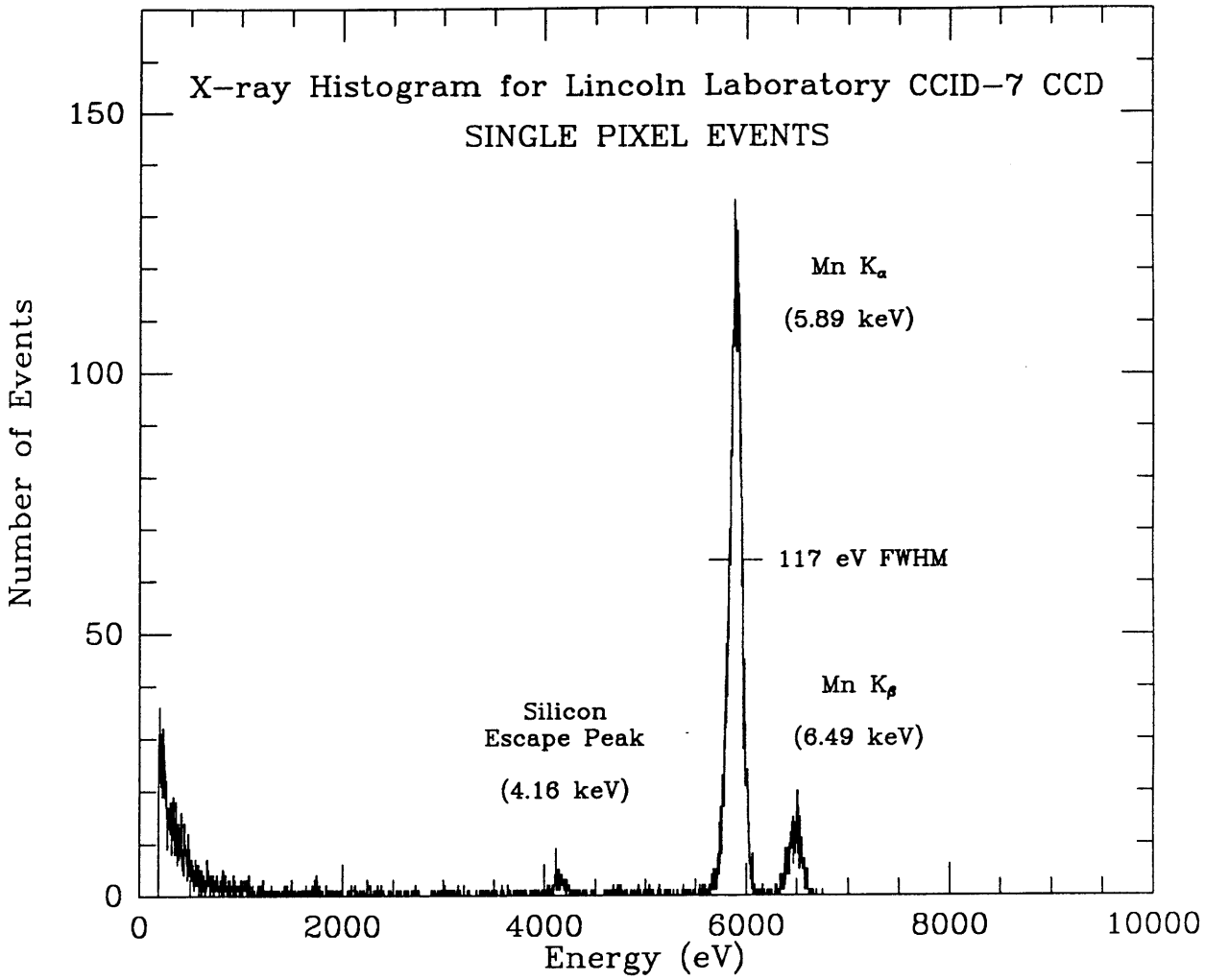

FIGURE 8.1 Histogram of events for an MIT Lincoln Laboratory CCID-7 CCD illuminated by an ^{55}Fe x-ray source (this data was kindly provided by Mark Bautz). Only events confined to a single pixel, over the the entire 420 × 420 pixel area of the imager, were used to generate this plot. This histogram illustrates the very low noise and excellent charge-transfer properties of this CCD. The gaussian x-ray peak with FWHM of 117 eV has an rms noise of 117/2.35=50 eV which is equivalent to 13.7 electrons. When the shot noise contribution is removed from the total noise, the readout noise is 5 electrons.

scales are reduced to 0.40 arcsec/pixel and 0.48 arcsec/pixel for the TI and LL CCDs. Clearly, these standard 35mm camera lenses cannot cover a focal plane as large as the Quad TI mosaic. These optics will only be used for a single TI chip, or the LL 840 × 840 CCD.

Table 8.1 Image Scales and Field of View for Instrument CCDs with Reducing Optics

	58mm camera		85mm camera	
CCD	Scale	Field	Scale	Field
TI 4849	0.58	5'.6 × 3'.8	0.40	3'.9 × 2'.6
TI 850 × 750	0.58	8'.2 × 7'.3	0.40	5'.7 × 5'.0
LL 840 × 840	0.72	9'.8 × 9'.8	0.49	6'.7 × 6'.7

The assembly drawing illustrating the layout of the optical components as well as the filter wheel and the mechanical design of the box to "hold it all together" is shown in Figure 8.2.

Construction of the reducing optics has proceeded in parallel with the work described in the earlier chapters. All of the optics are in hand, and machining of the "foundation" of the instrument box is complete. The optics were tested briefly on the 2.4m telescope during the "disaster run" of December 1988. The image quality was excellent, but the throughput of the optics was terrible. It was later discovered that the collimator lens is uncoated and is probably the cause of the greatly reduced system efficiency. Once this suspicion is verified in the lab, the lens will be sent out to be disassembled and anti-reflection coated.

c) Conversion of the Instrument to a Low-Resolution, Multi-Object Spectrograph

The extremely low readout noise of the Lincoln Laboratory CCDs makes them ideal detectors for spectroscopy of faint objects. Therefore, the reducing optics are were designed so that the instrument can be easily converted to a low-resolution, multi-object spectrograph. This section outlines the steps necessary for this conversion.

The primary components of the spectrograph are the 1) slit (or multi-slit assembly), 2) collimator optics, 3) dispersing element 4) camera optics, and 5) detector. The collimator, camera and detector already exist for this instrument: we merely need to add a slit (or multi-slit) assembly and a dispersing element that are chosen so their properties, coupled with those of the reimaging optics, yield the spectroscopic performance required. The quantitative relationships between the various components that make up the spectrograph are described below.

In order to preserve the mechanical simplicity of the reimaging optics, we chose a grating-prism (grism) as the dispersing element. A grism is simply a blazed transmission grating that is mounted on the hypotenuse face of a right-angle prism. The grism is inserted in the parallel beam just in front of the camera. When used in the

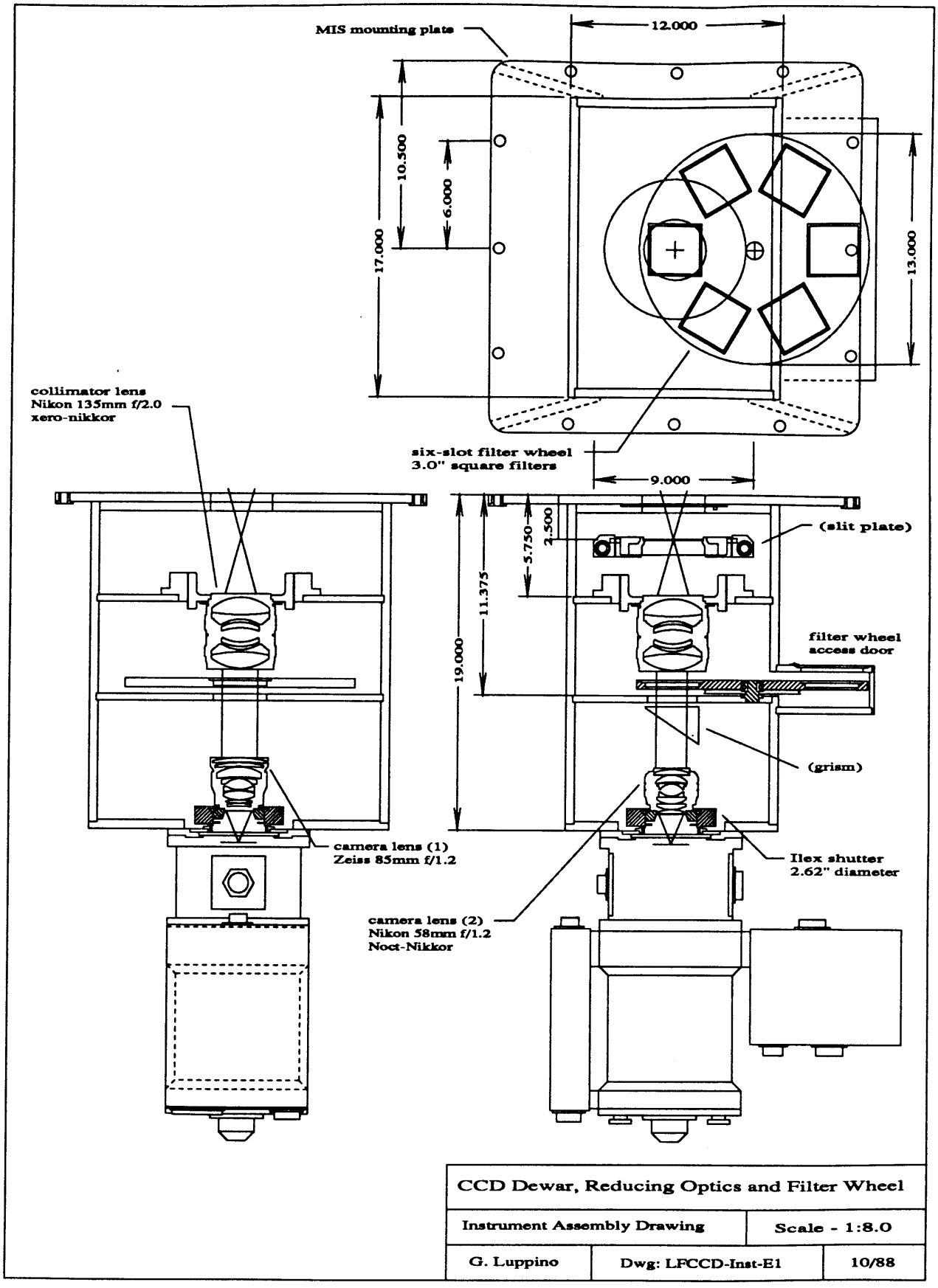

FIGURE 8.2 Instrument reducing optics. Position of slit (or multi-slit) and grism are shown in lower right view.

configuration shown in Figure 8.2, where the normal to a face is parallel to the optical axis, the light is bent out of the optical axis by the prism, only to be diffracted back in line by the transmission grating. The prism deflects the zeroth order well out of the beam, but the first order dispersed spectrum is centered on the optical axis. The prism angle, θ, is chosen so that the central, undeviated wavelength, λ_0, is given by

$$\lambda_0 = \frac{a}{m}(n-1)\sin\theta \tag{8.1}$$

where n is the index of refraction of the prism material (typically around 1.5 for most glasses), m is the order, and a is line spacing (period) of the grating. This equation is only true when the grism is used as in Figure 8.2, and the prism angle and the grating blaze angles are equal. This orientation is best because it yields the highest throughput for the grism (Bausch and Lomb *Diffraction Grating Handbook*). The prism has no effect on the dispersion of the spectrograph: it only serves to keep the dispersed spectrum centered on the optical axis. Therefore, the equations for a normal grating spectrograph are true here. The angular dispersion of the spectrograph, $d\theta/d\lambda$, is given by

$$\frac{d\theta}{d\lambda} = \frac{m}{a\cos\theta} \tag{8.2}$$

and the corresponding linear dispersion, D, in Å/mm is

$$D = \frac{1}{f_{cam}\dfrac{d\theta}{d\lambda}} \tag{8.3}$$

if the camera focal length, $f_{\rm cam}$, is given in mm and the angular dispersion is given in Å^{-1}. For a 30° prism with n=1.5, and a 600 l/mm grating (600 l/mm so a = 16700 Å), the central wavelength is 4180 Å. When coupled with the 58mm camera lens, this grism has a linear dispersion of 250 Å/mm: or 6.7 Å/pixel with the Lincoln Laboratory CCD. This, however, is not the limiting resolution of the spectrograph. The resolution will be determined by the width of the slit that is imaged onto the CCD, and this depends on the actual slit size and the minification of the collimator/camera combination. The optimal slit width depends critically on the seeing. Ideally, one would like a narrow slit, but it must be large enough to encompass as much of the light as possible from a faint galaxy. For illustration, we will assume we are using a two arcsecond slit, a realistic number for these types of observations. The 2.4m telescope has a focal-plane scale of 11.46 arcsec/mm, and the minification of the reducing optics (with the 58mm camera) 2.33:1. As listed in Table 8.1, the image scale at the CCD is 0.72 arcsec/pixel and a 2 arcsec slit maps onto 2.76 CCD pixels. Since the linear dispersion of the grism is 6.7 Å/pixel, the limiting resolution of the spectrograph in this configuration is 18.5 Å.

d) Next-generation, Improved, Very-Large-Format CCD Designs

Observational astronomers will always want larger and larger detectors. Early-generation CCD mosaics, such as those described in §4.3 and §8.1, are just the first steps toward very-large-format sensors that will tile the focal planes of large telescopes and provide photographic-plate size, panoramic images of the night sky. However, two technical goals that must be achieved first. The quantum-efficiency of the devices must be maximized, and the size of the CCD–tiles (the individual CCDs that make up the mosaic) must be increased.

The optical quantum-efficiency of CCDs can be increased by building the devices on high-resistivity silicon, and by thinning and illuminating through the anti-reflection-coated back side[1]. The Lincoln Laboratory Group plans to produce thinned backside-illuminated versions of these CCD mosaics, built on high-resistivity (100-1000 Ω-cm) epitaxial silicon. The planned thinning and mounting procedure is briefly described below. The completed wafers are bonded, face (gateside) down onto a substrate. The wafer is then etched from the backside until the proper thickness (~tens of microns) is achieved. The backside surface is then treated by ion implantation and is laser annealed. Holes are etched through the silicon to pick up the bonding pads that are on the frontside of the device. The individual CCD dies are then sawed from the wafer and assembled into a mosaic as described for the frontside illuminated devices.

This ion implantation and laser annealing process should eliminate backside surface traps and allow good blue response without special treatments such as UV flooding (Janesick *et al.* 1987). The properly passivated backside can also be anti-reflection (AR) coated which will dramatically improve the optical quantum efficiency of the devices. AR coating is particularly important: the index of refraction of silicon has a value $n = 4$ over most of the optical portion of the spectrum (Lesser 1987). There is a sharp peak at ~4000Å where the index rises to 7 and then drops to ~5 on the blue side. The normal incidence reflection coefficient for light traveling from a medium of index of refraction n_1 into a material of index of refraction n_2 is given by

$$R = \left(\frac{n_2 - n_1}{n_2 + n_1} \right)^2 \tag{8.4}$$

Therefore, 36% of the light with $\lambda > 4000$Å is lost by reflection from bare silicon. In the narrow region around 4000Å, 56% of the light is reflected while blueward of 4000Å, 44% is lost. Clearly, the QE of a CCD can be

---

[1] For long-wavelength optical light, the quantum-efficiency (QE) of a CCD depends on the thickness of the depleted epitaxial silicon in which photogenerated electrons can be collected; however, the short-wavelength optical QE depends on the transparency of any absorptive layers that may exist on the surface of the device through which the photons must pass. CCDs are often illuminated through the polysilicon gates on the frontside. These gates are essentially opaque for photons with $\lambda<4000$. In order to improve their short-wavelength optical response, CCDs can be thinned from the backside, exposing the sensitive epitaxial layer silicon. These thinned devices can then be illuminated from the backside.

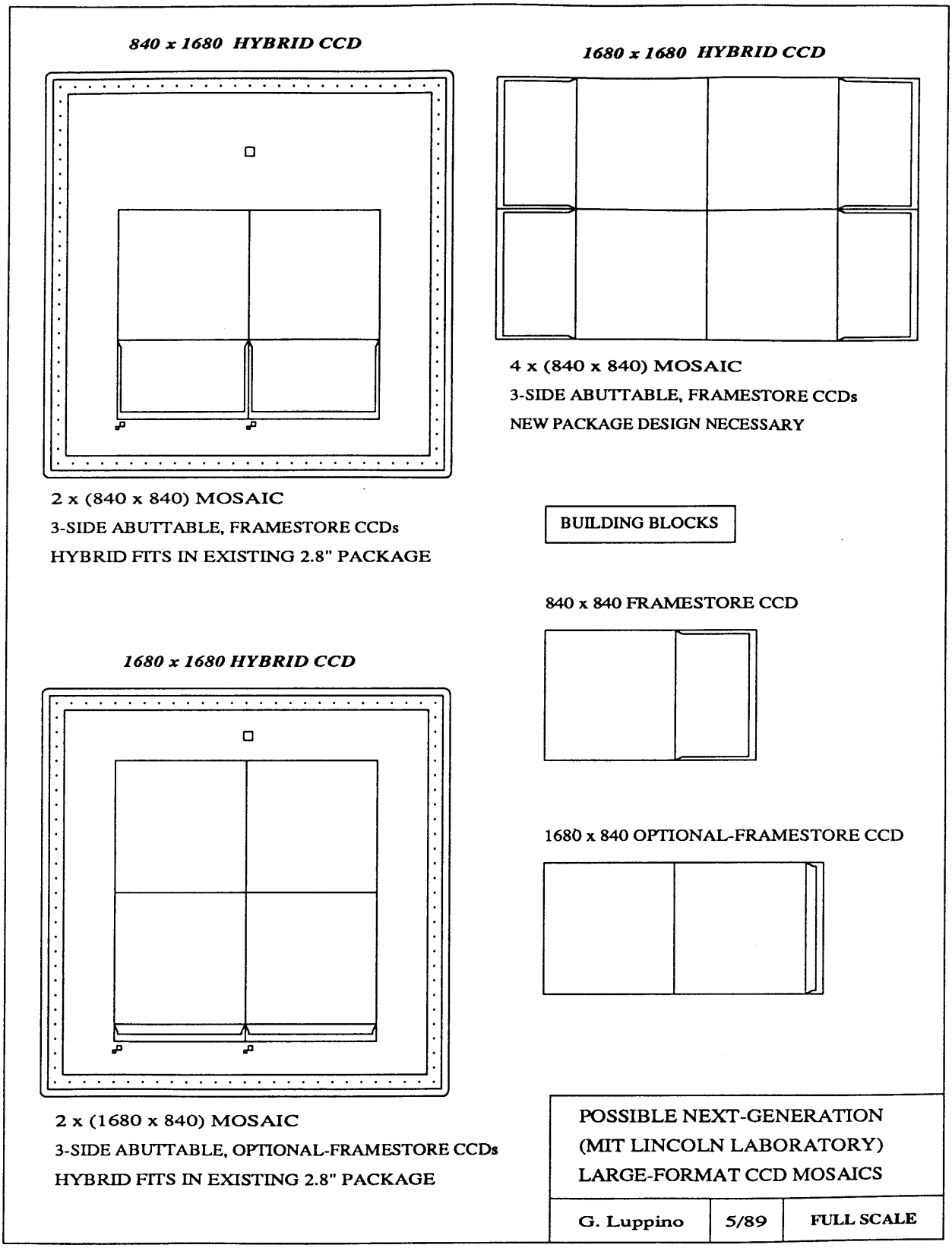

FIGURE 8.3 Some possible designs and configurations for future, large-format, abuttable CCDs. All CCDs are drawn to scale and have 27 μm square pixels.

improved dramatically if materials of the proper index of refraction can be found from which to make AR coatings. See Lesser (1987) and Lesser (1988) for additional details concerning AR coating of CCDs.

In addition to improving the QE of the devices, we hope to develop designs for a larger, abuttable CCD–tile that can be used to make very–large–format CCD mosaics. Two possible designs for these "building blocks," and some mosaics based on these building blocks are shown in Figure 8.3. The framestore device has smaller, rectangular pixels in the framestore region (similar to the LL CCID-7). The optional-framestore device is built with the framestore region having the same size pixels as the imaging area; therefore, the framestore region can be used for imaging if the framestore cover is not applied to the sensor. Unfortunately, the horizontal gap size will increase by about 2-4 pixels to 8-10 pixels for mosaics built with these devices, since room must be made for the extra set of parallel clock busses that run up the side of the device (see Figure 4.13 and 4.14).

REFERENCES:

Bausch and Lomb *Diffraction Grating Handbook* 1970 (Rochester: Bausch and Lomb).

Couch, W., and Sharples, R. 1988, "A Spectroscopic Study of Three Rich Galaxy Clusters at z=0.31," *M.N.R.A.S.*, **229**, 423.

Dressler, A., and Gunn, J.E. 1982, "Spectroscopy of Galaxies in Distant Clusters. I. First Results for 3C295 and 0024+1654," *Ap.J.*, **263**, 533.

Dressler, A., and Gunn, J.E. 1983, "Spectroscopy of Galaxies in Distant Clusters. II. The Population of the 3C295 Cluster," *Ap.J.*, **270**, 7.

Ellis, R. and Parry, I. 1988, "Multiple Object Spectroscopy," in *Instrumentation for Ground-Based Optical Astronomy*, ed, L. Robinson, (New York: Springer), p192.

Geary, J.C., Huchra, J.P., and Latham, D.W. 1986, "A Faint-Object Grism Spectrograph with Multiple Slits and CCD Detector," in *Proceedings of the SPIE: Instrumentation in Astronomy VI*, **627**, 509.

Gunn, J.E., and Westphal, J.A. 1981, *Proc. S.P.I.E.*, **290**, 16.

Gunn, J.E. 1989, in *Clusters of Galaxies: STScI Workshop on Clusters of Galaxies.*

Janesick, J., Elliot, T., Collins, S., Blouke, M., and Freeman, J. 1987, "Scientific Charge-Coupled-Devices," *Optical Engineering*, **26**, 692.

Lavery, R.J., and Henry, J.P. 1988, "Evidence for Galaxy-Galaxy Interactions as an Active Agent of the Butcher-Oemler Effect at a Redshift of 0.2," *Ap.J.*, **330**, 596.

Lesser, M. 1987, "Antireflection Coatings for silicon CCDs," *Optical Enginering*, **26**, 911.

Lesser M. 1988, "CCD Optimizations for Astronomy," Ph.D. Thesis, University of Arizona.

Newberry, M.V., Kirshner, R.P., and Boroson, T.A. 1988, "Spectra of Galaxies in Clusters. I. The Butcher-Oemler Effect," *Ap.J.*, **335**, 629.

Sharples, R., Ellis, R., Couch, W., and Gray, P. 1985, "Multi-object Spectroscopy of the Distant Cluster AC103," *M.N.R.A.S.*, **212**, 687.